

OBSERVATIONS AND MODELING OF THE CO₂-CARBONIC ACID
SYSTEM ON HAWAIIAN CORAL REEFS: IMPLICATIONS OF FUTURE
OCEAN ACIDIFICATION AND CLIMATE CHANGE

A DISSERTATION SUBMITTED TO THE GRADUATE DIVISION OF THE
UNIVERSITY OF HAWAI‘I AT MĀNOA IN PARTIAL FULFILLMENT
OF THE REQUIREMENT FOR THE DEGREE OF

DOCTOR OF PHILOSOPHY

IN

OCEANOGRAPHY

DECEMBER 2015

By

Patrick S. Drupp

Dissertation Committee:

Eric H. De Carlo, Chairperson

Fred T. Mackenzie

Michael Guidry

Frank Sansone

Margaret McManus

Megan Donahue

Keywords: carbon dioxide, ocean acidification, coral reefs, sediments

TABLE OF CONTENTS

Acknowledgements.....	v
Abstract.....	vii
List of Tables.....	ix
List of Figures.....	xi
Chapter 1 Anthropogenic Effects on Ocean Chemistry.....	1
1.1 Introduction.....	1
1.2 Ocean Acidification and Coral Reefs.....	9
1.3 Dissertation Objectives.....	11
1.4 References.....	16
Chapter 2 Comparison of CO ₂ Dynamics and Air-Sea Exchange in Differing Tropical Reef Environments.....	19
2.1 Abstract.....	19
2.2 Introduction.....	20
2.3 Study Rationale.....	21
2.4 Methodology.....	23
2.4.1 Environmental Setting.....	23
2.4.2 In-situ Measurements.....	27
2.4.3 Sample Analysis.....	29
2.4.4 Calculations.....	29
2.5 Results.....	31
2.6 Discussion.....	45
2.6.1 Physical Controls of pCO ₂	45
2.6.2 Biogeochemical Controls of pCO ₂	48
2.6.3 Air-Sea Gas Exchange.....	54
2.7 Conclusions.....	57
2.8 Acknowledgments.....	59
2.9 References.....	60
Chapter 3 Porewater CO ₂ -Carbonic Acid System Chemistry in Permeable Carbonate Reef Sands	65
3.1 Abstract.....	65
3.2 Introduction.....	66
3.3 Methodology.....	70
3.3.1 Study Sites.....	70
3.3.1.1 Kaneohe Bay barrier reef.....	71
3.3.1.2 Ala Wai.....	71
3.3.2 Porewater sampling protocol.....	73
3.3.3 Porewater and sediment sample analyses.....	74
3.3.3.1 Field determinations.....	74
3.3.3.2 Laboratory porewater analysis.....	74

3.3.3.3 Laboratory sediment analysis	76
3.3.3.4 CO ₂ -carbonic acid system calculations.....	78
3.4 Results	79
3.4.1 Porewater profiles.....	79
3.4.1.1 Measured parameters – CRIMP-2	79
3.4.1.2 Measured parameters – Ala Wai.....	80
3.4.1.3 Calculated parameters – CRIMP-2.....	82
3.4.1.4 Calculated parameters – Ala Wai	83
3.4.2 Sediment analysis	87
3.4.2.1 CRIMP-2.....	87
3.4.2.2 Ala Wai	88
3.5 Discussion	92
3.5.1 TA depth profiles.....	92
3.5.2 TA vs. DIC	94
3.5.3 Saturation state of porewater with respect to carbonate minerals	107
3.5.4 Flushing events	108
3.6 Conclusions and Future Considerations.....	112
3.7 Acknowledgments.....	116
3.8 References	117
Chapter 4 The Effects of Increasing Ocean Acidification and Temperatures on a Barrier Reef Ecosystem, Kaneohe Bay, Hawai‘i.....	124
4.1 Abstract	124
4.2 Introduction	125
4.3 CRESCAM Model Development.....	131
4.3.1 CRESCAM Domain and Initial Carbon Reservoirs.....	132
4.3.1.1 Surface water domain	132
4.3.1.2 Permeable sediments domain.....	134
4.3.1.3 Reef framework domain	137
4.4 CRESCAM Initial Carbon Fluxes.....	139
4.4.1 Surface water domain	140
4.4.1.1 Physical processes.....	140
4.4.1.2 Biogeochemical processes	146
4.4.2 Permeable sediments domain	150
4.4.2.1 Physical Processes	150
4.4.2.2 Biogeochemical Processes	153
4.4.3 Reef framework domain	158
4.5 Model Forcings	159
4.6 Results and Discussion of the Standard Run.....	161
4.6.1 Surface water response to increased atmospheric CO ₂	161
4.6.2 Porewater CO ₂ -carbonic acid system chemistry	166

4.6.3 Net Ecosystem Carbonate Production (NECP)	175
4.6.4 Ocean-Atmosphere CO ₂ Exchange	181
4.6.5 Net Ecosystem Production (NEP)	184
4.7 Case Studies	191
4.7.1 Case Study 1: Changing TA in the surface water.....	192
4.7.2 Case Study 2: Air-Sea CO ₂ Gas Exchange.....	195
4.7.3 Case Study 3: Sediment and Framework Porewaters.....	199
4.7.4 Case Study 4: Analysis of NEP	204
4.8 Conclusions	209
4.9 References	212
Chapter 5 Conclusions	220
5.1 Summary of Results	220
5.2 References	226
Appendix Model Code and Calculations	228
A.1 MATLAB Code.....	228
A.2 Mass Balance Equations.....	264
A.3 Flux Equations.....	266
A.4 Calculations for Initial Carbon Reservoirs.....	270
A.5 Calculations for Initial Carbon Fluxes	273
A.6 References	284

ACKNOWLEDGEMENTS

Many people were instrumental in the completion of this research. I would like to first acknowledge and thank Eric De Carlo, my advisor, colleague, and friend since I first began my graduate research as a Master's student at University of Hawai'i in 2007. Without his continuous support, this dissertation could not have happened. I would also like to thank Fred Mackenzie, who served as a vital co-advisor and mentor. Our many coffee breaks and long discussions provided the basis for much of this research. Thank you both for your mentorship and friendship over the years. I would also like to thank my other committee members. Thanks to Michael Guidry for his advice and support on how to survive as a grad student, as well as helping me through the struggles of the modeling research. Thanks also to Frank Sansone for his substantial input and Margaret McManus, who is the only reason I was accepted into the program in 2007. Finally, thanks to Megan Donahue for her important and helpful insights as the outside member of the committee.

I would also like to thank all of the past and present members of the De Carlo lab: Gerianne Terlouw, Ryan Tabata, Bobby Thompson, Kristen Fogaren, Michelle Wong, Didier Dumas, Keo Lopes, Rachel Solomon-Massaró, Jeff Jaegger, Joelle Kubunec, and Sami Chen. Their help in the field and the lab was critical to the success of this research. Thank you to my friends, classmates, and colleagues Becca Simpson, Max Grand, Saulo Soares, and many more, including my many teachers and the entire Oceanography Class of 2007. A huge thanks goes to Kathy Kozuma, our division secretary. Kathy's expertise and help with everything necessary to keep our lab functioning was instrumental. I am also thankful for the wonderful help of the Oceanography Office staff: Nancy Koike, Pamela Petras, Catalpa Kong, and especially Kristen Momohara who continually ensured that I had the proper forms and documents necessary to

graduate. I am grateful for the help of the support staff at both the Marine Science Building and Coconut Island: Fritz King, Phil Rapoza, Jason Jones, and many more who helped with marine operations over the years.

Thanks to Christos Michalopoulos, Carrie McDougall, and everyone from the NOAA Office of Education who have been so supportive during my fellowship year and who have cheered me through the final months of the dissertation process.

I would also like to acknowledge the financial support for both this research and my salary provided by the University of Hawai'i Sea Grant, the NOAA PMEL Carbon Group, PacIOOS, and the NOAA Ocean Acidification Program. Thanks to the folks at PMEL: Chris Sabine, Dick Feely, Stacy Maennar-Jones, and especially Sylvia Musielewicz for the continued support of the buoy network that was vital to this research. In addition, thanks to Darren Lerner, Darren Okimoto, and Cindy Knapman for support of my research assistantship, as well as their help in my Knauss Fellowship year.

I want to thank my friends and family back home for the continued love and support of my mom and dad, my brother Rob, and everyone else who have helped me reach this point. Finally, thank you Carrie for all that you have done. There is no way I could have completed this adventure without you.

ABSTRACT

The CO₂-carbonic acid system of nearshore and coral reef ecosystems is highly variable, and often poorly constrained. In addition to the natural processes altering the carbon system of coral reefs, increased atmospheric and seawater carbon dioxide (CO₂) concentrations, from the anthropogenic burning of fossil fuels and land use changes, have the potential to alter the fragile biogeochemical balance of these ecosystems. Autonomous seawater CO₂ monitoring buoys are becoming an increasingly utilized method for studying the CO₂ chemistry of coastal waters, and these systems provide accurate, high-resolution CO₂ data that were previously unobtainable a decade ago. This research presents the results of the longest running, continuous CO₂ time-series for a coral reef environment in the world. A network of three monitoring buoys was established in 2008 around Oahu, Hawai‘i, providing high-resolution data. Net annualized air-sea CO₂ gas exchange was calculated at each study location and was comparable to estimates at other reef locations around the world. An *in-situ* study of the permeable carbonate sediment-porewater system at two locations showed that porewater carbon biogeochemistry in permeable reef sediments is strongly controlled by microbial respiration of organic matter. The short residence time of the porewater, due to increased advection, is another major control on the biogeochemical parameters such as total alkalinity and pH. Finally, the data collected by the observing buoys, along with the *in-situ* porewater data and previous data collected in Kaneohe Bay, were used to create a carbon biogeochemical box model, the Coral Reef and Sediment Carbonate Model (*CRESCAM*), for the Kaneohe Bay barrier reef flat. The model was forced using the Representative Concentration Pathway CO₂ emissions scenarios from the 2013 Intergovernmental Panel on Climate Change 5th Assessment Report. Several case studies were conducted to determine important parameters and to identify possible future conditions on the

barrier reef under increasing ocean acidification, rising temperature, and land use changes.

Model runs predicted that the barrier reef flat could experience a 20% decrease in coral calcification, by 2100. Although carbonate dissolution is expected to increase in the sediments, dissolution will not provide a sufficient buffer to mitigate any decreases in surface water pH.

LIST OF TABLES

Table 2.1: Seawater pCO ₂ for the CRIMP-2, Ala Wai, and Kilo Nalu study locations	32
Table 2.2: Seawater pCO ₂ daily range statistics for the CRIMP-2, Ala Wai, and Kilo Nalu study locations	37
Table 2.3: Seawater pCO ₂ and pO ₂ correlations and pCO ₂ autocorrelation at CRIMP-2, Ala Wai, and Kilo Nalu	37
Table 2.4: Instantaneous and annualized air-sea CO ₂ fluxes at CRIMP-2, Ala Wai, and Kilo Nalu.....	42
Table 2.5: Annualized and seasonal air-sea CO ₂ fluxes at CRIMP-2, Ala Wai, and Kilo Nalu..	42
Table 2.6: CO ₂ -carbonic acid system parameters at CRIMP-2, Ala Wai, and Kilo Nalu	43
Table 3.1: Sediment grain size fractions at CRIMP-2 and Ala Wai	90
Table 3.2: Total carbon, total inorganic carbon, and C/N ratios at CRIMP-2 and Ala Wai	91
Table 3.3: Mol% MgCO ₃ content of the sediments at CRIMP-2 and Ala Wai	92
Table 4.1: Initial reservoir sizes for <i>CRESCAM</i>	139
Table 4.2: Initial DIC concentrations used to calculate initial steady-state fluxes and reservoir sizes in <i>CRESCAM</i>	144
Table 4.3: Annualized air-sea CO ₂ gas exchange for several coral reef ecosystems.....	146
Table 4.4: CO ₂ -carbonic acid system parameters of <i>CRESCAM</i> for the reef surface water in 2015 and 2100 under the various IPCC RCP CO ₂ emissions scenarios	164
Table 4.5: Surface water saturation state with respect to 11 -18 mol% Mg-calcite compositions in <i>CRESCAM</i>	165
Table 4.6: Oxidic porewater CO ₂ -carbonic acid system parameters from <i>CRESCAM</i> , under the various IPCC RCP CO ₂ emissions scenarios.....	174
Table 4.7: Anoxic porewater CO ₂ -carbonic acid system parameters from <i>CRESCAM</i> , under the various IPCC RCP CO ₂ emissions scenarios.....	175
Table 4.8: Framework porewater CO ₂ -carbonic acid system parameters from <i>CRESCAM</i> , under the various IPCC RCP CO ₂ emissions scenarios.....	175
Table 4.9: Net ecosystem carbonate production from <i>CRESCAM</i> , under the various IPCC RCP CO ₂ emissions scenarios	179

Table 4.10: Photosynthesis, respiration, and NEP from CRESCAM, under the various IPCC RCP CO ₂ emissions scenarios	188
Table 4.11: Summary of the overall changes of important processes and parameters in CRESCAM by 2100 under each RCP forcing scenario.....	190
Table 4.12: List of case studies and the changes made to various parameters within CRESCAM, as compared to the standard run.....	191
Table 4.13: Surface water TA under various $\Delta TA:\Delta DIC$ ratios used in CRESCAM	194
Table 4.14: Percent offset in pH values for each sensitivity analysis of the case study relative to the standard run in the final year 2100.....	194
Table 4.15: Air-sea CO ₂ gas exchange rates under various CRESCAM case studies	199
Table 4.16: Net ecosystem carbonate production in the oxic layer sediments for the CRESCAM standard run and case studies.....	201
Table 4.17: Net ecosystem carbonate production of the reef flat under the standard CRESCAM run and case studies.	204
Table 4.18: Net ecosystem production under various scenarios of increasing organic carbon and nitrogen loading to the reef	208
Table 4.19: Net ecosystem carbonate production of the overall reef system under the standard run and the case study where OC and N were doubled	209

LIST OF FIGURES

Figure 1.1: Anthropogenic contributions to the global carbon cycle from 2004-2013	3
Figure 1.2: Atmospheric CO ₂ concentrations, measured at the Mauna Loa Observatory	3
Figure 1.3: Global averaged temperature anomaly	5
Figure 1.4: Representative concentration pathways CO ₂ emissions scenarios.....	6
Figure 1.5: Surface pH observations and projections	9
Figure 1.6: Conceptual model of CRESCAM	11
Figure 1.7: Number of publications per year from 2005-2013 about dissolution	12
Figure 2.1: Map of Oahu and Kaneohe Bay study areas.	25
Figure 2.2: pCO ₂ data from CRIMP-2, Ala Wai, and Kilo Nalu locations	33
Figure 2.3: Monthly mean pCO ₂ and weekly water temperature	36
Figure 2.4: pCO ₂ and pO ₂ at CRIMP-2 buoy	38
Figure 2.5: Autocorrelation of hourly pCO ₂ at CRIMP-2	39
Figure 2.6: Air-sea gas exchange of CO ₂ at all three buoy locations	40
Figure 2.7: Total alkalinity measured at each buoy location from 2009-2011	44
Figure 2.8: A _T vs. C _T at CRIMP-2, Ala Wai, and Kilo Nalu.....	44
Figure 2.9: A _T vs. salinity plot at CRIMP-2	49
Figure 3.1: CRIMP-2 and Ala Wai buoy study locations.....	72
Figure 3.2: Total alkalinity porewater profiles at CRIMP-2 and Ala Wai	81
Figure 3.3: pH porewater profiles at CRIMP-2 and Ala Wai.....	82
Figure 3.4: Dissolved inorganic carbon porewater profiles at CRIMP-2 and Ala Wai.....	85
Figure 3.5: pCO ₂ profiles at CRIMP-2 and Ala Wai.....	85
Figure 3.6: Aragonite and high magnesian-calcite mineral saturation state porewater profiles at CRIMP-2 and Ala Wai.....	86
Figure 3.7: Permeability and porosity of sediments at CRIMP-2 and Ala Wai	89

Figure 3.8: TA vs. DIC in the porewaters at CRIMP-2 and Ala Wai.....	104
Figure 3.9: ΔnTA vs. $\Delta nDIC$ of CRIMP-2 and Ala Wai porewater	105
Figure 3.10: Current and historic nTA vs. nDIC in the porewater data from the carbonate and terrigenous facies of Kaneohe Bay	105
Figure 3.11: Effect of the C/N ratio of respired organic matter on DIC and saturation state....	106
Figure 3.12: Current and historic pH vs. TA in the porewater data from the carbonate and terrigenous facies of Kaneohe Bay.	106
Figure 3.13: Difference in TA between the surface water and at various sediment depths over three days at the Ala Wai location showing the flushing of porewater.	112
Figure 4.1: Map of the CRESCAM model area, Kaneohe Bay barrier reef	129
Figure 4.2: Conceptual diagram of <i>CRESCAM</i> showing the magnitude of the reservoirs and fluxes.....	130
Figure 4.3: Diagram of the surface water reservoirs and fluxes used in <i>CRESCAM</i>	133
Figure 4.4: Diagram of the sediment reservoirs and fluxes used in <i>CRESCAM</i>	135
Figure 4.5: Diagram of the reef framework reservoirs and fluxes.....	138
Figure 4.6: Major forcings of the <i>CRESCAM</i> model.....	162
Figure 4.7: Surface water CO ₂ -carbonic acid system outputs from <i>CRESCAM</i>	165
Figure 4.8: Saturation state calculations in <i>CRESCAM</i>	166
Figure 4.9: Porewater DIC concentrations from 2015 to 2100 from <i>CRESCAM</i>	168
Figure 4.10: Sediment Mg-calcite gross dissolution rates from <i>CRESCAM</i>	170
Figure 4.11: Gross calcification, bioerosion, and NECP fluxes from <i>CRESCAM</i>	178
Figure 4.12: Precipitation of aragonite and dissolution of Mg-calcite in the porewaters in <i>CRESCAM</i>	180
Figure 4.13: pCO ₂ in the surface seawater and atmosphere under each RCP scenario from 2015 to 2100 in <i>CRESCAM</i>	183
Figure 4.14: Air-sea CO ₂ exchange for each RCP from 2015 to 2100 in <i>CRESCAM</i>	183
Figure 4.15: Net ecosystem production (NEP) from 2015 to 2100 in <i>CRESCAM</i>	187
Figure 4.16: Surface water photosynthesis and respiration rates in <i>CRESCAM</i>	188

Figure 4.17: Total organic carbon in the seawater and sediment reservoirs from 2015 to 2100 in <i>CRESCAM</i>	189
Figure 4.18: Respiration rates in the porewaters from 2015 to 2100 in <i>CRESCAM</i>	189
Figure 4.19: Respiration rates, DIC, organic carbon flux, and reservoir size in the anoxic sediment layer domain from 2015 to 2100 in <i>CRESCAM</i>	190
Figure 4.20: Surface water pH from 2015 to 2100 under various surface water $\Delta TA:\Delta DIC$ ratios case studies in <i>CRESCAM</i>	195
Figure 4.21: Air-sea CO_2 gas exchange under the various surface water $\Delta TA:\Delta DIC$ ratios from 2015 to 2100 in <i>CRESCAM</i>	197
Figure 4.22: Comparison of porewater pH outputs from the standard <i>CRESCAM</i> run and a case study where the $\Delta TA:\Delta DIC$ ratio was set to 1.....	200
Figure 4.23: Comparison of aragonite saturation state of the oxic porewater from the standard <i>CRESCAM</i> run and a case study where $\Delta TA:\Delta DIC$ was set to 1	201

Chapter 1 ANTHROPOGENIC EFFECTS ON OCEAN CHEMISTRY

1.1 Introduction

For much of Earth's history, global climate and ocean chemistry have varied in a natural, cyclical fashion, and for thousands of years, humans have altered the environment on a local or regional scale via activities such as fishing, hunting, raising livestock, cultivating farmland, and mining resources. There is some evidence that human influence on the climate system began thousands of years ago (Ruddiman 2003), however, it was not until the mid-18th century, with the beginning of the Industrial Revolution, that humans significantly began to alter the *global* environment and began a period dominated by human influence known as the Anthropocene (e.g., Crutzen, 2002). The rise of a technologically advanced society, built on the combustion of fossil fuels as a cheap and plentiful energy source, caused us to begin what Professor Roger Revelle, former Director of the Scripps Institute of Oceanography, referred to as "Man's greatest geophysical experiment," recognizing the fact that "human beings are now carrying out a large scale geophysical experiment of a kind that could not have happened in the past" (Revelle and Suess 1957). In just 250 years, humans have significantly changed the environment by altering the temperature and chemical composition of both the global atmosphere and the global ocean through the release of ~ 2000 petagrams of carbon dioxide (1 Pg = 1 billion tons; 1 Pg of CO₂ = 0.27 Pg C) to the atmosphere from fossil fuel burning and deforestation (Le Quéré et al. 2014).

By actively burning fossil fuels that have been a geologic reservoir of carbon for millions of years, humans are altering the global carbon cycle at such a rapid pace that natural carbon removal processes cannot keep up on such short time scales (decades to centuries). Figure 1.1 shows the average anthropogenic (human-caused) effect on the global carbon system from 2004 - 2013. Approximately 50% of the CO₂ released from fossil fuel burning, cement production, and

land use changes (e.g., deforestation) remains in the atmosphere, resulting in atmospheric CO₂ concentrations increasing ~43% over pre-industrial levels (see Figure 1.2), from ~280 to 400 ppm (Le Quéré et al. 2014). The global surface ocean absorbs ~25% and the remaining amount is taken up by the terrestrial biosphere (land sink). Current atmospheric CO₂ concentrations are higher than they have been in the past 800,000 years (Petit et al. 1999; Augustin et al. 2004; Siegenthaler et al. 2005) and are probably higher than any time in the past 20 million years (Pearson and Palmer 2000).

Since 1880, the earth has warmed by approximately 0.85 °C, largely due to the emission of CO₂ (and its atmospheric accumulation) and the subsequent greenhouse effect (Intergovernmental Panel on Climate Change 2013a). According to the Intergovernmental Panel on Climate Change's 5th Assessment Report (IPCC 5th AR),

“Warming of the climate system is unequivocal, and since the 1950’s, many of the observed changes are unprecedented over decades to millennia”

Nearly the entire planet is experiencing some surface warming, and the last 30 years were “likely” the warmest 30-year period in the last 1400 years (see Figure 1.3) (Intergovernmental Panel on Climate Change 2013b). In addition, this warming trend has altered the cryosphere, the hydrologic cycle, sea level, and the occurrence of extreme weather events.

“Human influence has been detected in warming of the atmosphere and the ocean, in changes in the global water cycle, in reductions in snow and ice, in global mean sea level rise, and in changes in some climate extremes. This evidence for human influence has grown since AR4. It is extremely likely that human influence has been the dominant cause of the observed warming since the mid-20th century.” – IPCC 5th AR (Summary for Policymakers)

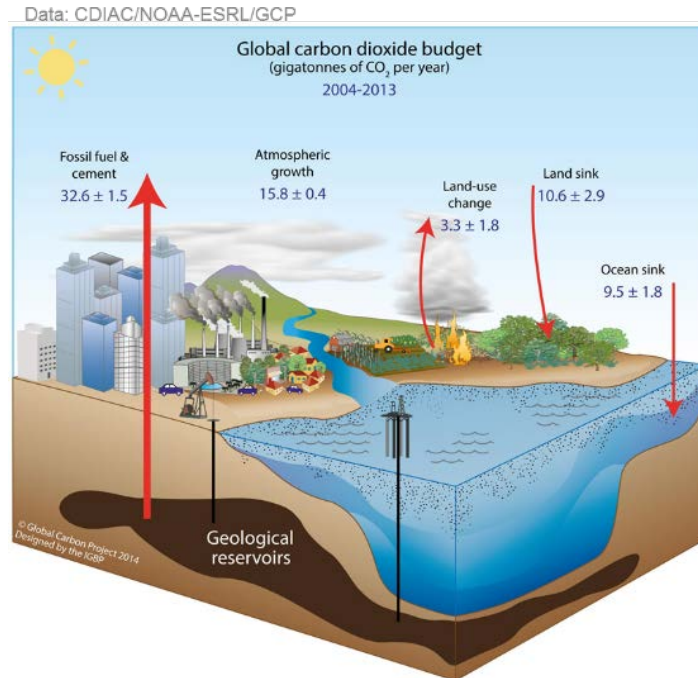


Figure 1.1: Anthropogenic contributions to the global carbon cycle from 2004-2013. Values are in gigatonnes (Pg) of CO₂ per year and are averaged globally. Approximately 90% of the total emissions are due to fossil fuel burning and cement production, with the remaining amount deriving from land-use changes and deforestation. The ocean absorbs ~26% , with ~50% remaining in the atmosphere (figure adapted from Global Carbon Project, 2014).

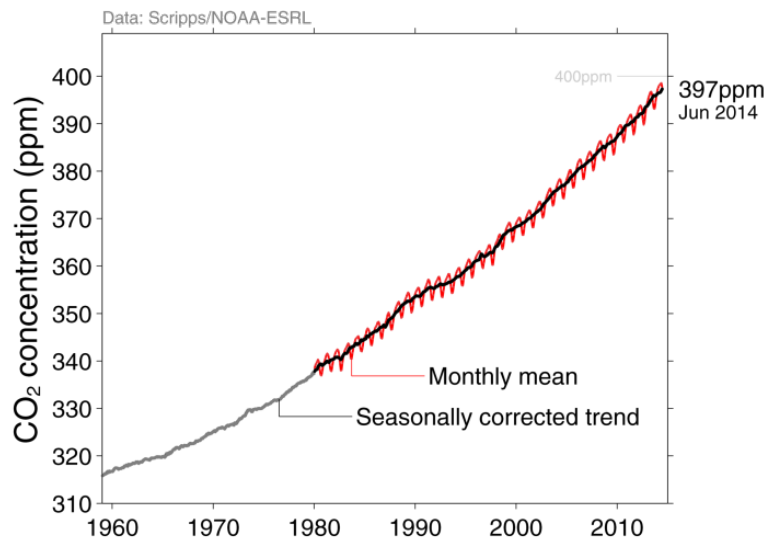


Figure 1.2: Atmospheric CO₂ concentrations, measured at the Mauna Loa Observatory in Hawai‘i have been steadily rising since the mid-20th century and are currently about 40% higher than pre-industrial levels (~280 ppm). In the early months of 2014, CO₂ concentrations passed 400 ppm (<http://scripps.ucsd.edu/programs/keelingcurve/>). The yearly oscillation in the data is due to seasonal changes in the CO₂ uptake via photosynthesis/respiration in the Northern Hemisphere biosphere (figure adapted from Global Carbon Project, 2014)

Much of the excess heat has been absorbed by the global ocean, accounting for ~90% of the total energy accumulated between 1971 and 2010 (Intergovernmental Panel on Climate Change 2013b). The planetary warming has caused a dramatic loss in ice mass and volume from both the Greenland and Antarctic ice sheets over the past two to three decades. The annual mean sea ice extent and summer sea ice minimum extent have decreased by ~4% and 10%, respectively, per decade since 1980 (Intergovernmental Panel on Climate Change 2013b). The warming and melting ice have led to rate of sea level rise in the past 50 years greater than the average rate over the past 2000 years (Intergovernmental Panel on Climate Change 2013b), and global sea level has risen by 0.19 m from 1901 to 2010.

Representative Concentration Pathway scenarios (Figure 1.4) were developed for the IPCC AR5 and project CO₂ emissions based on potential changes in the radiative forcing of the earth. Currently, emissions are keeping pace with the RCP 8.5 scenario (worst case), which will likely result in atmospheric CO₂ concentrations of ~1000 ppm and a 3 to 5.5 °C temperature change, by 2100, relative to the period from 1850 - 1900. An increase of 2 °C is widely considered the threshold that cannot be exceeded without catastrophic consequences (Intergovernmental Panel on Climate Change 2013b) but it would require sustained mitigation efforts to reach that goal (Global Carbon Project 2014).

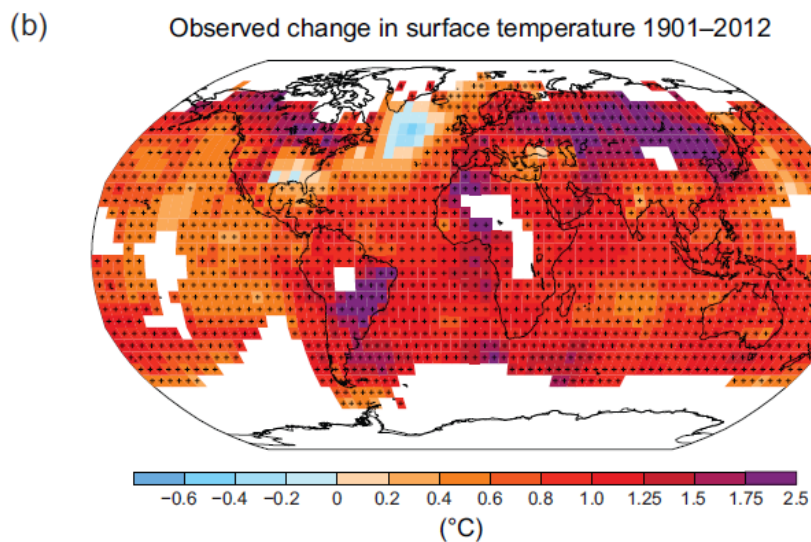
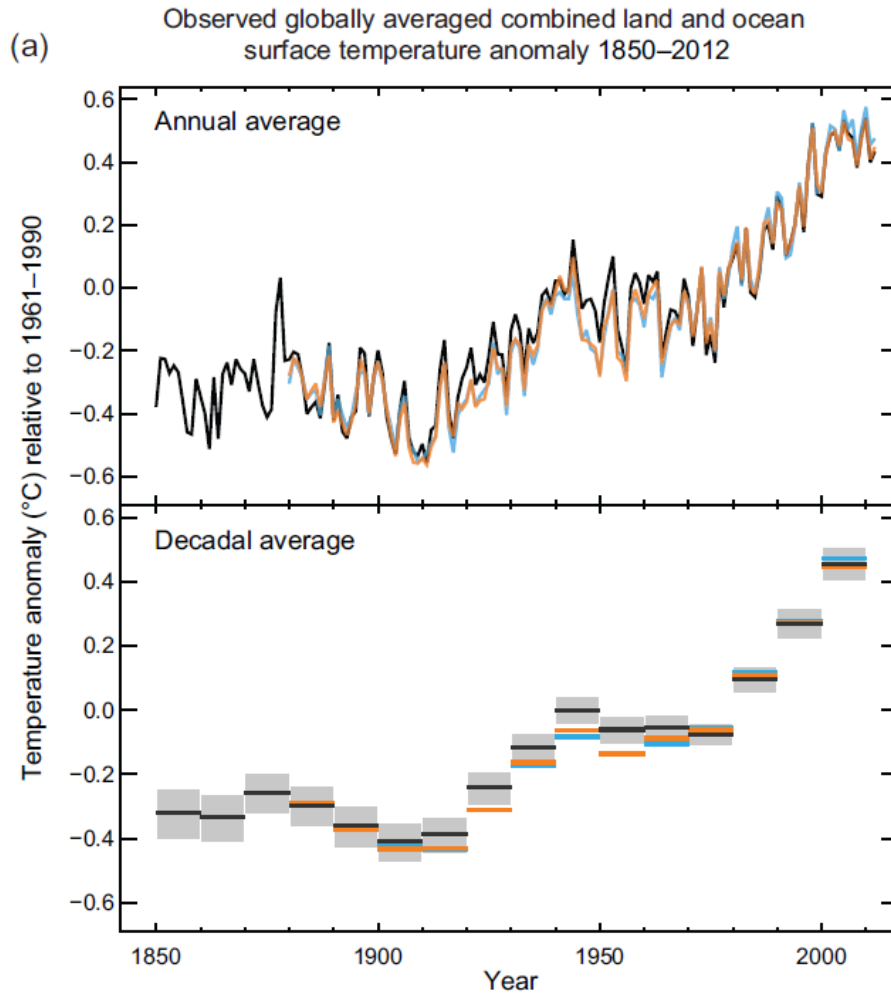


Figure 1.3: (a) Global averaged temperature anomaly, yearly and decadal, from 1850–2012 show a significant increase in temperature over the past ~150 years. (b) Much of Earth’s surface has undergone some warming in the past 100 years. (Figures adapted from IPCC 5th AR Summary for Policymakers)

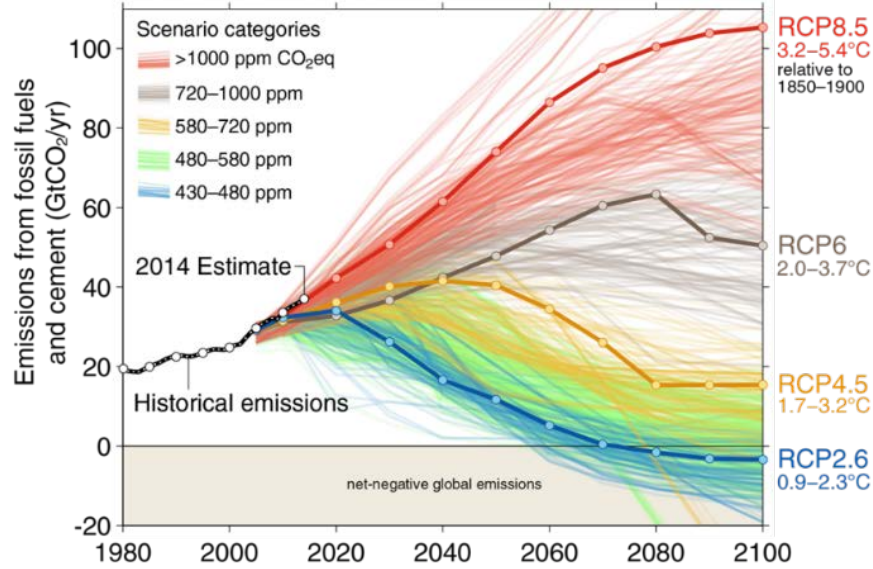
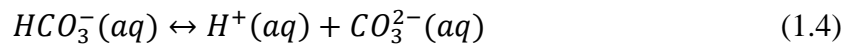
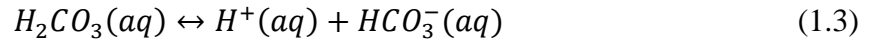


Figure 1.4: Representative concentration pathways (RCP) are predicted CO₂ emissions scenarios based on potential changes in the radiative forcing of the planet (2.6, 4.5, 6.0, 8.5 W·m⁻²). Each scenario has a projected atmospheric CO₂ concentration and possible temperature change by 2100. These scenarios were created as part of the Coupled Model Intercomparison Project (CMIP 5) for the IPCC 5th AR. (Figure adapted from Global Carbon Project, 2014).

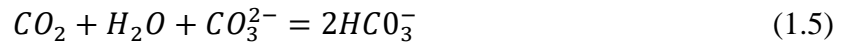
Despite all of the international attention on the effects of rising CO₂ emissions and atmospheric concentrations, a secondary, often overlooked consequence of increased emissions is the process of ocean acidification (OA), sometimes referred to as “global warming’s little brother” (e.g. Broecker and Clark, 2001; Caldeira and Wickett, 2003; Orr et al., 2005). As previously mentioned, the surface ocean acts as a CO₂ sink, removing CO₂ from the atmosphere, currently absorbing ~26%, or 10 Pg, of the emitted CO₂ per year. Since the Industrial Revolution, approximately 50%, or 500 Pg, of the emitted CO₂ has been absorbed by the global ocean. This absorption of CO₂ has a clearly measurable effect on seawater chemistry. The chemical process of OA can be described by the following four equations. In equations (1.1) and (1.2) gaseous CO₂ is absorbed into seawater and converted to aqueous CO₂, which is then hydrated to form carbonic acid (H₂CO₃):



The carbonic acid partially dissociates and releases a hydrogen ion (1.3), which can subsequently lower the pH of the solution. The added H^+ ions are then titrated by carbonate (CO_3^{2-}) as shown in equation 1.4. Seawater is strongly buffered to changes in pH due to the presence of bicarbonate (HCO_3^-) and carbonate (CO_3^{2-}) ions, which absorb or release hydrogen ions as necessary to maintain a stable pH.



The net reaction can be written as:



which clearly demonstrates how the addition of CO_2 to seawater results in a removal of carbonate ions, which leads to a decrease in seawater pH.

The oceanic uptake of nearly 500 Pg of CO_2 in the last 200 years has had a significant effect on ocean pH. The IPCC 5th AR reports that since the beginning of the industrial era, the pH of the global surface ocean has declined by 0.1 units (high confidence), a decrease that equates to a 26% increase in hydrogen ion concentration (Caldeira and Wickett 2003; Orr et al. 2005; Intergovernmental Panel on Climate Change 2013a). Predictions for the future suggest pH declines of ~0.3 by 2100 (Feely et al. 2009).

The decrease in carbonate ions results in lowered saturation states with respect to various carbonate minerals such as calcite, aragonite, and magnesian calcite. Saturation state is a measure of whether seawater is over- or undersaturated with respect to a specific mineral phase and is defined by equation 1.6.

$$\Omega_x = \frac{[Ca^{2+}][CO_3^{2-}]}{K_{spx}} \quad (1.6)$$

where x is the mineral phase and K is the solubility product constant of the given carbonate mineral. The surface ocean is supersaturated ($\Omega > 1$) with respect to calcite, aragonite (except in a few specific locations), and some magnesian calcites. The ability for most calcifying organisms to produce calcium carbonate skeletons and shells is directly related to saturation state, and declining saturation states and carbonate ion availability are expected to cause a decline in calcification rates of these organisms (e.g., Andersson and Gledhill, 2013; Buddemeier et al., 2004; Kleypas et al., 2006; Kuffner et al., 2007). When seawater saturation state falls below one, dissolution of abiotic and biogenic carbonates is predicted to occur. OA decreases the saturation state in seawater by removing carbonate ions, and because this effect is more intense in colder waters, the polar regions will be impacted first (Feely et al., 2009; Intergovernmental Panel on Climate Change, 2013a). Fisheries in colder regions such as the American Pacific Northwest and Northern Atlantic are especially vulnerable to increased OA, where calcifying organisms that form the base of the food web, such as coccolithophores (e.g., *E. huxleyi*), may be negatively affected by OA (Ekstrom et al. 2015). Feely et al. (2009) predict that Arctic surface water and the surface Southern Ocean will become undersaturated with respect to aragonite by 2020 and 2050, respectively, and the Arctic could be undersaturated with respect to calcite by 2100, which would have an extremely detrimental effect on the polar ecosystems and food webs (Ekstrom et al. 2015). Figure 1.5 shows the projected change in pH of the Arctic, Antarctic, and tropics under RCP 2.6 and RCP 8.5. Projected decreases of 0.3 to 0.5 pH units would be larger than those over the past 800,000 (and potentially even 2 million) years (Orr et al., 2005; Orr, 2011; Zeebe and Ridgwell, 2011).

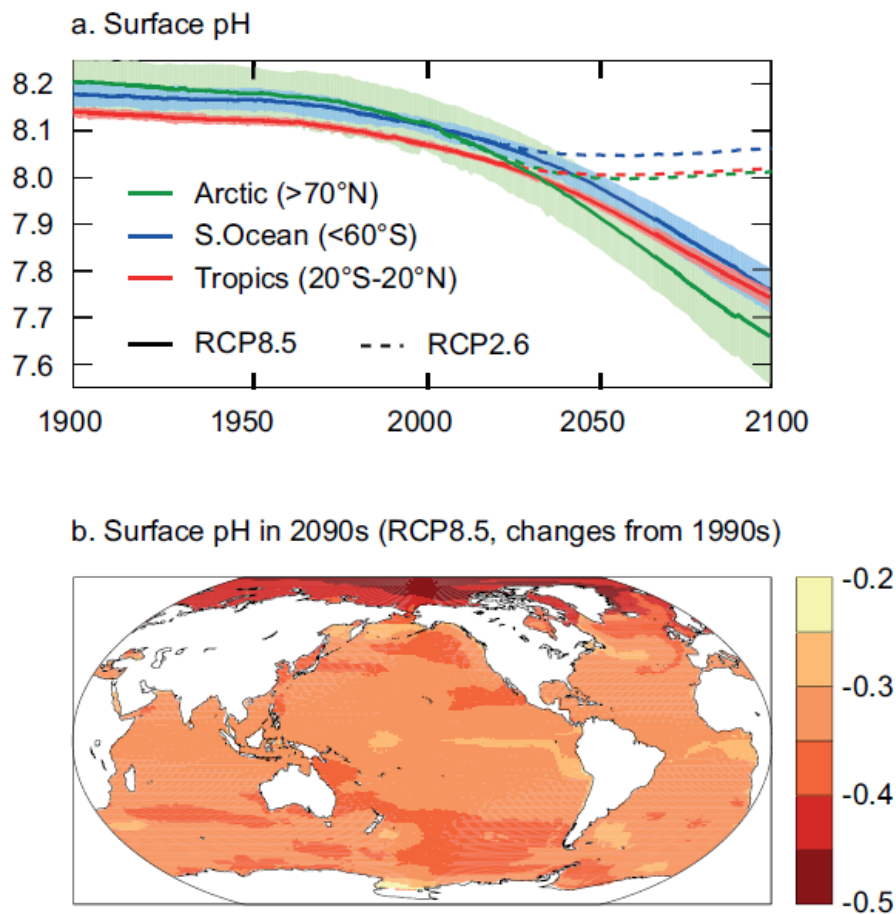


Figure 1.5: (a) Surface pH observations and projections from 1900-2100 for the Arctic, Southern Ocean, and Tropical Ocean under various RCP emissions scenarios predict a decline of ~0.1-0.3 pH units. (b) The global projections for pH by 2090 under RCP 8.5, with the Arctic decreasing by as much as 0.5 units relative to 1990-2000. (Figure adapted from IPCC 5th AR)

1.2 Ocean Acidification and Coral Reefs

While many of the projections of global surface water pH for the next century predict decreases to as low as 7.7 to 7.8 by 2100 (Feely et al. 2009), with seawater becoming undersaturated with respect to aragonite, many coastal regions are already experiencing these conditions. Coastal regions are particularly susceptible to acidification due to local river inputs, upwelling conditions, human development, and eutrophication. Lowered pH in coastal waters can have deleterious effects on local fisheries that produce shellfish such as oysters, mussels,

scallops, and clams, and particularly on coral reefs ecosystems (Kleypas et al. 2006; Barton et al. 2012; Ekstrom et al. 2015).

Coral reef ecosystems are vulnerable to a variety of anthropogenic changes including warming, eutrophication, overfishing, and ocean acidification. It has been widely shown that calcification rates of corals and coralline algae (an important reef framework-building organism in some regions) slow with decreasing carbonate mineral saturation state (e.g., Andersson and Gledhill, 2013; Morse et al., 2006). In addition, many abiotic cements that help stabilize the reef system are high Mg-calcites, a mineral form that is even more soluble than aragonite (Morse and Mackenzie 1990; Andersson and Gledhill 2013). Reef sands often account for the largest carbon reservoir on a coral reef (up to 90%, see Cyronak et al., 2014) and their porewaters are already undersaturated in many locations due to microbial activity that lowers the pH of interstitial porewater due to the production of respiration-derived CO₂ (e.g., Drupp et al., in review; Mackenzie et al., 1981; Moulin et al., 1985; Morse and Mackenzie, 1990; Sansone et al., 1990; Tribble et al., 1990; Mackenzie and Andersson, 2011; Andersson and Gledhill, 2013). This microbially mediated reaction is referred to as metabolic dissolution. The potential dissolution of carbonate sands could result in net erosion of reefs and a loss of CaCO₃ even if calcification rates were to remain constant under future OA conditions (Eyre et al. 2014). In addition, as acidification increases over the next century, seawater may become undersaturated with respect to certain mineral phases, initially high Mg-calcites, and coral reefs may become subject to environmental dissolution. Environmental dissolution occurs when mineral phases are exposed to surface seawater undersaturated with respect to the mineral phase, as compared to metabolic dissolution where CO₂ produced by organic matter respiration leads to undersaturation of the seawater (e.g., within sediment porewater). Combined with metabolic dissolution and bioerosion

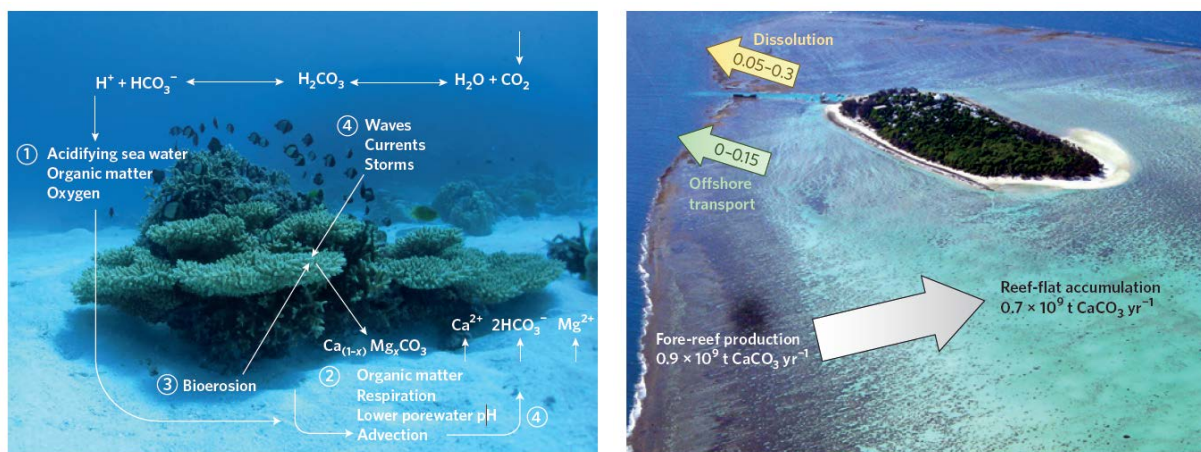


Figure 1.6: Conceptual model of processes controlling coral reef carbonate removal (left). These processes include environmental dissolution (1), metabolic dissolution (2), bioerosion (3), and mechanical breakdown (4), all of which contribute to reducing the size of the reef $CaCO_3$ reservoir through either chemical dissolution or mechanical erosion. The right panel presents global production and accumulation rates affecting coral reef accretion (units are tons of $CaCO_3$ yr^{-1}). Increases in dissolution and bioerosion from OA will change these fluxes and lower the total reef-flat accumulation, potentially leading to net erosion (loss) of $CaCO_3$ on some reef environments. (Figure adapted from Eyre et al., 2014)

(see Figure 1.6), both of which are expected to increase with rising CO_2 , reef ecosystem carbon budgets will be profoundly affected by the changing chemistry of the coastal ocean CO_2 -carbonic acid system.

1.3 Dissertation Objectives

This dissertation investigates natural processes that control CO_2 -carbonic acid system chemistry of both the surface water and sediment porewater of coral reefs. In addition, the data derived from this study are used to model natural reef processes and the effects of increasing OA and rising temperatures on the coral reef ecosystem. The techniques described herein can be applied to any coral reef but this dissertation focuses mainly on reefs around Oahu, Hawai‘i, and specifically the Kaneohe Bay barrier reef. Because coral reefs are dynamic ecosystems that exhibit large natural variability in their biogeochemical cycles – specifically those associated with the carbon system - it can be difficult to separate out the natural processes from the anthropogenic effects. While there are many factors that influence the marine carbon system, this

dissertation focuses primarily on carbonate mineral dissolution. Dissolution has been a largely overlooked component of how coral reef systems will respond to rising OA, with the majority of the focus being placed on the effects of decreased pH and Ω on biogenic calcification (see Figure 1.7). The dissolution process – the reverse of calcification – is largely abiotic and potentially more sensitive to OA than calcification (Eyre et al. 2014).

Only a combination of study methods such as those described in this dissertation can yield a complete understanding of the carbon system, both natural and human-induced, on coral reefs. In the open ocean, conditions are less variable, and sampling and monitoring techniques can be applied less frequently, whereas coral reefs require a multi-systems approach that includes monitoring at a high temporal resolution, an understanding of the specific biogeochemical processes and carbon balance in the area through discrete and focused sampling, and biogeochemical modeling to elucidate processes, and make predictions about future changes.

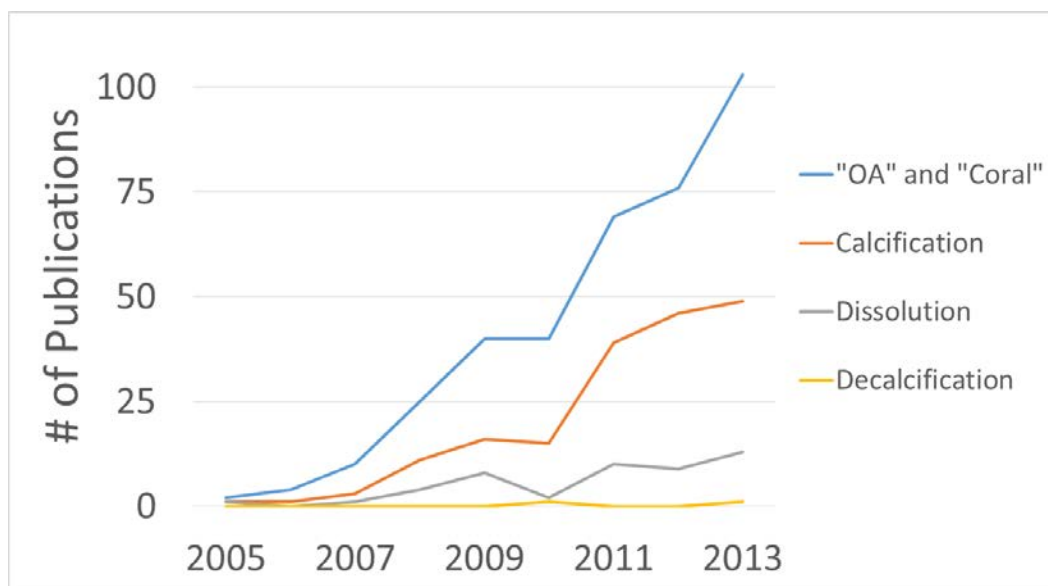


Figure 1.7: Number of publications per year from 2005-2013 that included the words ocean acidification, coral, calcification, dissolution, or decalcification in the title, abstract, or keywords, as determined from a SCOPUS search. (Figure courtesy of T. Cyronak, adapted from Eyre et al., 2014)

The overarching questions that guided this dissertation were:

1. *What are the current baseline conditions for CO₂ on Hawaiian coral reefs?*
2. *How do these conditions vary temporally and spatially?*
3. *What are the dominant processes that control CO₂ variability on the reefs?*
4. *What is the general CO₂ chemistry of the porewater of permeable reef sands?*
5. *What processes, biological and physical, control the chemistry of porewater CO₂?*
6. *How will biogeochemical processes in porewater respond to increasing OA?*
7. *How will the CO₂-carbonic acid system of the Kaneohe Bay barrier reef ecosystem respond to future changes in OA, temperature, and land-use over the next century?*

Chapter 2 is a journal article recently published in *Aquatic Geochemistry*, Drupp et al. (2013), that attempts to answer questions 1-3. A network of CO₂ and water quality monitoring buoys was deployed at three locations around the island of Oahu that continuously measured pCO₂ in the air and seawater every 3 hours from 2008 to the present (although Ch. 2 only presents the data through 2012). This work, representing the most complete and longest CO₂ record to date in tropical coral reef settings, provides a baseline for the first time for the natural processes that occur on both short-, intermediate-, and long-term time scales, and highlights the air-sea CO₂ gas exchange rates at three different reef locations.

With a better understanding of the water column baseline conditions and processes, Chapter 3, a manuscript submitted to *Marine Chemistry* (Drupp et al., in review), is a study of questions 4-6, designed to elucidate porewater processes under entirely natural conditions (i.e., no manipulation of the system) that control the carbon biogeochemistry of the sediment-porewater continuum. Some of the processes and the resulting changes in the total alkalinity (TA), dissolved inorganic carbon (DIC) concentration, pH and saturation state (Ω) are presented

herein. The processes include oxic respiration and sulfate reduction, both coupled with carbonate dissolution, as well as physical advection due to changes in waves and current speeds in the overlying water column. The effects of future ocean acidification are considered to be compounding factors on the already occurring natural processes and may force some coral reefs into a state of net erosion.

Many of the measurements from Chapter 2 and 3 were then combined, along with data from a wealth of other literature over the past ~50 years, to build an ecosystem biogeochemical box model, the Coral Ref Ecosystem and Sediment Carbonate Model (*CRESCAM*), for the barrier reef flat of Kaneohe Bay. Chapter 4 details the development of this unique conceptual model and its initial steady state solution. The model was subsequently “perturbed” or “forced” using the previously described RCP CO₂ emissions scenarios (see Section 1.1). The results of the various model runs and scenarios (for the period 2015-2100) answer question 7 and provide insight into how the various reef biological and physical processes in the water column, sediment porewater, and reef framework interact under both current and future conditions. I use the *CRESCAM* model to attempt to answer several questions that are crucial to understanding future changes in coral reef ecosystems. I present a new concept, net ecosystem carbonate production (NECP), which refers to the net carbonate produced (or removed) in a reef environment. NECP includes both biogenic and abiotic processes, as well as physical processes such as mechanical erosion.

Chapter 5 presents a summary of the important results from Chapters 2-4. In addition, the MATLAB code used to run *CRESCAM* can be found in the Appendix, along with the mass-balance and flux equations, as well as the calculations involved in estimating the initial steady state reservoirs and fluxes for *CRESCAM*.

These studies represent the first holistic effort to fully understand how coral reefs respond to changing ocean carbon chemistry. Each part of the overall study builds on the previous, with Chapters 2-3 answering previously overlooked questions, and Chapter 4 combining new results with past research to investigate the Kaneohe Bay barrier reef at the ecosystem level.

1.4 References

- Andersson AJ, Gledhill D (2013) Ocean acidification and coral reefs: effects on breakdown, dissolution, and net ecosystem calcification. *Ann Rev Mar Sci* 5:321–48. doi: 10.1146/annurev-marine-121211-172241
- Augustin L, Barbante C, Barnes PRF, et al (2004) Eight glacial cycles from an Antarctic ice core. *Nature* 429:623–628. doi: 10.1038/nature02599
- Barton A, Hales B, Waldbusser G, et al (2012) The Pacific oyster, *Crassostrea gigas*, shows negative correlation to naturally elevated carbon dioxide levels: Implications for near-term ocean acidification impacts. *Limnol Oceanogr* 57:698–710.
- Broecker W, Clark E (2001) A dramatic Atlantic dissolution event at the onset of the last glaciation. *Geochemistry Geophysics Geosystems*. doi: 10.1029/2001GC000185
- Buddemeier RW, Kleypas JA, Aronson RB (2004) Coral reefs & Global Climate Change: Potential Contributions of Climate Change to Stresses on Coral Reef Ecosystems.
- Caldeira K, Wickett M (2003) Anthropogenic carbon and ocean pH. *Nature* 425:2003.
- Crutzen PJ (2002) Geology of mankind. *Nature* 415:23. doi: 10.1038/415023a
- Cyronak T, Schulz KG, Santos IR, Eyre BD (2014) Enhanced acidification of global coral reefs driven by regional biogeochemical feedbacks. *Geophys Res Lett* 41:5538–5546. doi: 10.1002/2014GL060849. Received
- Drupp PS, De Carlo EH, Mackenzie FT, et al (2013) Comparison of CO₂ Dynamics and Air–Sea Gas Exchange in Differing Tropical Reef Environments. *Aquat Geochemistry* 19:371–397. doi: 10.1007/s10498-013-9214-7
- Drupp PS, De Carlo EH, Mackenzie FT Porewater CO₂-Carbonic Acid System Chemistry in Permeable Carbonate Reef Sands, *in review at Marine Chemistry*
- Ekstrom JA, Suatoni L, Cooley SR, et al (2015) Vulnerability and adaptation of US shellfisheries to ocean acidification. *Nat Clim Chang* 5:207–214. doi: 10.1038/nclimate2508
- Eyre BD, Andersson AJ, Cyronak T (2014) Benthic coral reef calcium carbonate dissolution in an acidifying ocean. *Nat Clim Chang* 4:969–976. doi: 10.1038/nclimate2380
- Feely R, Doney S, Cooley S (2009) Ocean Acidification: Present Conditions and Future Changes in a High-CO₂ World. *Oceanography* 22:36–47. doi: 10.5670/oceanog.2009.95
- Global Carbon Project (2014) Global Carbon Budget.
- Intergovernmental Panel on Climate Change (2013a) Climate Change 2013: The Physical Science Basis. Contribution of Working Group I to the Fifth Assessment Report of the Intergovernmental Panel on Climate Change. Cambridge University Press, Cambridge, United Kingdom and New York, NY, USA
- Intergovernmental Panel on Climate Change (2013b) IPCC, 2013: Summary for Policymakers. In: Stocker TF, Qin D, Plattner G-K, et al. (eds) Climate Change 2013: The Physical Science Basis. Contribution of Working Group I to the Fifth Assessment Report of the Intergovernmental Panel on Climate Change. Cambridge University Press, Cambridge, United Kingdom and New York, NY, USA, p 1535

- Kleypas JA, Feely RA, Fabry VJ, et al (2006) Impacts of Ocean Acidification on Coral Reefs and Other Marine Calcifiers : A Guide for Future Research, report of a workshop held 18-20 April 2005, St. Petersburg, FL, sponsored by NSF, NOAA, and the U.S. Geological Survey.
- Kuffner IB, Andersson AJ, Jokiel PL, et al (2007) Decreased abundance of crustose coralline algae due to ocean acidification. *Nat Geosci* 1:114–117. doi: 10.1038/ngeo100
- Le Quéré C, Moriarty R, Andrew RM, et al (2014) Budget 2014 Global carbon budget 2014. *Earth Syst Sci Data Discuss* 7:521–610. doi: 10.5194/essdd-6-1-2014
- Mackenzie FT, Andersson AJ (2011) Biological control on diagenesis: influence of bacteria and relevance to ocean acidification. In: Reitner J, Thiels V (eds) *Encyclopedia of Geobiology*. Springer Verlag, Dordrecht, The Netherlands,
- Mackenzie FT, Ristvet B, Thorstenson DC, et al (1981) Reverse weathering and chemical mass balance in a coastal environment. In: Martin JM, Burton JD, Eisma D (eds) *River Inputs to Ocean Systems*. UNEP and UNESCO, Switzerland, pp 152–187
- Morse JW, Andersson AJ, Mackenzie FT (2006) Initial responses of carbonate-rich shelf sediments to rising atmospheric pCO₂ and “ocean acidification”: Role of high Mg-calcites. *Geochim Cosmochim Acta* 70:5814–5830. doi: 10.1016/j.gca.2006.08.017
- Morse JW, Mackenzie FT (1990) *Geochemistry of Sedimentary Carbonates*. Elsevier, Amsterdam, The Netherlands
- Moulin E, Jordens A, Wollast R (1985) Influence of the Aerobic Bacterial Respiration on the Early Dissolution of Carbonates in Coastal Sediments. In: *Progress in Belgian Oceanographic Research*. p 13
- Orr JC (2011) Recent and future changes in ocean carbonate chemistry. In: Gattuso J-P, Hansson L (eds) *Ocean Acidification*. Oxford University Press, New York, p 326
- Orr JC, Fabry VJ, Aumont O, et al (2005) Anthropogenic ocean acidification over the twenty-first century and its impact on calcifying organisms. *Nature* 437:681–686. doi: 10.1038/nature04095
- Pearson PN, Palmer MR (2000) Atmospheric carbon dioxide concentrations over the past 60 million years. *Nature* 406:695–699. doi: 10.1038/35021000
- Petit J, Jouzel J, Raynaud D, Barkov N (1999) Climate and atmospheric history of the past 420,000 years from the Vostok ice core, Antarctica. *Nature* 399:429–436.
- Revelle R, Suess HE (1957) Carbon Dioxide Exchange Between Atmosphere and Ocean and the Question of an Increase of Atmospheric CO₂ During the Past Decades.
- Ruddiman WF (2003) The Anthropogenic Greenhouse Era Began Thousands of Years Ago. *Clim Change* 61:261–293. doi: 10.1007/s10584-005-7278-0
- Sansone FJ, Tribble G, Andrews CC, Chanton JP (1990) Anaerobic diagenesis within Recent, Pleistocene, and Eocene marine carbonate frameworks. *Sedimentology* 37:997–1009.
- Scripps Institute of Oceanography The Keeling Curve.
<https://scripps.ucsd.edu/programs/keelingcurve/>.
- Siegenthaler U, Stocker TF, Monnin E, et al (2005) Stable Carbon Cycle: Climate Relationship during the Late Pleistocene. *Science* (80-) 310:1313–1317.

Tribble GW, Sansone FJ, Smith S V. (1990) Stoichiometric modeling of carbon diagenesis within a coral reef framework. *Geochim Cosmochim Acta* 54:2439–2449.

Zeebe RE, Ridgwell A (2011) Past changes in ocean carbonate chemistry. In: Gattuso J-P, Hansson L (eds) *Ocean Acidification*. Oxford University Press, New York, p 326

Chapter 2 COMPARISON OF CO₂ DYNAMICS AND AIR-SEA EXCHANGE IN DIFFERING TROPICAL REEF ENVIRONMENTS

This chapter is published in *Aquatic Geochemistry*, 19 (5-6), 371-397, 2013.

Authors are: Patrick S. Drupp¹, Eric Heinen De Carlo¹, Fred T. Mackenzie¹, and Christopher L. Sabine²

¹Department of Oceanography, University of Hawai‘i at Manoa
1000 Pope Road, Honolulu, HI 96822

²NOAA/PMEL 7600 Sand Point Way, Seattle, WA 98115

2.1 Abstract

An array of MAPCO₂ buoys, CRIMP-2, Ala Wai, and Kilo Nalu, deployed in the coastal waters of Hawai‘i have produced multiyear high temporal resolution CO₂ records in three different coral reef environments off the island of Oahu, Hawai‘i. This study, which includes data from June 2008-December 2011, is part of an integrated effort to understand the factors that influence the dynamics of CO₂-carbonic acid system parameters in waters surrounding Pacific high island coral reef ecosystems and subject to differing natural and anthropogenic stresses. The MAPCO₂ buoys are located on the Kaneohe Bay backreef, and fringing reef sites on the south shore of O‘ahu, Hawai‘i. The buoys measure CO₂ and O₂ in seawater and in the atmosphere at 3-hour intervals, as well as other physical and biogeochemical parameters (CTD, chlorophyll-a, turbidity). The buoy records, combined with data from synoptic spatial sampling, have allowed us to examine the interplay between biological cycles of productivity/respiration and calcification/dissolution and biogeochemical and physical forcings on hourly to inter-annual time scales.

Air-sea CO₂ gas exchange was also calculated to determine if the locations were sources or sinks of CO₂ over seasonal, annual, and inter-annual time periods. Net annualized fluxes for CRIMP-2, Ala Wai, and Kilo Nalu over the entire study period were 1.15 mol C m⁻² yr⁻¹, 0.045

mol C m⁻² yr⁻¹, and -0.0056 mol C m⁻² yr⁻¹, respectively, where positive values indicate a source or a CO₂ flux from the water to the atmosphere, and negative values indicate a sink or flux of CO₂ from the atmosphere into the water. These values are of similar magnitude to previous estimates in Kaneohe Bay as well as those reported from other tropical reef environments. Total alkalinity (A_T) was measured in conjunction with pCO₂ and the carbonic acid system was calculated to compare with other reef systems and open ocean values around Hawai‘i. These findings emphasize the need for high-resolution data of multiple parameters when attempting to characterize the carbonic-acid system in locations of highly variable physical, chemical, and biological parameters (e.g. coastal systems, reefs).

2.2 Introduction

Atmospheric concentrations of carbon dioxide (CO₂) have been on the rise for the past 200 years due to human activities releasing more than 400 petagrams of carbon into the atmosphere since 1750. Approximately half of these emissions occurred during the past 40 years (CDIAC cdiac.ornl.gov/). Atmospheric concentrations of ~395 μatm, as observed at Mauna Loa in 2012 (<http://www.esrl.noaa.gov/gmd/ccgg/trends/>), are significantly higher than those at any time in the past 800,000 years (Petit et al., 1990; Augustin et al., 2004; Siegenthaler et al., 2005). Although the atmospheric record is now well characterized, much work remains to be done in the oceanic realm especially on the strength of the CO₂ exchange flux and its future.

The vast majority of research on the effect of the rise of atmospheric CO₂ on the oceans has been focused on the open ocean. (Andersson et al., 2007; Feely et al., 2004; Feely et al., 2008; Orr et al., 2005; Takahashi et al., 2009; Wanninkhof et al., 2012). The open ocean, in general, is regarded as a sink for atmospheric CO₂, meaning that the net flux of CO₂ presently is into the ocean. However, the global coastal ocean is quite variable with respect to the net flux of

CO₂ into or out of the atmosphere. Values of coastal net CO₂ flux (mol C m⁻² yr⁻¹) range from 438 and 3330 in some European estuaries (Frankignoulle et al., 1998) to -34.6 and -33.6 in both the Gulf of Biscay and the East China Sea (Frankignoulle and Borges, 2001; Wang et al., 2000) and as high as -87.6 (Hales et al., 2003) in a highly productive upwelling region off the Oregon coast. Massaro et al. (2012) reported a net flux of 1.80 mol C m⁻² yr⁻¹ in the southern sector of Kaneohe Bay. Positive values indicate a flux of CO₂ from the ocean into the atmosphere (source) and negative values indicate a flux into the ocean (sink). However, many of these flux estimates were obtained through periodic synoptic sampling of the surface waters of these systems and very few long-term, high resolution, *in-situ* studies on the CO₂-carbonic acid system and CO₂ exchange dynamics have been performed in coastal environments (e.g. De Carlo et al., this volume; Drupp et al., 2011; Massaro et al., 2012).

As atmospheric CO₂ levels continue to rise for (at least) the remainder of the 21st century, the global shallow ocean environment, which has been a source of CO₂ to the atmosphere for at least the past 300 years, may reverse its net flux to that of a sink for atmospheric CO₂ just like the open ocean (Andersson and Mackenzie, 2004; Andersson et al., 2006; Mackenzie et al., 2011; Wanninkhof et al., 2012).

2.3 Study Rationale

This study expands upon a 2.5 year *in-situ* high-resolution time series study that was carried out in southern Kaneohe Bay, Oahu, Hawai‘i (Figure 2.1a and 2.1b) through the use of the Coral Reef Instrumented Monitoring and CO₂ Platform (CRIMP-CO₂) buoy (Drupp et al. 2011; Massaro et al., 2012). Kaneohe Bay, in particular its southern sector, has been extensively studied for the past 40 years (e.g., Roy, 1970; Cox et al., 1973; Hollett, 1977; Smith et al., 1981; Taguchi and Laws, 1987, 1989; Jokiel et al., 1993; Hunter and Evans, 1995; Laws and Allen,

1996; Atkinson, 2000; Hearn and Atkinson, 2000; Kinzie et al., 2001; Falter et al., 2004; Ringuet and Mackenzie, 2005; Tanaka and Mackenzie, 2005; Hoover et al., 2006; De Carlo et al., 2007; Fagan and Mackenzie, 2007; Hoover and Mackenzie, 2009; Drupp et al. 2011; Massaro et al., 2012; Shamberger et al., 2011). The bay is thought to be representative of other high-island tropical reef environments found throughout the Pacific Ocean.

The Coral Reef Instrumented and CO₂ Monitoring (CRIMP-CO₂) program, initiated in late 2005, was the first long-term, high resolution CO₂ monitoring program conducted in tropical coastal waters. The CRIMP-CO₂ buoy also served as a platform for deploying additional water quality sondes measuring a variety of standard physical and biogeochemical parameters. In June 2008, the CRIMP buoy was relocated to its current location (CRIMP-2, Figure 2.1b) at a depth of 3 m on the inside edge of the Kaneohe Bay barrier reef, in the central sector of Kaneohe Bay. Two additional buoys, Water Quality Buoys Ala Wai and Kilo Nalu (WQB-AW and WQB-KN, respectively, Figure 2.1c) were also deployed at that time, on the south shore of Oahu in ~12 m water depth on sand patches adjacent to fringing reefs in Mamala Bay, approximately 200 m offshore of urban Honolulu. These three buoys provide high frequency (3 hr) CO₂ and ancillary water quality parameters of conditions in differing coastal coral reef environments, and complementary data are obtained through periodic synoptic sampling.

Periodic synoptic sampling, often performed during the day under favorable weather conditions (e.g. De Carlo et al., this volume), misses diel cycles and, frequently, changes induced by local rainfall and storm events. The latter have been shown to induce rapid and brief changes in stream flow (e.g., Tomlinson and De Carlo, 2003; Hoover and Mackenzie, 2009) and have a significant effect on short-term CO₂ variability and general biogeochemistry (e.g., nutrient concentrations) in the nearshore semi-estuarine environment of Kaneohe Bay (Ringuet and

Mackenzie, 2005; De Carlo et al., 2007; Fagan and Mackenzie, 2007; Hoover and Mackenzie, 2009; Drupp et al., 2011; Massaro et al., 2012). Strong diel signals, due to water column and reef productivity/respiration and calcification/dissolution processes, have been observed by both Drupp et al. (2011) and Shamberger et al. (2011) in Kaneohe Bay. Seasonal and annual trends in water column pCO₂ were clearly evident in previous work by Fagan and Mackenzie (2007), Drupp et al. (2011), and Massaro et al. (2012). Based on these studies, it is evident that only a monitoring program that is both long-term (multiple years) and high resolution (multiple samples per day) can adequately characterize CO₂ exchange fluxes and processes controlling them in dynamic biogeochemical environments such as Kaneohe Bay and other tropical reef environments.

2.4 Methodology

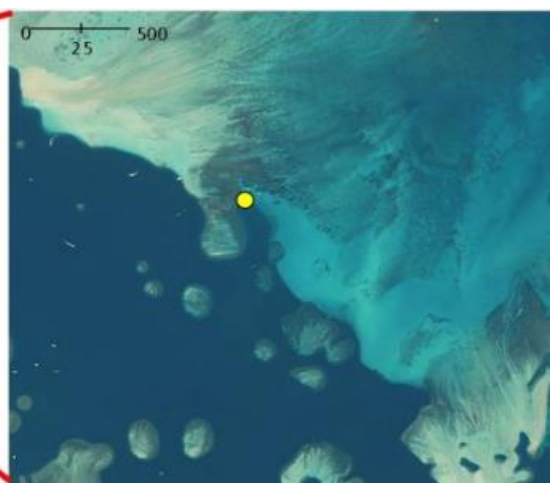
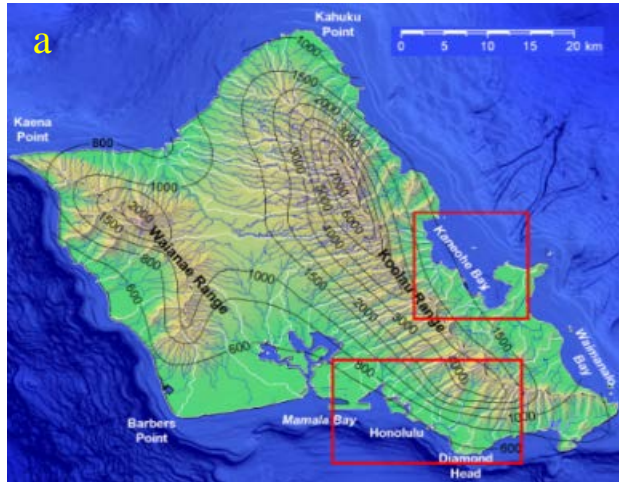
2.4.1 *Environmental Setting*

Kaneohe Bay, the location of the CRIMP-2 buoy, is the largest semi-enclosed body of water on the island of Oahu, Hawai‘i (Figure 2.1) and is located on the northeast (windward) coast. It is host to numerous fringing and patch reefs as well as a large barrier reef. The bay has a mean depth of 9.5 meters, with the barrier reef averaging ~2 meters depth (Bathen, 1968). Northeasterly tradewinds blow the majority (~80%) of the year and their speed is a major factor in governing the magnitude of air-sea CO₂ gas exchange fluxes (Massaro et al., 2012). Water residence time in the bay ranges from hours on the barrier reef to 30+ days in the more hydrologically isolated southern sector (Lowe et al., 2009a), where the original CRIMP buoy was deployed. CRIMP-2 was deployed in 3 m of water over sandy sediment on the inside edge of the barrier reef (Figure 2.1b) in the central sector of Kaneohe Bay. The site was chosen due to its proximity to the barrier reef (~20 m distance from the backreef edge) and because the flow of

water at this site is nearly unidirectional, thereby allowing measurements of water chemistry and its CO₂ content after the water flows across the barrier reef from the open ocean. Effectively, the water chemistry at this site represents an end-member following the alteration of its chemistry due to biological and physical processes during its transit across the barrier reef. It is important to note that much of the reef may not have been exposed to the same water chemistry that is measured at this buoy, as the water has been undergoing biogeochemical alteration continuously during its transit across the reef. For example, data from Shamberger et al., 2011 (discussed later) collected from a mid-reef location falls in between the open ocean values and our CRIMP-2 end-member. The CRIMP-2 location is also generally isolated from direct terrestrial and riverine inputs from the Kaneohe Bay watershed.

Recent work has shown that the biogeochemistry of the CRIMP-2 location is driven largely by benthic productivity and calcification occurring on the barrier reef (Shamberger et al., 2011). This is in sharp contrast to the original CRIMP location, where land runoff combined with the physical characteristics of the site modified considerably the biogeochemistry of the water and CO₂ exchange dynamics on various time scales (Ringuet and Mackenzie, 2005; De Carlo et al. 2007; Drupp et al., 2011; Massaro et al., 2012). At the CRIMP-2 location, runoff has very little effect on the magnitude of the air-sea flux of CO₂ and the location also can be considered a relatively healthy coral reef environment in which to study the CO₂-carbonic acid system and CO₂ exchange.

Figure 2.1: (a) The island of Oahu, highlighting Kaneohe Bay on the windward (East) coast and the Honolulu watershed on the southern coast (Figure courtesy of Mike Tomlinson). (b) Kaneohe Bay on the windward coast, highlighting the CRIMP-2 buoy (yellow circle) on the backside of the barrier reef (right). The original CRIMP location is marked as a red circle in the left figure (Images modified from Digital Globe). (c) Two buoys are located 200m offshore of urban Honolulu above fringing reefs. Ala Wai buoy (WQB-AW) is located near the mouth of the Ala Wai canal, which drains part of the Honolulu city watersheds The Kilo. Nalu buoy (WQB-KN) is located ~2 km west of WQB-AW (Images from Google Earth modified by Mike Tomlinson).



Fringing reefs in Mamala Bay on the south shore of Oahu are rather unprotected. These reefs are generally subject to the direct physical effects of tides, winds, and open ocean wave action, and nearshore water exchanges readily with surrounding open ocean water. The two sites (Ala Wai and Kilo Nalu) differ from each other in the presence or absence, respectively, of riverine input from the Ala Wai Canal. The canal drains approximately 1/3 of urban Honolulu (population ~850,000) and contributes significant amounts of fluvial discharge containing high nutrient and suspended sediment loads to coastal waters. The effects of this discharge are especially evident at the Ala Wai buoy following (large) storm events (Tomlinson et al., 2011). Occasionally, depending on wind and swell conditions, this riverine signal can reach the Kilo Nalu buoy, about 1.6 km to the west, although the impacts of the fluvial discharge on water quality at that site are typically highly attenuated. The substrate in Mamala Bay out to the 30m isobaths consists mainly of sand, limestone pavement, and spur and groove coral reef. Encrusting algae and coral dominates the reef with some *Porites lobata* and *Pocillopora meandrina*. Macroalgae have 10-90% local coverage of the pavement (Battista et al., 2007, Tomlinson et al., 2011).

2.4.2 *In-situ Measurements*

The buoys are equipped to make a broad range of measurements. A LICOR-820 infrared sensor and a MextexMAXTM-250 Series sensor measuring CO₂ and O₂, respectively, are located within the buoy body, as well as a Sensirion humidity sensor. Data are collected every 3 hours and transmitted daily via Iridium satellite to NOAA/PMEL (Pacific Marine Environmental Laboratory). The accuracy of the LICOR-820 is conservatively estimated to be 2.5% of the measured value. Details regarding the analytical scheme of the buoy can be found in Massaro et

al. (2012) and Shamberger et al. (2011). CO₂ and O₂ data from all three buoys can be viewed in “near real time” at <http://www.pmel.noaa.gov/co2/coastal/HI/>

Both WQB-AW and KN buoys are also equipped with Sea-Bird Electronics SeaCat16 v2plus CTD's (Conductivity, Temperature, Depth) and WET Labs FLNTUS ECO fluorometer/turbidity sensors. Temperature, conductivity (salinity), dissolved oxygen, chlorophyll, and turbidity are measured at 20 minute intervals. SBE16 data from WQB-AW and WQB-KN are transmitted every 20 minutes via a Satlantic STOR-X data logger and cell phone modem. A Yellow Springs Instrument (YSI) 6600 Multi-Parameter sonde and a Sea-Bird Electronics MicroCat CT (37-SMP) are attached to the CRIMP-2 buoy and measure temperature, conductivity, dissolved oxygen, chlorophyll, turbidity, and pH. Water quality data from the SBE16's can be viewed in real time on the Pacific Islands Ocean Observing System (PacIOOS) website.

http://oos.soest.hawaii.edu/pacioos/data_product/WQ/

Wind and tidal data were obtained from the NOAA National Ocean Service (NOS) Station OOUH1 in downtown Honolulu (for south shore buoys) and from the Hawai'i Institute of Marine Biology (HIMB) weather station on Coconut Island (for CRIMP-2). Rainfall data for the windward coast were obtained from gauges at the Hawai'i Institute of Marine Biology (HIMB) on Coconut Island in southern Kaneohe Bay and the National Weather Service (NWS) HI15 Luluku gauge in the Kaneohe Stream watershed. South shore rainfall was measured at the NWS HI-18 Manoa Lyon Arboretum and NWS HI-20 Nuuanu Valley gauges (in the upper watersheds which drain much of Honolulu) and from NWS HI-26 Aloha Tower within Honolulu harbor.

2.4.3 Sample Analysis

Discrete water samples were collected at each location, during periods of routine equipment maintenance, usually every 4 weeks. Samples for total alkalinity (A_T) were collected from the surface waters in 300 mL borosilicate bottles. Each sample was fixed with 200 μ L of saturated $HgCl_2$ to inhibit any biological activity. The bottles were sealed with Apiezon-greased ground glass stoppers. Total alkalinity was determined using the open cell potentiometric titration method (Dickson et al., 2007) on a Metrohm Titrando 905. The accuracy of the A_T determinations was evaluated using certified reference materials (CRM) from the Scripps Institution of Oceanography (Dickson et al., 2001; Dickson et al., 2003; Dickson et al., 2007) and found to be $1.37 \mu\text{mol kg}^{-1}$ ($n=26$). The precision between replicates was $1.52 \mu\text{mol kg}^{-1}$ ($n=63$).

2.4.4 Calculations

Concentrations of CO_2 measured by the LICOR-820 were corrected using the relative humidity in the equilibrator to calculate a dry xCO_2 (mole fraction at 0% humidity). Using the methods from Zeebe and Wolf-Gladrow (2001), originally developed by Weiss and Price (1980). pCO_2 was calculated utilizing ambient water vapor pressure, dependent on T and S, and assuming that the air directly above the sea surface was 100% saturated.

Calculations of air-sea fluxes were made using Equation (2.1) below:

$$F=k\alpha\Delta pCO_2 \quad (2.1)$$

where k is the CO_2 gas transfer velocity, α is the solubility of CO_2 in seawater at the specified temperature and salinity, and ΔpCO_2 is the difference between atmospheric and seawater pCO_2 concentrations (Weiss, 1974; Liss, 1983; Wanninkhof, 1992).

The gas transfer velocity, k , was calculated using the Ho et al. (2006) parameterization shown in equation (2.2):

$$k_{(600)} = (0.266 \pm 0.019) (U_{10})^2 \quad (2.2)$$

where U_{10} is the wind speed measured at (or corrected to) ten meters above sea level. Error bars for fluxes were calculated by error propagation, using a 2.5% error for the CO_2 measurement and an uncertainty of 0.019 in the Ho et al. parameterization.

Normalization of pCO_2 to an average seawater temperature was performed according to Takahashi et al. (1993, 2002) assuming a 4.23% change in pCO_2 per 1°C change in temperature (equation 2.3). The effect of only temperature on pCO_2 at a given time was also calculated (equation 2.4) from Takahashi et al. (1993 and 2002) using the mean pCO_2 of the study period. This represents the pCO_2 changes induced by temperature fluctuations under isochemical conditions.

$$\text{pCO}_2 \text{ at } T_{\text{mean}} = \text{pCO}_{2\text{obs}} * \exp(0.0423*(T_{\text{mean}}-T_{\text{obs}})) \quad (2.3)$$

$$\text{pCO}_2 \text{ at } T_{\text{obs}} = \text{pCO}_{2\text{mean}} * \exp(0.0423*(T_{\text{obs}}-T_{\text{mean}})) \quad (2.4)$$

where T_{obs} and $\text{pCO}_{2\text{obs}}$ are the measured *in-situ* temperature and pCO_2 , and T_{mean} and $\text{pCO}_{2\text{mean}}$ are the annual mean values of temperature and pCO_2 .

Dissolved inorganic carbon (C_T), pH (total scale), and calcium carbonate saturation state (Ω) were calculated using CO2SYS (Lewis and Wallace, 1998) with carbonic acid constants by Mehrbach et al. (1973) refit by Dickson and Millero (1987).

Nutrient analyses were performed on a Seal Analytical AA3 HR Nutrient Autoanalyzer. Nitrate (NO_3^-) and nitrite (NO_2^-) were analyzed according to the methods of Armstrong et al. (1967) and Grasshoff et al. (1983) with a detection limit of $0.006 \mu\text{mol L}^{-1}$ and a relative standard deviation (CV) of 0.3%. Silicate (Si(OH)_4) was analyzed based on the methods of

Grasshoff et al. (1983) with a detection limit of $0.350 \mu\text{mol L}^{-1}$ and a CV of 0.5%. Soluble reactive phosphate (PO_4^{3-}) was analyzed according to the colorimetric method of Murphy and Riley (1962) with a detection limit of $0.018 \mu\text{mol L}^{-1}$ and a CV of 0.4%.

2.5 Results

Figure 2.2a shows the pCO_2 of seawater at all three buoy locations over the entire study period of June 2008-December 2011. A seasonal trend is evident in all three data sets; however, CRIMP-2 (blue) shows much greater short term variations in pCO_2 . The solid yellow line in this figure indicates $377 \mu\text{atm}$, which was the mean air pCO_2 during the study period. When seawater pCO_2 is above this line, the location is a source of CO_2 to the atmosphere and when seawater pCO_2 is below the line, the location is a sink for CO_2 from the atmosphere. However, source or sink activity is dependent upon the instantaneous flux, which was calculated from the *in-situ* measured atmospheric pCO_2 at the time of the seawater measurement. The mean seawater pCO_2 values at CRIMP-2, Kilo Nalu, and Ala Wai were $439 \pm 11 \mu\text{atm}$, $379 \pm 10 \mu\text{atm}$, and $389 \pm 10 \mu\text{atm}$, respectively. Minimum and maximum values are reported in Table 2.1. CRIMP-2 displayed the largest variation with a range of $780 \mu\text{atm}$. The standard deviation of the mean was $83.4 \mu\text{atm}$ at CRIMP-2 compared to values of 18.2 and $25.3 \mu\text{atm}$ for KN and AW, respectively, further demonstrates the greater short-term variations which occur at the CRIMP-2 location.

Figure 2.2b displays the pCO_2 normalized to average T during the entire study period, as calculated by Equation 2.3. Even when normalized to the mean temperature of 25°C , pCO_2 still exhibits large short term fluctuations at all three buoys. The T-normalized pCO_2 also displays a seasonal trend (albeit much less than in the raw pCO_2 data shown in Figure 2.2a) which can be difficult to discern due to the short term variations.

Table 2.1: pCO₂ statistics are shown for each of the three buoys from 6/10/08-12/31/11, as well as from the original CRIMP-1 buoy in southern Kaneohe Bay from 11/30/05-5/17/08.

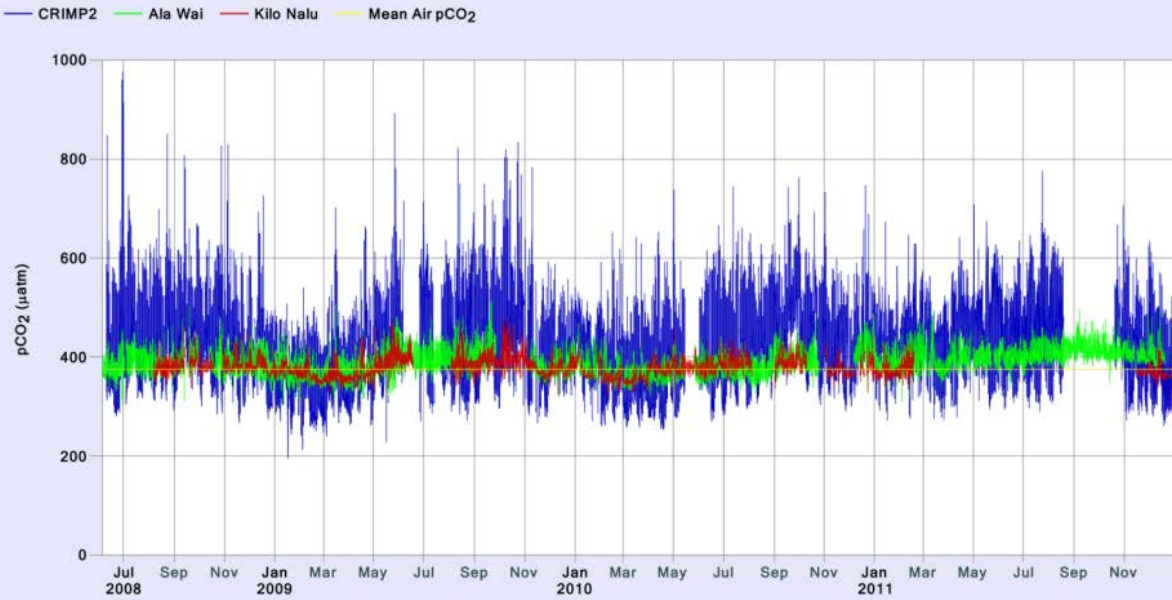
pCO_{2 sw}	Min (μatm)	Max (μatm)	Mean (μatm)	St. Dev
CRIMP-2	196	976	439	83.4
Kilo Nalu	316	479	378	18.2
Ala Wai	302	514	389	25.3
CRIMP-1	225	671	448	50.8

Monthly mean pCO₂ was calculated at each location and is shown in Figure 2.3a. The trend of higher pCO₂ in the summer and lower pCO₂ in the winter was also observed at the original CRIMP location (Drupp et al., 2011; Massaro et al., 2012). Figure 2.3b shows the weekly temperatures throughout the study period. All three locations follow the same trend of maximum temperatures (~27 °C) during the summer and minimum temperatures (~23-24 °C) in the winter. Water at CRIMP-2 does become slightly cooler than water at AW and KN during the winter months, but does not become warmer than water at AW and KN during the summer.

Figure 2.2: (a) pCO₂ data, taken every 3 hours, from all 3 buoys shows the long term seasonal variability, due largely to temperature changes, as well as the short term (hourly-weekly) variability, due to both biological and physical forcings. CRIMP-2 (blue) located on the Kaneohe Bay barrier reef exhibits the largest variability owing to the reef flat's high rates of calcification and productivity. Kilo Nalu (red) shows little variability and is fairly representative of the surrounding open ocean water. The yellow line indicates the mean air pCO₂ of 377 μatm over the study period. (b) pCO₂ was normalized to a mean temperature to show temperature independent (net biology) effects on pCO₂. Normalizations were calculated according to Takahashi et al. (2002). (c/d) pCO₂ data and normalized pCO₂ data from Ala Wai and Kilo Nalu is shown.

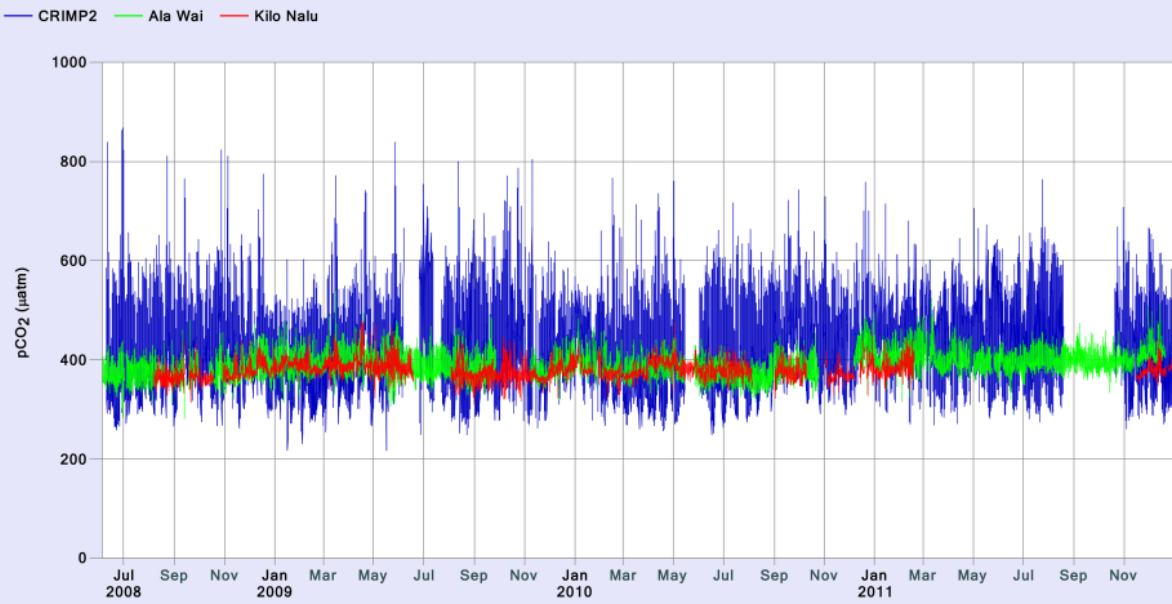
a

pCO₂ June 2008-December 2011



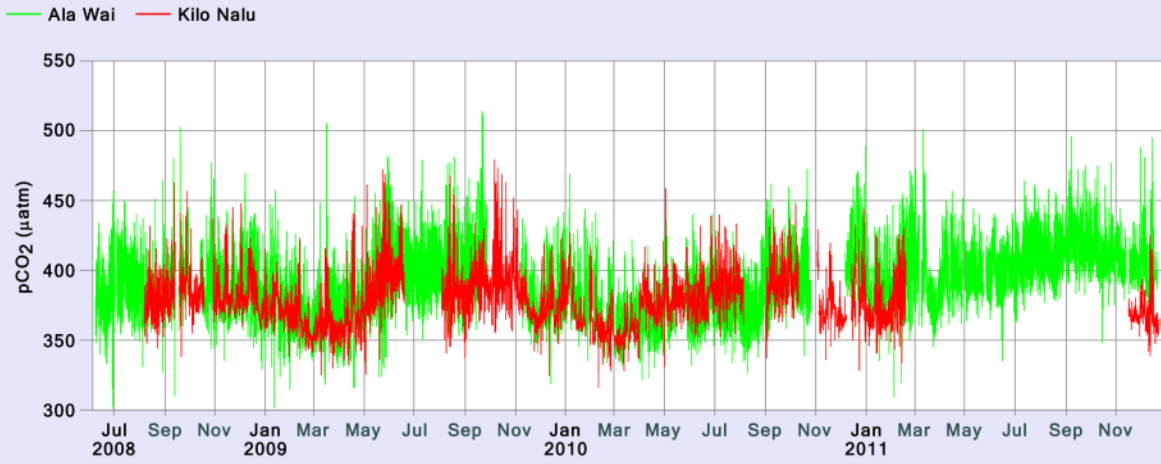
b

pCO₂ Normalized to Mean Temperature



c

pCO₂ June 2008-December 2011



d

pCO₂ Normalized to Mean Temperature

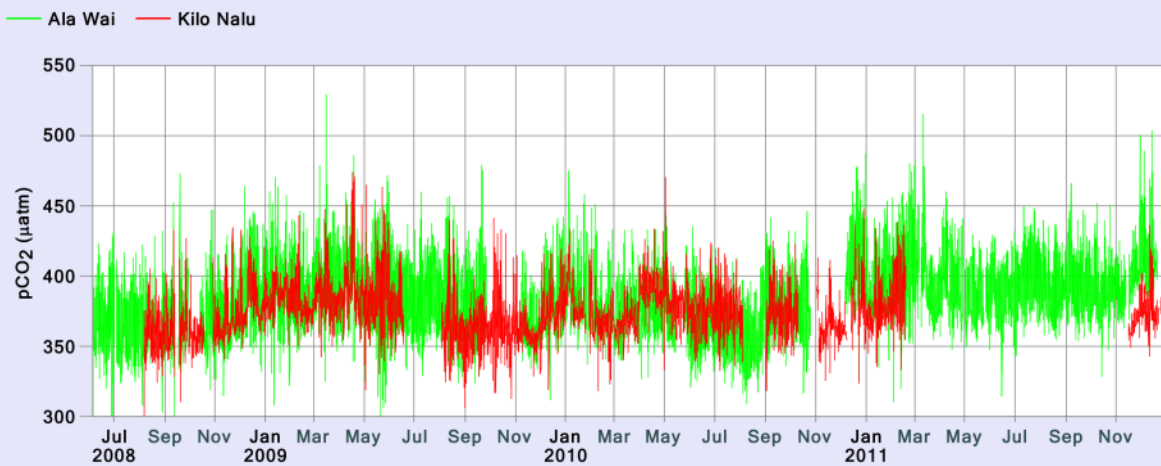




Figure 2.3: (a) Monthly mean pCO₂ was calculated for each buoy clearly showing a seasonal trend. Temperature changes affect seawater pCO₂ by 4.23% per degree Celsius (Takahashi et al. 1993). The warmer “dry” season from May-Oct. (b) Weekly mean water temperatures display a typical summer/winter seasonal trend.

The daily range of pCO₂ was also calculated for each day throughout the study period.

Table 2.2 shows statistics for the daily ranges at all three buoys, as well as the original CRIMP buoy. CRIMP-2 exhibited a mean daily range of $196 \pm 16 \mu\text{atm}$, four times greater than observed at the Ala Wai location. The maximum daily ranges at AW and KN are considerably lower than the mean daily range at CRIMP-2. At each location, pCO₂ dropped throughout the

day reaching a minimum value in the afternoon, around ~14:00 hrs. Maximum daily pCO₂ values occurred late at night to the early morning (~4:00-8:00 hrs). The pCO₂ varied in the opposite direction of oxygen concentrations, which peaked in the mid-afternoon and reached minimum concentrations during the night. Pearson correlations between pCO₂ and pO₂ at each buoy are shown in Table 2.3. An anti-correlation of -0.75 was observed at CRIMP-2: negative, albeit weak, correlations were also observed at Ala Wai and Kilo Nalu. An example of the diel anti-correlation cycle is shown in Figure 2.4

Table 2.2: Daily ranges of pCO₂ for each buoy over the study period were calculated and a mean, min, max, and standard deviation of the ranges were calculated. Daily pCO₂ values at CRIMP-2 on the reef fluctuate with a range 4x greater than any other buoy due to elevated levels of productivity, respiration, calcification, and dissolution.

pCO _{2 sw}	Daily Range Mean (µatm)	Daily Range Max (µatm)	Daily Range St. Dev
CRIMP-2	196	557	72.2
Ala Wai	52	146	21.3
Kilo Nalu	30	124	19.3
CRIMP-1	42	204	25.4

Table 2.3: A negative (albeit weak for AW and KN) anti-correlation is exhibited between pCO₂ and pO₂. Autocorrelation shows a strong 24 hour periodicity indicative of P/R cycles.

Location	pCO ₂ vs pO ₂ Correlation	pCO ₂ Autocorrelation		
		12 hrs	24 hrs	72 hrs
CRIMP-2	-0.75	-0.20	0.76	0.59
Ala Wai	-0.29	0.31	0.72	0.62
Kilo Nalu	-0.23	0.48	0.75	0.59

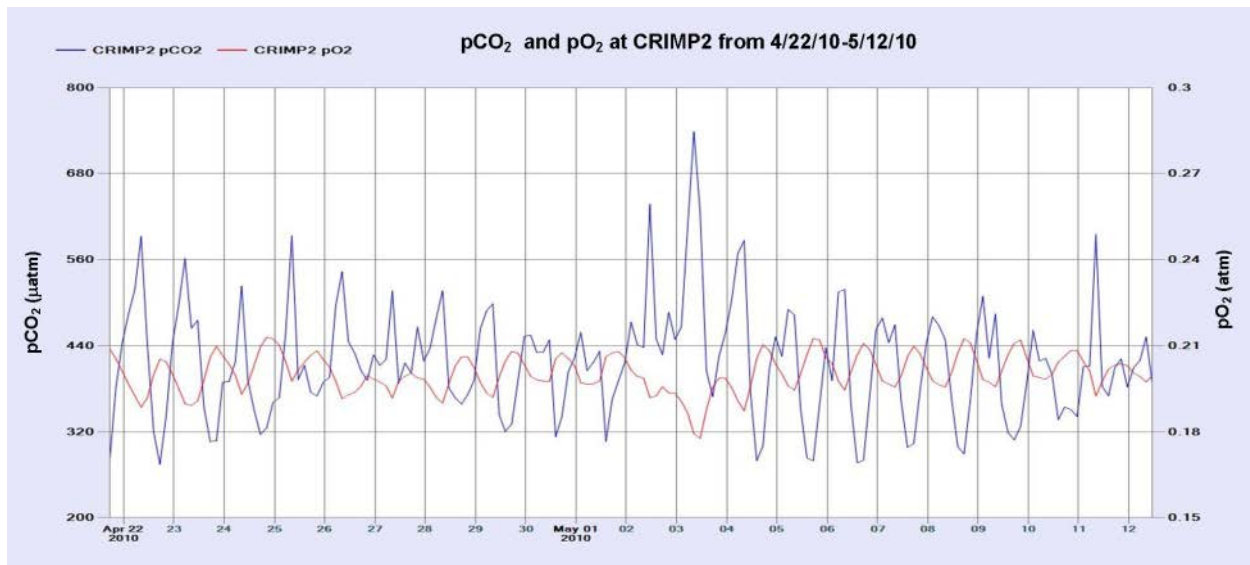


Figure 2.4: $p\text{CO}_2$ and $p\text{O}_2$ at CRIMP-2 buoy are anti-correlated (see Table 2.3) since the reef is highly productive. Photosynthesis during the day decreases $p\text{CO}_2$ while increasing $p\text{O}_2$, with a max O_2 saturation resulting at $\sim 14:00$. Respiration at night drives $p\text{CO}_2$ up, with maximum values measured around 04:00-07:00. Elevated $p\text{CO}_2$ from 5/2-5/4 was caused by low wind period ($0\text{-}2\text{ m s}^{-1}$ rather than normal $6\text{-}8\text{ m s}^{-1}$) increasing residence time and lowering the gas transfer velocity resulting in a buildup of CO_2 from respiration and calcification.

Autocorrelation was also evaluated for each buoy data set to determine the periodicity of $p\text{CO}_2$. This value indicates the correlation between all points separated by specific time intervals in the same data set. A strong autocorrelation was found at a period of 24 hours for each location. An autocorrelation plot for CRIMP-2 is shown in Figure 2.5. This correlation stayed relatively strong for 48 and 72 hours but dropped off (<0.5) over greater multiples of 24 hours. The correlation of 0.74 at 24 hrs observed at CRIMP-2 was the highest of the three locations during the study period (see Table 2.3). A correlation greater than 0.50 existed out to 72 hours (24 hr intervals), meaning that even points 72 hours (3 days) apart had a correlation value of greater than 0.50. A much lower (and sometimes negative) correlation occurred between points 12 hours apart.

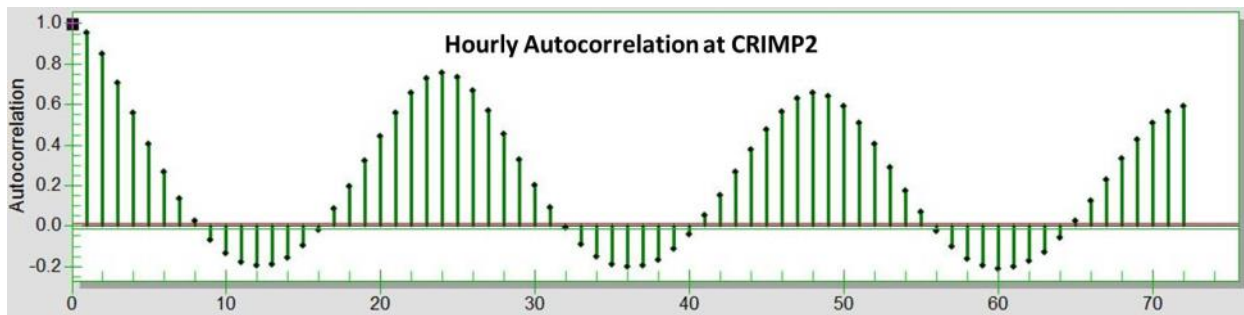


Figure 2.5: Autocorrelation of hourly pCO₂ at CRIMP-2 clearly shows a daily cycle which is highly correlated even up to 72 hours.

Instantaneous CO₂ fluxes at the three buoy sites are presented in Figure 2.6 in units of mmol C m⁻² hr⁻¹ during the entire study period of June 2008 to December 2011. Statistics for these fluxes are shown in Table 2.4. As expected from the larger range of pCO₂ values, CRIMP-2 displayed the largest range of flux and had a mean instantaneous flux of 0.13 ± 0.030 mmol C m⁻² hr⁻¹. The mean flux at Kilo Nalu was 0 and 0.005 ± 0.005 at Ala Wai. Percentage of time spent as a source and a sink was also computed for the three sites. The CRIMP-2 and Ala Wai water columns were CO₂ sources to the atmosphere 78% and 66% of the study period, respectively. The Kilo Nalu location was a source 51% of the time.

Net annualized fluxes for all three locations are also shown in Table 2.4 in units of mol C/m²/yr. CRIMP-2 was a source of 1.15 ± 0.27 mol C m⁻² yr⁻¹, while Ala Wai and Kilo Nalu were essentially neutral at 0.045 ± 0.048 mol C m⁻² yr⁻¹ and -0.0050 ± 0.072 mol C m⁻² yr⁻¹,

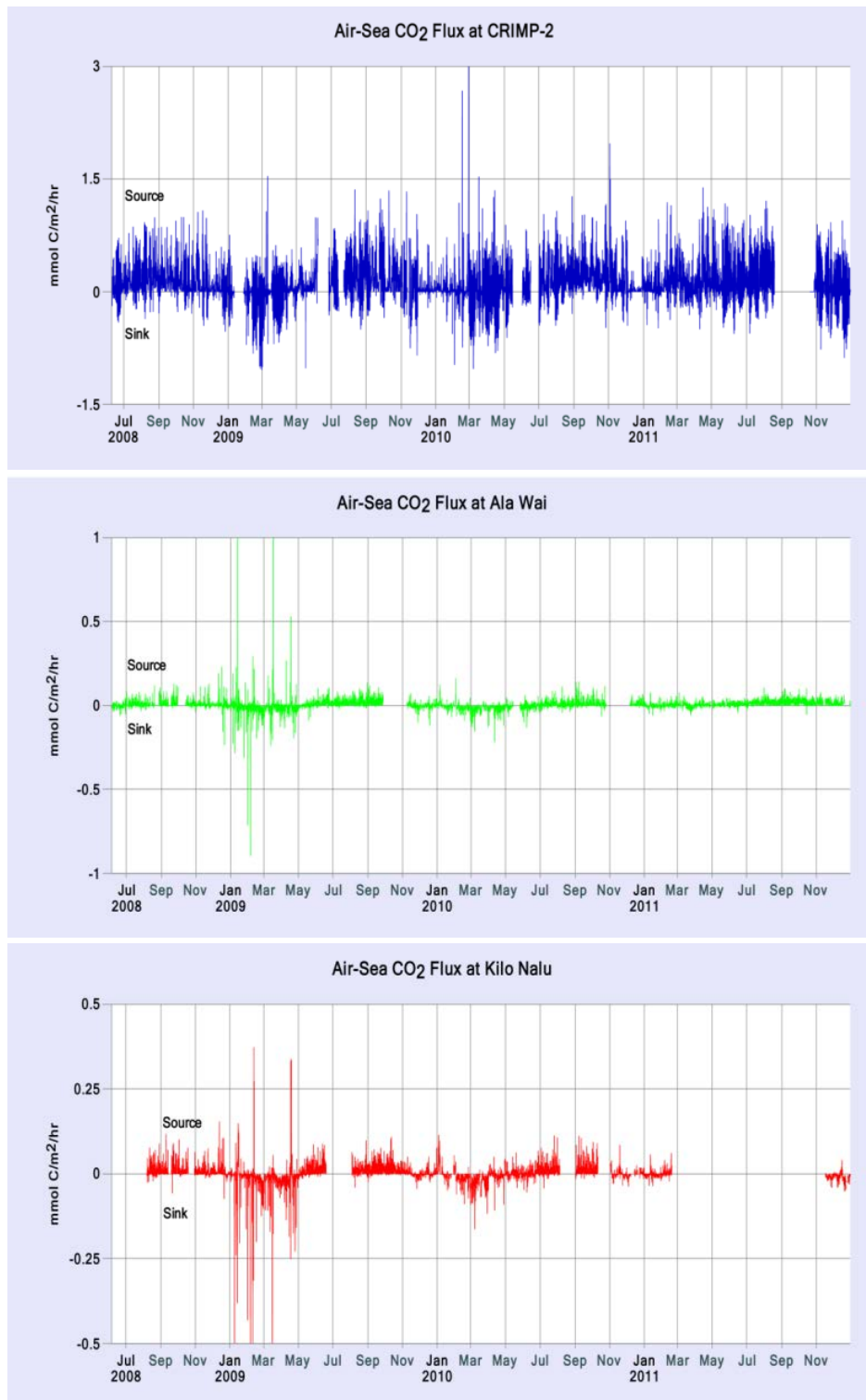


Figure 2.6: Instantaneous air-sea gas exchange of CO₂ at all three buoy locations is shown. Note that positive values represent a source of CO₂ to the atmosphere, while negative values represent a sink of CO₂ from the atmosphere. Each environment displays a seasonal trend of source activity in the summer and sink activity in the winter.

respectively. For comparison, CRIMP displayed an annualized flux of $1.76 \pm 0.37 \text{ mol C m}^{-2} \text{ yr}^{-1}$ for the time period of December 2005 to June 2008 (Massaro et al., 2012).

Table 2.5 shows net annualized fluxes (in $\text{mol C m}^{-2} \text{ yr}^{-1}$) for each year (2008-2011) of the study period as well as for each season of the study period. Seasons are separated as summer dry periods from May through October and the winter wet periods from November through April. The water at CRIMP-2 was a source of CO_2 to the atmosphere every year of the study period ($1.39 \pm 0.25 \text{ mol C m}^{-2} \text{ yr}^{-1}$, $0.82 \pm 0.20 \text{ mol C m}^{-2} \text{ yr}^{-1}$, $1.10 \pm 0.28 \text{ mol C m}^{-2} \text{ yr}^{-1}$, and $1.31 \pm 0.36 \text{ mol C m}^{-2} \text{ yr}^{-1}$). The water at Ala Wai was initially a source of CO_2 in 2008 and 2009, switched to a sink of CO_2 (albeit a small sink) in 2010 of $-0.003 \pm 0.013 \text{ mol C m}^{-2} \text{ yr}^{-1}$ and back to a source of $0.092 \text{ mol C m}^{-2} \text{ yr}^{-1}$ in 2011. Initially, in 2008, the Kilo Nalu environment was a source ($0.073 \pm 0.081 \text{ mol C m}^{-2} \text{ yr}^{-1}$) but from 2009-2011, the surface seawater most likely transitioned to a sink ($-0.018 \text{ mol C m}^{-2} \text{ yr}^{-1}$, $0.00 \text{ mol C m}^{-2} \text{ yr}^{-1}$, and $-0.032 \text{ mol C m}^{-2} \text{ yr}^{-1}$, respectively). Because of the small value of $\Delta p\text{CO}_2$ and resulting high relative uncertainty, it is not possible to classify at present the Kilo Nalu location as a CO_2 source or sink. Each location also displayed a seasonal trend in flux. At CRIMP-2, waters oscillate between strong sources in the summers (mean of $1.66 \text{ mol C m}^{-2} \text{ yr}^{-1}$) and weaker sources in the winter (mean of $0.66 \text{ mol C m}^{-2} \text{ yr}^{-1}$). The same trend was observed at both the Ala Wai and Kilo Nalu locations, as the water column switched between source and sink behavior on a summer to winter time scale. Data are not shown from the Kilo Nalu buoy for the winter of 2010-2011 or the summer of 2011 due to problems with the equilibrator.

Table 2.4: Instantaneous flux ranges are shown for each buoy as well as the percentage of time spent as a source or a sink. Note that these values do not add up to 100% due to periods of no wind or of $p\text{CO}_{2\text{sw}}$ equaling $p\text{CO}_{2\text{air}}$. Net annualized flux measurements show that the CRIMP-2 buoy environment is a significant source of CO_2 to the atmosphere (positive values indicate source), while the Ala Wai and Kilo Nalu environments are barely a net source and sink, respectively.

*CRIMP-1 data set from Nov. 2005 to June 2008.

June 2008 - Dec 2011	Max Source	Max Sink	Mean	% Time As Source	% Time As Sink	Net Annualized Flux
	mmol C m ⁻² hr ⁻¹					mol C m ⁻² yr ⁻¹
CRIMP-2	3.25	-1.04	0.13	78.0%	21.3%	1.15
Ala Wai	1.72	-0.89	0.005	66.0%	33.9%	0.045
Kilo Nalu	0.373	-1.56	0.00	51.4%	48.4%	-0.0056
CRIMP-1*	1.34	-0.71	0.20	94.2%	5.5%	1.78*

Table 2.5: Annualized fluxes for each year of the study period as well as broken into the summer and winter (dry and wet) seasons. Note that positive values indicate source behavior of CO_2 to the atmosphere while negative (and red) values indicate sink behavior of CO_2 from the atmosphere. Because the buoys were deployed in June 2008, the annualized flux for 2008 is only calculated from June 2008 – December 2008. Each buoy oscillates between source behavior in the summer and weak source or sink behavior in the winter. Summer (dry season) is defined as May-October and winter (wet season) is November-April. All fluxes are in mol C m⁻² yr⁻¹.

	2008		2009		2010		2011
CRIMP-2	1.39		0.82		1.10		1.31
Ala Wai	0.064		0.027		-0.003		0.092
Kilo Nalu	0.073		-0.018		0.00		-0.032

	Summer '08	Winter '08-'09	Summer '09	Winter '09-'10	Summer '10	Winter '10-'11	Summer '11
CRIMP-2	1.60	0.31	1.63	0.56	1.71	1.12	1.71
Ala Wai	0.069	-0.035	0.12	-0.057	0.049	0.028	0.13
Kilo Nalu	0.074	-0.082	0.086	-0.040	0.055	N/A	N/A

Total alkalinity at the buoy locations ranged from a mean of 2225 $\mu\text{mol kg}^{-1}$ at CRIMP-2 to 2306 and 2298 at Kilo Nalu and Ala Wai, respectively. A_T data from synoptic sampling are shown in Figure 2.7. C_T and pH (total scale), calculated from A_T and $p\text{CO}_2$, were lower at CRIMP-2 (1960 $\mu\text{mol kg}^{-1}$ and 7.99) than at Ala Wai and Kilo Nalu (~1993 $\mu\text{mol kg}^{-1}$ and ~8.06). Carbon system parameters and statistics are shown in Table 2.6. The Kilo Nalu

environment displayed the least amount of variability, while the water at CRIMP-2 and at Ala Wai had similar absolute variability, despite differences in the mean values. Data from surface waters at Station ALOHA, from the Hawaiian Ocean Time-series (HOT, <http://hahana.soest.hawaii.edu/hot/hot-dogs/>), during the same time period, are also shown and are most comparable with Kilo Nalu. Data from Shamberger et al. (2011) taken from 3 separate synoptic experiments at the CRIMP-2 site and a mid-reef site, during 6/08, 8/09, and 2/10, are consistent with the data from this study. Figure 2.8 shows the relationship between A_T and C_T at each location. Both A_T and C_T have been normalized to a salinity of 35 (nA_T and nC_T) to help reduce the effects of mixing of water masses with different properties. HOT data from 2008-2011 (<25m) are also shown as an end-member point included in each regression.

Table 2.6: Carbon system parameters C_T , pH, and Ω_{Ar} were calculated from A_T and pCO_2 samples collected at each buoy. Both A_T and C_T have been normalized to salinity = 35 (nA_T and nC_T). Ω_{Ar} data from other studies in Kaneohe Bay compare well with the values calculated for CRIMP-2 during this study. Data from Station ALOHA and the HOT program also agree with our findings that the water column at Ala Wai and Kilo Nalu represents open ocean water that has been slightly altered by respiration and organic matter remineralization.

Location	nA_T ($\mu\text{mol kg}^{-1}$)		nC_T ($\mu\text{mol kg}^{-1}$)		pH		Ω_{Ar}	
	Mean	Range	Mean	Range	Mean	Range	Mean	Range
CRIMP-2 (this study)	2230	2182- 2279	1967	1851- 2021	7.99	7.90-8.13	2.96	2.40- 3.77
Ala Wai (this study)	2306	2167- 2350	2001	1880- 2050	8.05	7.99-8.09	3.40	3.04- 3.73
Kilo Nalu (this study)	2302	2263- 2335	1988	1946- 2013	8.06	8.03-8.08	3.50	3.26- 3.63
HOT (2009- 2011)	2307	2298- 2317	1985	1969- 1999	8.07	8.06-8.08	3.63	3.56- 3.71
CRIMP-2 (Shamberger et al., 2011)							2.83	2.50- 3.07
K-Bay Midreef (Shamberger et al., 2011)							3.18	3.08- 3.25

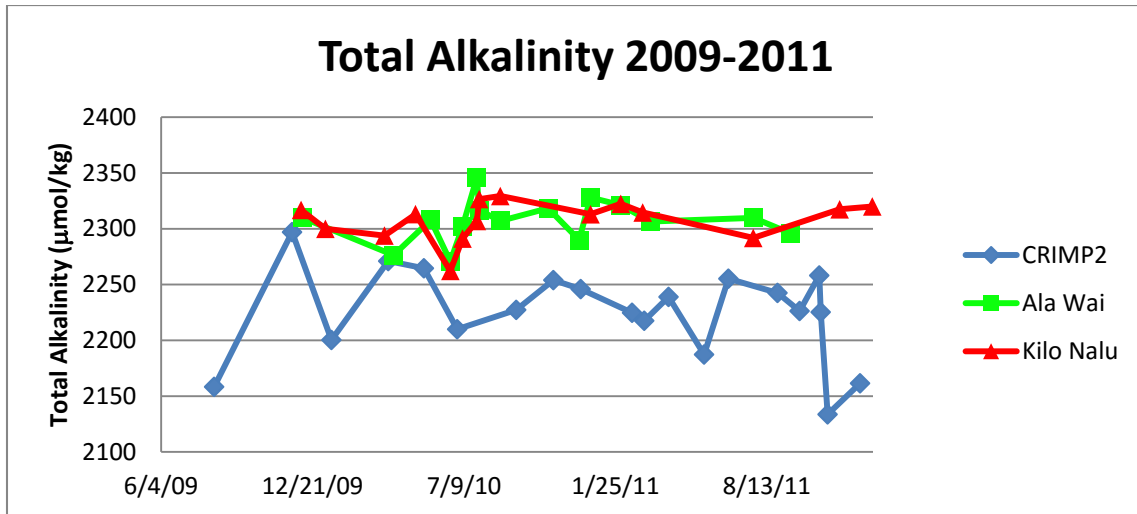


Figure 2.7: Total alkalinity measured at each buoy location from 2009-2011 is displayed. A_T at the CRIMP-2 buoy is consistently lower, due to calcification as open ocean water flows across the barrier reef. Water at the Ala Wai and Kilo Nalu sites is more representative of open ocean water, showing only a small change from typical offshore water, which far less variability over time.

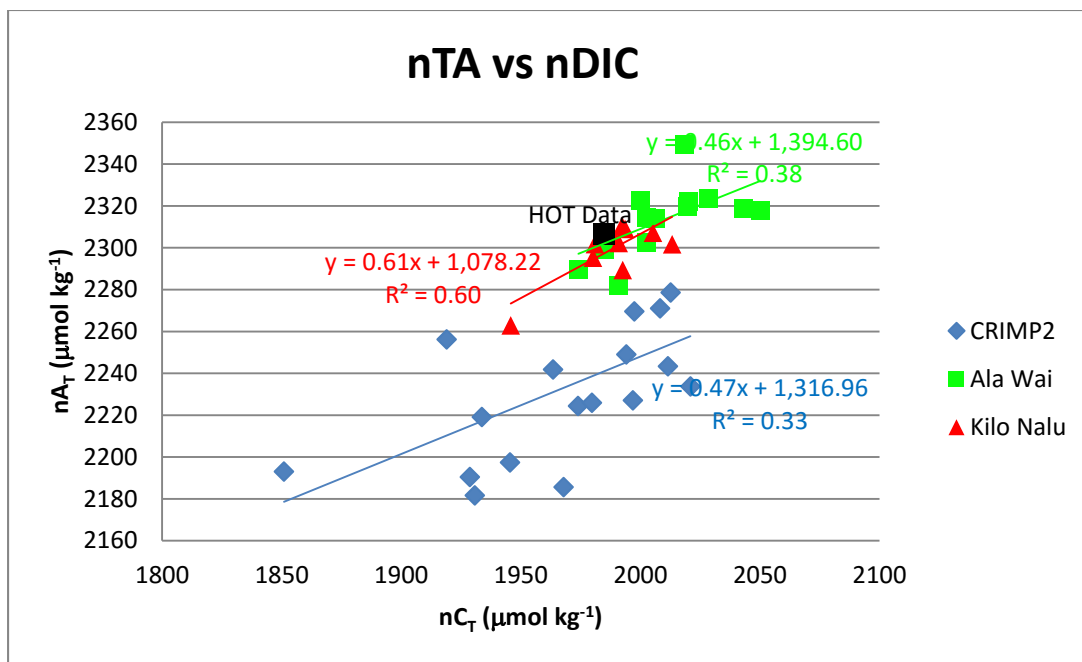


Figure 2.8: A_T and C_T have been normalized to $S=35$ to remove mixing effects and show the relationship between the two parameters. Regression lines include the HOT mean data from 2008-2011 to serve as an end-member point. A system controlled solely by photosynthesis and respiration would have a theoretical slope of 1, while a system controlled only by calcification and dissolution would have a slope of 2. The data for Ala Wai and Kilo Nalu cluster around typical open ocean values, although a small addition of pCO_2 from organic matter remineralization results in higher C_T values at Ala Wai. CRIMP-2 is highly variable due to the combined effects of P/R, calcification/dissolution and residence time across the reef.

2.6 Discussion

2.6.1 Physical Controls of $p\text{CO}_2$

During the 3.5 year study period, all three buoy environments displayed temporal cycles of $p\text{CO}_2$ on time scales ranging from daily to seasonal. Data (in Figure 2.2a), collected every three hours, from all three buoys show the long term seasonal variability, due in part to temperature changes, as well as the short term (hourly-weekly) variability due to both biological activity and physical forcing.

Monthly mean $p\text{CO}_2$ is shown in Figure 2.3a to clarify the seasonal trends of $p\text{CO}_2$. The summer dry period, from May-October, is marked by warmer water and air temperatures and significantly less precipitation, resulting in less nutrient-rich land runoff (Ringue and Mackenzie, 2005; De Carlo et al. 2007, Hoover and Mackenzie, 2009; Drupp et al. 2011). CRIMP-2 exhibited a seasonal amplitude of $p\text{CO}_2$ of $\sim 100 \mu\text{atm}$, while seasonal amplitudes at Kilo Nalu and Ala Wai were $\sim 35 \mu\text{atm}$. These amplitudes are based on monthly mean data in order to eliminate large transient increases or decreases unrelated to seasonal variation. Because increasing temperature raises seawater $p\text{CO}_2$ (and vice versa) by 4.23% per degree Celsius (Takahashi et al. 1993), $p\text{CO}_2$ is elevated in the summer and depressed in the winter at all three locations. Temperature changes, however, are not the only cause of $p\text{CO}_2$ changes in the water column at any of these locations. If temperature was the only factor, the annual seasonal amplitudes (based on monthly means) should be nearly twice the observed ranges at Kilo Nalu and Ala Wai, and slightly less than the observed range at CRIMP-2. The other main factors driving long-term $p\text{CO}_2$ trends include biological processes, residence time (a function of mixing), and air to sea gas exchange (a function of wind speed and $\Delta p\text{CO}_2$). These processes are discussed below.

In order to separate the effects of temperature and biological processes on pCO₂, two different normalizations were applied (Takahashi et al., 1993). Equation 2.4 was used to derive the temperature-dependent effects on pCO₂. The values are calculated based on a mean pCO₂ at each location for the entire study period, and are representative of temperature-induced changes under isochemical conditions (i.e. no biological/mixing effects on water chemistry). On short time scales, greater variation is observed at CRIMP-2 than at either Kilo Nalu or Ala Wai, due to larger daily temperature fluctuations, the shallow depth of the reef and the longer water residence time of water in Kaneohe Bay. On a seasonal to annual scale, greater variation (~1.5 times) is also observed at CRIMP-2 compared to the other locations. This enhanced variation in pCO₂ is caused by an annual temperature range at CRIMP-2 approximately 1.5 times larger than at either Kilo Nalu or Ala Wai (Figure 2.3b). Temperature is the strongest contributor to long-term pCO₂ variations, and it even has a daily effect (mean daily range of 21 μatm), but it is not the only physical factor affecting pCO₂.

Residence time is another important physical factor impacting pCO₂, as it controls the amount of time the water column is exposed to biological processes. Longer residence times allow for an accumulation of CO₂ from continuous respiration and calcification by the biological community. The residence time of water in Kaneohe Bay is controlled by wave action and wind speed and less by tidal mixing. Tradewinds blow from the northeast approximately 80% of the year with a mean speed of 4.9 m s⁻¹, and wave action is considered to be the dominant control on current speed across the reef (Lowe et al., 2009b). Water takes only a few hours to travel across the reef flat, although during light winds (and the consequent low wave action), the water can take more than a day to flow across the reef (Shamberger et al., 2011). Lowe et al. (2009 a/b) also show some model runs with residence times exceeding 24 hours. An example of longer

residence time leading to increased pCO₂ is shown in Figure 2.4. Beginning on May 1, 2010 and lasting until May 5, wind speeds were dramatically lower (<2 m s⁻¹) than typical (~4-6 m s⁻¹). The current speed across the reef, based on offshore significant wave height using the relationship developed for the Kaneohe Bay barrier reef by Lowe et al. (2009b) immediately prior to this period was approximately 30 cm s⁻¹ and dropped to a low of ~10 cm s⁻¹ on May 3. The reduction in wind/current speed significantly increased the water residence time on the reef, resulting in an accumulation of CO₂ derived from calcification and respiration. In addition, low wind speeds reduce air-sea gas exchange, thereby lowering gas evasion rates, and further enhancing the accumulation of CO₂ in the water column (Massaro et al., 2012). In a related study on the Kaneohe Bay barrier reef, Shamberger et al. (2011) found that daily cycles of A_T were enhanced and pCO₂ was elevated on days when wind speeds were low and residence time was long (13+ hours). The higher mean pCO₂ at CRIMP in southern Kaneohe Bay, despite considerably lower rates of calcification (Drupp et al., 2011; Massaro et al., 2012), was attributed primarily to a longer residence time of approximately 15-30 days (Ostrander et al., 2008; Lowe et al., 2009a), which further supports our findings.

The chemistry of water at Kilo Nalu, in stark contrast to Kaneohe Bay, displays little short- or long-term variability. It is reasonably representative of the surrounding open ocean water, with a mean pCO₂ of 378 μatm for the study period and a standard deviation that is four times less than that at CRIMP-2. The Kilo Nalu location is very weakly stratified and consistently flushed by tides, currents, and waves. Stratification of the water column at Kilo Nalu is mainly caused by daily heating and is relatively weak, if present at all, while convective mixing destabilizes the site at night (Hamilton et al., 1995; Sevadjan et al., 2010). Water column productivity is generally low and chlorophyll-a concentrations rarely exceed 0.5-1.0 μg L⁻¹

(Tomlinson et al., 2011). Benthic productivity is also likely low as the bottom substrate is primarily sand over limestone pavement with very little coral or algal cover. This deeper (relative to CRIMP-2), fairly well mixed water column masks much of the CO₂ signal, which is low to begin with at this site. The Ala Wai buoy location experiences similar physical forcings as Kilo Nalu, which contribute to a similar mean pCO₂ of 389 μatm, although its proximity to the mouth of the Ala Wai Canal results in stronger land-ocean interactions at this site due to enhanced fluvial runoff and nutrient inputs (discussed below).

2.6.2 Biogeochemical Controls of pCO₂

The water column at CRIMP-2 (blue in Figure 2.2) exhibits the largest short-term variability of pCO₂ observed at all three locations owing to high rates of daily calcification and productivity on the reef flat (Shamberger et al., 2011). A similar trend of short-term variability was described by Drupp et al. (2011) at the CRIMP location in southern Kaneohe Bay.

Normalization of pCO₂ to both mean temperature and mean pCO₂ separates the effects of temperature-independent and temperature-dependent processes on pCO₂ (Takahashi et al. 1993, 2002). Temperature normalization (equation 2.3) alone removes the effect of temperature on pCO₂ and provides a value that Takahashi (1993) refers to as reflective of the “net biology effect.” It is clearly evident in Figure 2.2b that T-normalized pCO₂ (“net biology effect”) accounts for the vast majority of short-term variability of pCO₂ and even displays a slight seasonal trend. The standard deviation at all three study locations barely changes between the *in-situ* pCO₂ and the T-normalized value, indicating that the majority of the variance in the *in-situ* pCO₂ values cannot be attributed to temperature. The CRIMP-2, Kilo Nalu, and Ala Wai sites have T-normalized standard deviations of 84.5 μatm, 17.5 μatm, and 24.4 μatm, respectively, nearly identical to the standard deviations of the *in-situ* values of 83.4 μatm, 18.2 μatm, and 25.3

μatm , respectively.

Figure 2.9 shows the A_T at CRIMP-2 versus salinity. The conservative mixing line (black dashed line) was derived by Massaro et al. (2012) for Kaneohe Bay, using offshore seawater and a zero salinity intercept derived from water samples collected at the mouth of Kaneohe Stream, the major river flowing into Kaneohe Bay. All of the CRIMP-2 samples, except for 11/14/2009, fall below the mixing line supporting the hypothesis that calcification/productivity processes across the reef are the main drivers of temporal changes in $p\text{CO}_2$ and A_T . The only sample that does not fall below the mixing line was taken on a day with stronger than average trade winds (gusts up to 9 m s^{-1}) resulting in faster current speeds (short residence time), as well as below average solar radiation reducing photosynthetic and calcification rates. The point falls virtually on the mixing line ($A_T=2297 \mu\text{mol kg}^{-1}$) suggesting that the seawater sampled at that time may have represented open ocean water.

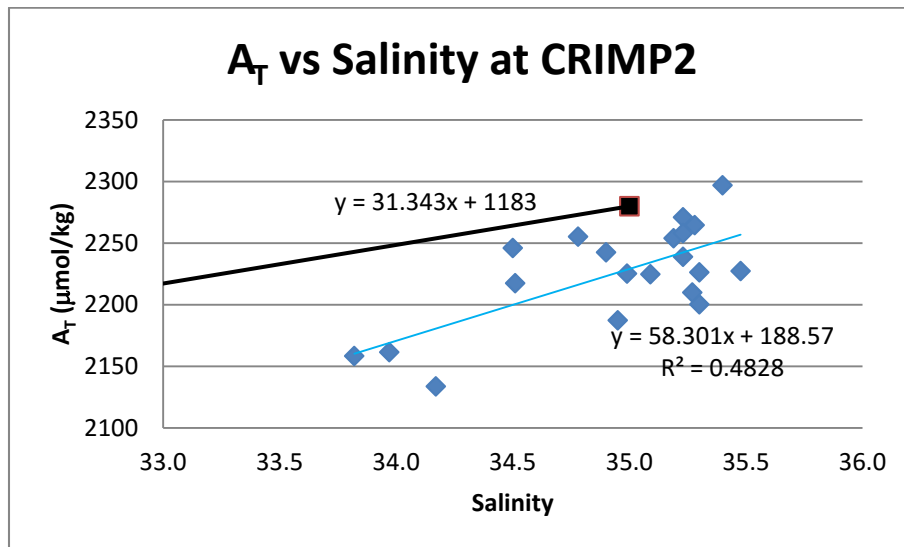


Figure 2.9: The A_T vs salinity plot can help identify whether alkalinity was added or removed as water flowed across the reef as water moved towards CRIMP-2. Because all but one of the samples fall below the conservative mixing line, alkalinity was biogeochemically removed across the reef flat. The black square is the open ocean end member point used to calculate the conservative mixing line.

Daily pCO₂ values at CRIMP-2 on the reef fluctuate widely with a mean range four times greater than the two other buoys. Chlorophyll measured at all three buoys is low (mean < 0.6 μg L⁻¹), implying that most of the photosynthesis/respiration and calcification/dissolution signals observed at CRIMP-2 are driven by the benthic reef flat organisms, rather than organisms in the water column. Average values of total nitrogen (NO₃⁻ + NO₂⁻ + NH₃) were 0.55 μmol at sites across the reef and 0.46 μmol at CRIMP-2, and inorganic phosphate was below detection levels (0.29 μmol L⁻¹ for all samples. Water column production was likely nutrient limited as previously shown by Ringuelet and Mackenzie (2005) and Drupp et al., (2011). A study performed by Shamberger et al. (2011) found that net ecosystem production (NEP) on a daily basis ranged from -378 mmol m⁻² d⁻¹ to 80 mmol m⁻² d⁻¹ (negative values indicate net respiration, positive values indicate net production). The reef varied from net autotrophic during the day to net heterotrophic at night during this study, a characteristic of many reef systems.

Daily cycles of pCO₂, typical of what would be expected from daytime photosynthesis and nighttime respiration, are characterized by a maximum pCO₂ occurring at night/early morning, usually between 04:00-08:00, with a corresponding minimum pCO₂ occurring in the mid-afternoon, ~14:00-17:00. This cycle mirrors that of pO₂, which peaks in the late-afternoon and reaches a minimum in the early morning. This same cycle, caused by photosynthesis consuming CO₂ and producing O₂ during the day while respiration at night consumes O₂ and produces CO₂, was also observed at CRIMP (Drupp et al., 2011 and Massaro et al., 2012).

Autocorrelations, highlighted in the results and Table 2.3 shows that points separated by multiples of 24h (same time each day) are highly correlated even up to 72h apart (all points separated by 72h have correlations of ~0.56). After 72h, no points have a correlation better than 0.50. Because of this, CO₂ levels at the buoy locations can be fairly accurately predicted

approximately three days into the future under normal conditions. All points separated by 12h show weak or negative correlations. Because the points 12h apart are not strongly anti-correlated, daytime pCO₂ values are not an indication of what the nighttime values will be and vice versa. This is due to daytime photosynthesis and calcification being controlled primarily by solar radiation and nutrient availability, which change day to day. In addition, the water chemistry is affected by changes in residence time, which is primarily a function of wind speeds and forereef wave action. Because many of these factors are transient in nature, it is difficult to predict pCO₂ more than 2-3 days in advance. This makes long-term high resolution monitoring all the more valuable.

Although the data at CRIMP-2 are consistent with P/R cycles, Shamberger et al. (2011), in a complementary study on the barrier reef, showed that calcification increases during the day, with some dissolution occurring at night, and daily net ecosystem calcification ranged from 174 to 331 mmol CaCO₃ m⁻² d⁻¹ (positive values indicate net calcification, negative values indicate net dissolution). The release of CO₂ during calcification would counter its uptake during photosynthesis. Because of this, the observed pCO₂ is a **net concentration** that would be much lower were it not for calcification concurrent with photosynthesis. The opposite can be true at night when the uptake of CO₂ during dissolution counters the release of CO₂ from respiration.

The subdued seasonal trend remaining in the T-normalized pCO₂ data is different between CRIMP-2 and the south shore buoys, Kilo Nalu and Ala Wai. T-normalized pCO₂ at CRIMP-2 decreases during the winter (Nov.-Apr.) and increases in the summer (May-Oct.). This trend, however, is reversed in both Kilo Nalu and Ala Wai where T-normalized pCO₂ decreases during the summer months and increases in the winter. The trend on the south shore is consistent with summer/winter photosynthetic/respiration cycles (and a relative lack of calcification), as

shown, for example, by De Carlo et al. (this volume) in the Bay of Villefranche in the NW Mediterranean. Decreasing SST lowers the rate of water column primary production during the winter, leading to a slight increase in pCO₂ at Kilo Nalu and Ala Wai. In addition, at Ala Wai, increased organic rich runoff in the winter can cause periods of elevated pCO₂. However, at CRIMP-2 on the barrier reef, where calcification exerts a major biological control on pCO₂, decreased wintertime temperatures also favor lower rates of calcification (e.g. Jokiel and Coles, 1977; Coles and Jokiel, 1978; Marshall and Clode, 2004; Langdon and Atkinson, 2005), driving the T-normalized pCO₂ down. However, this effect may be somewhat mitigated by the simultaneous temperature-driven decrease in primary productivity (raising pCO₂ via increased respiration).

Although the mean pCO₂ and seasonal pCO₂ trends at the Ala Wai buoy are similar to those at the nearby Kilo Nalu site, seawater does experience greater short-term variability (evident as a slightly higher standard deviation), owing to its location near the mouth of the Ala Wai canal. This canal drains a considerable portion of the Honolulu urban watershed and its waters are enriched both in nutrients and organic matter as well as a number of pollutant chemical species (e.g., De Carlo et al., 2004, 2005; Tomlinson et al., 2011). This continuous and occasionally strong supply of nutrients and organic matter from the Ala Wai canal contributes to an enhanced daily photosynthesis/respiration cycle. During periods of heavy rainfall, the Ala Wai delivers large pulses of freshwater, sediment, and nutrients (Tomlinson et al., 2011). Tomlinson et al. (2011) described a storm in the Honolulu watershed that occurred on 13 March 2009 resulting in elevated chlorophyll at the Ala Wai buoy, peaking at 3-5 times the baseline values observed during the week following this intense 24-hour storm. In the two days following this storm, daily pCO₂ cycles, measured by WQB-AW, were significantly dampened due to an

increase in photosynthesis. However, the large amount of terrestrial organic matter, introduced by runoff, also enhanced respiration, driving pCO₂ levels back up at night. On 17 March 2011, pCO₂ reached its highest value of the season, 505 μatm. The following two days were marked by a phytoplankton bloom with chlorophyll levels 4.5 times greater than baseline values (Tomlinson et al., 2011), most likely caused by an increased nutrient subsidy following the remineralization of runoff derived organic matter. This same trend was also observed at the Kilo Nalu location, albeit on a considerably smaller scale. Following this storm, Kilo Nalu experienced daily cycles of pCO₂ of ~65 μatm, with maximum pCO₂ above 400 μatm from March 15 to 19. In comparison, the Kilo Nalu location had not shown pCO₂ over 400 μatm in more than a month. The response of Kilo Nalu to runoff from the Ala Wai canal is not typically this strong but particularly large amounts of rain in the Ala Wai watershed and overland flow near the buoy location undoubtedly contributed to additional non-point source runoff and an influx of organic material. Runoff-induced phytoplankton blooms and subsequent remineralization were also shown to affect similarly the pCO₂ levels in southern Kaneohe Bay at the original CRIMP location (Drupp et al., 2011).

Even under baseline conditions, the effect of remineralization of runoff derived organic matter can be observed at the Ala Wai location. Figure 2.8 shows nA_T versus nC_T at the three buoy locations. After normalization, the sample values, especially those from Kilo Nalu, cluster around values similar to the open ocean. Mean HOT surface (<20 m depth) samples have nA_T=2307 μmol kg⁻¹ and nC_T=1986 μmol kg⁻¹ (updated from Keeling et al., 2004; <http://hahana.soest.hawaii.edu/hot/hot-dogs/>) and have been added as an end-member point included in the regression. Some of the Ala Wai samples have elevated C_T due to the higher levels of pCO₂ derived from net respiration and remineralization of organic rich runoff from

land. The elevated A_T concentrations at Ala Wai, relative to the HOT data may reflect dissolution within the water column as it is very unlikely that sufficient alkalinity is being added from the land runoff. In contrast, the nA_T vs nC_T plot for CRIMP-2 is scattered due to the variety and greater variability of physical and biological processes previously discussed. Residence time is an important factor affecting A_T , as current speed and, on the rare occasion, direction across the reef are not always constant. Future plans include the deployment of acoustic Doppler current profilers (ADCP) to understand more fully the effects of residence time on pCO_2 and A_T in these different reef settings.

2.6.3 Air-Sea Gas Exchange

Instantaneous CO_2 fluxes are shown in Table 2.4 and Figure 2.6a-c. CRIMP-2 shows the largest range from $3.08 \text{ mmol C m}^{-2} \text{ hr}^{-1}$ to $-1.00 \text{ mmol C m}^{-2} \text{ hr}^{-1}$. Although this range was nearly two times greater than the CRIMP range reported by Massaro et al. (2012), the mean instantaneous flux was $0.128 \text{ mmol C m}^{-2} \text{ hr}^{-1}$, only about half that of the CRIMP mean. This can be attributed to the latter location having higher average pCO_2 concentrations despite having smaller variations in pCO_2 and lower levels of biological activity (including very little calcification). The lower variation, but higher mean concentration, is a result of the longer residence time of the south bay waters, which is on the order of days to weeks rather than a few hours as observed over the barrier reef. The waters surrounding all three buoys during parts of the study period acted as CO_2 sources to the atmosphere (positive flux), as well as sinks from the atmosphere (negative flux) during other time periods due to seasonal and diel variations in water column pCO_2 and transient events (often storms), resulting in phytoplankton blooms (pCO_2 drawdown) or organic matter respiration (pCO_2 increase). The net annualized fluxes for CRIMP-2, Ala Wai, and Kilo Nalu were $1.15 \text{ mol C m}^{-2} \text{ y}^{-1}$, $0.045 \text{ mol C m}^{-2} \text{ y}^{-1}$, and $-0.0056 \text{ mol C m}^{-2}$

y^{-1} , respectively. The flux at CRIMP-2, on the barrier reef, is consistent with, but lower than the flux obtained by Massaro et al. (2012) at CRIMP of $1.76 \text{ mol C m}^{-2} \text{ y}^{-1}$ in southern Kaneohe Bay from 2006-2008, and Fagan and Mackenzie's (2007) value of $1.45 \text{ mol C m}^{-2} \text{ y}^{-1}$ for the entire Kaneohe Bay lagoon. However, these three flux estimates are considerably greater than those calculated for the fringing reefs of Honolulu.

The Ala Wai study site is strongly influenced by mixing with open ocean seawater. However, it remains a net annual source of CO_2 to the atmosphere due to its proximity to frequent nutrient- and organic carbon-rich freshwater discharges and to respiration of labile organic matter in the water column (previously discussed). Waters near the Ala Wai buoy do, however, switch between source and sink seasonally. In the rainy winter months, enhanced nutrient-rich discharge from the watershed stimulates primary productivity during the day, although delivery of pre-existing organic matter also can increase respiration at night. Furthermore, the enhanced solubility of CO_2 at lower seawater temperature during the winter leads to a lower seawater pCO_2 relative to the atmosphere, resulting in air-sea gas exchange. This seasonality is reflected in the data in Table 2.5.

At all three locations, the seasonality in CO_2 flux (source in summer, sink in winter) is further enhanced by the seasonality of atmospheric CO_2 . In the winter, CO_2 in the Hawaiian atmosphere is significantly higher than during the summer (<http://www.esrl.noaa.gov/gmd/ccgg/trends/>). The higher atmospheric winter concentrations are part of the annual northern hemisphere P/R cycles. Because the seasonal variability of temperature and pCO_2 in the water column and in the atmosphere are in opposite directions, the ΔpCO_2 is affected throughout the entire year. For example, lower atmospheric CO_2 , coupled with higher temperature-driven water column pCO_2 during the summer, enhances gas exchange by

increasing the concentration gradient between the two reservoirs. In the winter, high atmospheric CO₂ and lower water column pCO₂ reduce the size of the ΔpCO₂ term. These opposing effects contribute to the seasonality in the source/sink function. At CRIMP-2, the ΔpCO₂ during the summer is driven even higher by calcification. Despite the finding from a recent short-term Kaneohe Bay barrier reef study of Shamberger et al. (2011) that did not show a significant increase in summertime calcification, many other studies support this conclusion. It has been found that corals in Hawai‘i and at other reef sites reach a maximum calcification rate at approximately 26°C, the ambient temperature of Hawaiian summers (Jokiel and Coles, 1977; Coles and Jokiel, 1978; Marshall and Clode, 2004; Langdon and Atkinson, 2005). Thus in general, we would anticipate higher calcification during the warm summertime. In contrast, at both Kilo Nalu and Ala Wai, the biological processes (higher summertime productivity) counteract the temperature seasonality (see Figure 2.6a-c), causing a decrease in ΔpCO₂.

In addition to the changes in the CO₂-carbonic acid system chemistry of the water, Hawaiian summers typically have stronger and more persistent tradewinds, which increase the rate of the gas exchange. It is these additive effects that lead to CRIMP-2 being a significant net annual source, and opposing effects that lead to Ala Wai and Kilo Nalu being a very mild source and mild sink, respectively.

Flux values presented here compare well to previous studies. Above we already compared the fluxes reported in Kaneohe Bay by Fagan and Mackenzie (2007) and Massaro et al. (2012). The fluxes estimated in this study are also of similar magnitude to those reported for other tropical reef environments. Ohde and Van Woesik (1999) calculated a flux of 1.8 mol C m⁻² yr⁻¹ for an Okinawan reef in Japan. Comparable reef environments in Bermuda (1.2 mol C m⁻²

yr⁻¹ at Hog Reef Flat, Bates et al., 2001) and the northern Great Barrier Reef (1.1 to 1.5 mol C m⁻² yr⁻¹ on Yonge Reef, Frankignoulle et al., 1996) also exhibited comparable fluxes.

2.7 Conclusions

Coastal tropical reef surface waters at multiple buoy moorings around the island of Oahu, Hawai‘i, exhibit highly variable CO₂–carbonic acid system chemistry and magnitude and direction of CO₂ exchange due to differences in land/ocean interactions, water column and benthic (CRIMP-2) photosynthesis/respiration, and residence time. Data from this study and previous work in Kaneohe Bay (De Carlo et al., 2007; Drupp et al., 2011; Ringuet and Mackenzie, 2005; Massaro et al., 2012) demonstrate the utility of long-term, high-resolution sampling to characterize accurately the carbon chemistry of the coastal surface waters of Hawai‘i and other similar tropical reef environments where diel cycles, land-derived runoff, and seasonal changes and physical characteristics can all combine to alter the CO₂-carbonic acid system chemistry of the water column on multiple time scales

Seasonal biological and temperature effects on the pCO₂ of the water column were in phase at CRIMP-2, due to vigorous benthic calcification, but at the Ala Wai and Kilo Nalu, where there is much less of an overall calcification signal, these seasonal effects were out of phase, leading to a smaller range of pCO₂. Total alkalinity data showed that the carbon chemistry of surface waters at the Ala Wai and Kilo Nalu buoy sites is primarily controlled by water mass mixing that is driven by tides and waves. At these locations, A_T and C_T values are very similar to open ocean values, with slightly elevated pCO₂ due to increased remineralization of organic matter derived from land runoff and respiration of organic matter produced *in situ* during nutrient-rich pulses of land runoff. A_T and C_T at the CRIMP-2 barrier reef location are primarily controlled by biological activity and the residence time of water on the reef.

Air-sea CO₂ exchange also showed seasonality. Both the Ala Wai and Kilo Nalu buoy locations became a sink during the winter months as cooler temperatures and brief phytoplankton blooms drew down pCO₂. While waters at CRIMP-2 never became a net sink during the winter months, it did display periods of sink activity causing an overall reduction in source strength in winter. During the summer months, high temperatures coupled with lower atmospheric CO₂ and stronger winds, as well as enhanced calcification (at CRIMP-2), led to each location acting as a source of CO₂ to the atmosphere. However, as previously stated, the processes controlling pCO₂ at CRIMP-2 are in phase, likely amplifying the net air-sea gas exchange by increasing seasonal variability, whereas, at Ala Wai and Kilo Nalu these processes are competing (out of phase) and likely reduce the net air-sea gas exchange. Currently Kaneohe Bay, both within the inner lagoon (Fagan and Mackenzie, 2007; Massaro et al., 2012) and its barrier reef, is a net source of CO₂ to the atmosphere, while the Ala Wai and Kilo Nalu areas are a weak source and weak sink of this gas, respectively.

It is important to note that this study along with the previous studies in southern Kaneohe Bay detailed by Drupp et al. (2011) and Massaro et al. (2012) have found significant differences in CO₂-carbonic acid system chemistry and CO₂ exchange between four Hawaiian reef settings located in close proximity to each other. It is critical that we do not over-extrapolate results from one setting to a global perspective as more and more studies show that CO₂ dynamics in coral reef environments are highly variable and often quite different between various locations.

2.8 Acknowledgments

The authors would like to thank the Hawai‘i Institute of Marine Biology (HIMB), including Dr. Jo Ann Leong, director of HIMB, and her support staff of Jim Lakey, Stan Ige, Fritz King, and Darren Oshiro. Our work in Kaneohe Bay could not have been completed without their ongoing help and cooperation, as well as the assistance of the engineering and technical personnel at NOAA/PMEL, in particular Stacy Maenner-Jones, Hendrick Miller, Sylvia Musielewicz, and Noah Lawrence-Slavas. We would also like to thank Jeff Jaegger, Jason Jones, and Robert Thompson for their assistance with boat operations and sample analysis as well as the two reviewers whose comments substantially improved this manuscript. This work was supported in part by a grant/cooperative agreement from the National Oceanic and Atmospheric Administration, Project R/IR-3, which is sponsored by the University of Hawai‘i Sea Grant College Program, SOEST, under Institutional Grant No. NA09OAR4170060 from NOAA Office of Sea Grant, Department of Commerce. The views expressed herein are those of the author(s) and do not necessarily reflect the views of NOAA or any of its subagencies. Funding was also provided by Pac-IOOS in support of the MAP-CO₂ monitoring program. This is UNIH-Sea Grant contribution JC-12-28 and SOEST contribution no. 8958

2.9 References

- Andersson AJ, Mackenzie FT (2004) Shallow-Water Oceans: A Source or Sink of Atmospheric CO₂? *Frontiers in Ecology and the Environment* 2: 348-353.
- Andersson AJ, Mackenzie FT, Lerman A (2006) Coastal ocean CO₂-carbonic acid-carbonate sediment system of the Anthropocene. *Global Biogeochemical Cycles* 20: GB1S92.
- Andersson AJ, Bates N, Mackenzie FT (2007) Devil's Hole as a natural laboratory. *Meridian* 2:14-17.
- Armstrong FAJ, Sterns CR, Strickland JDH (1967) The measurement of upwelling and subsequent biological processes by means of Technicon AutoAnalyzer and associated equipment. *Deep Sea Research* 14: 381
- Atkinson MJ (2000) Kaneohe Bay. In: Talbot F and Wilkinson C (eds) *Coral reefs, mangroves and seagrasses: a sourcebook for managers*. Science Communications AIMS
- Augustin L, Barbante C, Barnes PRF, et al. (2004) Eight glacial cycles from an Antarctic ice core. *Nature* 429: 623-628.
- Bates NR, Samuels L, Merlivat L (2001) Biogeochemical and Physical Factors Influencing Seawater fCO₂ and Air-Sea CO₂ Exchange on the Bermuda Coral Reef. *Limnology and Oceanography* 46: 833-846.
- Battista TA, Costa BM, Anderson SM (2007) Atlas of the Shallow-Water Benthic Habitats of the Main Hawaiian Islands. NOAA Technical Memorandum NOS NCCOS 61. NCCOS Biogeography Branch, Silver Springs, MD, 331 pp.
- Coles, SL and Jokiel PL (1978) Synergistic effects of temperature, salinity and light on the hermatypic coral *Montipora verrucosa*. *Marine Biology* 49:187-195.
- Cox DC, Fan PF, Chave KE, et al. (1973) Estuarine pollution in the State of Hawai'i; Kaneohe Bay study. University of Hawai'i Water Resources Research Center
- De Carlo, EH, Mousseau, L, Passafiume, O, Drupp, PS, and Gattuso, J-P (2013) Carbonate chemistry and air-sea CO₂ flux in a NW Mediterranean bay over a four year period: 2007-2011. *Aquatic Geochemistry* (this volume).
- De Carlo EH, Laudato B, Tomlinson MS (2004) Composition of water and suspended sediment in streams of urbanized subtropical watersheds in Hawai'i. *Applied Geochemistry* 19: 1011-1037.
- De Carlo EH, Tomlinson MS, Anthony SS (2005) Trace elements in streambed sediments of small subtropical streams on O'ahu, Hawai'i: Results from the USGS NAWQA program. *Applied Geochemistry* 20: 2157-2188.
- De Carlo EH, Hoover DJ, Young CW, Hoover RS, Mackenzie FT (2007) Impact of storm runoff from subtropical watersheds on coastal water quality and productivity. *Applied Geochemistry* 22:1777-1797. <http://dx.doi.org/10.1016/j.apgeochem.2007.03.034>
- Dickson AG (2001) Reference materials for oceanic measurements. *Oceanography* 14: 21-22.
- Dickson AG, Afghan JD, Anderson GC (2003) Reference materials for oceanic CO₂ analysis: a method for the certification of total alkalinity. *Marine Chemistry* 80: 185-197.

- Dickson AG, Millero FJ (1987) A comparison of the equilibrium constants for the dissociation of carbonic acid in seawater media. *Deep-Sea Research* 34: 1733-1743.
- Dickson AG, Sabine CL, Christian JR (2007) Guide to best practices for ocean CO₂ measurements. PICES Special Publication 3:191.
- Drupp PS, De Carlo EH, Mackenzie FT, Bienfang P, Sabine CL (2011) Nutrient inputs, dynamics and phytoplankton response in a semi-enclosed subtropical embayment, Kaneohe Bay, Hawai'i. *Aquatic Geochemistry* 17: 473-498.
<http://dx.doi.org/10.1007/s10498-010-9115-y>
- Fagan KE, Mackenzie FT (2007) Air-sea CO₂ exchange in a subtropical estuarine-coral reef system, Kaneohe Bay, Oahu, Hawai'i. *Marine Chemistry* 106:174–191
- Falter JL, Atkinson MJ, Merrifield MA (2004) Mass-transfer limitation of nutrient uptake by a wave dominated reef flat community. *Limnology & Oceanography* 49:1820–1831
- Falter JL, Lowe RJ, Atkinson MJ, Monismith SG, and Schar DW (2008) Continuous measurements of net production over a shallow reef community using a modified Eulerian approach. *Journal of Geophysical Research -Oceans* 113: CO7035.
- Feely RA, Sabine CL, Hernandez-Ayon JM, Ianson D, Hales B (2008) Evidence for upwelling of corrosive "acidified" water onto the continental shelf. *Science* 320:1490-1492.
- Feely RA, Sabine CL, Lee K, Berelson W, Kleypas J, Fabry VJ, Millero FJ (2004) Impact of anthropogenic CO₂ on the CaCO₃ system in the oceans. *Science* 305:362-366.
- Frankignoulle M, Canon C, and Gattuso JP (1994) Marine calcification as a source of carbon dioxide – positive feedback of increasing atmospheric CO₂. *Limnology and Oceanography* 39: 458-462.
- Frankignoulle M, Gattuso JP, Biondo R, Bourge I, Copin-Montegut G, and Pichon M (1996) Carbon fluxes in coral reefs. II. Eulerian study of inorganic carbon dynamics and measurement of air-sea CO₂ exchanges. *Marine Ecology Progress Series* 145: 123-132.
- Frankignoulle M, Abril G, Borges A, Bourge I, Canon C, Delille B, Libert E, Theate J-M. (1998) Carbon Dioxide Emission from European Estuaries. *Science* 282:434-436.
- Frankignoulle M., Borges A (2001) European continental shelf as a significant sink for atmospheric carbon dioxide. *Global Biogeochemical Cycles* 15: 569-576.
- Grasshoff K, Ehrhardt M, Kremling K (1983) *Methods of Seawater Analysis*, 2nd edition.
- Hales B, Bandstra L, Takahasi T, Covert P, Jennings J (2003) The Oregon coastal ocean: A sink for Atmospheric CO₂? *Newsletter of Coastal Ocean Processes* 17:4-5.
- Hamilton PJ, Singer J, Waddell E (1995) Mamala Bay study, ocean current measurements: a report to the Mamala Bay Commission, HI. Technical report. Scientific Applications International Corporation, Raleigh, NC.
- Hearn C, Atkinson MJ (2000) Effects of sea-level rise on the hydrodynamics of a coral reef lagoon: Kaneohe Bay, Hawai'i. In: Noye J (ed) *Sea-level changes and their effects*. World Scientific Publishing Co. Pte. Ltd, Singapore, pp 25–48.
- Ho DT, Law CS, Smith MJ, Schlosser P, Harvey M, Hill P (2006) Measurements of air-sea gas exchange at high wind speeds in the Southern Ocean: Implications for global

- parameterization. *Geophysical Research Letters* 31, L16611.
<http://dx.doi:10.1029/2006GL026817>
- Hollet KJ (1977) Shoaling of Kaneohe Bay, Oahu, Hawai'i in the period 1927–1976, based on bathymetric, sedimentological, and geographical studies. M.S. Thesis, University of Hawai'i, Honolulu, Hawai'i, p 145.
- Hoover D, Mackenzie FT (2009) Fluvial fluxes of water, suspended particulate matter, and nutrients and potential impacts on tropical coastal water biogeochemistry: Oahu, Hawai'i. *Aquatic Geochemistry* 15: 547–570.
- Hoover RS, Hoover D, Miller M, Landry MR, De Carlo EH, Mackenzie FT (2006) Zooplankton response to storm runoff in a tropical estuary: bottom up and top down controls. *Marine Ecology Progress Series* 318:187–201.
- Hunter CL, Evans CW (1995) Coral reefs in Kaneohe Bay, Hawai'i: two centuries of western influence and two decades of data. *Bulletine of Marine Science* 57:501–515
- Jokiel PL and Coles SL (1977) Effects of Temperature on the Mortality and Growth of Hawaiian Reef Corals. *Marine Biology* 43: 201-208.
- Jokiel PL, Hunter CL, Taguchi S, Watarai L (1993) Ecological impact of a fresh water “reef kill” on the reefs of Kaneohe Bay, Oahu, Hawai'i. *Coral Reefs* 12:177–184.
- Keeling CD, Brix H, Gruber N (2004) Seasonal and long-term dynamics of the upper ocean carbon cycle at Station ALOHA near Hawai'i. *Global Biogeochemical Cycles* 18: GB4006.
- Kinzie RA, Mackenzie FT, Smith SV, Stimson J (2001) CISNet: linkages between a tropical watershed and reef ecosystem. Final project report to NOAA. University of Hawai'i, Honolulu
- Langdon C and Atkinson MJ (2005) Effect of elevated pCO₂ on photosynthesis and calcification of corals and interactions with seasonal change in temperature/irradiance and nutrient enrichment. *Journal of Geophysical Research* 110:C09S07.
- Laws EA, Allen CB (1996) Water quality in a subtropical embayment more than a decade after diversion of sewage discharges. *Pacific Science* 50:194–210.
- Lewis E, Wallace DWR (1998) In: ORNL/CDIAC-105 (ed) Program Developed for CO₂ System Calculations. Carbon Dioxide Information Analysis Center, Oak Ridge National Laboratory, US Department of Energy, Oak Ridge, TN.
- Liss PS (1983) Gas Transfer: Experiments and Geochemical Implications, p. 241-298. In Liss PS and Slinn WGN (eds) *Air-Sea Exchange of Gases and Particles*. D. Reidel Publishing Company.
- Lowe RJ, Falter JL, Monismith SG, Atkinson MJ (2009a) A numerical study of circulation in a coastal reef-lagoon system. *Journal Geophysical Research-Oceans*. 114, C06022, <http://dx.doi:10.1029/2008/JC005081>.
- Lowe RJ, Falter JL, Monismith SG, Atkinson MJ (2009b) Wave-Driven Circulation of a Coastal Reef-Lagoon System. *Journal of Physical Oceanography* 39: 873-893.

- Mackenzie FT, De Carlo EH, Lerman A (2011) Coupled C, N, P, and O Biogeochemical Cycling at the Land-Ocean Interface. In: Wolanski E and McLusky DS (eds.) *Treatise on Estuarine and Coastal Sciences*, Vol 5, Waltham: Academic Press, pp. 317-342.
- Marshall AT and Clode P (2004) Calcification rate and the effect of temperature in zooxanthellate and an azooxanthellate scleractinian reef coral. *Coral Reefs* 23:218-224.
- Massaro RFS, De Carlo EH, Drupp PS, Mackenzie FT, Maenner-Jones S, Shamberger KE, Sabine CL, Feely RA (2012) Multiple Factors Driving Variability of CO₂ Exchange Between the Ocean and Atmosphere in a Tropical Coral Reef Environment. *Aquatic Geochemistry* 18: 357-386.
- Mehrbach C, Culberso CH, Hawley JE, Pytkowic RM (1973) Measurement of apparent dissociation-constants of carbonic-acid in seawater at atmospheric-pressure. *Limnology & Oceanography* 18: 897-907.
- Murphy J, Riley IP (1962) A modified single solution method for the determination of phosphate in natural waters. *Analytica Chimica Acta* 27: 31-36.
- Ohde S, Van Woesik R (1999) Carbon dioxide flux and metabolic processes of a coral reef, Okinawa. *Bulletin of Marine Science* 65: 559-576.
- Orr JC, Fabry VJ, Aumont O, et al. (2005) Anthropogenic ocean acidification over the twenty first century and its impacts on calcifying organisms. *Nature* 437:681-686.
- Ostrander CE, McManus MA, De Carlo EH, Mackenzie FT (2008) Temporal and spatial variability of freshwater plumes in a semi-enclosed estuarine-bay system. *Estuaries Coasts* 31:192-203. <http://dx.doi.org/10.1007/s12237-007-9001-z>
- Petit JR, Jouzel J, Raynaud D, et al. (1999) Climate and atmospheric history of the past 420,000 years from the Vostok ice core, Antarctica. *Nature* 399:429-436
- Ringuet S, Mackenzie FT (2005) Controls on nutrient and phytoplankton dynamics during normal flow and storm runoff conditions, Southern Kaneohe Bay, Hawai'i. *Estuaries* 28:327-337
- Roy KJ (1970) Change in bathymetric configuration, Kaneohe Bay, Oahu, 1882-1969. University of Hawai'i, HIG Report 70-15, p 26
- Sevadjian JC, McManus MA, Pawlak G (2010) Effects of physical structure and processes on thin zooplankton layers in Mamala Bay, Hawai'i. *Marine Ecology Progress Series* 409: 95-106.
- Shamberger KEF, Feely RA, Sabine CL, Atkinson MJ, De Carlo EH, Mackenzie FT, Drupp PS, Butterfield DA (2011) Calcification and Organic Production on a Hawaiian Coral Reef. *Marine Chemistry* 127: 64-75.
- Siegenthaler U, Stocker TF, Monnin E, et al. (2005) Stable Carbon Cycle: Climate Relationship during the Late Pleistocene. *Science* 310: 1313-1317.
- Smith SV, Kimmerer WJ, Laws EA, Brock RE, Walsh TW (1981) Kane'ohe Bay sewage diversion experiment: perspective on ecosystem responses to nutritional perturbation. *Pacific Science* 35:279-395

- Taguchi S, Laws EA (1987) Patterns and causes of temporal variability in the physiological condition of the phytoplankton community in Kaneohe Bay, Hawai'i. *J Plankton Res* 9:1143–1157
- Takahashi T, Olafsson J, Goddard JG, Chipman DW, Sutherland SC (1993) Seasonal-variation of CO₂ and nutrients in the high-latitude surface oceans – a comparative study. *Global Biogeochem Cycles* 7: 843-878.
- Takahashi T, Sutherland SC, Sweeney C, et al. (2002) Global sea-air CO₂ flux based on climatological surface ocean pCO₂ and seasonal biological and temperature effects. *Deep-Sea Research II* 49:1601-1622.
- Takahashi T, Sutherland SC, Wanninkhof R, et al. (2009) Climatological mean and decadal change in surface ocean pCO₂, and net sea-air CO₂ flux over the global oceans. *Deep Sea Research Part II* 56: 554-577.
- Tanaka K, Mackenzie FT (2005) Statistical and stability analysis of subtropical ecosystem dynamics in southern Kaneohe Bay. *Hawai'i Ecol Model* 188:296–326
- Tomlinson MS, De Carlo EH (2003) The need for high-resolution time series data to characterize Hawaiian streams. *Journal of American Water Resources Association* 39(1): 113-123.
- Tomlinson MS, De Carlo EH, McManus MA, et al. (2011) Characterizing the Effects of Two Storms on the Coastal Waters of O'ahu, Hawai'i, Using Data from the Pacific Islands Ocean Observing System. *Oceanography* 24: 182-199.
- Wang SL, Chen CTA, Hong GH, Chung CS (2000) Carbon dioxide and related parameters in the East China Sea. *Continental Shelf Research* 20: 525-544.
- Wanninkhof R (1992) Relationship between wind speed and gas exchange over the ocean. *Journal of Geophysical Research* 97: 7373-7382.
- Wanninkhof R, Park GH, Takahashi T, et al. (2012) Global ocean carbon uptake: magnitude, variability and trends. *Biogeosciences Discussions* 9: 10961-11012.
- Weiss RF (1974) Carbon dioxide in water and seawater: The solubility of a non-ideal gas. *Marine Chemistry* 2:203-215.
- Weiss RF, Price BA (1980) Nitrous oxide solubility in water and seawater. *Marine Chemistry* 8: 347-359.
- Zeebe RE, Wolf-Gladrow DA (2001) CO₂ in Seawater: Equilibrium, Kinetics, Isotopes. In Halpern D (ed). Elsevier Oceanography Series. Amsterdam, The Netherlands.

Chapter 3 POREWATER CO₂-CARBONIC ACID SYSTEM CHEMISTRY IN PERMEABLE CARBONATE REEF SANDS

This chapter is a manuscript submitted to *Marine Chemistry*.

Authors are: Patrick S. Drupp¹, Eric Heinen De Carlo¹, and Fred T. Mackenzie¹

¹Department of Oceanography, University of Hawai‘i at Manoa
1000e Road, Honolulu, HI 96822, USA

3.1 Abstract

Porewater was collected from highly permeable, carbonate-rich, sandy sediments at two locations, CRIMP-2 and Ala Wai, on coral reefs on Oahu, Hawai‘i. Samples were collected at the sediment-water interface and from porewater wells installed at sediment depths of 2, 4, 6, 8, 12, 16, 20, 30, 40, and 60 cm. Total alkalinity and dissolved inorganic carbon were enriched, relative to the overlying water column, and ratios of TA:DIC at the two sites (0.80 and 0.93) suggest that aerobic respiration and sulfate reduction - both coupled with carbonate mineral dissolution - in the oxic and anoxic layers, respectively, are the major controls on the biogeochemistry of the sediment-porewater system. The porewater was approaching thermodynamic saturation with respect to aragonite and was found to be undersaturated with respect to all phases of magnesian calcite containing greater than 12 mol% MgCO₃. In addition to microbial controls on porewater diagenesis, transient physical events in the water column, such as swells and changing bottom current speeds, appear to exert a strong influence on the porewater chemistry due to the highly permeable and porous nature of the sediments. Profiles collected before and after swell events at each location show an apparent flushing of the porewater system, replacing low pH, high DIC interstitial waters with seawater from the overlying water column. Based partially on the results of our porewater analysis, we hypothesize

that future changes in surface water DIC and pH resulting from ocean acidification (OA) could have a very significant impact on the dissolution rates of metastable skeletal and abiotic carbonate phases of varying magnesian calcite compositions (Mg-calcite) and aragonite, especially in sandy reef sediments like those of this study. As the carbonate mineral saturation state of the overlying water column continues to decrease due to OA, an increase in carbonate mineral dissolution is expected and the high advective rate of water exchange between the porewater of sandy sediments and the overlying water column, as observed in this study and others, along with increased rates of dissolution of metastable carbonate phases, could lead to significantly higher future rates of mass transfer of TA and DIC between the sediments and the overlying water column. This may result in a deficit of the CaCO_3 balance in some reef ecosystems and a decrease in accretion rates. Analysis of our porewater work coupled with previous studies of the porewater chemistry of Kaneohe Bay, Oahu siliciclastic-rich and siliciclastic-poor carbonate sediments leads to the conclusion that the porewaters of the former are more strongly buffered with respect to pH than those of the latter due to reverse weathering” reactions. Thus carbonate-rich sandy sediments of reefs with little terrestrial influence and aluminosilicate detritus may become more susceptible to calcium carbonate loss due to the enhanced environmental and microbial dissolution of carbonate substrates expected due to OA.

3.2 Introduction

Permeable sandy carbonate sediments can constitute up to 90% of the calcium carbonate (CaCO_3) found on coral reefs (e.g., Cyronak et al., 2013; Gattuso et al., 1998), but despite their ubiquitous presence in reef ecosystems, they were largely ignored in terms of porewater studies prior to the 1980’s (Boudreau et al. 2001; Jahnke et al. 2005; Janssen et al. 2005). These sands are composed primarily of skeletal reef material from the aragonitic and magnesian-calcitic

shells and tests of many organisms (e.g., Chave, 1954; Morse et al., 1985; Morse and Mackenzie, 1990). Despite the high concentrations of these metastable carbonate mineral phases, it was believed that these sandy sediments were biogeochemically unimportant reservoirs in terms of mineral-water reactions and early diagenetic processes were insignificant due to the lack of organic matter, whose abundance in sediments generally decreases with increasing mineral particle grain size (Janssen et al. 2005). Given their larger grain size, permeability (measured in Darcys, $1 D = 10^{-8} \text{ cm}^2$) can be orders of magnitude higher in sands (7 - 455 D) than in silts (0.0026 - 3.4 D) (Burdige 2006). This higher permeability was one factor that led to the recognition of the increased relative importance of advective solute fluxes, driven by changes in pressure gradients, in sands as opposed to diffusive solute fluxes in fine grained sediments, where molecular diffusion is the main driver of solute transport (e.g., Huettel and Gust 1992; Shum 1993; Boudreau 1997; Precht and Huettel 2004; Jahnke et al. 2005; Janssen et al. 2005). Surface waves, topographical sediment features such as ripples, tidal pumping, changes in near-bed current velocities, and temperature and salinity gradients can all alter pressure gradients and drive advection within highly permeable sediments (Huettel and Webster 2001).

The differences in physical properties between permeable sands and fine-grained sediments require that very different sampling methods be used when studying biogeochemical reactions and solute mass transfer in the two mediums (Jahnke et al. 2005). Although possible - with vibracores and to some extent, manual push cores - obtaining a permeable (e.g., sandy) sediment core and its interstitial waters without disrupting the physical structure of the sediment and its porewater gradient (or losing porewater) is more difficult than with fine-grained sediments. In addition, it is difficult to bring a permeable sediment core back to the laboratory and recreate the process of advection, driven by currents and pressure gradient forces, in a

laboratory environment during the incubation of a sandy core. Thus, studies of solute fluxes in sands, including total alkalinity (TA) and dissolved inorganic carbon (DIC), are often limited to interpretations based on diffusive transport, oversimplifying the processes occurring in these systems (Huettel et al. 1996; Janssen et al. 2005). As a result, *in-situ* studies of permeable sediments are highly desirable, if not necessary.

The use of annular-flow benthic chambers, as with fine-grained sediments, has been one approach to study sandy sediment/water column fluxes because the chambers represent more accurately the circulation patterns of water movement in the natural environment than do laboratory core incubations. Once the chamber is anchored in the sediment, a stirring disc produces water flow within the chamber that mimics turbulent motion in the overlying water and induces more natural advection of porewater (Huettel and Rusch 2000). Annular-flow benthic chambers have been employed in a wide variety of studies to measure solute fluxes in sandy sediments, including studies involving calcium carbonate (CaCO_3) dissolution and TA fluxes (Huettel and Rusch, 2000; Rao et al., 2012; and Cyronak et al., 2013a/b). Nevertheless, while chamber studies can provide valuable data for determining solute fluxes and can reasonably simulate natural conditions, these experiments do not provide detailed porewater solute concentration profiles extending into the sediments.

The only reasonably reliable method for measuring the depth concentration profiles of biogeochemically important solutes in porewater under natural conditions is via direct *in situ* sample collection (e.g., Sansone et al., 1988a/b; Tribble et al., 1988; Falter and Sansone, 2000b; Burdige et al., 2008; Burdige et al., 2010; Fogaren et al., 2013). Morse et al. (1987) made use of a harpoon sampler (“sand sucker”) to extract interstitial water directly from permeable sediments, and Burdige and colleagues have employed porewater “sippers” designed to be

inserted directly into the sediment (Burdige and Zimmerman 2002). Sippers are extremely valuable because they can collect water samples from multiple locations down to a depth of ~20 cm in the sediment column. This technique has been utilized with great success in determining the role of seagrass beds in carbonate dissolution processes (Burdige and Zimmerman 2002; Burdige et al. 2008; Burdige et al. 2010). Sansone et al. (1988a/b) developed another method of collecting shallow (< 1 m) porewater from permeable sandy sediments. Initially they found that the approach for sampling porewater from consolidated dense reef frameworks using cased wells did not work in unconsolidated sediments, so they utilized pseudo-permanently installed stainless steel, porewater wells (e.g., Sansone et al., 1988a/b; Falter and Sansone, 2000b). Eventually PVC wells were used to eliminate metal contamination and corrosion. These wells allowed relatively easy sampling at a fine vertical spatial resolution in the sediment (see Section 0). More recently, Fogaren et al. (2013) measured oxygen penetration and nutrient remineralization employing porewater wells deployed on the south shore of Oahu near one of the locations of the present study.

In this paper, we present the first quantitative temporal study of TA and pH as a function of depth in sediment interstitial water of highly permeable, carbonate reef sands using a well-point methodology down to a depth of 60 cm. The study primarily focuses on the high temporal and spatial variability of the porewater CO₂-carbonic acid system chemistry in this type of sediment facies and its relationship to the carbon chemistry of the overlying water column. We investigate how microbial activity affects DIC, TA, and carbonate mineral saturation states (Ω) under oxic and anoxic conditions. In addition, we hypothesize that the highly permeable nature of sandy carbonate reef sediments will have a significant effect on the sediment porewater geochemistry. Changes in porewater CO₂-carbonic acid system chemistry due to both natural

processes and ocean acidification, combined with the expected decreases in coral and coralline algae calcification rates under increasing OA and temperature, make it probable that many coral reefs will experience a net deficit in their CaCO₃ budget, potentially leading to a switch from net accretion to net erosion of some reef ecosystems (Kleypas et al. 1999; Andersson et al. 2005; Andersson et al. 2006; Silverman et al. 2009; Andersson et al. 2009; Mackenzie and Andersson 2013; Eyre et al. 2014). Thus, it is critical that we investigate and understand the complex processes and multiple mechanistic factors that contribute to the biogeochemistry of the highly permeable, sandy sediment-porewater CO₂-carbonic acid system.

3.3 Methodology

3.3.1 Study Sites

Sampling was performed at two main locations around Oahu, Hawai'i: the CRIMP-2 and Ala Wai buoys (Figure 3.1). Both buoys have been deployed since June 2008 and are part of the NOAA/PMEL (Pacific Marine Environmental Laboratory) carbon program. The buoys contain MAPCO₂ systems (Moored Autonomous pCO₂) that measure atmospheric and seawater CO₂ every three hours, along with a complement of ancillary data. Data are transmitted to PMEL servers once per day via Iridium satellite and can be viewed on the internet in near-real time at <http://pmel.noaa.gov/co2/story/Coral+Reef+Moorings>. Details of the measurement technique and buoy schematics can be found in Massaro et al. (2012) and Drupp et al. (2013). In addition to the CO₂ measurements, each buoy serves as a platform for various other instruments and experimental work. These locations, described in the following sections, serve as central hubs for the porewater work described here and provide continuous data about the overlying water physical, chemical, and biological conditions.

3.3.1.1 Kaneohe Bay barrier reef

Kaneohe Bay, the site of the CRIMP-2 buoy, is the largest semi-enclosed bay in Hawai'i and located on the northeast (windward) coast of the island of Oahu. The bay is home to a large barrier reef, approximately 2 km wide and 5 km in length. The CRIMP-2 buoy is moored over a sand patch, in ~3.5 m of water, immediately adjacent to the leeward back edge of the barrier reef (see Figure 3.1). The mean depth across the reef is ~2 m, but varies from <1 m to 4 m.

Tradewinds blow from the northeast ~80% of the year, resulting in a nearly linear flow of water across the reef flat (Giambelluca et al. 1986; Lowe et al. 2009a; Massaro et al. 2012; Drupp et al. 2013). Water chemistry is biogeochemically altered in transit across the reef (4 - 24 hrs), resulting in decreased alkalinity and pH of reef surface water relative to the open ocean source waters (Shamberger et al. 2011; Drupp et al. 2013).

3.3.1.2 Ala Wai

The Ala Wai buoy is located on the south shore of Oahu, about 200 m offshore from urban Honolulu in a mean water depth of 14 m (Figure 3.1). This location is situated over a sand patch adjacent to a fringing reef extending from shore past the buoy location. The site is influenced by its proximity to the mouth of the Ala Wai canal, which drains ~1/3 of the area of Honolulu (population ~850,000) resulting in a significant amount of fluvial discharge containing high concentrations of organic matter, nutrients, and suspended solids, especially following large storm events (Tomlinson et al. 2011). Because its location is relatively unprotected, the waters around the Ala Wai site are rapidly mixed with the surrounding open ocean.

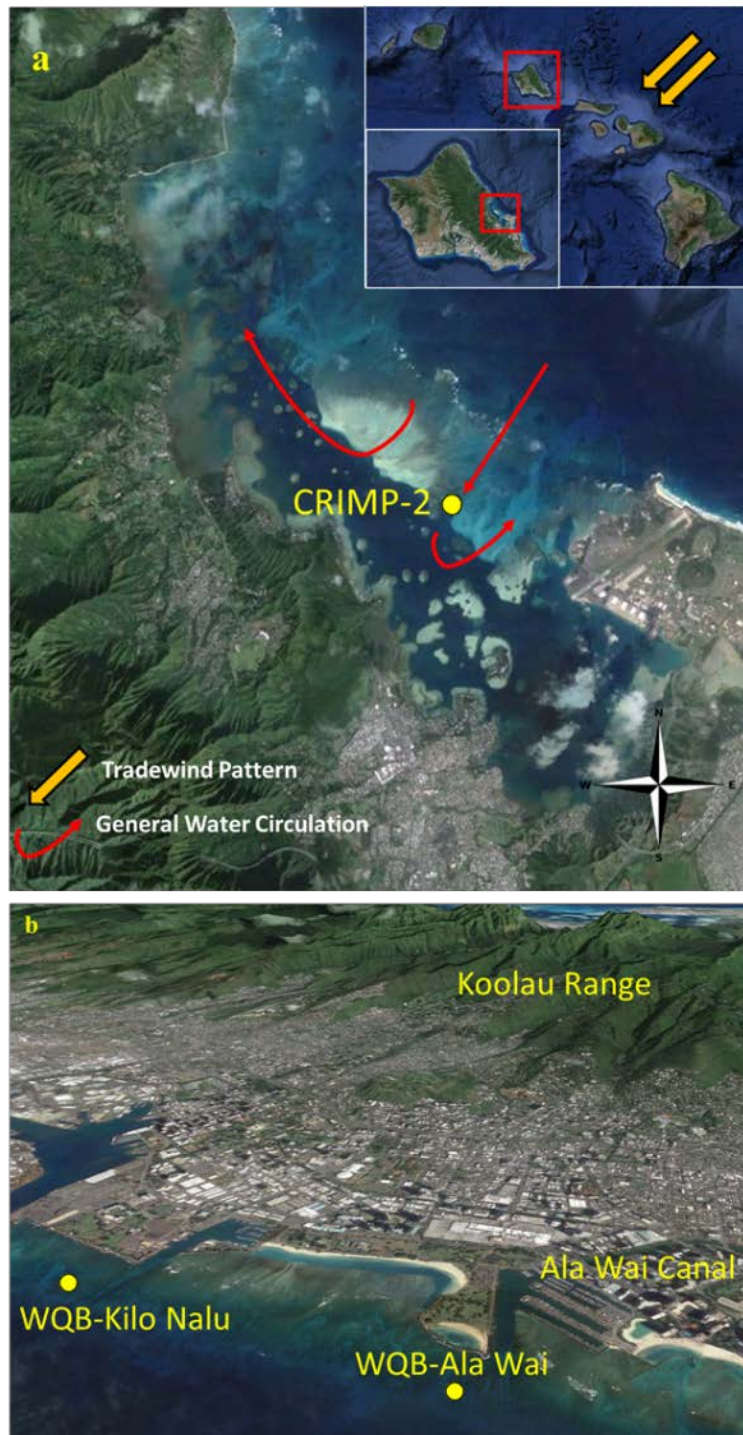


Figure 3.1: (a) The CRIMP-2 buoy is located on the leeward interior edge of the Kaneohe bay barrier reef on the windward (see inset) coast of Oahu. The yellow arrows represent the typical northeasterly tradewind patterns, which drive wave setup and flow across the reef. The red arrows represent the general flow of water linearly across the reef and then back out two channels on either edge of the reef flat. (b) The Ala Wai buoy (WQB-AW) is located just offshore of urban Honolulu, near the mouth of the Ala Wai canal. The buoy WQB-KN to the west was not used in this study but was the site of a porewater study by Fogaren et al. (2013).

3.3.2 Porewater sampling protocol

An array of porewater wells was deployed by divers in the sediments at both the CRIMP-2 and Ala Wai locations. The wells were constructed of 1-meter long, 0.75-cm inner diameter PVC piping and fitted with a PVC ball valve (Falter and Sansone 2000a; Falter and Sansone 2000b; Fogaren et al. 2013). Small sampling ports (~3 mm diameter) were drilled around each pipe at a specific depth from a reference line just below the ball valve. The sampling ports were designed to yield field samples from 2, 4, 6, 8, 12, 16, 20, 30, 40, and 60 cm below the sediment-water interface. The first step in deployment involved pounding a steel rod with a spiked tip into the sediment. The rod was removed quickly and the well was inserted into place before the hole collapsed. After installation, all of the wells were adjusted vertically so that the reference lines were even with the sediment-water interface. The wells were installed within a 30 cm x 30 cm grid pattern designed to limit potential overlap between sampling ports.

Porewater samples were collected from the wells by SCUBA divers using 50-mL Poulten and Graf Fortuna™ Air-Tite glass syringes fitted with a 3-way stopcock, a 47-mm Whatman 934-AH glass microfiber pre-filter (nominal pore size 1.5 μm), and ~10 cm of Tygon tubing. The Tygon tubing was attached to the ball valve of the desired well and the valve opened. The dead volume (specific to each well) was removed by suction and disposed of through the 3-way stopcock, and approximately 50 - 60 mL of sample were subsequently collected from each well and brought to the surface for processing. The syringes draw in porewater from a “sphere of influence,” (Falter and Sansone, 2000b; Fogaren et al., 2013). The size of the sphere of influence is determined by the sample volume, density of seawater, and porosity of the sediments. A typical 60 mL sample creates a sphere of influence of ~3 cm in radius. The wells are specifically arranged to be closely spaced (< 15 cm) to one another without creating overlapping spheres of

influence in which any sampled porewater would also include chemical characteristics of a nearby neighbor. A close layout is also important because the chemistry of porewaters in sandy sediments displays a large amount of horizontal variability. Spacing the wells as closely as possible to each other helps reduce some of the natural horizontal variability of the system.

3.3.3 Porewater and sediment sample analyses

3.3.3.1 Field determinations

Measurements of pH_t (total scale) and dissolved oxygen in porewater were made within 20 minutes of sample recovery. Approximately 5 mL of sample were dispensed into a glass vial and pH_t was measured using a Thermo Scientific Orion Glass Micro pH electrode and a Thermo Scientific Orion Star A214 pH meter. Electrode performance was monitored in the field using TRIS and 2-amp buffers (Dickson et al. 2007) . On average, the electrode was within 2% of Nernstian response, with an accuracy and precision of 0.015 and 0.002 pH_t units, respectively. A second 5-mL aliquot of sample (in a glass vial) was analyzed for dissolved oxygen using a Microelectrodes, Inc. model MI-730 O₂ microelectrode. Both glass vials were then sealed and returned to the lab. The remaining porewater was filtered through a 0.2- μ m nylon Acrodisc® into a series of Wheaton borosilicate glass serum vials (20 mL and 2 mL for total alkalinity and sulfate, respectively) using a 17-gauge hypodermic needle to puncture the septum. The serum vials had been previously sealed in a nitrogen-filled glove bag to minimize oxygen contamination. The vials were then returned to the laboratory for analysis of total alkalinity (TA) and dissolved sulfate.

3.3.3.2 Laboratory porewater analysis

TA was measured using the standard open cell potentiometric titration method (Dickson et al. 2007) using a Metrohm Titrando 905 automatic titrator within 12-36 hours of sample

collection. A water-jacketed cell was used to maintain a constant temperature of $25^{\circ}\text{C} \pm 0.02$ using a temperature-controlled water bath circulator. The accuracy of the TA titration was determined using certified reference materials (CRM) obtained from the Scripps Institution of Oceanography (Dickson et al. 2003; Dickson et al. 2007) and was found to be $2\ \mu\text{mol kg}^{-1}$. Precision was determined via replicate analyses of the samples and CRM. However, because of the limited volume of porewater available, duplicate measurements were rarely possible. The precision of the TA measurement in porewater was based primarily on that of the CRM analysis and estimated to be $3\ \mu\text{mol kg}^{-1}$. Surface water and sediment-water interface samples for the determination of TA were collected in 300-mL borosilicate bottles and fixed with 200 μL of saturated aqueous HgCl_2 to inhibit biological activity. The bottles were sealed with ground glass stoppers with Apiezon-M grease. Initially, the vials used for the porewater TA subsample were pre-poisoned (prior to sealing in the glove bag) with HgCl_2 , but mercuric sulfide and iron sulfides formed in some vials and the contaminated samples had to be discarded. To eliminate the problem of precipitate formation, samples were not pre-poisoned but were kept on ice in the dark and analyzed immediately upon returning to the laboratory (<12 hrs).

Sulfate was determined following precipitation of BaSO_4 (modified from Kremling, 1983). Samples were kept in serum vials sealed in an N_2 glove bag and returned to the laboratory where 100 μL of 0.82 M BaCl_2 solution were added. The samples were fixed with BaCl_2 within 6 hours of sample collection. After settling of the BaSO_4 precipitate, the excess Ba^{2+} remaining in the supernatant was determined by inductively coupled plasma optical emission spectroscopy (ICP-OES) (Martin et al. 1994). The SO_4^{2-} in the precipitate was calculated by subtracting the remaining supernatant Ba^{2+} from the amount initially added and assuming a 1:1 ratio between Ba^{2+} and SO_4^{2-} . The original BaCl_2 (spiking) solution was analyzed concomitantly with each set

of samples to account for potential changes in molarity due to evaporation. The analytical precision of the barium analysis by ICP-OES was estimated to be $0.02 \mu\text{g}\cdot\text{mL}^{-1}$ based on three replicates per sample with an accuracy of $\sim 1\%$ based on analysis of certified reference materials. Because of the assumed 1:1 molar ratio between barium and sulfate, this yields an uncertainty in the sulfate measurement of $0.15 \mu\text{mol}\cdot\text{L}^{-1}$.

3.3.3.3 *Laboratory sediment analysis*

Because of the difficulty inherent in collecting a core of sandy sediments (Boudreau et al. 2001; Jahnke 2004), only one 14.5-cm push core from the CRIMP-2 location and one 16-cm push core from the Ala Wai site were collected by divers. The presence of deep rubble layers at both sites prevented the recovery of longer cores. However, we feel that one core at each site is sufficient to characterize in general terms the mineralogy, chemistry, and physical properties of the sediment. The CRIMP-2 core was sectioned in the field, immediately upon retrieval, into seven layers $\sim 2 - 2.5$ cm thick, which were stored in a -20 °C freezer until subsequent analysis of chemical, physical, and mineralogical properties, approximately 1-2 weeks after collection. The Ala Wai core was sectioned in the laboratory but was stored in the same manner as the CRIMP-2 core. Sediment permeability was measured in duplicate by subsampling each section (for CRIMP-2 only) and using the constant head method (Klute and Dirksen 1986). The average standard deviation of duplicates was 0.10 D. Porosity was determined gravimetrically (Breitzke 2006). Grain size distributions (see Table 3.1) were determined via wet-sieving of the sediments (Krumbein and Pettijohn 1938; Ginsburg 1956).

Each core section was analyzed for total carbon, hydrogen, and nitrogen (CHN) using an Exeter Analytical model CE-440 elemental analyzer, following the methods of Gordon (1969) and Sharp (1974). Total inorganic carbon (TIC) in the sediment samples was measured using a

UIC front-end acidification unit (CM5230) coulometer following the method of Dickson et al. (2007). Total organic carbon (TOC) was determined by the difference between total carbon (from CHN analysis) and TIC (Briggs et al. 2013).

Sediment samples were ground into a fine powder for mineralogical analysis by X-ray diffraction spectrometry, which was performed at the University of California-Merced. A cobalt anode was used with a $K_{\alpha 1}$ and $K_{\alpha 2}$ of 1.78901 and 1.79290, respectively. Fluorite (CaF_2) was added as an internal standard to each sample (~20 wt. %) to correct for any mounting artifacts in the diffraction analysis and d-spacing. Two scans were performed for each sample. A short continuous scan covered a 2Θ range of $29 - 56^\circ$ at $0.5 \text{ deg}\cdot\text{min}^{-1}$ and a 2Θ step size of 0.002° , although the Ala Wai sample was also scanned over $2 - 56^\circ$ to identify any potential clay minerals whose characteristic peaks occur at lower 2Θ . A long (slower) run covered a range of 2Θ of $30-36^\circ$ at a scan rate of $0.1 \text{ deg}\cdot\text{min}^{-1}$ with a 2Θ step size of 0.002° . Mg-calcite peaks occur between 30 and 36° , so the slower scan was utilized to quantify more accurately the mole fraction of Mg-calcite. The d-spacings were calculated according to the Bragg diffraction law

$$n\lambda = 2d\sin\theta \quad (3.1)$$

where n is the order and λ is the wavelength of the incident radiation. The d-spacings for the sample peaks were adjusted, if necessary, based on the differences between measured and reference peaks for CaF_2 . This adjustment was between $0.001 - 0.002 \text{ \AA}$, depending on the sample. Carbonate minerals were identified based on the d-spacings and relative peak intensities compared to those found in the JCPDS files (as cited in Brindley and Brown, 1980). Mg-calcite composition was calculated from the shift in d-spacing of the calcite 104 reflection using the following equation from Goldsmith et al. (1961) as described by Bischoff et al. (1983)

$$\text{mol\% MgCO}_3 = -347.84(d_{104}) + 1055.8 \quad (3.2)$$

where the shift in the d_{104} diffraction peak of calcite is taken to be a proxy for magnesium content.

3.3.3.4 CO₂-carbonic acid system calculations

Dissolved inorganic carbon (DIC), pCO₂, and calcite and aragonite saturation states (Ω_x) were calculated using the CO2SYS Excel macro adapted from Lewis and Wallace (1998), using K_1 and K_2 equilibrium constants from Mehrbach et al. (1973) as refit by Dickson and Millero (1987). Magnesian calcite saturation states were calculated using the “Om” function in Seacarb developed for R software (Lavigne and Gattuso 2011), using K_1 and K_2 from Lueker et al. (2000). Total alkalinity and pH data were corrected to T=25°C and S=35 before use in the calculations. Saturation state with respect to Mg-calcite was calculated as:

$$\Omega_x = \frac{\{Ca^{2+}\}^{1-x}\{Mg^{2+}\}^x\{CO_3^{2-}\}}{K_x} \quad (3.3)$$

where x is the mole fraction of Mg²⁺ (e.g., 0.15). Ion activities $\{a\}$ were determined from the equation

$$\{a\} = \gamma_T [C] \quad (3.4)$$

where γ_T is the total ion activity coefficient from Millero and Pierrot (1998) and $[C]$ is the ion concentration in mol·kg⁻¹. The γ_T for Ca²⁺, Mg²⁺, and CO₃²⁻ are 0.198, 0.203, and 0.043, respectively. The K_x , determined experimentally, represents what Plummer and Mackenzie (1974) and Thorstenson and Plummer (1977) term the stoichiometric saturation constant. The Seacarb package returns two values: an Ω for minimally prepared biogenic Mg-calcite, using a K_x from the Mg composition versus stability curve of Plummer and Mackenzie (1974), and an Ω for cleaned and annealed biogenic Mg-calcite, using a K_x from the stability curve of Bischoff et

al. (1993). The Plummer and Mackenzie minimally prepared Ω s are lower than those for cleaned and annealed substrates, reflecting the higher solubility of individual Mg-calcite phases as a function of Mg content than the Bischoff et al. results. Values in this paper are calculated using the minimally prepared biogenic Mg-calcite curves, as recent studies have indicated that these are more representative of the natural environment (Bischoff et al. 1993; Morse et al. 2006).

3.4 Results

3.4.1 Porewater profiles

3.4.1.1 Measured parameters – CRIMP-2

Eleven sets of porewater samples were collected from the CRIMP-2 site and analyzed for TA. Measurements of pH_t were made but only for some of the sampling days due to problems with electrode calibration. However, the lack of pH_t measurements is not a problem in terms of the conclusions of our paper. The CRIMP-2 porewater TA profiles (Figure 3.2a-c) generally display a considerable amount of variability, but concentrations generally increase relative to the overlying water column. TA is usually greater deeper in the sediments than at the sediment-water interface (SWI), but in one profile (09/06/2012), TA concentrations are lower at some depths than in the overlying water column. All reported TA and DIC concentrations have been normalized to a salinity of 35 (nTA or nDIC). The minimum alkalinity measured was 2131 $\mu\text{mol}\cdot\text{kg}^{-1}$, at 4 cm, and the maximum was 2644 $\mu\text{mol}\cdot\text{kg}^{-1}$, at 12 cm, demonstrating the high variability in TA in sediments close to the seawater interface.

The pH decreases rapidly below the sediment-surface maximum to a subsurface minimum around 6 - 8 cm, before increasing in the middle sediment layers (~8 - 20 cm, Figure 3.3a). The pH ultimately decreases from 20 to 60 cm to an overall minimum at 60 cm. The maximum pH_t measured was 8.087 in the overlying surface water, while the maximum pH_t

measured within the sediments was 8.013 at 20 cm. The minimum pHt was 7.414 at 60 cm, and pH was never higher in the sediments than in the overlying water column. Several pH samples in the deeper layers, between 30 - 60 cm, were discarded because the samples became aerated during the collection process, resulting in erroneously high pH values due to CO₂ degassing.

3.4.1.2 Measured parameters – Ala Wai

Porewater samples were collected on seven different days at the Ala Wai site. Total alkalinity profiles from 0 - 60 cm were determined for each sampling period, and pH measurements were made on four of the sampling days. Total alkalinity (Figure 3.2d) increased from the overlying surface water values to a maximum concentration of ~2900 $\mu\text{mol}\cdot\text{kg}^{-1}$, typically between 12 - 20 cm, before decreasing slightly and then remaining fairly constant (on a given sampling day) at ~2600 - 2800 $\mu\text{mol}\cdot\text{kg}^{-1}$ between 30 - 60 cm. The minimum alkalinity for the entire study period was 2297 $\mu\text{mol}\cdot\text{kg}^{-1}$ in the overlying surface and the maximum in the porewater was 3682 $\mu\text{mol}\cdot\text{kg}^{-1}$, at 12 cm.

Porewater pH (Figure 3.3b) follows the opposite trend as TA, decreasing from the surface maximum of ~8.0 and reaching a minimum value around 12 - 20 cm in depth. It remains essentially constant – sometimes decreasing slightly – with depth, down to the maximum sampling depth of 60 cm. The maximum pHt for the study period was 8.102 and the minimum pHt was 7.493, measured at the SWI and at 60 cm, respectively. For both TA and pH, no value in the sediment was below or above, respectively, those measured at the SWI.

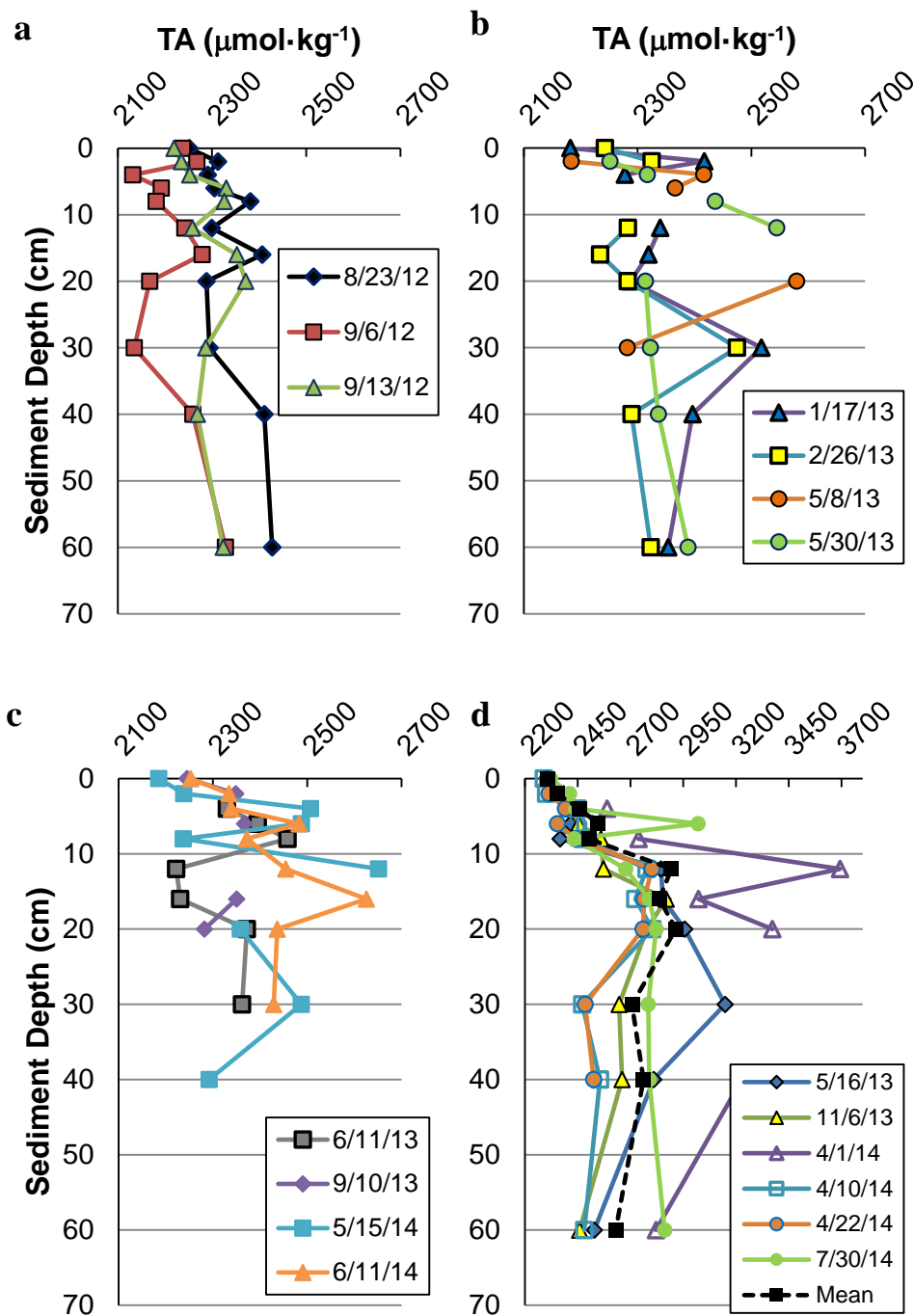


Figure 3.2: Salinity normalized ($S=35$) alkalinity profiles at various times for the porewater of carbonate sediments from the SWI (0 cm) to 60 cm depth at the CRIMP-2 (a/b/c) and Ala Wai (d) locations. The mean profile at Ala Wai, black dashed line, was calculated by plotting the mean alkalinity at each depth from all of the samples. A mean profile for CRIMP-2 is not shown due to the high variability of the data, which would render a mean profile somewhat unrepresentative of the conditions extant at any given time.

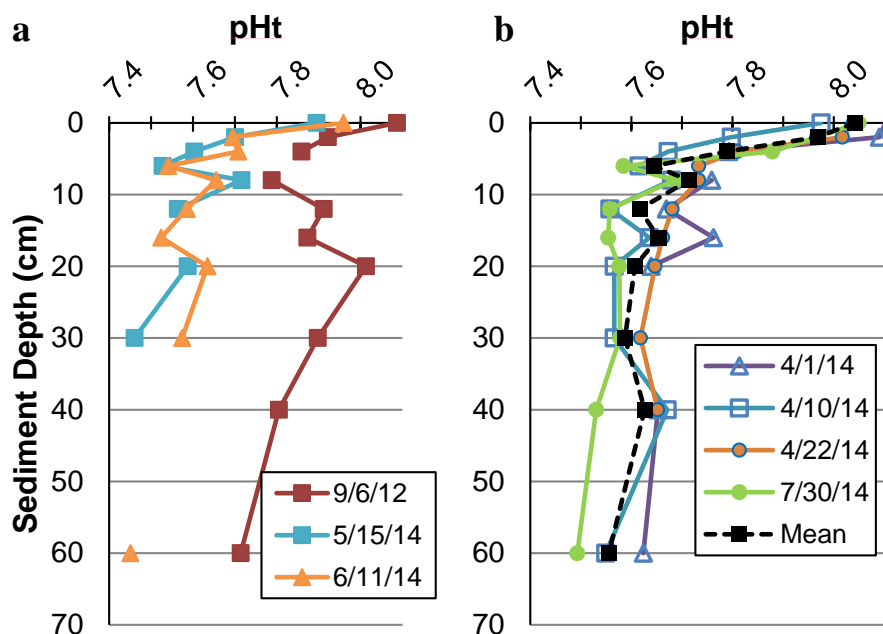


Figure 3.3: pHt of carbonate sediment porewater at the CRIMP-2 (a) and Ala Wai (b) locations. The mean pHt at Ala Wai, black dashed line, was calculated by taking the mean of every pHt value at each depth.

3.4.1.3 Calculated parameters – CRIMP-2

Using the TA and pHt measurements, the remaining parameters of the CO₂-carbonic acid-carbonate system, including DIC, pCO₂, [CO₃²⁻], and Ω, were calculated according to the methods described in Section 3.3.3.4. DIC (Figure 3.4) and pCO₂ (Figure 3.5) generally increase with depth although there are fluctuations between 8 - 20 cm. DIC and pCO₂ in the sediments were greater than in the overlying water column, except for DIC calculated for the 09/06/2012 samples. The minimum and maximum calculated DIC concentrations were 1967 μmol·kg⁻¹ and 2569 μmol·kg⁻¹, in the overlying water and at 12 cm, respectively. The minimum DIC in the sediments was 1967 μmol·kg⁻¹ at 20 cm. A minimum pCO₂ of 399 μatm was calculated for the overlying water column, hence in equilibrium with the atmosphere, otherwise all other samples were supersaturated. A pCO₂ maximum of 1989 μatm was calculated for porewater at 30 cm, although no values below 30 cm depth were calculated for this profile because of erroneous pH

values due to sample aeration and escape of CO₂ during the collection process (as discussed in Section 3.4.1.2). The minimum pCO₂ within the sediments at CRIMP-2 was 599 µatm at 20 cm.

The saturation state of the seawater with respect to aragonite, Ω_{Ar} , decreased from an average of 2.69 in the surface water to an average of 1.37 at 60 cm in the porewaters (Figure 3.6a). A minimum Ω_{Ar} of 1.18 was calculated at 30 cm on 05/15/2014. The Ω_{Ar} did not exceed 2.0 in the sediment porewater except for the 2-cm and 20-cm samples collected on 09/06/2012. An Ω of one implies that the interstitial water is at saturation with respect to the mineral phase. No sample was undersaturated ($\Omega < 1$) with respect to aragonite. The Ω of calcite (not shown) follows the same trend as aragonite, with a mean surface value of 4.08 (the highest calculated) and a mean value of 2.09 at 60 cm.

Figure 3.6c shows the mean saturation state of seawater with respect to 15 mol% Mg-calcite, calculated using the solubility curves from Plummer and Mackenzie (1974). Every sample, including the overlying seawater, was undersaturated with respect to 15% Mg-calcite, with Ω ranging from 0.80 in the surface water to 0.28 at 30 cm (05/15/2014 and 06/11/2014 profiles do not continue below 30 cm for reasons previously discussed). Porewater Ω with respect to biogenic Mg-calcites, calculated from the Bischoff et al. (1993) solubility curve, are similar to aragonite and are never undersaturated with respect to this phase ($\Omega < 1$).

3.4.1.4 Calculated parameters – Ala Wai

CO₂-carbonic acid-carbonate system parameters for the Ala Wai samples were calculated in the same way as previously discussed for CRIMP-2. At the Ala Wai location, profiles of DIC and pCO₂ (Figure 3.4b and Figure 3.5b) follow the same trend as TA, increasing to a subsurface maximum between 12 - 20 cm and then remaining constant or increasing slightly with depth to 60 cm. Surface water nDIC had a mean concentration of 2006 µmol·kg⁻¹ with a minimum of

1962 $\mu\text{mol}\cdot\text{kg}^{-1}$. The mean nDIC profile reaches its maximum of 2873 $\mu\text{mol}\cdot\text{kg}^{-1}$ at 12 cm. The highest nDIC for the entire dataset (3518 $\mu\text{mol}\cdot\text{kg}^{-1}$) was calculated for porewater at 12 cm depth on 04/01/2014. The pCO_2 also generally increased with depth to about 8 - 12 cm before displaying several reversals between 10 – 20 cm, and continuing to increase to a mean pCO_2 of 1655 μatm at 60 cm. The profile from 04/22/2014, however, did not show any changes in direction in 8 – 20 cm region.

The saturation state of the sediment porewater with respect to aragonite, Ω_{Ar} , was on average 3.5 in the overlying surface water and decreased to an average of 1.60 at 60 cm (Figure 3.6b). For the entire Ala Wai dataset, Ω_{Ar} was never less than one, with a minimum of 1.36. The Ω of calcite (not shown) follows the same trend as aragonite, decreasing from 5.3 in the surface waters to 2.4 at 60 cm depth.

Saturation state for 15 mol% magnesian calcite (Figure 3.6d) decreases from a maximum in the overlying water column to a minimum at 60 cm (0.85 to 0.40 for the mean porewater profile). All of the calculated Ω values using the Plummer and Mackenzie (1974) IAP vs MgCO_3 content curve were less than one at all depths, while the Ω 's calculated using the Bischoff et al. (1993) solubility vs. MgCO_3 content curve for cleaned and annealed Mg-calcite biogenic phases are similar to the calculated Ω_{Ar} values, with no saturation state below one.

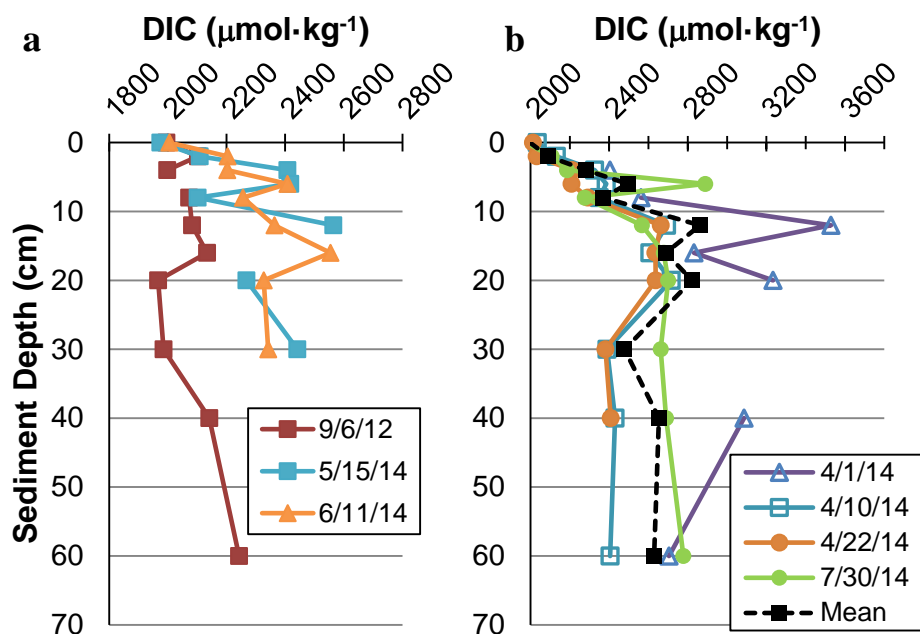


Figure 3.4: Salinity normalized ($S=35$) dissolved inorganic carbon concentrations in carbonate sediment porewater. DIC was calculated from TA and pH_t for the sediment column at CRIMP-2 (a) and Ala Wai (b). The dashed line shows the mean Ala Wai profile calculated by averaging the concentrations found at each depth.

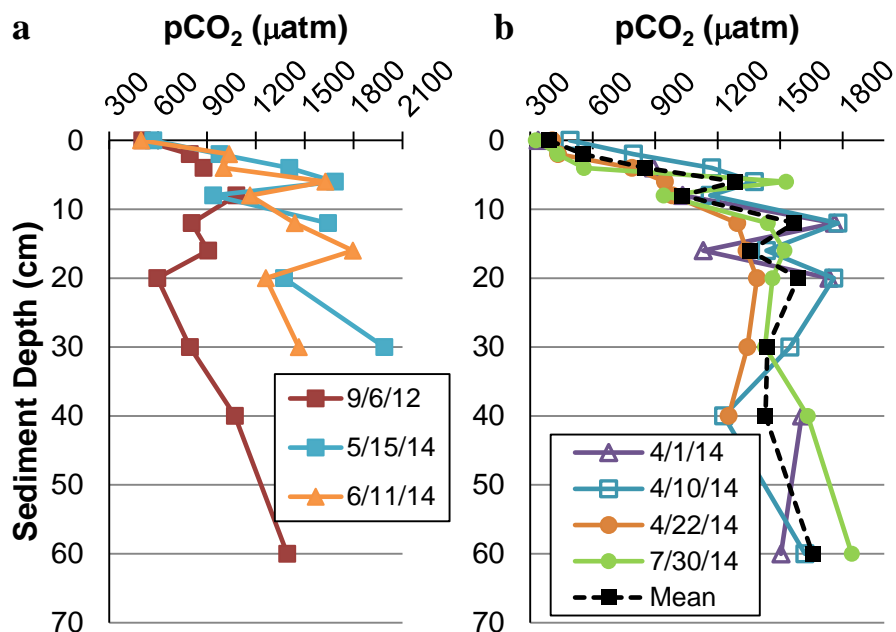


Figure 3.5: Profiles of pCO₂ from the overlying surface water (0 cm) to 60 cm depth at the CRIMP-2 (a) and Ala Wai (b) sites. pCO₂ was calculated from TA and pH_t. The black dashed line is the mean pCO₂ at each sampling depth for the entire Ala Wai dataset.

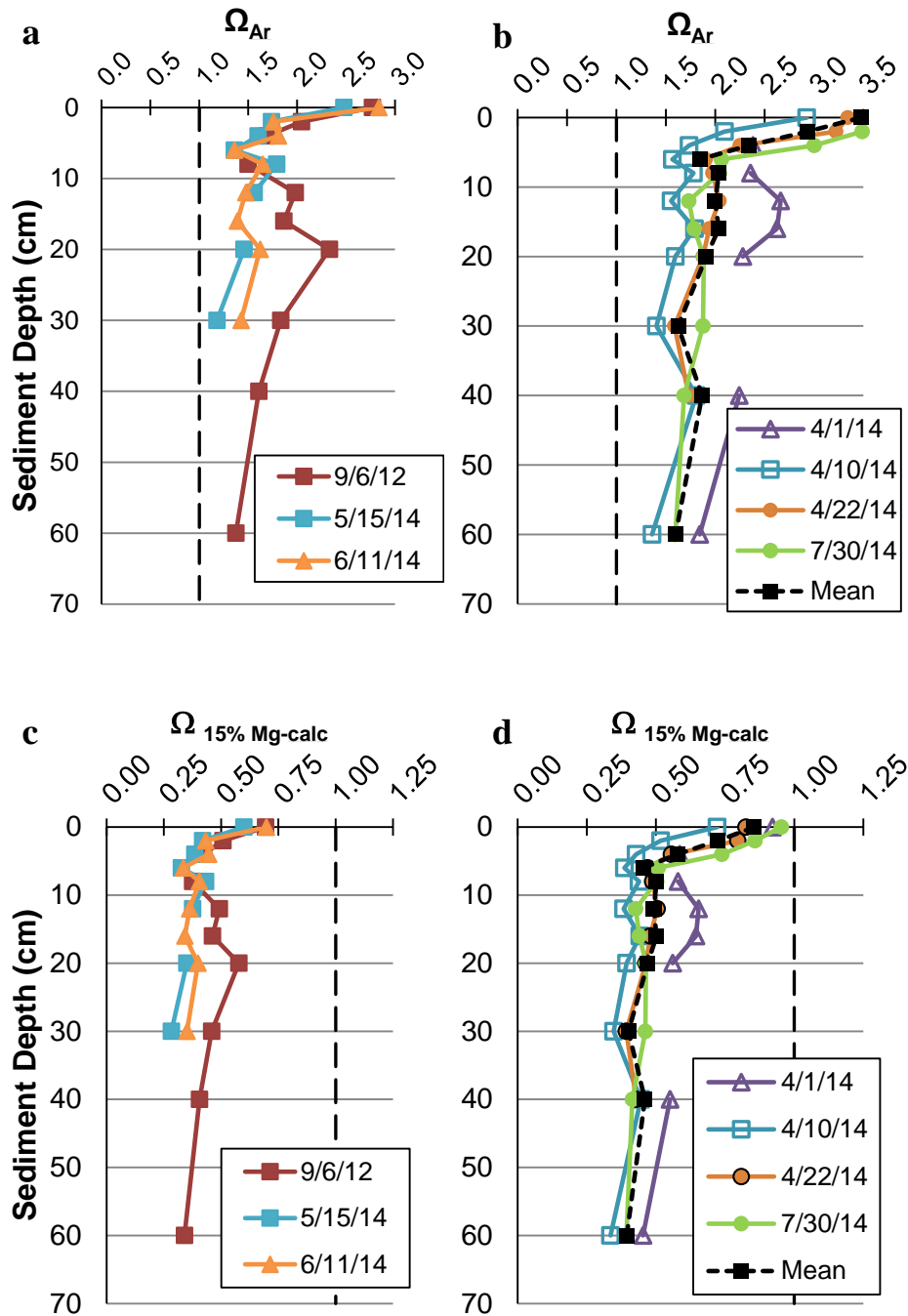


Figure 3.6: Saturation state of the carbonate sediment porewater with respect to aragonite and 15 mol% Mg-calcite at the CRIMP-2 (a/c) and Ala Wai (b/d) sites. Saturation state was calculated from TA and pH_t, assuming that dissolved calcium and magnesium behaved conservatively with respect to salinity. $\Omega_{15\% \text{ Mg-calc}}$ was calculated using the stoichiometric solubility product for a 15 mol % Mg-calcite from Plummer and Mackenzie (1974). The thick black dashed line/squares shows the mean Ω at each depth interval. The dashed line at $\Omega = 1$ marks the threshold between thermodynamic undersaturation and oversaturation.

3.4.2 Sediment analysis

3.4.2.1 CRIMP-2

The average permeability (Figure 3.7) of the sediments at CRIMP-2 was 16 D and ranged from 9 - 32 D overall. Porosity increases from 44% in the top layer (0 - 2 cm) to 59% in the 9.5 - 12 cm layer, due to the presence of a subsurface rubble layer. Permeability and porosity both increase with depth to maximum values in the 9.5 - 12 cm core section, before decreasing dramatically in the deepest layer. The upper sediments (0 - 6 cm) are dominated by grain sizes between 63 – 700 μm , but the sediments transition to larger grain sizes with depth (see Table 3.1). The 7 - 14.5 depth layers are dominated by sediments $> 700 \mu\text{m}$ with the 2-4 mm fraction making up ~30% of the sediment mass.

The results for the total carbon (TC), hydrogen, and nitrogen content of the sediment are shown in Table 3.2. The sediment has an average of 11.7 wt.% C. Some hydrogen is present in the organic matter in the upper two layers but decreases to below detection levels by 4 cm. Nitrogen content increases slightly with depth from 0.04 wt. % in the 0 - 2 cm layer to 0.1 wt.% in the 12 - 14.5 cm layer.

Total inorganic carbon (TIC, Table 3.2) varies from 11.3 wt.% in the surface sediment layer to ~11.6 wt.% in the deepest core section and generally increased with depth. A comparison of total carbon (TC), total organic carbon (TOC), TIC, and organic carbon to nitrogen molar ratios (OC/TN) is given in Table 3.2.

X-ray diffraction analysis of the CRIMP-2 sediment core was used to identify carbonate minerals present in the sediments, as well as the average composition of Mg-calcite. Aragonite and a high Mg-calcite were the dominant mineral phases in all seven core layers. The average mol% MgCO_3 in the Mg-calcites was 16.4% and ranged from 15.5 - 17.5% (Table 3.3). These

compositions probably consist of the detritus of organisms such as *Lithothamnion sp.* and *Amphiroa sp.* Both skeletal organisms are found growing on the reef and as detritus in the reef sediments (Agegian 1985; Agegian and Mackenzie 1989). Only one layer, 0 - 2 cm, contained pure calcite in any significant amount; the diffractogram of this sediment layer showed a peak corresponding to a 2% Mg-calcite composition, as well as a high Mg-calcite phase of ~15.5% (data not shown). Vaterite may also be present in each layer, as two XRD peaks of this phase were found, but the presence of three peaks is typically required to confirm unambiguously the presence of any mineral.

3.4.2.2 Ala Wai

Porosity in the Ala Wai sediments ranges from 53 - 56% over 0 - 16 cm depth (see Figure 3.7) and shows no consistent trend with depth. This is likely due to the fact that the 250 - 700 μm and 125 - 250 μm grain size fractions account for 80 - 90% of the sediment mass in each core layer (see Table 3.1). Fine grained sediments (<63 μm and 63 - 125 μm) are virtually non-existent in the top 16 cm of the sediment column, whereas larger size fractions (>700 μm) increase with depth from about 7% at the surface to 20% at depth. The coarse sand fraction (250 - 700 μm) usually represents more than 65% of the total sediment mass. Permeability was not measured for the Ala Wai core, but because of the relative consistency in grain size and porosity through the core, permeability is anticipated to be similar throughout with depth.

The TC, hydrogen, and nitrogen content of the Ala Wai sediments (solid phase) is very similar to that of CRIMP-2 (see Table 3.2). The average wt. % C of the sediments is 11.6%. Hydrogen decreases to below detection by 4 cm, as observed at CRIMP-2, and nitrogen does not show a clear trend with depth. TIC, shown in Table 3.2, remains constant with depth, with a mean of 11.3%. OC averages ~0.3%, with little change throughout the core. The OC/TN molar

ratio at Ala Wai is slightly higher than that at CRIMP-2, 8.49 vs. 6.52, respectively, which is likely a result of the land-based runoff from the Ala Wai canal.

The average composition of Mg-calcite in the Ala Wai sediments is 16.5%, as determined by XRD, with a range of 14.2% - 17.7% (see Table 3.3). The mole percentage of MgCO₃ decreased from the surface layer to a minimum in the 6 - 8 cm layer, before increasing again to 17.7% at 16 cm. In addition to Mg-calcite, aragonite was a dominant phase in all eight core sections (XRD data not shown). No pure calcite was detected in the Ala Wai sediments. In addition, no clay minerals were detected, largely due to the dilution effect of a high abundance of carbonate minerals, as it was difficult to identify any peaks in the 2 θ angle range where diagnostic peaks for clay minerals occur. As with CRIMP-2, two XRD peaks that may correspond to vaterite were observed in the diffractogram.

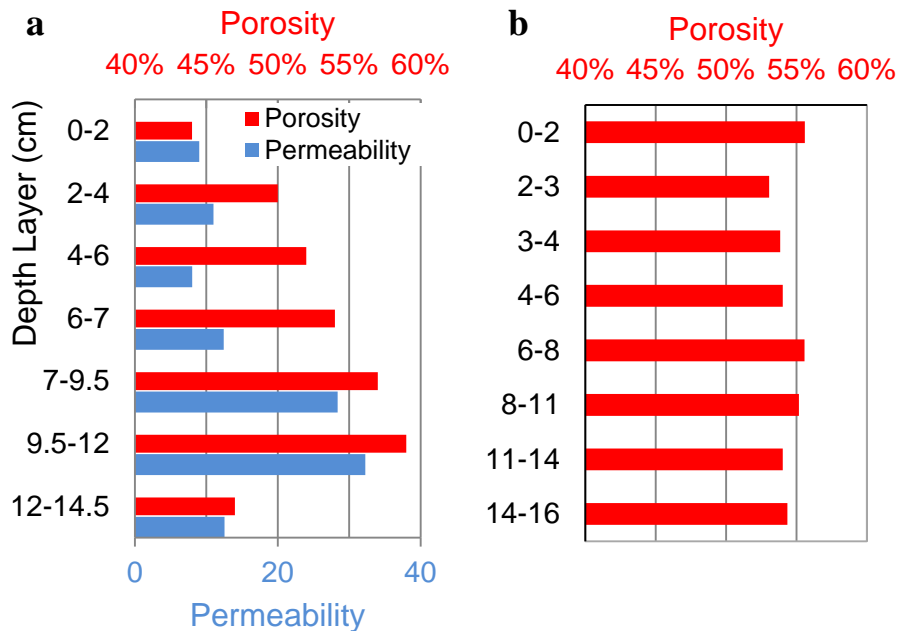


Figure 3.7: Permeability and porosity of the sandy carbonate sediments at CRIMP-2 (a) and Ala Wai (b) sites. Permeability and porosity at CRIMP-2 increase with depth to a maximum around 9.5 - 12 cm depth range where a rubble layer is present.

Table 3.1: Grain size fractions as a percentage of total sediment layer mass by depth for the CRIMP-2 (a) and Ala Wai (b) sediment cores. The >2 mm size fractions increase significantly with depth, and more than ~80% of the sediment mass is found in the 125-700 μm fraction at Ala Wai.

(a) CRIMP-2 Sediment Sample Depth Range	Grain Size Fraction						
	>4 mm	2-4 mm	700 μm - 2mm	250-700 μm	125-250 μm	63-125 μm	<63 μm
0-2 cm	0.7%	4.3%	22.7%	23.5%	29.0%	18.0%	1.8%
2-4 cm	0.4%	9.6%	33.1%	24.8%	22.5%	8.7%	1.0%
4-6 cm	0.5%	8.2%	28.3%	20.2%	31.7%	10.0%	1.1%
6-7 cm	4.2%	13.9%	34.6%	21.9%	18.1%	6.8%	0.5%
7-9.5 cm	10.1%	29.7%	38.0%	11.9%	7.3%	2.8%	0.3%
9.5-12 cm	17.2%	30.7%	25.8%	13.8%	7.5%	4.5%	0.5%
12-14.5 cm	13.0%	30.8%	29.2%	5.2%	13.8%	7.1%	1.1%

(b) Ala Wai Sediment Sample Depth Range	Grain Size Fraction						
	>4 mm	2-4 mm	700 μm - 2mm	250-700 μm	125-250 μm	63-125 μm	<63 μm
0-2 cm	0.1%	0.9%	7.0%	81.4%	10.4%	0.1%	0.1%
2-3 cm	0.1%	1.3%	5.0%	78.5%	14.9%	0.1%	0.0%
3-4 cm	0.4%	2.3%	4.8%	75.6%	16.4%	0.4%	0.1%
4-6 cm	2.1%	2.0%	4.5%	77.3%	13.7%	0.3%	0.0%
6-8 cm	1.6%	2.2%	4.0%	71.5%	19.9%	0.7%	0.0%
8-11 cm	0.7%	2.2%	5.3%	70.4%	20.9%	0.5%	0.0%
11-14 cm	6.4%	6.5%	7.3%	64.9%	14.5%	0.4%	0.0%
14-16 cm	4.9%	8.0%	8.7%	66.0%	12.1%	0.4%	0.0%

Table 3.2: Analytically determined total carbon (wt.% C) and total inorganic carbon (wt.% TIC) for the CRIMP-2 (a) and Ala Wai (b) sediment cores. The difference between wt.% C and wt.% TIC was taken to be the organic carbon (wt.% OC) content of the sediments. Calcium carbonate, which comprises most of the sediment mass, has a carbon wt.% of 11.99%. Hydrogen values of b/d indicate a wt. % below the analytical detection limits. An OC/TN molar ratio of organic carbon to total nitrogen was calculated using wt.% OC and wt.% N and converting to a molar ratio with appropriate atomic weights.

(a) CRIMP-2 Sediment Sample Depth Range	wt.% C	wt.% TIC	wt.% OC	wt.% H	wt.% N	OC:TN
0-2 cm	11.7	11.4	0.3	0.1	0.04	9.2
2-4 cm	11.7	11.4	0.3	0.02	0.03	11.3
4-6 cm	11.6	11.4	0.3	b/d	0.04	7.3
6-7 cm	11.7	11.5	0.3	b/d	0.05	6.0
7-9.5 cm	11.7	11.5	0.2	b/d	0.05	5.1
9.5-12 cm	11.9	11.6	0.2	b/d	0.06	4.4
12-14.5 cm	11.8	11.6	0.2	b/d	0.1	2.4
Mean	11.7	11.5	0.3	b/d	0.05	6.52

(b) Ala Wai Sediment Sample Depth Range	wt.% C	wt.% TIC	wt.% OC	wt.% H	wt.% N	OC:TN
0-2 cm	11.6	11.4	0.3	0.1	0.05	6.0
2-3 cm	11.6	11.3	0.3	0.03	0.04	8.0
3-4 cm	11.7	11.3	0.3	0.03	0.04	9.9
4-6 cm	11.6	11.3	0.3	b/d	0.03	12.2
6-8 cm	11.6	11.4	0.2	b/d	0.06	3.4
8-11 cm	11.6	11.4	0.3	b/d	0.06	5.1
11-14 cm	11.6	11.4	0.3	b/d	0.03	9.6
14-16 cm	11.6	11.4	0.2	b/d	0.02	13.77
Mean	11.6	11.3	0.3	0.01	0.04	8.5

Table 3.3: Mol% MgCO₃ content of specific core layers at CRIMP-2 (a) and Ala Wai (b). The MgCO₃ content was calculated from the XRD analysis (see section 3.3.3.3).

(a) CRIMP-2 Sediment Sample Depth Range	%MgCO₃
0-2 cm	15.4
2-4 cm	15.4
4-6 cm	16.1
6-7 cm	17.4
7-9.5 cm	16.5
9.5-12 cm	17.5
12-14.5 cm	16.6

(b) Ala Wai Sediment Sample Depth Range	%MgCO₃
0-2 cm	17.1
2-3 cm	17.7
3-4 cm	16.3
4-6 cm	16.9
6-8 cm	14.2
8-11 cm	15.1
11-14 cm	16.6
14-16 cm	17.7

3.5 Discussion

3.5.1 TA depth profiles

The concentration depth profiles of TA at the CRIMP-2 and Ala Wai sites are similar but show some key differences. The most obvious difference is in the range of porewater TA concentrations observed at the two sites. In general, CRIMP-2 porewater has a narrower range of TA concentrations, with a more variable concentration-depth pattern than at Ala Wai. The inconsistent structure of the CRIMP-2 profiles can be attributed in part to the much greater variability in source water chemistry than at Ala Wai. Drupp et al. (2013) showed that biogeochemical changes during the transport of open ocean water across the reef result in highly altered water at CRIMP-2 with TA being depleted by ~75 - 120 $\mu\text{mol}\cdot\text{kg}^{-1}$ relative to the source waters. In contrast, at Ala Wai, there is a more consistent surface water chemistry because the

water at this site is well mixed with the open ocean, except during large storm events when land-derived runoff can become an important driver of water chemistry (Tomlinson et al. 2011; Drupp et al. 2013). The standard deviation of the mean of the TA in the overlying water column is nearly three times greater at CRIMP-2 than at Ala Wai, clearly illustrating the greater variability in the overlying (source) water chemistry at the former location. In addition, the sediment permeability and porosity are more variable at CRIMP-2, at least in the upper 15 cm, as compared to Ala Wai, where those properties remain fairly constant. At CRIMP-2, a porous rubble layer at ~10 - 12 cm, with a much more impermeable layer directly below, may be an additional factor in the large changes in structure between profiles.

Despite the differences in overlying water chemistry between the two locations, the general trend in porewater TA is an increase in concentration from the surface to a maximum between 8 - 16 cm depth. This trend is more evident at Ala Wai, where TA increases by ~600 $\mu\text{mol}\cdot\text{kg}^{-1}$ from the sediment surface down to 12 cm, likely due to enhanced dissolution of carbonate sediments resulting from the production of CO_2 during oxic respiration of organic matter (OM, see e.g., Moulin et al. 1985). Oxygen (not shown) exhibits a depletion from the oxygenated surface waters, reaching hypoxic, if not anoxic, conditions at a depth of ~12 cm. This observation is consistent with oxygen data reported by Fogaren et al. (2013), who showed depletion of oxygen to near zero by 15 cm sediment depth at the Kilo Nalu Observatory, located approximately 2 km west of the Ala Wai site (see Figure 3.1). The Kilo Nalu site has a nearly identical sediment mineralogy and low OM content. The sharp decrease in the pH profile over the 0 – 12 cm depth range at Ala Wai is consistent with the large pCO_2 increase of ~1200 μatm above overlying seawater in the upper 12 cm of the sediment column, and is further evidence of vigorous oxic respiration. The sub-surface TA maximum, however, appears to occur at a

shallower depth at CRIMP2, suggesting that microbial respiration of OM depletes oxygen at a shallower depth within the sediments than at Ala Wai. Oxygen concentrations are consistent with this idea and reach hypoxic levels at a depth of ~6 cm at CRIMP-2 compared to ~12 cm at Ala Wai. This is again likely due to differences in the porosity and permeability of the sediments at shallow burial depths. At CRIMP-2 the upper layer (~0 - 10 cm) is less porous (and probably slightly less permeable) than at Ala Wai, which reduces advective flow into the sediments (see 3.5.4), thereby limiting the resupply of oxygenated surface water and reducing the oxygen penetration depth.

3.5.2 TA vs. DIC

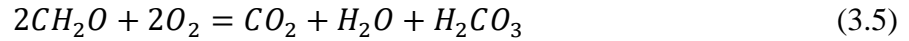
Plots of TA vs. DIC are often used to interpret the processes affecting reef framework and sediment biogeochemistry due to the varying ways in which photosynthesis, respiration, calcification, and dissolution can alter these parameters (e.g., Moulin et al. 1985; Mackenzie and Andersson 2011; Andersson and Gledhill 2013). The slope of the regression line is dependent on the dominant biogeochemical processes occurring within the porewater (or across the reef). If photosynthesis and respiration were the only processes occurring, then TA and DIC would vary at a 0:1 ratio because photosynthesis and respiration consume or release DIC but do not change TA to any significant degree. In this hypothetical case (see Figure 3.8), a plot of TA vs. DIC would have a slope of zero (horizontal line). If calcification and carbonate dissolution were the only processes altering the water chemistry, then the slope of a TA vs. DIC plot would be 2:1, as these processes consume or release two moles of TA per mole of DIC. In nature, however, the slope will be representative of some combination of these processes. If net ecosystem production (NEP) and net ecosystem calcification (NEC) were equal, a slope of 1:1 would be expected under aerobic conditions. When plotted over isopleths of constant saturation state, as in Figure

3.8, it is easy to visualize how biogeochemical processes can affect the carbonate saturation state of the water. An increase in TA relative to DIC ($\text{TA}:\text{DIC} > 0.95$) due to dissolution would increase the saturation state by adding CO_3^{2-} ions into the water, whereas an increase in DIC, with no change in TA, would reduce the saturation state. Any change in TA and DIC with a ratio less than 0.95 will also result in a decreased saturation state due to the effects on carbonate ion distribution (Andersson and Gledhill 2013; Andersson et al. 2013).

The slope of $n\text{TA}$ vs. $n\text{DIC}$ in porewater, along with the chemistry of the overlying seawater are shown in Figure 3.8. The slope of the regression lines for CRIMP-2 and Ala Wai porewater are 0.80 and 0.93, respectively. The overlying seawater points (blue circles) are offset from the regression line. Both Moulin et al. (1985) and Tribble et al. (1990) showed that this offset is related stoichiometrically to the consumption of oxygen by respiration. Until the porewaters reach undersaturation with respect to a mineral phase, DIC will be added to the system while TA remains constant (and pH decreases). Once the system reaches saturation ($\Omega=1$), any additional DIC and subsequent pH drop will be accompanied by an increase in TA as carbonate dissolution begins. This offset between the overlying seawater and the regression line is equivalent to the x-intercept of each regression line of $\Delta n\text{TA}$ vs. $\Delta n\text{DIC}$ (where Δ is the difference between the parameter at depth and at the SWI) in Figure 3.9, and is representative of the amount of DIC that must be added to the system before dissolution of carbonate minerals can occur leading to a change in TA. The x-intercepts for the CRIMP-2 and Ala Wai curves are 100 and $150 \mu\text{mol}\cdot\text{kg}^{-1}$, respectively, which are roughly the same as the offsets shown in Figure 3.8.

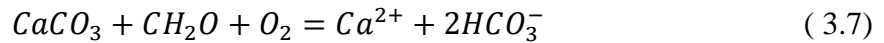
Moulin et al. (1985) measured TA and DIC in cores recovered from carbonate-rich lithothamnoid sediments deposited in the Bay of Calvi, Corsica and found the slope of the regression of $\Delta n\text{TA}$ vs. $\Delta n\text{DIC}$ to be 1.04, with an x-intercept of $\sim 100 \mu\text{mol}\cdot\text{kg}^{-1}$, very similar

findings to those above for CRIMP-2 and Ala Wai. Using suspended sediments in a respirometer, the authors determined that the carbonic acid produced by bacterial respiration was being used to dissolve carbonate materials, as represented in the following equations:



where CH₂O represents a simplified formula for the organic matter undergoing respiration.

When the equations are combined, a 1:1 relationship between dissolution of carbonate minerals and aerobic respiration of organic matter becomes evident.

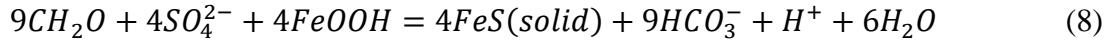


In this situation, the extent of carbonate mineral dissolution is directly related to the rate of respiration of OM within the sediments. The data from the Ala Wai and CRIMP-2 porewaters are consistent with this concept. The lesser slope (relative to Moulin et al. 1985)) is potentially due to several factors. Denitrification and/or sulfate reduction outside the oxic zone would lower the slope below one. Kinetic limitations on carbonate dissolution such as the presence of both phosphate and DOC can also cause a TA:DIC ratio less than one as carbonate minerals are not instantaneously dissolved, so that the release of TA is slower than the production of DIC (Berner et al. 1978; Morse 1983; Walter and Morse 1985; Morse et al. 2006). In addition, the larger grain size of carbonate sediments at Ala Wai and CRIMP-2 compared to the Bay of Calvi sediments results in less reactive surface areas and could impose another kinetic limitation on dissolution resulting in a lower rate, so that DIC increases more rapidly than TA.

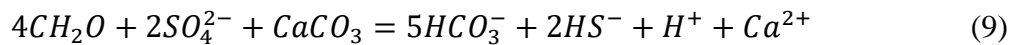
Whereas oxic respiration coupled with carbonate mineral dissolution is likely the most significant control on the TA:DIC ratio in the upper sediments where porewater is still oxygenated, numerous redox reactions occur throughout the sediment column during the early

stages of diagenesis. These microbially-mediated processes include denitrification, ferric iron, manganic manganese, and sulfate reduction as well as FeS_x precipitation (e.g. Morse and Mackenzie, 1990; Sansone et al., 1990; Tribble et al., 1990; Mackenzie and Andersson, 2011). The TA:DIC ratio at CRIMP-2 (0.80) is similar to the slope expected for denitrification, 0.81 calculated by Bouillon et al. (2007). Nevertheless, aerobic respiration is still likely the dominant metabolic process in the oxic layer, while sulfate data suggests that sulfate reduction (coupled with carbonate dissolution) is likely the primary control on TA and DIC in the anoxic depths, and the overall slope is a combination of the two processes. The TA:DIC ratio at Ala Wai (0.93) is closer to the expected slope of one from oxic respiration combined with carbonate dissolution. The higher porosity and permeability of the AW sediments, relative to CRIMP-2, result in deeper oxygen penetration, with oxygen present down to at least ~16 cm sediment depth at AW, compared to only ~8 cm at CRIMP-2. Nevertheless, sulfate depletion (sulfate data not shown) was found in the porewater of both the AW and CRIMP-2 sediments; the loss of sulfate was ~2 - 5% at both locations in the deeper sediments. Sulfate reduction of this magnitude (2 - 30%) decreases pH and reduces carbonate saturation state as the produced H^+ ions effectively titrate CO_3^{2-} ions. Beyond 30% sulfate reduction, production of alkalinity from the reaction raises total alkalinity and can promote the precipitation of carbonate minerals (Morse and Mackenzie 1990; Tribble et al. 1990; Stoessell 1992; Morse et al. 2006; Mackenzie and Andersson 2011) Sulfate reduction can be coupled with other processes - iron oxide reduction, FeS_x (iron monosulfides and pyrite) formation, and carbonate dissolution - in the sediments, which results in TA:DIC ratios of ≤ 1 . Sulfate reduction coupled with carbonate dissolution and pyrite formation can also result in a TA:DIC ratio of 1 (Sansone et al. 1990). In addition, Ben-Yaakov (1973) and Mackenzie and Andersson, (2011) showed that sulfate reduction coupled with iron (or

manganese) oxide reduction (eqn 8), in the absence of carbonate precipitation, can cause porewater to be buffered at higher pH's.



The lack of iron in sandy carbonate reef sediments with little terrigenous influence makes this process unlikely to be an important factor at CRIMP-2 and Ala Wai, but may be an important biogeochemical process in the lagoonal Kaneohe Bay reef sediments discussed later in the text (Ristvet 1978; Mackenzie et al. 1981; Mackenzie and Andersson 2011). Some CRIMP-2 sediment was examined under a microscope and pyrite crystals were present, but CHN analysis shows that the sediment is virtually pure carbonate material so authigenic pyrite formation would be at most only a minor factor. Pyrite framboids were found by Sansone et al. (1988b) on a patch reef within Kaneohe Bay, so while unlikely at CRIMP-2 due to the lack of requisite iron from terrestrial input, more nearshore sites, such as Ala Wai, may be significantly influenced by this reaction (see Ristvet 1978, for a more complete discussion of the formation of FeS₂ in Kaneohe Bay sediments). A more likely process occurring in the CRIMP-2 and Ala Wai sediments is sulfate reduction coupled to carbonate dissolution:



This reaction, described by Tribble et al. (1990) in a study of Kaneohe Bay reef framework interstitial water, results in a slope of the TA-DIC line of 0.83. Whereas oxic respiration is the most significant factor in the upper sediment depths, it is clear that anaerobic processes such as sulfate reduction - coupled with carbonate dissolution - and possibly denitrification and FeS_x formation, are controlling the TA:DIC ratio in the CRIMP-2 and AW porewaters. In addition to the microbial processes that can alter the TA:DIC ratio, kinetic limitations on the rate of carbonate dissolution also change TA:DIC. Carbonate dissolution is not an instantaneous process

(e.g., Berner and Morse, 1974; Walter and Morse, 1985; Morse and Mackenzie, 1990) and the buildup of CO₂ (see Figure 3.5) from microbial respiration can occur faster than the release of TA due to dissolution, which will result in a TA to DIC ratio less than one.

In an earlier study involving Kaneohe Bay fine-grained sediment porewaters, Ristvet (1978) and colleagues (Mackenzie et al. 1981) measured TA, pH, and other dissolved constituents in porewater extracted from sediment cores throughout various sectors of Kaneohe Bay (delineated by the authors into north, central, and south bay) representing much of the surface area of the bay's lagoon. These authors also investigated the solid phase chemistry and mineralogy of the sediments to elucidate early diagenetic reaction pathways in the sediments. The cores they studied penetrated deeper, but the sediments were much more fine grained, than those of the current study, and were separated into two sediment facies characterized by >50% carbonate or <50% carbonate. The latter were termed terrigenous by the authors because of a significant siliciclastic component. Despite the use of the term "carbonate facies," none of the sediments sampled by Ristvet were as close to pure carbonate as those sampled for our study. In addition, the physical properties of the sediments (e.g., permeability and porosity) were quite different.

Figure 3.10 shows the nTA vs. nDIC (calculated from TA and pH) from the study of Ristvet and colleagues, along with our current data from CRIMP-2 and Ala Wai. The relatively high TA and DIC concentrations of the porewaters studied by Ristvet et al. are due to their sediment cores being deeper and finer grained than the CRIMP-2 and Ala Wai cores, resulting in much higher TA and DIC concentrations in the former due to enhanced dissolution as a result of factors such as lower pH due to a longer porewater residence time and greater available reactive surface area. The regression lines of each set of cores are similar to those from CRIMP-2 and

AW. The central bay carbonate cores (CBC) studied by Ristvet et al. were collected in finer grained sediment than those of CRIMP-2 and were from the inner lagoon of Kaneohe Bay rather than the backreef, but they show a very similar slope of 0.85, suggesting that similar processes may be controlling the porewater biogeochemistry, despite the physical differences in hydrodynamics and sediment properties. The AW data most closely resemble the Ristvet data from the north and south Kaneohe Bay carbonate groups (NBC and SBC), which may be due to the difference in organic matter composition (higher OC/TN) in the AW, NBC, and SBC cores relative to the CBC and CRIMP-2 cores. Morse and Mackenzie (1990; see also Tribble, 1990, Mackenzie et al., 1995; Mackenzie and Andersson, 2011) used CO₂-carbonic acid system data from the porewater of Mangrove Bay, Bermuda and a theoretical path calculation to show that the C/N ratio of the organic matter deposited in the sediments and respired (via oxic and anoxic microbial processes) can have a strong influence on the degree of undersaturation that the porewater reaches with respect to carbonate mineral phases (Figure 3.11). As DIC is progressively added to the porewater from the aerobic oxidation of organic matter and sulfate reduction processes, the saturation state of the water initially falls with respect to carbonate minerals (aragonite is the example shown in Figure 3.11), but with continuing organic matter decomposition, the waters can become oversaturated with respect to a carbonate mineral, perhaps leading to precipitation of a carbonate mineral phase (Ben-Yaakov 1973; Berner 1980; Aller and Rude 1988; Morse and Mackenzie 1990; Stoessell 1992; Tribble 1993). The trend in the carbonate mineral Ω of the porewater - with increasing DIC produced from aerobic oxidation or anaerobic sulfate reduction of organic matter - will depend on the C:N ratio of the decomposing labile marine organic matter, as respiration of OM with higher C:N ratios leads to a greater release of DIC. The respiration of organic matter with higher OC:TN ratios may also be

responsible for the greater degree of undersaturation in the AW, NBC, and SBC porewater (see also Mackenzie and Andersson, 2011; Morse and Mackenzie, 1990; Tribble, 1990).

The difference in terrigenous vs. carbonate facies described by Ristvet and colleagues (1978) and Mackenzie et al. (1981) is also reflected in Figure 3.12, a plot of pH_t vs. TA. Despite large concentrations of organic matter in the terrigenous cores, relative to the carbonate facies, which supports high rates of respiration, production of CO₂, and the consequent dissolution of Mg-calcite phases (and possibly aragonite in some cases) the porewater in the terrigenous facies appears to be buffered at a higher pH than that in the carbonate facies. This observation was attributed by Mackenzie et al. (1981) to reverse weathering reactions involving aluminosilicate minerals in the sediments that buffer porewater pH (Mackenzie and Garrels 1966; Mackenzie and Kump 1995). Evidence supporting this assertion can especially be seen in the pH of porewater from the sediments of the CBC core, where pH drops below 6.8 due to increased CO₂ from respiration and a lack of major buffering of the pH by aluminosilicate reactions. In addition, the presence of iron (or manganese) oxides in the terrigenous, aluminosilicate-rich sediments has been shown to result in buffering of the porewater at higher pH values through the production of pyrite (FeS₂) via sulfate and iron oxide reduction (Sansone et al. 1990; Mackenzie and Andersson 2011). The presence of pyrite in the terrigenous-rich cores, along with its absence in the carbonate-rich cores collected by Ristvet and colleagues likely confirms this process. Although iron was not measured in this study, it is not expected to be present in an appreciable amount on the Kaneohe Bay barrier reef as the sediments are almost purely derived from reef erosion (Smith et al. 1981). The CRIMP-2 pH and TA data appear to be an extension (towards the sediment-water interface) of the deeper CBC core data and CRIMP-2 could possibly exhibit the same behavior at greater depth. Because of the lack of iron and terrigenous-derived

aluminosilicates, it is likely that reef sediments, like at CRIMP-2, which are largely free of terrestrial influence may experience lower pH and higher rates of carbonate sediment dissolution, altering the CaCO_3 budget. Another key difference between our study and the Kaneohe Bay study of Ristvet and colleagues is the grain size of the sediments investigated in the two studies. Sediments from CRIMP-2 and Ala Wai have an overall larger grain size and most likely a higher permeability than the fine-grained sediments collected by Ristvet and colleagues, who did not measure the permeability of their cores. The effect of higher permeability is discussed in Section

It is also important to note that the putative dissolving phase in our current study is a high Mg-calcite (>13 - 15 mol% MgCO_3) as porewaters do not reach undersaturation with respect to aragonite in any of the collected samples (Figure 3.8), but it is undersaturated with respect to high Mg-calcite compositions (see Section 3.5.3). It is clear from Figure 3.8 that an increase in the DIC concentration of the source waters, from rising atmospheric emissions of CO_2 and ocean acidification, would lead to a decrease in Ω . As previously discussed, when the overlying waters are oversaturated with respect to a given carbonate mineral phase, CO_2 must first be added to the porewater, via microbial respiration, to lower Ω before carbonate mineral dissolution can begin. Such dissolution is controlled almost entirely by microbial processes and is referred to as “metabolic dissolution.” As the overlying seawater Ω decreases, a lesser initial addition of DIC as CO_2 is required to initiate dissolution, thereby driving an overall higher rate of dissolution. In support of this conclusion, Cyronak et al. (2014) demonstrated, using benthic chambers, that sediment dissolution rates and TA fluxes increased dramatically under high pCO_2 conditions coupled with advective flow regimes. It is also expected that the average pCO_2 of coral reefs will increase at a faster rate than the open ocean under rising anthropogenic CO_2 emissions as a result of regional effects such as nutrient and organic matter loading, coral bleaching, and overfishing,

all of which can alter the metabolic state of a reef ecosystem (Cyronak et al. 2014). If the overlying seawater were to become undersaturated with respect to a carbonate mineral phase, then dissolution of this phase within the sediments could begin without the addition of any additional CO₂ from microbial activity, resulting in what is termed “environmental dissolution” (e.g., Andersson and Gledhill 2013). The combination of metabolic dissolution with enhanced environmental dissolution could ultimately lead to an increase in carbonate dissolution rates relative to carbonate accretion. Combined with the possible slowdown in carbonate accretion as reef calcification declines with rising pCO₂, these changes have the potential to alter dramatically the CaCO₃ balance and biogeochemistry of reef environments.

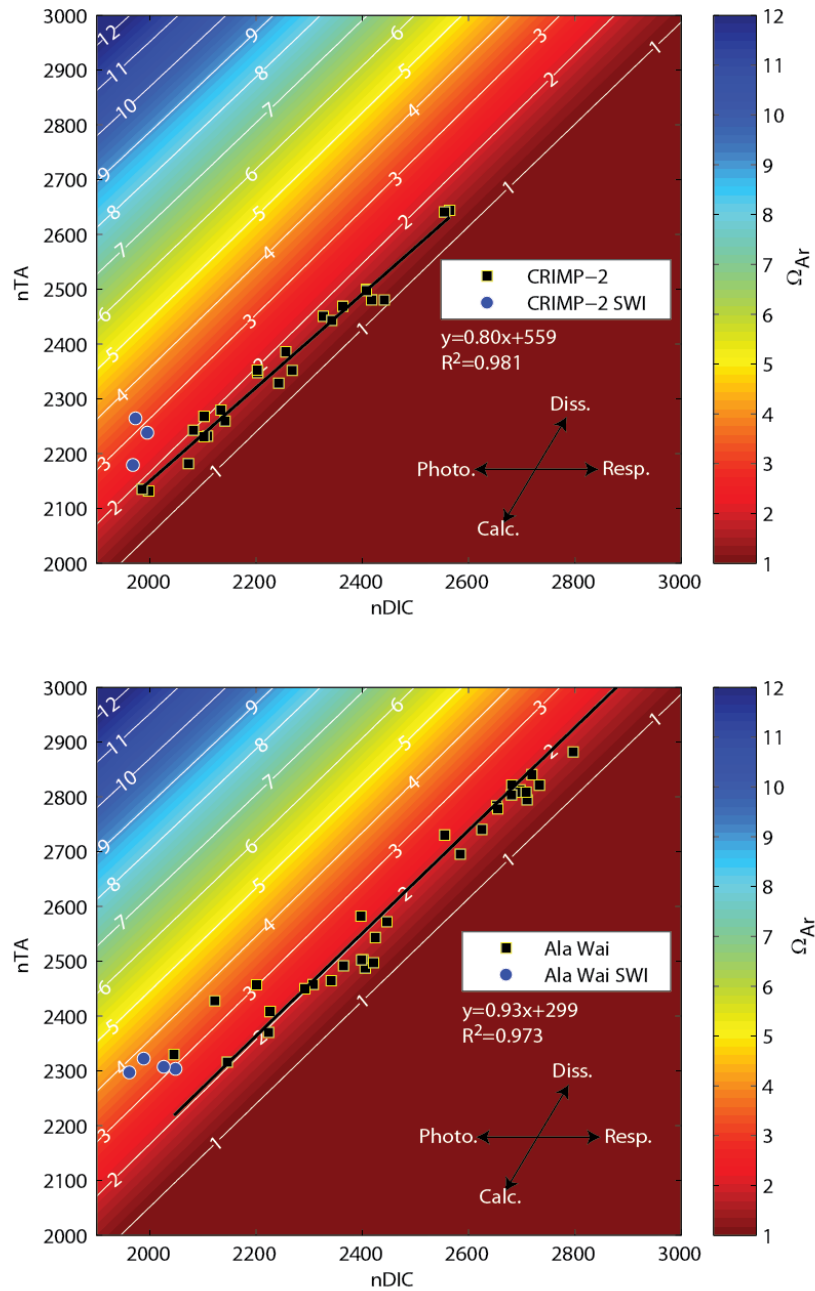


Figure 3.8: TA and DIC normalized (n) to salinity=35 with isopleths of constant aragonite saturation state. Blue circles are sediment-water interface data and black squares are data from porewater wells (2 - 60 cm), which are permanently installed in the sediments at both CRIMP-2 (a) and Ala Wai (b). There are 5 additional points outside the range of the diagram for the Ala Wai data set; these samples all fall directly on the regression line, with maximum values of 3682 and 3518 $\mu\text{mol}\cdot\text{kg}^{-1}$ for nTA and nDIC, respectively. Linear regression equations and R^2 values are shown for each data set. Arrows showing the theoretical slopes for a system controlled by calcification/dissolution and photosynthesis/respiration are plotted in the bottom right corner of (a) and (b).

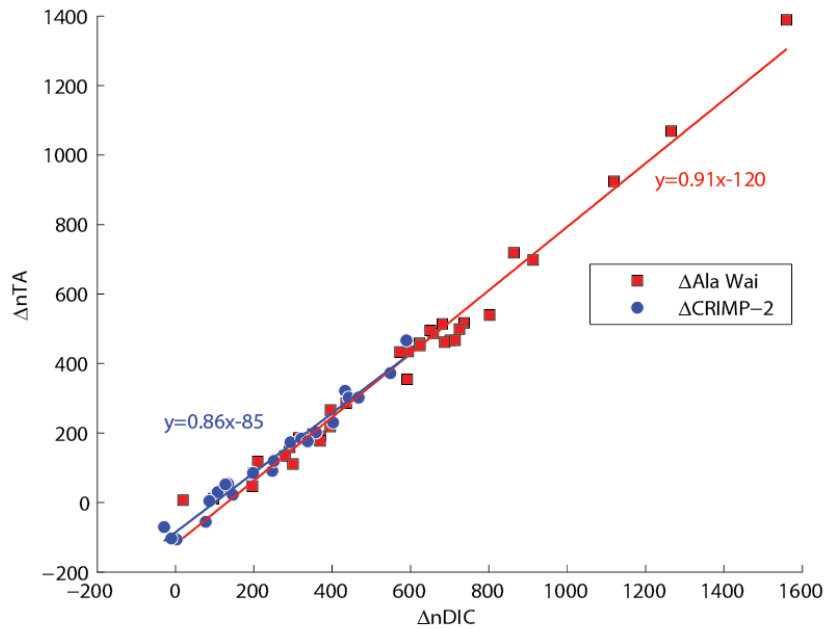


Figure 3.9: ΔnTA and $\Delta nDIC$ of CRIMP-2 and Ala Wai porewater. ΔnTA and $\Delta nDIC$ are the difference in nTA and $nDIC$ concentrations between the overlying surface water and the porewater normalized to $S=35$. The x-intercept is the amount of DIC as CO_2 that must be added to the system before any change in TA in the porewater can occur via dissolution.

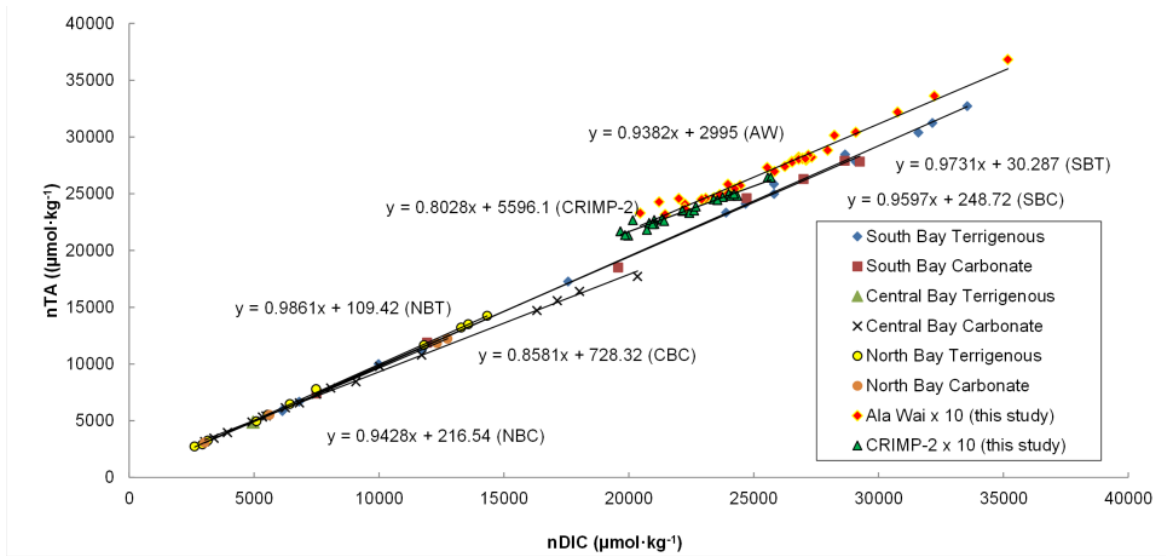


Figure 3.10: nTA vs. $nDIC$ plot of porewater data from the carbonate and terrigenous facies of Kaneohe Bay (data from Ristvet 1978) and the CRIMP-2 and Ala Wai porewater of this study. There appears to be three distinct slopes: CRIMP-2 and the Central Bay Carbonate cores; Ala Wai (AW), Southern Bay Carbonate, and North Bay Carbonate cores; and the terrigenous-rich cores. Note that the AW and CRIMP-2 data have been multiplied by 10 so that they can be plotted along with the much higher porewater TA and DIC concentrations measured by Ristvet and colleagues.

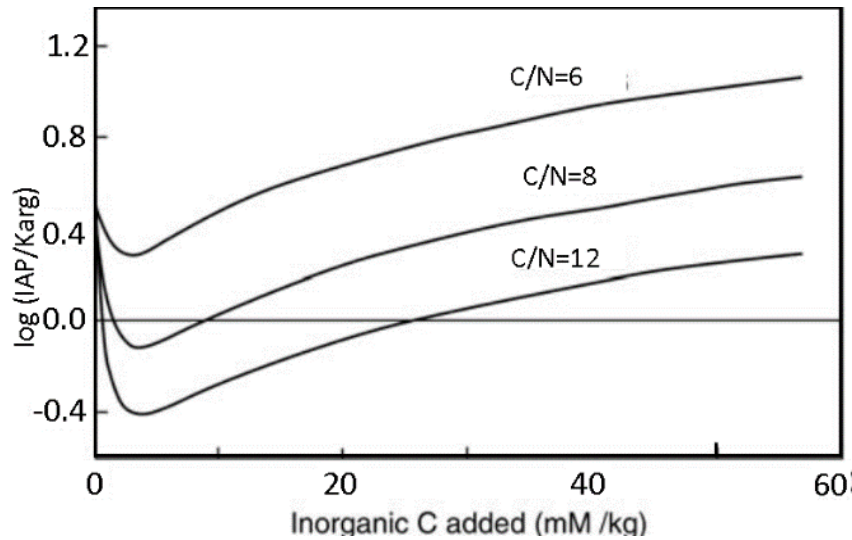


Figure 3.11: Diagram illustrating the effect of the C/N ratio of respired organic matter on the diagenetic reaction pathway of DIC vs. $\log(IAP/K_{arag})$ as DIC is added to the porewaters from the oxidation of organic matter by aerobic oxygen consumption and anaerobic sulfate reduction processes. [Fig. is adapted from Morse and Mackenzie, 1990; the various C/N pathways of $\log(IAP/K_{arag})$ vs. DIC for various C/N ratios are calculated theoretically and agree well for a ratio of 6 with changes in these variables with depth in Mangrove Bay, Bermuda porewaters, Mackenzie et al. 1995]. Respiration of organic matter with a higher C/N ratio (and the subsequent production of DIC) leads more rapidly to a condition of undersaturation (solid horizontal black line at $y = 0.0$) in the porewaters with respect to aragonite (or other carbonate phases) than respiration of organic matter with a lower C/N ratio.

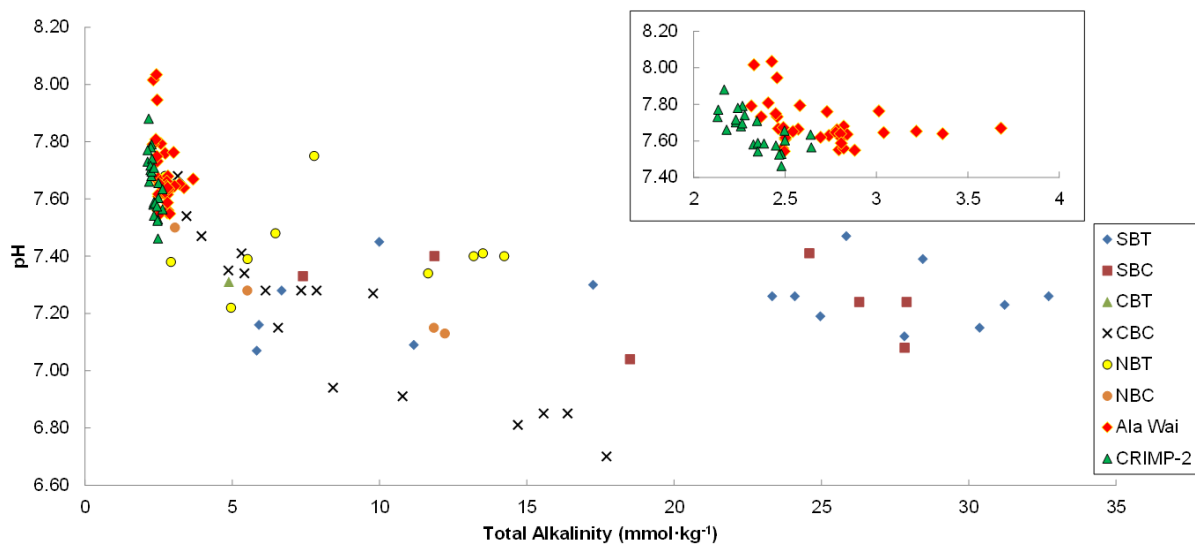


Figure 3.12: pH vs. TA for the porewater of the current study and those measured by Ristvet and colleagues in Kaneohe Bay sediments (Ristvet 1978; Mackenzie et al. 1981). Symbols are the same as in Figure 3.10. The terrigenous facies porewaters are buffered at a higher pH than in the carbonate facies due to reverse weathering reactions involving aluminosilicate minerals or the reduction of iron oxides coupled with sulfate reduction. The inset at the top highlights the Ala Wai and CRIMP-2 data.

3.5.3 Saturation state of porewater with respect to carbonate minerals

The saturation state with respect to aragonite in the porewater, at either the CRIMP-2 or Ala Wai location, never fell below one at any depth within the sediments (see Figure 3.6 although it decreased steadily from ~3.5 or ~3.0 at AW and CRIMP-2, respectively, to ~1.5 by 60 cm depth. Although aragonite is likely not dissolving in the bulk sediments, microzones can form within the sediments where the water chemistry might be corrosive and fine-grained particles might potentially dissolve (Morse and Mackenzie 1990).

The porewater throughout the sediment column at both locations was undersaturated with respect to a 15 mol% Mg-calcite phase when calculated using the stoichiometric solubility products from Plummer and Mackenzie (1974). The surface waters at CRIMP-2 and Ala Wai are, on average, in metastable equilibrium ($\Omega=1$) with ~13 mol% and ~14 mol% MgCO₃ Mg-calcite phases, respectively. Results of XRD analysis of CRIMP-2 sediments showed a dominant Mg-calcite peak with a composition between 15.5-17.5 mol%, depending on depth. Such high Mg-calcite phases, such as *Lithothamnion sp.* and *Amphiroa sp.*, are likely dissolving within the sediment porewater at these sites. Pickett and Andersson (2015) have shown that dissolution rates of biogenic carbonates increase with increasing mol% MgCO₃ in natural seawater under pCO₂ levels that would be expected in the porewaters under increasing OA. By 60 cm depth at both CRIMP-2 and Ala Wai, the porewater is undersaturated with respect to all Mg-calcite phases of composition greater than 8 mol% and 9.5 mol% MgCO₃, respectively. Despite the nearly identical pH at depth in the sediment porewaters at both locations, the more elevated TA at Ala Wai (2635 $\mu\text{mol}\cdot\text{kg}^{-1}$) than at CRIMP-2 (2357 $\mu\text{mol}\cdot\text{kg}^{-1}$) renders the porewater at the former location slightly less corrosive to carbonate minerals.

The porewater carbonate mineral Ω 's calculated for the CRIMP-2 and Ala Wai sites compared well with those that we calculated from the Ristvet (1978) and Mackenzie et al. (1981) TA and pH data for the porewaters of their carbonate cores. Saturation states for porewaters of the NBC and CBC cores ranged between 3.45 - 1.69, 2.26 - 1.07, and 0.64 - 0.28 for calcite, aragonite, and 15% Mg-calcite (calculated using the solubilities of Plummer and Mackenzie, 1974), respectively. This suggests that although saturation states with respect to aragonite are approaching $\Omega=1$, high Mg-calcite compositions are still the dominant carbonate phases that are dissolving in these sediment-porewater systems. In the more terrigenous-rich sediment cores collected by Ristvet and colleagues, carbonate mineral saturation states of the porewaters were much higher, often oversaturated even with respect to 15% Mg-calcite, due to extremely high TA concentrations, despite low pH. This further confirms the assertion that the terrigenous sediment porewaters are more strongly buffered with respect to pH relative to the porewaters of the carbonate facies.

3.5.4 *Flushing events*

Porewater in the carbonate sandy sediments of reef environments can be significantly affected by the overlying water column because of their permeable and porous nature. Advective processes and differences in pressure gradients from waves, tides, formation of sand ripples, etc. will alter flow rates of water through the sedimentary column (e.g., Shum 1993; Precht and Huettel 2004; Fogaren et al. 2013; Fram et al. 2014). An important finding of our work is that swell events generated by storms and changes in wind and bottom current speeds at both the Ala Wai and CRIMP-2 locations appear to alter porewater gradients of chemical constituents in the sediments on short time scales. The effect of these physical processes are reflected in the

temporal changes in the CO₂-carbonic acid system chemistry of the porewater at both the CRIMP-2 and Ala Wai sites.

As evidence of these temporal changes, a TA profile was obtained at CRIMP-2 on 08/23/2012 (see Figure 3.2) when wind speeds in the bay averaged 3.6 m·s⁻¹. Using a parameterization from Lowe et al. (2009b), a current velocity of 5 cm·s⁻¹ across the reef was calculated based on measured offshore wave heights obtained from the Coastal Data Information Program wave buoys (CDIP 098, <http://cdip.ucsd.edu/>). The same parameterization was also used by Shamberger et al. (2011) in calculating free-water residence times for the Kaneohe Bay barrier reef system. Another alkalinity profile was collected on 09/06/2012 under wind and current speeds of 6.2 m·s⁻¹ and 18 cm·s⁻¹, respectively. Surface water TA and pCO₂ at the CRIMP-2 site were 2252 μmol·kg⁻¹ and 612 μatm on 08/23/2012 and 2238 μmol·kg⁻¹ and 475 μatm on 09/06/2012. Despite similar surface water TA values and a nearly identical profile structure, concentrations of TA in the porewater were ~100 μmol·kg⁻¹ higher at every depth on 08/23/2012. Falter and Sansone (2000a) and Fogaren et al. (2013) demonstrated flushing of permeable sediments, in Kaneohe Bay and on the South Shore of Oahu, following swell events by measuring changes in porewater O₂ and nutrients. In addition, Drupp et al. (2013) previously showed that low wind speeds are associated with high pCO₂ concentrations on the reef due to the increase in residence time, a buildup of CO₂ from respiration and calcification, and a lower gas exchange with the atmosphere. A reasonable interpretation of the 08/23 and 09/06 porewater data is that the higher current speeds on 09/06/2012 increased advection of overlying (lower TA and lower pCO₂) water into the sediments, resulting in porewater TA concentrations more similar to the surface water. In other words, the porewater was “flushed” of its moderately high TA concentrations generated by sediment-porewater reactions involving dissolution of biogenic

metastable Mg-calcite phases. Periods of low advection, (e.g., low wave activity, reduced wind and lower current speeds) are hypothesized to result in longer porewater residence times and allow for the buildup of TA due to microbial metabolic processes producing CO₂ and leading to carbonate mineral dissolution. This excess TA can then be “flushed” out of the system when advection increases: consequently, porewater is exchanged and replaced with overlying surface water. This process could facilitate carbonate dissolution as oxygen is constantly replenished and aerobic respiration can continue, similar to the enhanced carbonate dissolution that is seen in seagrass beds due to oxygen and organic matter replenishment through seagrass roots (e.g., Burdige and Zimmerman, 2002; Burdige et al., 2008; Morse et al., 1987). Experiments using benthic flux chambers by Cyronak et al. (2013b) also demonstrated an increase in TA fluxes out of the sediments under higher advective rates, supporting the idea that increased advection can “flush” the porewater system.

Porewater at Ala Wai is also periodically subjected to similar forcing due to large swell events on the south shore of Oahu. Profiles taken on 04/01/2014, 04/10/2014, and 04/22/2014 (Figure 3.2b) clearly illustrate the effect of flushing on porewater chemistry. The highest TA concentrations measured during the entire study period for either the CRIMP-2 or Ala Wai sites were observed on 04/01/2014, during a quiescent period. This quiescence period likely resulted in less advection within the sediments and a longer porewater residence time. A large swell, in which significant wave heights increased from a baseline of 1 m to > 2.5 m, reached the south shore on 04/04/2014 and peaked on 04/08/2014 (wave and swell data from National Data Buoy Center – Station 51204, <http://www.ndbc.noaa.gov/>), and sampling on 04/10/2014 showed decreased TA concentrations in the porewater (see Figure 3.13) that were more representative of the overlying water column. By 04/22/2014, although the swell event had ended, TA released by

carbonate mineral dissolution in the porewater had not had time to build back up to pre-swell concentration levels.

Despite the large changes in porewater TA between 04/01/2014 and 04/22/2014, pH remained essentially constant. This observation could reflect the difference between the relatively rapid changes in pH associated with microbial respiration of organic matter and the much slower kinetically controlled dissolution rates of metastable carbonate minerals driven by the metabolically produced CO₂. Because of the short residence time of the surface water at Ala Wai due to consistent tidal and convective mixing, even during periods of low wind speeds (Hamilton et al. 1995; Sevadjian et al. 2010), there is no obvious relationship between overlying seawater and porewater CO₂-carbonic acid system chemistry as there is at CRIMP-2. The surface water TA and pCO₂ at Ala Wai are less variable, and short term changes in wind speed, which can have noticeable geochemical effects on the CRIMP-2 surface water and porewater, likely have much less influence on chemical changes in the Ala Wai water column and porewater. The difference in depth (3 m vs. 15 m) between the two locations also means that the porewaters at CRIMP-2 can be affected by smaller changes in physical processes in the surface water, such as current speed and swell height.

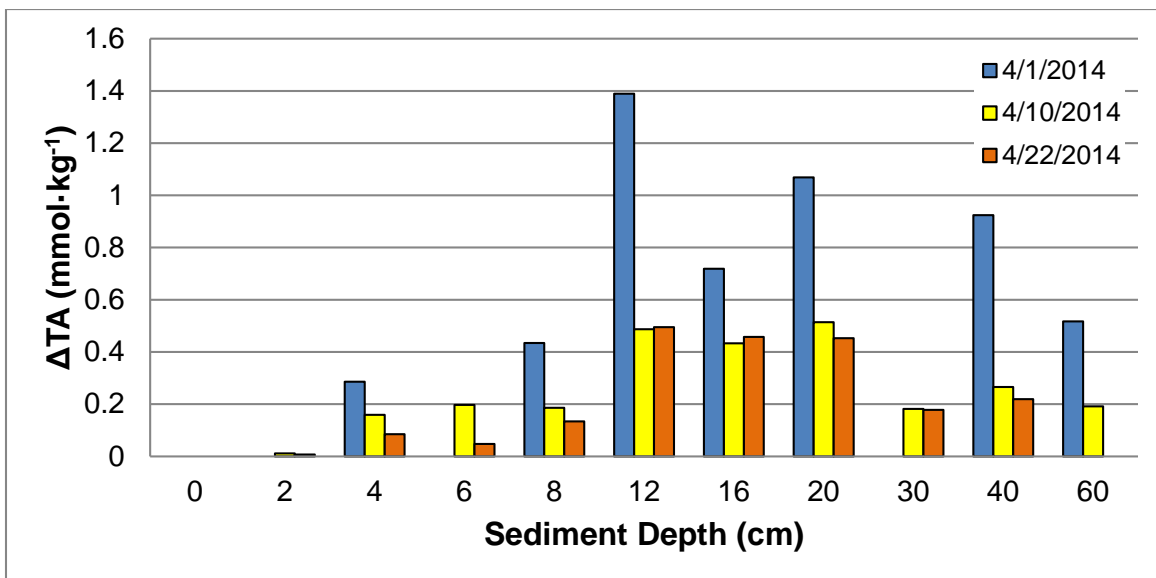


Figure 3.13: Difference in TA between the surface water and each sample depth over three days at the Ala Wai location. The large buildup of TA in the porewater can be seen on the 04/01/2014 sampling (blue bar) during a quiescent period. When a large swell (see Section 3.5.4) reached Oahu on 04/04/2014, porewater was rapidly flushed from the sediments and the Δ TA decreased at all depths. By 04/22/2014, although the physical conditions had returned to baseline, TA in the sediments had not yet built back up to pre-swell concentrations.

3.6 Conclusions and Future Considerations

Permeable carbonate sands are more biogeochemically active than previously thought and are capable of supporting a high rate of microbial respiration despite low organic matter concentrations. The high turnover rate is due to the relatively high permeability of the sediments and a generally shorter porewater residence time compared to fine-grained sediments. The shallow porewater chemistry is strongly tied to the residence time of the porewater and transient physical events such as swells or storms. These events can drastically change the shallow porewater chemistry, as enhanced physical pumping flushes the sediments and introduces seawater from the overlying water column. Porewater profiles collected before and after swell events, at both CRIMP-2 and Ala Wai, show high concentrations of TA prior to the events, whereas porewater chemistry more closely resembles the overlying water column following these physical events.

The CO₂-carbonic acid system chemistry of most sands is strongly controlled by metabolic processes, specifically oxic respiration of OM and the production of CO₂, which lead to the dissolution of metastable calcium carbonate phases, primarily the biogenic, and if present, abiotic Mg-calcites. It appears that the porewater of permeable sandy carbonate sediments in Hawai'i sampled to date is approaching saturation with respect to aragonite and is already undersaturated with respect to >12 mol% Mg-calcite phases, which are the be the dominant carbonate substrates at the CRIMP-2 and Ala Wai study locations.

Analysis of TA and DIC concentrations in the porewater indicate that oxic respiration and likely sulfate reduction, both coupled with carbonate dissolution, are the primary drivers of changes in the CO₂-carbonic acid system chemistry of the porewater. The production of DIC via oxic respiration and the subsequent dissolution of carbonate substrates are the primary controls on the TA:DIC ratio in the oxic layer. In the anoxic layer, a combination of sulfate reduction (~2-5%), denitrification, and potentially FeS₂ formation all contribute to a TA:DIC ratio ≤ 1 . The regression equations of TA vs. DIC and Δ TA vs. Δ DIC are very similar to those found in other carbonate sediment and framework studies – despite differences in organic matter, physical forcings, and sediment characteristics - and support this conclusion (e.g., Andersson and Gledhill, 2013; Mackenzie and Andersson, 2011; Mackenzie et al., 1981; Moulin et al., 1985; Ristvet, 1978; Sansone et al., 1990, 1988b; Tribble et al., 1990).

Based partially on the results of our porewater analysis, we hypothesize that future changes in surface water DIC and pH resulting from ocean acidification could have a very significant impact on the dissolution rates of metastable skeletal and abiotic carbonate phases of varying magnesian calcite compositions (Mg-calcite) and aragonite, especially in sandy reef sediments like those of this study. Because pure carbonate sediments tend to be buffered with

respect to pH at lower values than those containing terrigenous material [e.g., detrital and neoformed (via reverse weathering) aluminosilicates, iron oxides, etc.], coral reef carbonate sediment porewaters are particularly at risk of becoming increasingly undersaturated with respect to metastable carbonate minerals, thereby leading to enhanced dissolution of these phases. Furthermore and more importantly, as the Ω of the overlying water column continues to decrease due to OA, an increase in carbonate mineral dissolution is expected (e.g., Morse et al. 2006), because of the high advection rate between the porewater of sandy sediments and the overlying water column - as observed in this study and others (e.g., Boudreau et al. 2001; Janssen et al. 2005; Fram et al. 2014) - along with increased rates of dissolution of metastable carbonate phases, could lead to significantly higher future rates of mass transfer of TA and DIC between the sediments and the overlying water column. The high advection rate also serves to continually supply the sediments with oxygen and organic matter, thus promoting aerobic respiration, which is an effective driver of carbonate dissolution, similar to the process of oxygen and nutrient supply to the sediments via seagrass roots (e.g., Burdige and Zimmerman, 2002; Morse et al., 1987). In addition to metabolic dissolution, metastable carbonate phases in the porewater-sediment system could potentially undergo environmental dissolution further elevating dissolution rates. The increases in the amount of biogenic and abiotic carbonate mineral dissolution, coupled with potential increases in bioerosion (e.g., Tribollet et al. 2009), and possible changes in land runoff (e.g. Ver et al., 1999; Tomlinson and De Carlo, 2003; Andersson et al., 2005; Ringuet and Mackenzie, 2005; De Carlo et al., 2007; Hoover and Mackenzie, 2009) will directly affect the geochemical balance of the reef ecosystem, resulting in an increasing deficit in the CaCO_3 budget for the ecosystem (Kleypas et al. 1999; Andersson et al. 2005; Andersson et al. 2006; Silverman et al. 2009; Andersson et al. 2009; Mackenzie and Andersson

2013). It is essential that the processes directly affecting carbonate dissolution in the sediments and reef frameworks be understood and quantified because the magnitude and temporal pattern of a CaCO_3 deficit will have profound implications for the timing of when individual reefs may reach a “tipping point” - i.e., cross the threshold from net accretion to net erosion as OA continues and global temperatures rise due to anthropogenic emissions of CO_2 .

3.7 Acknowledgments

This work would not have been possible without the help and support of many colleagues. The authors would like to thank Ryan Tabata, Bobby Thompson, Gerianne Terlouw, and Kristen Fogaren for their assistance in collecting samples, as well as Angelos Hannides and Becky Briggs for their help with the sediment analysis. Special thanks to Peggy O'Day and Estela Reinoso-Maset for performing the XRD analysis. The quality of this manuscript was greatly improved from the invaluable comments and suggestions provided by Michael Guidry, Jane Schoonmaker, and Frank Sansone. This paper is funded in part by a grant/cooperative agreement from the National Oceanic and Atmospheric Administration, Project R/IR-29, R/IR-27, which is sponsored by the University of Hawai'i Sea Grant College Program, SOEST, under Institutional Grant No. NA14OAR4170071 from NOAA Office of Sea Grant, Department of Commerce. The views expressed herein are those of the author(s) and do not necessarily reflect the views of NOAA or any of its subagencies. UNIH-SEAGRANT-JC-15-03. Funding was also provided by Pac-IOOS in support of the MAP-CO₂ monitoring program.

3.8 References

- Agegian CR (1985) *The Biogeochemical Ecology of Porolithon Gardineri* (Foslie). University of Hawai'i
- Agegian CR, Mackenzie FT (1989) Calcareous organisms and sediment mineralogy on a mid-depth bank in the Hawaiian Archipelago. *Pacific Sci* 43:56–66.
- Aller RC, Rude PD (1988) Complete oxidation of solid phase sulfides by manganese and bacteria in anoxic marine sediments. *Geochim Cosmochim Acta* 52:751–765.
- Andersson AJ, Gledhill D (2013) Ocean acidification and coral reefs: effects on breakdown, dissolution, and net ecosystem calcification. *Ann Rev Mar Sci* 5:321–48. doi: 10.1146/annurev-marine-121211-172241
- Andersson AJ, Kuffner IB, Mackenzie FT, et al (2009) Net Loss of CaCO₃ from a subtropical calcifying community due to seawater acidification: mesocosm-scale experimental evidence. *Biogeosciences* 6:1811–1823. doi: 10.5194/bg-6-1811-2009
- Andersson AJ, Mackenzie FT, Lerman A (2005) Coastal Ocean and Carbonate Systems in the High CO₂ World of the Anthropocene. *Am J Sci* 305:875–918.
- Andersson AJ, Mackenzie FT, Lerman A (2006) Coastal ocean CO₂–carbonic acid–carbonate sediment system of the Anthropocene. *Global Biogeochem Cycles* 20:GB1S92. doi: 10.1029/2005GB002506
- Andersson AJ, Yeakel KL, Bates NR, de Putron SJ (2013) Partial offsets in ocean acidification from changing coral reef biogeochemistry. *Nat Clim Chang* 4:56–61. doi: 10.1038/nclimate2050
- Ben-Yaakov S (1973) pH Buffering of Pore Water of Recent Anoxic Marine Sediments. *Limnol Oceanogr* 18:86–94.
- Berner RA (1980) *Early Diagenesis: A Theoretical Approach*. Princeton University Press, Princeton, NJ
- Berner RA, Morse JW (1974) Dissolution kinetics of calcium carbonate in sea water; IV, Theory of calcite dissolution. *Am J Sci* 274:108–134. doi: 10.2475/ajs.274.2.108
- Berner RA, Westrich JT, Graber R, et al (1978) Inhibition of aragonite precipitation from supersaturated seawater; a laboratory and field study. *Am J Sci* 278:816–837.
- Bischoff WD, Bertram MA, Mackenzie FT, Bishop FC (1993) Diagenetic stabilization pathways of magnesian calcites. *Carbonates and Evaporites* 8:82–89.
- Bischoff WD, Bishop FC, Mackenzie FT (1983) Biogenically produced magnesian calcite inhomogeneities in chemical and physical-properties comparison with synthetic phases. *Am Mineral* 68:1183–1188.
- Boudreau BP (1997) *Diagenetic Models and Their Implementation*.
- Boudreau BP, Huettel M, Forster S, et al (2001) Permeable Marine Sediments : Overturning an Old Paradigm. *EOS Trans Am Geophys Union* 82:133–140.
- Bouillon S, Dehairs F, Velimirov B, et al (2007) Dynamics of organic and inorganic carbon

- across contiguous mangrove and seagrass systems (Gazi Bay, Kenya). *J Geophys Res Biogeosciences* 112:1–14. doi: 10.1029/2006JG000325
- Breitzke M (2006) Physical Properties of Marine Sediments. In: Schulz H, Zabel M (eds) *Marine Geochemistry*. Springer-Verlag, pp 27–71
- Briggs RA, Ruttnerberg KC, Glazer BT, Ricardo AE (2013) Constraining Sources of Organic Matter to Tropical Coastal Sediments: Consideration of Nontraditional End-members. *Aquat Geochemistry* 19:543–563. doi: 10.1007/s10498-013-9219-2
- Brindley GW, Brown G (eds) (1980) *Crystal Structures of Clay Minerals and their X-Ray Identification*. Mineralogical Society, London, England
- Burdige DJ (2006) *Geochemistry of Marine Sediments*. Princeton University Press, Princeton, NJ
- Burdige DJ, Hu X, Zimmerman RC (2010) The widespread occurrence of coupled carbonate dissolution/precipitation in surface sediments on the Bahamas Bank. *Am J Sci* 310:492–521. doi: 10.2475/06.2010.03
- Burdige DJ, Zimmerman RC (2002) Impact of seagrass density on carbonate dissolution in Bahamian sediments. *Limnol Oceanogr* 47:1751–1763.
- Burdige DJ, Zimmerman RC, Hu X (2008) Rates of carbonate dissolution in permeable sediments estimated from pore-water profiles: The role of sea grasses. *Limnol Oceanogr* 53:549–565. doi: 10.4319/lo.2008.53.2.0549
- Chave K (1954) Aspects of the biogeochemistry of magnesium 2. Calcareous sediments and rocks. *J Geol* 62:587–599.
- Cyronak T, Santos IR, Eyre BD (2013a) Permeable coral reef sediment dissolution driven by elevated pCO₂ and pore water advection. *Geophys Res Lett* 40:4876–4881. doi: 10.1002/grl.50948
- Cyronak T, Santos IR, McMahon A, Eyre BD (2013b) Carbon cycling hysteresis in permeable carbonate sands over a diel cycle : Implications for ocean acidification. *Limnol Oceanogr* 58:131–143. doi: 10.4319/lo.2013.58.1.0131
- Cyronak T, Schulz KG, Santos IR, Eyre BD (2014) Enhanced acidification of global coral reefs driven by regional biogeochemical feedbacks. *Geophys Res Lett* 41:5538–5546. doi: 10.1002/2014GL060849. Received
- De Carlo EH, Hoover DJ, Young CW, et al (2007) Impact of storm runoff from tropical watersheds on coastal water quality and productivity. *Appl Geochemistry* 22:1777–1797. doi: 10.1016/j.apgeochem.2007.03.034
- Dickson a. G, Afghan JD, Anderson GC (2003) Reference materials for oceanic CO₂ analysis: a method for the certification of total alkalinity. *Mar Chem* 80:185–197. doi: 10.1016/S0304-4203(02)00133-0
- Dickson AG, Millero FJ (1987) A comparison of the equilibrium constants for the dissociation of carbonic acid in seawater media. *Deep Sea Res* 34:1733–1743.
- Dickson AG, Sabine CL, Christian JR (eds) (2007) *Guide to best practices for ocean CO₂ measurements*. PICES Special Publication 3
- Drupp PS, De Carlo EH, Mackenzie FT, et al (2013) Comparison of CO₂ Dynamics and Air–Sea

- Gas Exchange in Differing Tropical Reef Environments. *Aquat Geochemistry* 19:371–397. doi: 10.1007/s10498-013-9214-7
- Eyre BD, Andersson AJ, Cyronak T (2014) Benthic coral reef calcium carbonate dissolution in an acidifying ocean. *Nat Clim Chang* 4:969–976. doi: 10.1038/nclimate2380
- Falter JL, Sansone FJ (2000a) Shallow pore water sampling in reef sediments. *Coral Reefs* 19:93–97. doi: 10.1007/s003380050233
- Falter JL, Sansone FJ (2000b) Hydraulic control of pore water geochemistry within the oxic-suboxic zone of a permeable sediment. *Limnol Oceanogr* 45:550–557.
- Fogaren KE, Sansone FJ, De Carlo EH (2013) Porewater temporal variability in a wave-impacted permeable nearshore sediment. *Mar Chem* 149:74–84. doi: 10.1016/j.marchem.2012.12.005
- Fram JP, Pawlak GR, Sansone FJ, et al (2014) Miniature thermistor chain for determining surficial sediment porewater advection. *Limnol Oceanogr Methods* 12:155–165. doi: 10.4319/lom.2014.12.155
- Gattuso J-P, Frankignoulle M, Wollast R (1998) Carbon and carbonate metabolism in coastal aquatic ecosystems. *Annu Rev Ecol Evol Syst* 29:405–434.
- Giambelluca TW, Nullet MA, Schroeder TA (1986) Rainfall Atlas of Hawai‘i.
- Ginsburg RN (1956) Environmental relationships of grain size and constituent composition in south Florida carbonate sediments. *Am Assoc Petroleum Geol Bull* 40:2384–2427.
- Goldsmith JR, Graf DL, Heard HC (1961) Lattice constants of the calcium-magnesium carbonates. *Am Mineral* 46:453–459.
- Gordon D. (1969) Examination of methods of particulate organic carbon analysis. *Deep Sea Res* 16:661–665.
- Hamilton PJ, Singer J, Waddell E (1995) Mamala Bay study, ocean current measurements: a report to the Mamala Bay Commission, HI. Raleigh, NC
- Hoover DJ, Mackenzie FT (2009) Fluvial Fluxes of Water, Suspended Particulate Matter, and Nutrients and Potential Impacts on Tropical Coastal Water Biogeochemistry: Oahu, Hawai‘i. *Aquat Geochemistry* 15:547–570. doi: 10.1007/s10498-009-9067-2
- Huettel M, Gust G (1992) Impact of bioroughness on interfacial solute exchange in permeable sediments. *Mar Ecol Prog Ser* 89:253–267.
- Huettel M, Rusch A (2000) Transport and degradation of phytoplankton in permeable sediment. *Limnol Oceanogr* 45:534–549.
- Huettel M, Webster IT (2001) Porewater flow in permeable sediments. In: Boudrea BP, Jorgensen BB (eds) *The benthic boundary layer: Transport processes and biogeochemistry*. Oxford University Press, pp 144–179
- Huettel M, Ziebis W, Forster S (1996) Flow-induced uptake of particulate matter in permeable sediments. *Limnol Oceanogr* 41:309–322.
- Jahnke RA (2004) Transport processes and organic matter in coastal sediments. In: Robinson AR, Brink K (eds) *The Sea, Volume 13: The Global Coastal Ocean*. Harvard University Press, Harvard, pp 163–192

- Jahnke RA, Richards M, Nelson J, et al (2005) Organic matter remineralization and porewater exchange rates in permeable South Atlantic Bight continental shelf sediments. *Cont Shelf Res* 25:1433–1452. doi: 10.1016/j.csr.2005.04.002
- Janssen F, Huettel M, Witte U (2005) Pore-water advection and solute fluxes in permeable marine sediments (II): Benthic respiration at three sandy sites with different permeabilities (German Bight, North Sea). *Limnol Oceanogr* 50:779–792. doi: 10.4319/lo.2005.50.3.0779
- Kleypas JA, Buddemeier RW, Archer D, et al (1999) Geochemical Consequences of Increased Atmospheric Carbon Dioxide on Coral Reefs. *Science* (80-) 284:118–120.
- Klute A, Dirksen C (1986) Hydraulic conductivity and diffusivity: laboratory methods. In: Klute A (ed) *Methods of soil analysis, Part 1: Physical and mineralogical methods*. American Society of Agronomy - Soil Science Society of America, pp 687–734
- Kremling K (1983) Determination of the major constituents. In: Grasshoff K, Ehrhardt M, Kremling K, Almgren T (eds) *Methods of Seawater Analysis*, 2nd edn. Verlag Chemie, Weinheim, pp 247–268
- Krumbein WC, Pettijohn FJ (1938) *Manual of Sedimentary Petrography*. Appleton-Century-Crofts, New York
- Lavigne H, Gattuso J (2011) Seawater carbonate chemistry with R.
- Lewis E, Wallace DWR (1998) Program developed for CO₂ system calculations. In: ORNL/CDIAC-105. Carbon Dioxide Information Analysis Center, Oak Ridge National Laboratory, Oak Ridge, TN,
- Lowe RJ, Falter JL, Monismith SG, Atkinson MJ (2009a) Wave-Driven Circulation of a Coastal Reef–Lagoon System. *J Phys Oceanogr* 39:873–893. doi: 10.1175/2008JPO3958.1
- Lowe RJ, Falter JL, Monismith SG, Atkinson MJ (2009b) A numerical study of circulation in a coastal reef-lagoon system. *J Geophys Res* 114:C06022. doi: 10.1029/2008JC005081
- Lueker TJ, Dickson AG, Keeling CD (2000) Ocean pCO₂ calculated from dissolved inorganic carbon, alkalinity, and equations for K₁ and K₂: validation based on laboratory measurements of CO₂ in gas and seawater at equilibrium. *Mar Chem* 70:105–119.
- Mackenzie FT, Andersson AJ (2011) Biological control on diagenesis: influence of bacteria and relevance to ocean acidification. In: Reitner J, Thiels V (eds) *Encyclopedia of Geobiology*. Springer Verlag, Dordrecht, The Netherlands,
- Mackenzie FT, Andersson AJ (2013) *The Marine Carbon System and Ocean Acidification during Phanerozoic Time*, Geochemica. European Union of Geochemistry
- Mackenzie FT, Garrels RM (1966) Silica-bicarbonate balance in the oceans and early diagenesis. *J Sediment Petrol* 36:1075–1084.
- Mackenzie FT, Kump LR (1995) Reverse weathering, clay mineral formation, and oceanic element cycles (Perspective). *Science* (80-) 270:586–587.
- Mackenzie FT, Ristvet B, Thorstenson DC, et al (1981) Reverse weathering and chemical mass balance in a coastal environment. In: Martin JM, Burton JD, Eisma D (eds) *River Inputs to Ocean Systems*. UNEP and UNESCO, Switzerland, pp 152–187
- Mackenzie FT, Vink S, Wollast R, Chou L (1995) Comparative biogeochemistry of marine saline lakes. In: Lerman A, Imboden D, Gat J (eds) *Physics and Chemistry of Lakes*.

- Springer-Verlag, Berlin, pp 265–278
- Martin TD, Brockhoff CA, Creed JT, Group EMW (1994) Method 200.7 Determination of Metals and Trace Elements in Water and Wastes by Inductively Coupled Plasma-Atomic Emission Spectrometry. Cincinnati, OH
- Massaro RFS, De Carlo EH, Drupp PS, et al (2012) Multiple Factors driving Variability of CO₂ Exchange Between the Ocean and Atmosphere in a Tropical Coral Reef Environment. *Aquat Geochemistry* 18:357–386. doi: 10.1007/s10498-012-9170-7
- Mehrbach C, Culberso CH, Hawley JE, Pytkowic RM (1973) Measurement of apparent dissociation constants of carbonic-acid in seawater at atmospheric pressure. *Limnol Oceanogr* 18:897–907.
- Millero FJ, Pierrot D (1998) A Chemical Equilibrium Model for Natural Waters. *Aquat Geochemistry* 4:153–199.
- Morse J, Zullig J, Bernstein L, et al (1985) Chemistry of calcium carbonate-rich shallow water sediments in the Bahamas. *Am J Sci* 285:147–185.
- Morse JW (1983) The kinetics of calcium carbonate dissolution and precipitation. In: Reeder RJ (ed) *Carbonates: mineralogy and chemistry*. Mineralogical Society of America, Reviews in Mineralogy, pp 227–264
- Morse JW, Andersson AJ, Mackenzie FT (2006) Initial responses of carbonate-rich shelf sediments to rising atmospheric pCO₂ and “ocean acidification”: Role of high Mg-calcites. *Geochim Cosmochim Acta* 70:5814–5830. doi: 10.1016/j.gca.2006.08.017
- Morse JW, Mackenzie FT (1990) *Geochemistry of Sedimentary Carbonates*. Elsevier, Amsterdam, The Netherlands
- Morse JW, Zullig JJ, Iverson RL, et al (1987) The influence of seagrass beds on carbonate sediments in the Bahamas. *Mar Chem* 22:71–83.
- Moulin E, Jordens A, Wollast R (1985) Influence of the Aerobic Bacterial Respiration on the Early Dissolution of Carbonates in Coastal Sediments. In: *Progress in Belgian Oceanographic Research*. p 13
- Pickett M, Andersson AJ (2015) Dissolution Rates of Biogenic Carbonates in Natural Seawater at Different pCO₂ Conditions: A Laboratory Study. *Aquat Geochemistry* 459–485. doi: 10.1007/s10498-015-9261-3
- Plummer LN, Mackenzie FT (1974) Predicting Mineral Solubility From Rate Data: Application to the Dissolution of Magnesian Calcite. *Am J Sci* 274:61–83.
- Precht E, Huettel M (2004) Rapid wave-driven advective pore water exchange in a permeable coastal sediment. *J Sea Res* 51:93–107. doi: 10.1016/j.seares.2003.07.003
- Rao AMF, Polerecky L, Ionescu D, et al (2012) The influence of pore-water advection, benthic photosynthesis, and respiration on calcium carbonate dynamics in reef sands. *Limnol Oceanogr* 57:809–825.
- Ringuet S, Mackenzie FT (2005) Controls on nutrient and phytoplankton dynamics during normal flow and storm runoff conditions, southern Kaneohe Bay, Hawai‘i. *Estuaries* 28:327–337. doi: 10.1007/BF02693916
- Ristvet B (1978) Reverse Weather Reactions Within Recent Nearshore Marine Sediments,

Kaneohe Bay, Oahu. University of Hawai'i

- Sansone FJ, Andrews CC, Buddemeier RW, Tribble GW (1988a) Well-point sampling of reef interstitial water. *Coral Reefs* 7:19–22.
- Sansone FJ, Tribble G, Andrews CC, Chanton JP (1990) Anaerobic diagenesis within Recent, Pleistocene, and Eocene marine carbonate frameworks. *Sedimentology* 37:997–1009.
- Sansone FJ, Tribble GW, Buddemeier RW, Andrews CC (1988b) Time and Space Scales of Anaerobic Diagenesis within a Coral Reef Framework. *Proc 6th Int Coral Reef Symp Aust* 3:367–372.
- Sevadjian J, McManus M, Pawlak G (2010) Effects of physical structure and processes on thin zooplankton layers in Mamala Bay, Hawai'i. *Mar Ecol Prog Ser* 409:95–106. doi: 10.3354/meps08614
- Shamberger KEF, Feely RA, Sabine CL, et al (2011) Calcification and organic production on a Hawaiian coral reef. *Mar Chem* 127:64–75. doi: 10.1016/j.marchem.2011.08.003
- Sharp JH (1974) Improved analysis for “particulate” organic carbon and nitrogen from seawater. *Limnol Oceanogr* 19:984–989.
- Shum KT (1993) The Effects of Wave-Induced Pore Water Circulation on the Transport of Reactive Solutes Below a Rippled Sediment Bed. *J Geophys Resarch Ocean* 98:10289–10301.
- Silverman J, Lazar B, Cao L, et al (2009) Coral reefs may start dissolving when atmospheric CO₂ doubles. *Geophys Res Lett* 36:L05606. doi: 10.1029/2008GL036282
- Smith S V., Kimmerer W, Laws E (1981) Kaneohe Bay sewage diversion experiment: perspectives on ecosystem responses to nutritional perturbation.
- Stoessell RK (1992) Effects of Sulfate Reduction on CaCO₃ Dissolution and Precipitation in Mixing-Zone Fluids. *J Sediment Petrol* 62:873–880.
- Thorstenson DC, Plummer LN (1977) Equilibrium Criteria for Two-Component Solids Reacting with Fixed Composition in an Aqueous Phase - Example: The Magnesian Calcites. *Am J Sci* 277:1203–1223.
- Tomlinson MS, De Carlo EH (2003) The Need For High Resolution Time Series Data To Characterize Hawaiian Streams. *J Am Water Resour Assoc* 39:113–123.
- Tomlinson MS, De Carlo EH, McManus MA, et al (2011) Characterizing the Effects of Two Storms on the Coastal Waters of O'ahu, Hawai'i, Using Data from the Pacific Islands Ocean Observing System. *Oceanography* 24:182–199. doi: 10.5670/oceanog.2011.38
- Tribble GW (1990) Early Diagenesis in a Coral Reef Framework. University of Hawai'i
- Tribble GW (1993) Organic Matter Oxidation and Aragonite Diagenesis in a Coral Reef. *SEPM J Sediment Res Vol.* 63:523–527. doi: 10.1306/D4267B45-2B26-11D7-8648000102C1865D
- Tribble GW, Sansone FJ, Li Y, et al (1988) Material Fluxes from a Reef Framework. *Proc 6th Int Coral Reef Symp Aust* 2:577–582.
- Tribble GW, Sansone FJ, Smith S V. (1990) Stoichiometric modeling of carbon diagenesis within a coral reef framework. *Geochim Cosmochim Acta* 54:2439–2449.

- Tribollet A, Godinot C, Atkinson M, Langdon C (2009) Effects of elevated pCO₂ on dissolution of coral carbonates by microbial euendoliths. *Global Biogeochem Cycles* 23:n/a–n/a. doi: 10.1029/2008GB003286
- Ver LM, Mackenzie FT, Lerman A (1999) Biogeochemical Responses of the Carbon Cycle to Natural and Human Perturbations: Past, Present, and Future. *Am J Sci* 299:762–801.
- Walter LM, Morse JW (1985) The dissolution kinetics of shallow marine carbonates in seawater: A laboratory study. *Geochim Cosmochim Acta* 49:1503–1515.

Chapter 4 THE EFFECTS OF INCREASING OCEAN ACIDIFICATION AND TEMPERATURES ON A BARRIER REEF ECOSYSTEM, KANEHOE BAY, HAWAI‘I

4.1 Abstract

A CO₂-carbonic acid system biogeochemical box model (Coral Reef and Sediment Carbonate Model, *CRESCAM*) of the Kaneohe Bay, Hawai‘i barrier reef flat was developed to determine how increasing temperature and dissolved inorganic carbon (DIC) content of open ocean source waters, resulting from rising anthropogenic CO₂ emissions and ocean acidification (OA), affect the CaCO₃ budget of coral reef ecosystems. *CRESCAM* consists of 17 reservoirs and 59 fluxes, including a surface water column domain, a two-layer permeable sediment domain, and a coral framework domain. Physical, chemical, and biological processes such as advection, carbonate precipitation/dissolution, and net ecosystem production and calcification were modeled. The initial model parameters were constrained by experimental and field data from previous coral reef studies, mostly in Kaneohe Bay over the past 50 years. The field studies include data collected by our research group for both the water column and sediment-porewater system.

The model system, initially in a quasi-steady state condition estimated for the early 21st century, was perturbed using future projections to the year 2100 of atmospheric CO₂ concentrations, temperature, and source water DIC. These perturbations were derived from the most recent (2013) Intergovernmental Panel on Climate Change’s Representative Concentration Pathway (RCP) scenarios, which project CO₂ atmospheric concentrations and temperature anomalies to 2100. A series of model case studies were also performed whereby one or more parameters (e.g., coral calcification response to declining surface water pH) were altered to investigate potential future outcomes. Our model simulations predict that although the Kaneohe Bay barrier reef will likely see a significant decline in net ecosystem calcification (NEC) over

the coming century, it is unlikely to reach a state of net erosion – a result contrary to several global coral reef model projections. Dissolution of carbonate minerals in some areas of the sediments is expected to increase, but the additional alkalinity added to the reef system via this reaction is unlikely to be sufficient to buffer the decrease in pH and saturation state to any significant extent. In addition, we show that depending on the future response of net ecosystem production and NEC to OA and rising temperatures, the surface waters could switch from being a present-day source of CO₂ to the atmosphere to a future sink. This ecosystem specific model can be applied to any reef system where data are available to constrain the initial model state and is a powerful tool for examining future changes in coral reef carbon budgets.

4.2 Introduction

Rising atmospheric carbon dioxide (CO₂) concentrations are widely predicted to cause a decline in ocean pH, a process known as ocean acidification (OA). OA can have negative effects on many marine organisms, specifically calcifying organisms that produce solid calcium carbonate tests or shells. As ocean pH and saturation state with respect to carbonate minerals decreases, biogenic calcification will likely be reduced. This will have drastic implications for ecosystems such as coral reefs, the stability of which is dependent on the corals' ability to accrete calcium carbonate faster than it is removed via mechanical breakdown or carbonate dissolution. While models have been developed to predict the effects of anthropogenic change on the coastal ocean and coral reefs (Ver et al. 1999; Andersson et al. 2005; Silverman et al. 2009; Jury et al. 2013; Andersson et al. 2013), to our knowledge there has not been any development of a detailed physical/biogeochemical model for a complete coral reef ecosystem, including its water column, coral framework, sediment, and porewater domains.

In this paper we present the development and application of a new coral reef ecosystem model, *CRESCAM* (Coral Ref and Sediment Carbonate Model). The *CRESCAM* model is a process driven biogeochemical box model constrained by physical processes and consisting of 17 reservoirs and 59 individual fluxes. In addition, *CRESCAM* employs a 2-layer sediment model including an upper oxic sediment layer where aerobic respiration is the dominant control on saturation state and an anoxic deeper sediment layer where sulfate reduction becomes an important control on saturation state and mineral stability. The 2-layer model – along with interstitial coral framework reservoirs – is unique to *CRESCAM* when compared to previously developed coastal or coral reef biogeochemical models, which either do not include the sediments (e.g., Silverman et al., 2009; Jury et al., 2013) or employ a 1-layer sediment reservoir (e.g., Ver et al., 1999; Andersson et al., 2005). Both the oxic and anoxic layers in *CRESCAM* are divided into five reservoirs containing the carbonate mineral phases of calcite, aragonite, and an average high-magnesian calcite (15 mol% MgCO_3), as well as organic carbon and the interstitial porewater. The model also incorporates physical and chemical bioerosion – processes that are often lumped into a single NEC or gross dissolution term – and aims to understand how these and other important reef processes will respond to decreasing ocean pH, increasing temperature, and possible land use changes.

CRESCAM was developed for the Kaneohe Bay barrier reef flat on Oahu, Hawai'i, but its application may be broader, as it could be coupled to more complex hydrodynamic models, total alkalinity or hydrogen ion budgets, or nutrient dynamic models for nitrogen and phosphorus (e.g., Tanaka and Mackenzie, 2005). We anticipate that any reef ecosystem where the described processes have been measured should be able to utilize the *CRESCAM* framework to investigate local process interactions and future changes from OA and temperature. The Kaneohe Bay

barrier reef (see Figure 4.1) was chosen as the model ecosystem because it is one of the most heavily studied reef ecosystems on the planet, with a wealth of literature to help constrain both the model fluxes and the reservoir sizes (e.g., Roy, 1970; Smith et al., 1981; Kinsey, 1985; Sansone et al., 1988; Tribble et al., 1988; Falter and Sansone, 2000; Shamberger et al., 2011; Drupp et al., 2013). A conceptual diagram of the full model is shown in Figure 4.2.

In the following sections, we describe first the processes considered in *CRESCAM* and the data used to determine reservoir sizes and fluxes at an initial steady-state condition following the standard methodology employed in numerous biogeochemical box model studies (Lerman and Mackenzie 1975; Ver et al. 1999; Andersson et al. 2005; Andersson et al. 2006; Mackenzie et al. 2011). We recognize the reef ecosystem is unlikely to be in a true steady-state condition on various time scales, but determining a *mean steady-state* of the system is a standard practice in the development of biogeochemical box models (Lerman et al. 1975; Ver et al. 1999; Andersson et al. 2006) and is essential to the perturbation analysis presented later in this paper (Sections 4.5-4.7). In broad terms, the overall perturbation analysis utilizes the various future anthropogenic CO₂ gas emissions scenarios – Representative Concentration Pathway (RCP) scenarios – of the Intergovernmental Panel on Climate Change (Intergovernmental Panel on Climate Change 2013) and the resultant changes in sea surface temperature and open ocean absorption of CO₂ and concomitant ocean acidification (OA). These scenarios are used as external forcings in *CRESCAM* to address the following questions concerning the behavior of the Kaneohe Bay crestal barrier reef under rising temperature and open ocean increases in acidity:

- 1) *How will increases in open ocean total inorganic carbon (DIC) and temperature over the next century affect the biogenic calcification bioerosion, and net ecosystem carbonate production on the reef?*

- 2) *Will a decrease in the pH of the overlying seawater – due to increasing pCO₂ – cause a significant increase in the dissolution rates of shallowly buried carbonate sediments, specifically the more soluble magnesian calcite (Mg-calcite) components?*
- 3) *How will dissolution of shallowly buried sediments affect biogeochemical processes on the reef?*
- 4) *How will precipitation and dissolution rates in the sediments change as a function of increasing or decreasing sediment organic matter input?*
- 5) *What effect will changing net ecosystem production (NEP) and net ecosystem carbonate production (NECP) have on air-sea gas exchange?*

These questions are addressed by the model standard run and 14 case studies where one or several initial parameters or equations are varied (e.g., total alkalinity to dissolved inorganic carbon ratios (TA:DICO) in the surface water, photosynthetic response to temperature change, additional input of organic matter to the system) to investigate how the reef will respond under various potential scenarios. Our results show it is unlikely that the future of any single coral reef can be accurately predicted by general models that extrapolate results over many reef ecosystems. Here, we show that the Kaneohe Bay barrier reef – while clearly affected by global change - is unlikely to reach a state of net erosion by the year 2100, in stark contrast to some studies (e.g., Kleypas et al., 2006; Silverman et al., 2009; Silbiger et al., 2014), which predict that all reefs will become net dissolving by the end of the century. This result does not invalidate these studies, but it serves as reminder of the complexities of these systems and proves that no two reef systems are alike.

This paper illustrates the interconnectivity of a coral reef ecosystem and its various physical and biogeochemical feedbacks. *CRESCAM* demonstrates that the fate of coral reefs is highly dependent on how several processes - such as sediment microbial respiration or water column photosynthesis – which are often poorly constrained, will respond to warming and OA.

Changes to the carbon balance of these ecosystems is highly specific to local conditions such as the hydrodynamic flow and residence time, sediment-porewater advection rates, and live coral coverage.

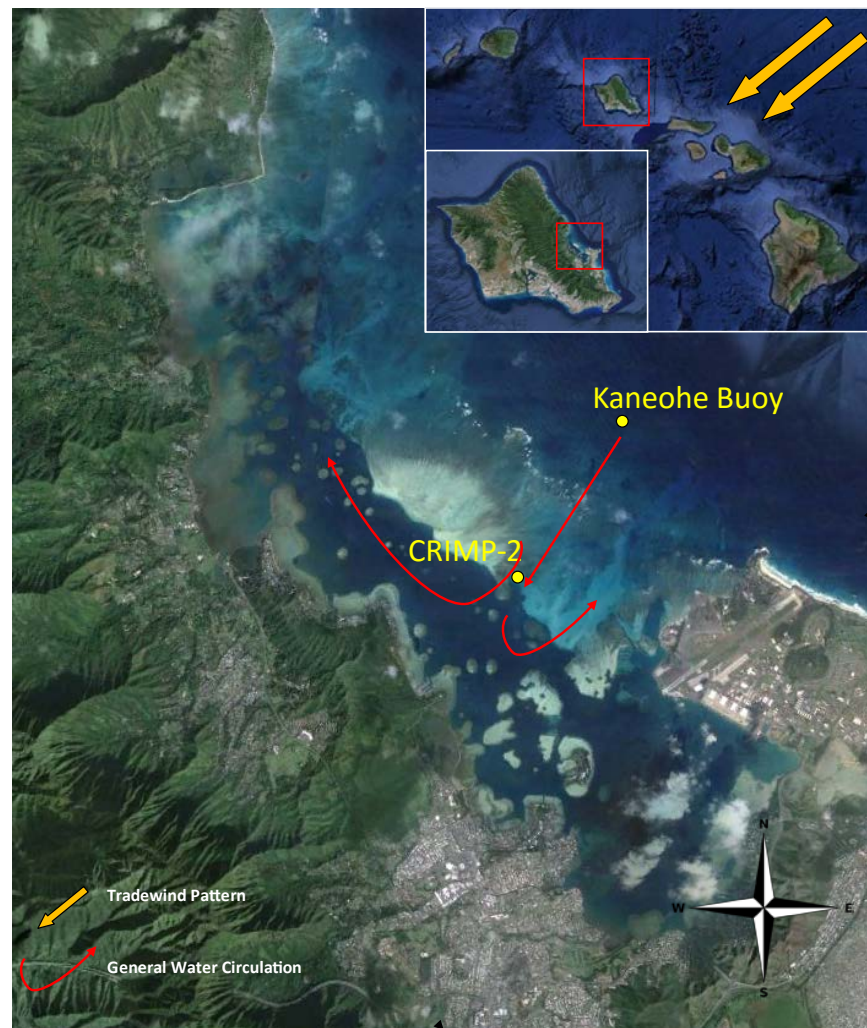


Figure 4.1: *CRESCAM* was developed for the Kaneohe Bay barrier reef, on the windward side of Oahu, Hawai‘i (see map insets). Surface water and porewater data from the CRIMP-2 buoy location were used to constrain some of the model’s initial steady-state conditions. The yellow arrows show the typical tradewind direction. Water circulation (red arrows) is generally linear across the reef flat and exits the bay through two channels on either side of the reef.

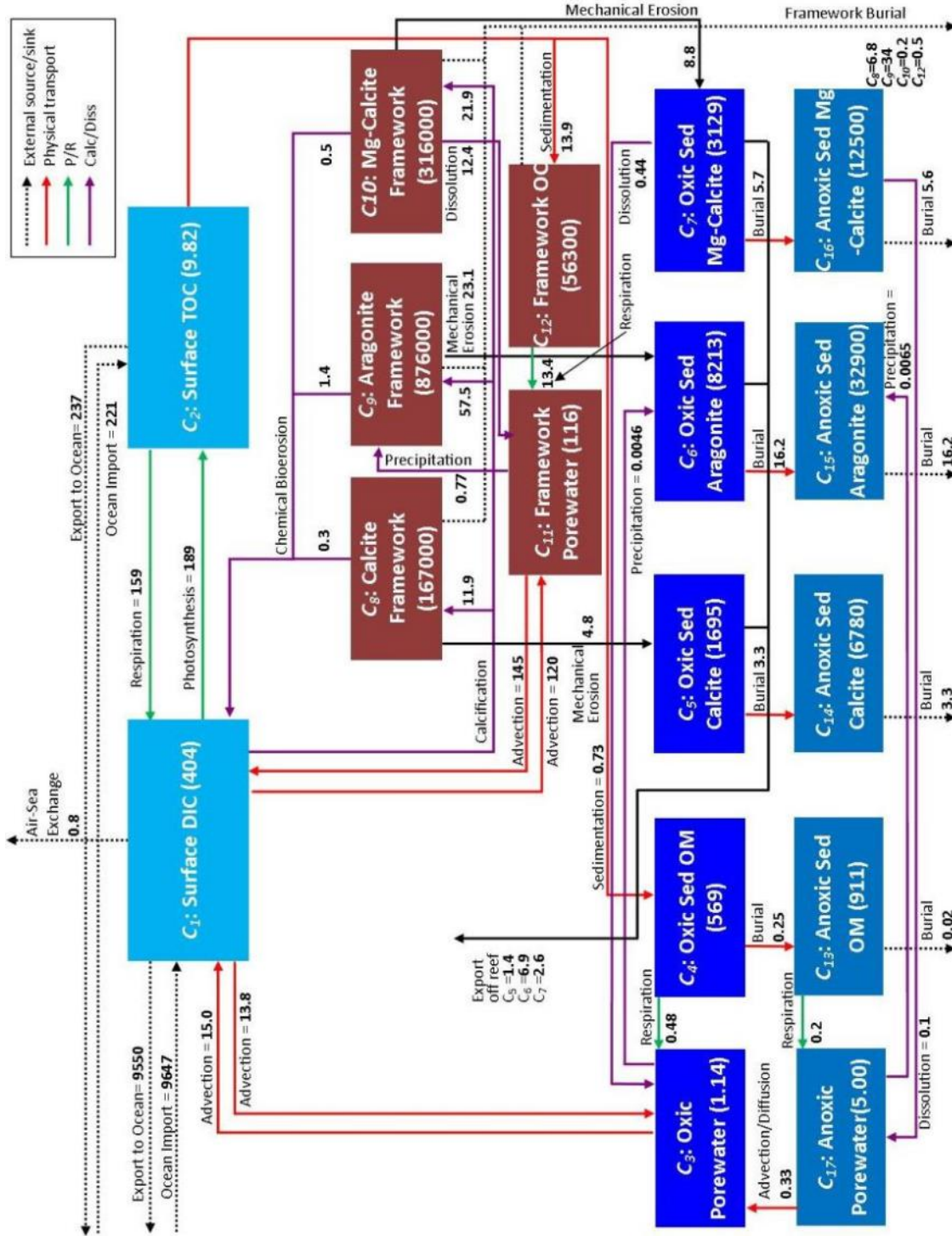


Figure 4.2: Conceptual diagram of *CRESCAM* showing the magnitude of the reservoirs and fluxes. Note the reservoir sizes are reported in 10^5 mol C and the fluxes in 10^7 mol C·yr⁻¹. Note that in this figure, the fluxes may not total exactly zero for each reservoir due to rounding, but significant figures are retained for the actual model run and the net flux for every reservoir is initially zero.

4.3 CRESCAM Model Development

CRESCAM is a carbon biogeochemical box model, constrained by physical processes, which was developed and run in MATLAB. *CRESCAM* uses a variable ordinary differential equation solver - designed for stiff systems (MATLAB function ODE15s) – with a time step (dt) of 0.001 years, to solve a set of 59 ordinary differential equations. The standard mass balance equation being solved is

$$\frac{dM_i}{dt} = \sum_j CF_{ji} - \sum_i CF_{ij} \quad (4.1)$$

where M_i is the mass of the reservoir in question and CF_{ji} is the flux from reservoir j to i , and CF_{ij} is the flux from reservoir i to j . The model assumes well mixed reservoirs and conservation of mass, so the rate of change of any reservoir mass is simply the net flux of carbon in or out of the reservoir. Known processes involving a particular reservoir are defined and represented by the fluxes related to the net mass exchange in the reservoir of interest (see Appendix A). As previously discussed, *CRESCAM* is initially defined as a steady-state system (net flux = 0 at $t = 0$), which is intended to represent our best approximation of the mean state of the natural environment as constrained by observational and experimental data. The initial model values are compiled from the literature from studies and experiments in both Kaneohe Bay and other similar reef ecosystems. The adoption of an initial steady-state allows us to perform perturbation analysis (discussed in Section 4.5) and is the standard procedure for building biogeochemical box models (e.g. Lerman et al. 1975; Ver et al. 1999; Andersson et al. 2003). To ensure *CRESCAM* was in a mathematical initial steady-state condition at $t = 0$ before perturbations, the model was run for three hundred years from present day (2015) to 2315 and no change in any reservoir sizes or flux rates occurred.

4.3.1 CRESCAM Domain and Initial Carbon Reservoirs

CRESCAM is composed of 17 carbon reservoirs in the reef ecosystem, where C_i denotes the reservoir. Reservoir carbon masses are given in terms of moles of carbon (mol C) and range in magnitude from 10^5 to 10^{10} mol. The model is divided into three distinct domains, the free surface water column, the sandy permeable sediments and porewater (subdivided into oxic and anoxic layers), and the hard reef framework and porewater. External carbon sources and sinks for the system are the atmosphere (A), open ocean (O), and deep sediment burial (B). The crestal reef area under consideration (see Figure 4.1) is defined as 2000 m in width (W), 5000 m in length (L), and 2 m in depth (Z), for a total area of 1×10^7 m² and a total volume of 2×10^7 m³. Seawater density ($\rho=1023$ kg·m⁻³ at the start of the model) is calculated continuously based on temperature and salinity. The sandy sediments were assumed to have an areal coverage of 5%, with the rest of the area consisting of reef framework/pavement, based on ArcGIS analysis of satellite imagery from the Shallow Water Benthic Habitat for the Hawaiian Islands survey conducted by NOAA (http://ccma.nos.noaa.gov/ecosystems/coralreef/main8hi_mapping.html). It is important to note that in order to obtain steady-state initial conditions, some values were altered slightly from the reported literature values. Any changes to literature values and the constraints they imply for the system are justified in the following sections. Details of the reservoir mass and flux calculations are given in Tables A1 and A2. A full list of the carbon reservoir sizes is presented in Table 4.1. In the following sections, highlights of these calculations are presented for each domain.

4.3.1.1 Surface water domain

CRESCAM's surface water domain is comprised of reservoirs C_1 and C_2 , surface water dissolved inorganic carbon ($\text{DIC} = \text{HCO}_3^- + \text{CO}_3^{2-} + \text{H}_2\text{CO}_3$) and total organic carbon ($\text{TOC} =$

particulate organic carbon, POC, plus dissolved organic carbon, DOC), respectively (see Figure 4.3). Surface water DIC concentrations are assumed to be evenly distributed across the reef flat, although this is an oversimplification of the system. The DIC concentration of the surface water was estimated to be $1.973 \text{ mmol}\cdot\text{kg}^{-1}$ (Drupp et al., 2013), which compares well with the $1.967 \text{ mmol}\cdot\text{kg}^{-1}$ concentration measured by Shamberger et al. (2011) on the middle of the reef flat. The total reservoir size, C_1 , is $4.04 \times 10^7 \text{ mol C}$.

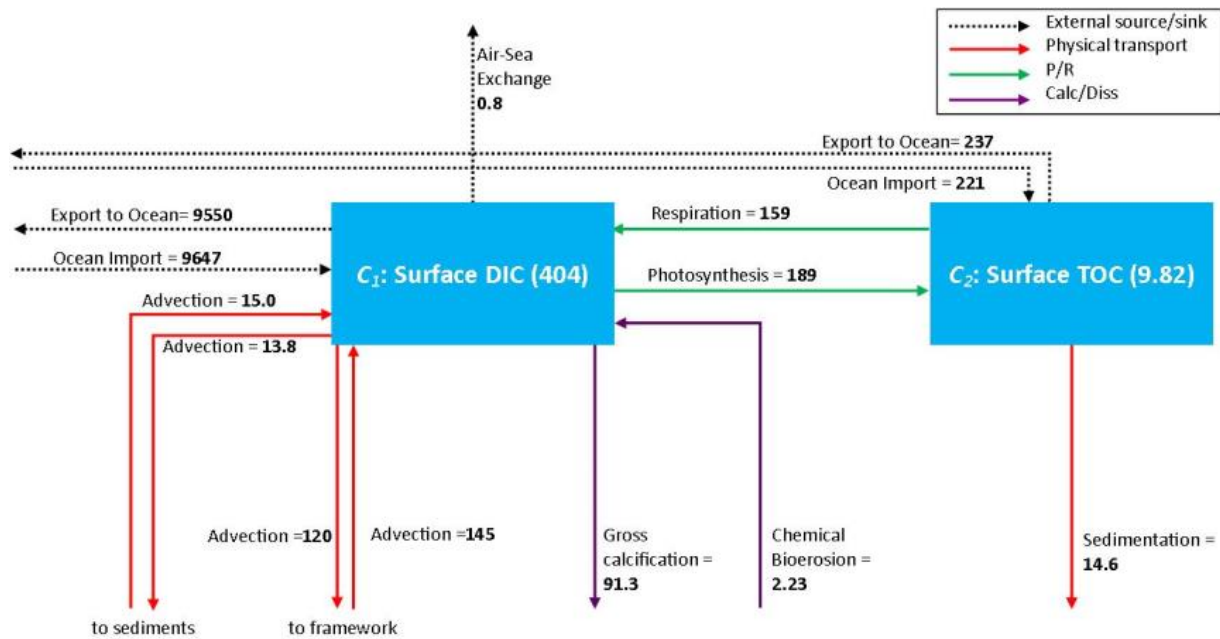


Figure 4.3: Diagram of the surface water reservoirs and fluxes used in *CRESCAM*. Reservoir sizes are given in 10^5 mol C and fluxes are in $10^7 \text{ mol C}\cdot\text{yr}^{-1}$.

The surface water organic carbon reservoir, C_2 , is the sum of both the POC and DOC masses in the reservoir. Because there are no measured DOC values for the reef flat, the average DON concentration of $6.2 \text{ mmol N}\cdot\text{m}^{-3}$ between the exterior and interior reef was adapted from Smith et al. (1981) and Cox et al. (2006), and converted to DOC assuming a 106:16 ratio of carbon to nitrogen (Redfield 1934). Surface water POC was estimated at $8 \text{ mmol C}\cdot\text{m}^{-3}$ based on a range of 4–12 $\text{mmol C}\cdot\text{m}^{-3}$ reported by Cox et al. (2006) between the open ocean and the central bay lagoon. This value is also within range of the POC estimates for an average reef of 2–

127 mmol C·m⁻³ (with a typical POC of ~10 mmol C·m⁻³) reported by Atkinson and Falter (2003). The total mass of the organic carbon reservoir for the reef surface water is equal to 9.82 × 10⁵ mol C.

4.3.1.2 *Permeable sediments domain*

Permeable sediments on the reef flat consist almost exclusively of eroded reef material with less than 1%, by weight, organic carbon and only trivial amounts of terrigenous material (Drupp et al., in review, Chapter 3). The carbonate sediments consist mostly of carbonate sands between 2 mm–63 µm in diameter and are of great interest biogeochemically because seawater is advected through the sediment at rates much faster than by molecular diffusion alone (e.g., Shum, 1993; Falter and Sansone, 2000; Precht and Huettel, 2004; Fram et al., 2014, Drupp et al., in review, Chapter 3). These sandy sediments are split into two layers; an oxic layer from 0–0.2 m sediment depth and an anoxic layer from 0.2–1 m depth. Each layer consists of five reservoirs: porewater DIC; organic carbon (TOC); and the three carbonate minerals phases calcite, aragonite, and Mg-calcite, which are mainly debris from the skeletons, tests, and shells of marine organisms (see Figure 4.4). The calcite reservoir represents pure calcite as well as low Mg-calcite (<3–4 mol% MgCO₃), and the Mg-calcite reservoir represents the biogenic “high” Mg-calcites, typically >13 mol% MgCO₃. These biogenic 13–15% Mg-calcites phases are commonly found in tropical, shoal water carbonate rich sediments and are by far the dominant form of Mg-calcite in reef environments (Garrels and Wollast 1978; Morse and Mackenzie 1990). For the model runs, all Mg-calcite is considered to be 15 mol% when calculating porewater saturation states.

Seawater/porewater saturation states (Ω) with respect to carbonate minerals in *CRESCAM* are calculated with the aqueous carbon dioxide model CO2SYS program (Lewis and

Wallace 1998), using K_1 and K_2 equilibrium constants from Mehrbach et al. (1973), refit by Dickson and Millero, (1987). Mg-calcite Ω were calculated initially in the Seacarb package (“Om function”) for R software (Lavigne et al. 2011; Lavigne and Gattuso 2011) but are continuously calculated during *CRESCAM* simulations within MATLAB using code adapted from CO2SYS and Seacarb (Lewis and Wallace 1998; Lavigne et al. 2011; Lavigne and Gattuso 2011). Details of the calculation can be found in Drupp et al (in review) and Chapter 3. Mg-calcite stoichiometric saturation constants from Plummer and Mackenzie (1974) were used in the Ω calculations. Salinity was assumed to be 35 ($\text{Ca}^{2+} = 10.2 \text{ mmol}\cdot\text{kg}^{-1}$) throughout the model reservoirs and was constant over the length of the simulation. Carbonate ion concentrations $[\text{CO}_3^{2-}]$ were calculated continuously in MATLAB (code adapted from CO2SYS) from total alkalinity (TA) and DIC.

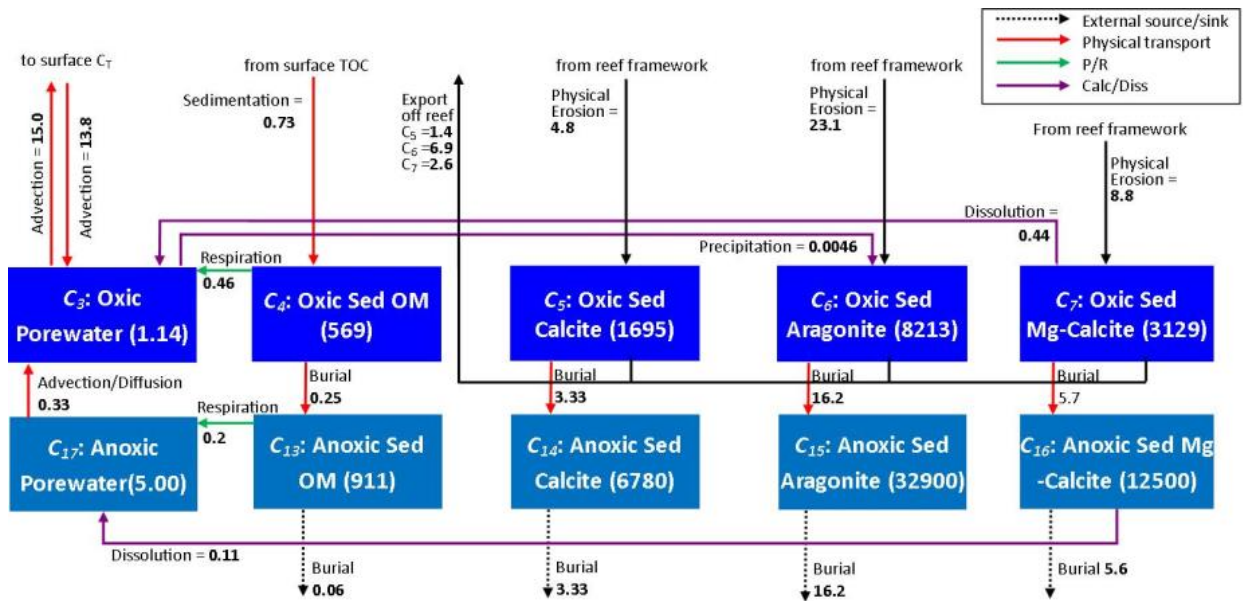


Figure 4.4: Conceptual model for the oxic and anoxic sediment regime used in *CRESCAM*. Reservoir sizes are given in 10^5 mol C and fluxes are in $10^7 \text{ mol C}\cdot\text{yr}^{-1}$.

Porewater DIC concentrations for this model were adapted from Drupp et al. (in review, see Chapter 3, Section 3.1) and were used to determine the porewater carbon reservoir sizes. A

concentration of $2.15 \text{ mmol}\cdot\text{kg}^{-1}$ was used for the oxic layer. Porosity – measured from a core collected at the CRIMP-2 buoy location (Drupp et al., in review, see Chapter 3, Section 3.2) – was estimated to be 52%, resulting in $C_3 = 1.14 \times 10^5 \text{ mol C}$.

The core collected at the CRIMP-2 buoy (Drupp et al., in review; Chapter 3, Section 3.2) had a weight percent (wt. %) total carbon content of 11.73% in the upper 14 cm and an inorganic carbon wt. % of 11.48%, suggesting the sediments are almost entirely CaCO_3 substrates. With these observations, the sediment reservoir composition in *CRESCAM* is considered to be exclusively CaCO_3 phases and organic matter.

An average organic carbon (OC) content of the sediments of wt. % 0.5 was used in *CRESCAM*, and was partially constrained by sedimentation and respiration rates. Suzumura et al. (2002) report a 0.25% organic carbon content in carbonate sands of similar porosity in a coral reef system in Japan. Drupp et al. (in review; Chapter 3, Section 3.2) reports an OC wt. % of ~0.25 at the CRIMP-2 buoy location in Kaneohe Bay. An average sediment density of $2.85 \text{ g}\cdot\text{cm}^{-3}$ was used for model calculations of OC mass based on the density and percent abundance of calcite, aragonite, and Mg-calcite. The organic carbon reservoir, C_4 , was estimated to be $5.69 \times 10^7 \text{ mol C}$.

Sediment reservoir masses for calcite (C_5), aragonite (C_6), and Mg-calcite (C_7) were estimated assuming a respective relative abundance of 13%, 63%, and 24% (Morse and Mackenzie 1990; Morse et al. 2006; Mackenzie and Andersson 2011). Calcite and Mg-calcite have a density of $2.71 \text{ g}\cdot\text{cm}^{-3}$, while aragonite is slightly denser, $2.93 \text{ g}\cdot\text{cm}^{-3}$. Carbonate mineral reservoir sizes were: $C_5 = 1.69 \times 10^8 \text{ mol C}$; $C_6 = 8.21 \times 10^8 \text{ mol C}$; and $C_7 = 3.13 \times 10^8 \text{ mol C}$.

The same calculations as previously mentioned were utilized in the anoxic layer, which was assumed to be 0.2 m – 1m in depth with a porosity of 52%. The DIC of the porewater was

estimated at $2.35 \text{ mmol}\cdot\text{kg}^{-1}$ (Drupp et al., in review, see Chapter 3, Section 3.1), resulting in a reservoir size, C_{17} , of $5.00 \times 10^5 \text{ mol C}$. The organic matter content of the anoxic layer was assumed to be 0.2% (see Drupp et al., in review, Chapter 3, Section 3.2), for a total reservoir size of $9.11 \times 10^7 \text{ mol C}$. Calcite (C_{14}), aragonite (C_{15}), and Mg-calcite (C_{16}) reservoir sizes were 6.78×10^8 , 3.29×10^9 , and $1.25 \times 10^9 \text{ mol C}$, respectively.

4.3.1.3 Reef framework domain

The remaining area of the reef not covered by permeable sands is defined as the reef framework. It is assumed to have a porosity of 50% (Tribble et al. 1990) and covers 95% of the crestral reef environment. The conceptual model for the framework domain is shown in Figure 4.5. The framework is composed of coral skeleton, live coral, coralline algae, abiotic cements, and the interstitial porewater.

The abundances of calcite, aragonite, and Mg-calcite in the reef framework were set equal to their relative proportions in the sediment. This approach also assumes erosional processes affect all components of the reef equally. In reality this is not the case, as more soluble components, such as high Mg-calcite cements and materials are probably more susceptible to mechanical and biochemical erosion (Wisshak et al. 2012; Wisshak et al. 2013; Andersson and Gledhill 2013; Silbiger and Donahue 2015). However, these proportions are not well-constrained in the literature. Using the same method to calculate the reservoir sizes as in the sediments (Section 4.3.1.2), the calcite (C_8), aragonite (C_9), and Mg-calcite (C_{10}) reservoirs for the respective reef framework are 1.67×10^{10} , 8.76×10^{10} , and $3.16 \times 10^{10} \text{ mol C}$. The organic carbon (C_{12}) within the upper meter of the framework was assumed to be 0.5%, resulting in a standing stock of $5.63 \times 10^9 \text{ mol C}$.

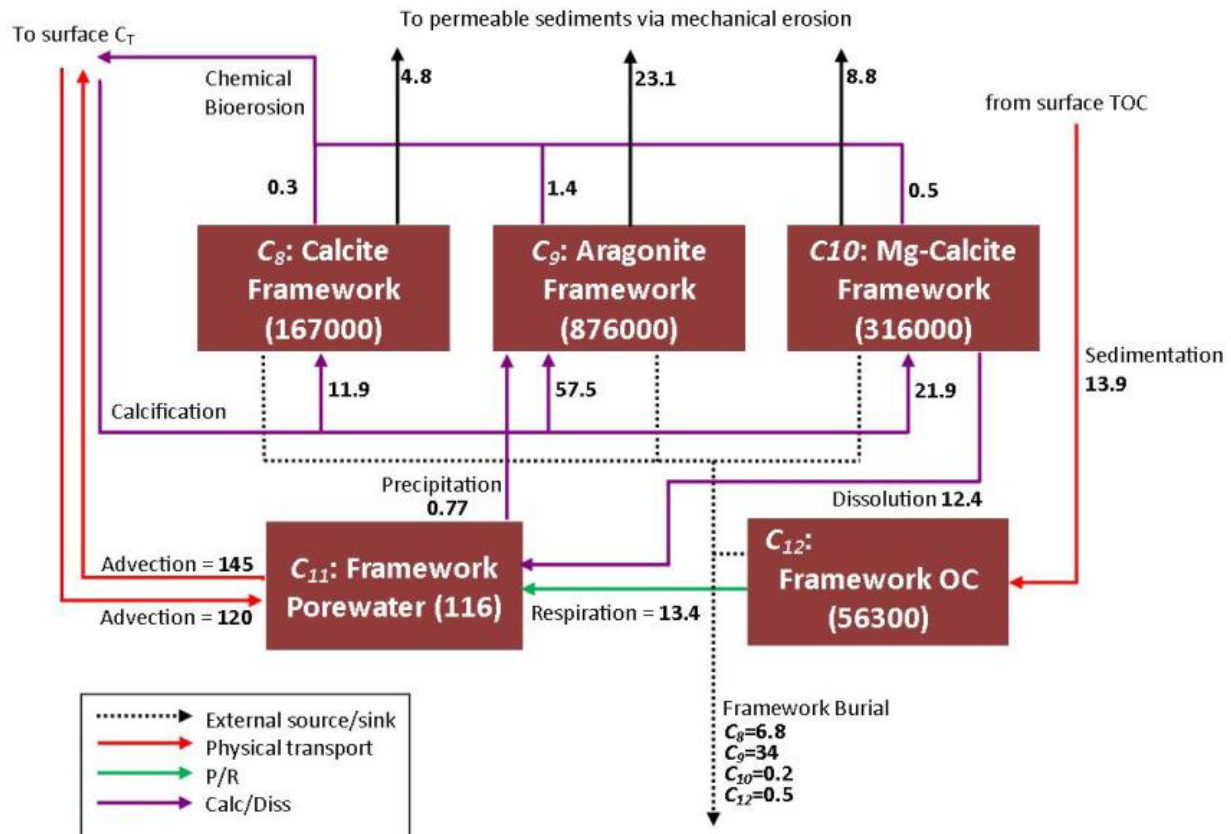


Figure 4.5: Conceptual model for the reef framework domain reservoirs and fluxes at the initial steady-state in *CRESCAM*. Reservoir sizes are given in 10^5 mol C and fluxes are in 10^7 mol C \cdot yr $^{-1}$.

In addition to the solid phase reservoirs, the interstitial porewater reservoir, C_{11} , was derived from a DIC of $2.38 \text{ mmol}\cdot\text{kg}^{-1}$ in the upper meter. This concentration was adopted from measurements made in the upper one meter framework of Checker Reef, a patch reef in the Kaneohe Bay lagoon, by Tribble (1990) and Tribble et al. (1990). While this reef is not a perfect analogue for the barrier reef, very few interstitial framework measurements have been made on reefs and none have been made on the Kaneohe Bay barrier reef, so the Checker Reef data are our best approximation. The concentration is calculated as the average between the overlying surface water and the measurement made at one meter depth and assumes a linear gradient across the porewater (Tribble 1990). This concentration yields a reservoir size of 1.16×10^7 mol C.

Table 4.1: Initial reservoir sizes for *CRESCAM* in 10^5 mol C.

Notation	Reservoir	10^5 mol C
C_1	Surface Water DIC	404
C_2	Surface Water TOC	9.82
C_3	Oxic Porewater DIC	1.14
C_4	Oxic Sediment OC	569
C_5	Oxic Sediment Calcite	1695
C_6	Oxic Sediment Aragonite	8213
C_7	Oxic Sediment Mg-calcite	3129
C_8	Calcite Reef Framework	167000
C_9	Aragonite Reef Framework	876000
C_{10}	Mg-calcite Reef Framework	316000
C_{11}	Reef Framework Porewater	116
C_{12}	Reef Framework OC	56300
C_{13}	Anoxic Sediment OC	911
C_{14}	Anoxic Sediment Calcite	6780
C_{15}	Anoxic Sediment Aragonite	32900
C_{16}	Anoxic Sediment Mg-calcite	12500
C_{17}	Anoxic Porewater DIC	5.00

4.4 *CRESCAM* Initial Carbon Fluxes

CRESCAM consists of 59 fluxes between 17 carbon reservoirs, which are denoted as $CF_{i,j}$, where carbon is transported from reservoir i to j . Fluxes involving the open ocean, atmosphere, and burial of sediments as either sources or sinks of carbon are denoted as i or $j = O, A, \text{ and } B$, respectively. In order to numerically balance the model and achieve steady-state initial conditions, some values were changed slightly from their literature values and significant figures were retained. The derivation of each flux and the mass balance equations for each reservoir can be found in Appendix A, Sections 0 and Appendix AA.3. Note that all fluxes are reported in units of $\text{mol C}\cdot\text{yr}^{-1}$. The following sections (4.4.1-4.4.3) explain the initial steady-state fluxes for each domain (surface water, permeable sediments, framework) and justify any alterations or constraints placed on the experimental and observational data.

4.4.1 Surface water domain

Carbon fluxes involving the surface water DIC and DOC reservoirs can be divided into two categories: physical processes and biogeochemical processes. Physical processes, such as DIC exchange with the open ocean, are controlled by current speeds, porewater velocities (advection rates), ocean-atmosphere gas exchange, and the residence time of the interacting reservoirs. Biogeochemical processes alter fluxes via processes such as photosynthesis, respiration, calcification, and dissolution.

4.4.1.1 Physical processes

The flux of DIC through the surface waters of the reef is dominated by the exchange of seawater with the open ocean. Because the generally southwest current flow across the reef flat is essentially linear (see Figure 4.1), residence time on the reef can be calculated based on current speeds (Lowe et al., 2009a; Lowe et al., 2009b). An average current speed of $15 \text{ cm}\cdot\text{s}^{-1}$ was used - based on measurements and models by Lowe et al. (2009a/b) - equating to an average residence time of 3.7 hr for surface water on the reef flat. This falls within the range of residence times calculated by Shamberger et al. (2011) based on offshore wave heights, using the wave height and current speed relationship of Lowe et al. (2009b). An open ocean DIC concentration of $1.993 \text{ mmol}\cdot\text{kg}^{-1}$ (see Table 4.2) was estimated from Shamberger et al. (2011) and the Hawaiian Ocean Time Series data (Keeling 2004; <http://hahana.soest.hawaii.edu/hot/hot-dogs/>). Shamberger et al. (2011) report DIC outside the bay equals 1.988 and $1.986 \text{ mmol}\cdot\text{kg}^{-1}$ from sampling periods in August 2009 and January/February 2010. The surface HOT samples (<20 m depth), collected 110 km north of Oahu, have a mean nC_T of $2.003 \text{ mmol}\cdot\text{kg}^{-1}$ (normalized to salinity = 35). These concentrations are found in exterior bay waters. The flux, $CF_{0:1}$ of DIC onto the reef from the source waters was determined to be $9.64 \times 10^{10} \text{ mol C}\cdot\text{yr}^{-1}$.

Transport of DIC off the reef, $CF_{1.0}$, was calculated in the same manner as previously discussed, but using an average interior backreef DIC of $1.973 \text{ mmol}\cdot\text{kg}^{-1}$. Drupp et al. (2013) reported an average DIC on the backreef at the CRIMP-2 buoy location, of $1.967 \text{ mmol}\cdot\text{kg}^{-1}$ with a range of $1.851\text{-}2.021 \text{ mmol}\cdot\text{kg}^{-1}$, so the concentration used here falls well within the reported range. In addition, most of the CRIMP-2 samples were collected in the early morning, when DIC is elevated due to nighttime respiration, so we are confident our value is a reasonable estimation of the average back reef mean water chemistry. This concentration yields a transport off the reef of $9.55 \times 10^{10} \text{ mol C}\cdot\text{yr}^{-1}$. Although most of the water leaving the backreef enters the inner lagoon and eventually exits the bay via two channels on either end of the barrier reef (Bathen 1968; Lowe et al. 2009a; Lowe et al. 2009b), some recirculation occurs, primarily onto the forereef. This recirculation is often a function of wind speed and tides and is not considered in the overall exchange rate in this model. The net exchange of DIC is an import of $1.2 \times 10^9 \text{ mol C}\cdot\text{yr}^{-1}$ to the crestal reef flat.

In addition to DIC, open ocean exchange with the reef is also the primary source of total organic carbon (TOC). In *CRESCAM* TOC is considered the sum of dissolved organic carbon (DOC) and particulate organic carbon (POC). Because of the lack of DOC measurements cited in the literature for outside the bay, dissolved organic nitrogen concentrations (DON) were converted to DOC using a C:N ratio of 6.625 (Redfield 1934; Cox et al. 2006). A DON of $6.1 \text{ mmol N}\cdot\text{m}^{-3}$ was used, which was slightly higher than the values measured (although within the error of the measurements) offshore by Smith et al. (1981) and Cox et al. (2006) of $4.5 \text{ mmol N}\cdot\text{m}^{-3}$ and $5.7\pm 0.53 \text{ mmol N}\cdot\text{m}^{-3}$, respectively. Both studies measured DON farther offshore than the reef crest, and due to the production of DON on the reef and the recirculation of water onto the forereef (previously discussed), a higher DON is justified. The POC concentration used to

balance the model was also slightly higher ($75 \text{ mg} \cdot \text{m}^{-3}$) than measured values offshore from Smith et al. (1981) and Cox et al. (2006) of $36 \text{ mg C} \cdot \text{m}^{-3}$ and $54 \pm 14 \text{ mg C} \cdot \text{m}^{-3}$, respectively, again due to organic carbon production on the forereef and the recirculation of interior reef waters (discussed in 4.4.1.1). Recirculation of the reef water occurs as surface water exits the bay via the channels on either side of the reef. Under certain conditions, primarily when winds are weak or blowing from another direction than the typical north east trades, the water flows back on to the forereef, before transiting across the reef flat again. The sum of the DOC and POC import was estimated as $2.21 \times 10^9 \text{ mol C} \cdot \text{yr}^{-1}$.

The open ocean is not the only source of TOC to the reef, as net autotrophy on the reef (see Section 4.4.1.2) produces additional TOC and results in a net export of organic carbon off the reef. TOC export was calculated by using the DOC and POC values from the lagoon edge of the reef. Because of the lack of DOC measurements in the bay, a DON concentration was again converted to DOC. Smith et al. (1981) and Cox et al. (2006) measured DON, in the central bay lagoon, of $5.7 \text{ mmol N} \cdot \text{m}^{-3}$ and $6.9 \pm 0.25 \text{ mmol N} \cdot \text{m}^{-3}$. We chose the average of the two measurements, $6.3 \text{ mmol N} \cdot \text{m}^{-3}$ for calculating a backreef DOC. POC concentrations from Smith et al. (1981) and Cox et al. (2006) were $144 \text{ mg C} \cdot \text{m}^{-3}$ and $140 \pm 11 \text{ mg C} \cdot \text{m}^{-3}$, respectively. A POC of $100 \text{ mg C} \cdot \text{m}^{-3}$ ($8.34 \text{ mmol C} \cdot \text{m}^{-3}$) was used in order to balance the total organic carbon flux. Although this is lower than the literature values, it does agree with the POC concentration for an average reef (range 2–127, typical $\sim 10 \text{ mmol C} \cdot \text{m}^{-3}$) described by Atkinson and Falter (2003) as discussed in Section 4.3.1.1, and inputs of additional POC from photosynthesis within the lagoon and terrestrial runoff likely elevate the measured POC values above what is present on the reef flat. Overall, the flux of TOC off the reef equaled $2.37 \times 10^9 \text{ mol C} \cdot \text{yr}^{-1}$, for a net export of $1.6 \times 10^8 \text{ mol C} \cdot \text{yr}^{-1}$.

The remainder of the TOC not exported from the reef or consumed via respiration is available for sedimentation. A sedimentation rate of $40.2 \text{ mmol C} \cdot \text{m}^{-2} \cdot \text{d}^{-1}$ was based on measurements made in the bay by Taguchi (1982), who reported rates of $38 \text{ mmol C} \cdot \text{m}^{-2} \cdot \text{d}^{-1}$. This rate yields an annual flux in *CRESCAM* of $7.34 \times 10^6 \text{ mol C} \cdot \text{yr}^{-1}$ to the sediments, assuming a 5% areal coverage. Organic carbon sedimentation is approximately 2.8 wt. % of total carbon sedimentation.

The surface water also exchanges DIC with the interstitial porewater of both the reef framework and the permeable sandy sediments via advection. Molecular diffusion across these interfaces does occur, but its rate is several orders of magnitude smaller than advective transport (e.g., Precht and Huettel, 2004; Fogaren et al., 2013; Fram et al., 2014; Drupp et al., in review/Chapter 3). Therefore, molecular diffusion is not considered in terms of the surface water exchange with the upper sediments. Advection between the permeable sediments and the surface water was estimated to be $3.0 \text{ cm} \cdot \text{hr}^{-1}$. An average porewater velocity of $3.5 \text{ cm} \cdot \text{hr}^{-1}$ in permeable sands was modeled by Shum (1993) and several studies on the south shore of Oahu at the Kilo Nalu observatory have measured and modeled porewater transport velocities in the upper 10–20 cm (Hebert et al. 2007; Fram et al. 2014). These studies at Kilo Nalu were at a water depth of 10–14 m, and the environment experiences larger wave activity than the backreef of Kaneohe. Hebert et al. (2007) report porewater velocities of $0\text{--}5 \text{ cm} \cdot \text{hr}^{-1}$ at 15 cm depth at Kilo Nalu. These experiments were performed using fluorescein dye under average wave heights of 0.3–1.5 m, slightly higher than would be expected on the Kaneohe reef flat. Fram et al. (2014) buried a miniature temperature chain in the upper sediments (0–20 cm) at the Kilo Nalu site and used temperature as a proxy for advection rates. The near bed velocities in their study ranged from 15 to $> 30 \text{ cm} \cdot \text{s}^{-1}$ with an average porewater velocity of $7.5 \text{ cm} \cdot \text{hr}^{-1}$. Mean current speeds

on the barrier reef were assumed to be $15 \text{ cm}\cdot\text{s}^{-1}$, which would result in near bed velocities and advection rates on the lower end of those measured by Fram et al. (2014). It is important to note that most studies of advection in sandy carbonate sediments occur at locations with sand ripples created by wave action, which can increase advection rates by facilitating pumping due to differences in the pressure gradient between the crests and troughs of ripples (Shum 1993; Precht and Huettel 2004). Ripples are not present at most locations in the sandy sediments on the reef flat, so porewater advection velocities are likely to be on the lower end of those reported in the literature for sediments with similar permeability, porosity, and near bed velocity.

Table 4.2: DIC concentrations used to calculate initial steady-state fluxes and reservoirs in *CRESCAM*.

Reservoir	DIC ($\text{mmol}\cdot\text{kg}^{-1}$)
C_1 , surface water	1.973
O , ocean	1.992
C_3 , oxic porewater	2.150
C_{11} , framework porewater	2.385
C_{17} , anoxic porewater	2.350

Using a mean advection rate of $3.0 \text{ cm}\cdot\text{hr}^{-1}$ results in a residence time of 6.7 hours for the upper 20 cm of the sediment column. The flux of DIC into the sediments, based on an average surface water DIC of $1.973 \text{ mmol}\cdot\text{kg}^{-1}$ (see Table 4.2; Shamberger et al., 2011; Drupp et al., 2013), was determined to be $1.38 \times 10^8 \text{ mol C}\cdot\text{yr}^{-1}$. The flux of DIC out of the sediments was $1.50 \times 10^8 \text{ mol C}\cdot\text{yr}^{-1}$, assuming a DIC of $2.150 \text{ mmol}\cdot\text{kg}^{-1}$ (Drupp et al., in review, see Chapter 3 add section number), resulting in a net flux out of the sediments of $1.2 \times 10^7 \text{ mol C}\cdot\text{yr}^{-1}$.

The reef surface water also exchanges with the framework porewater via advection. The residence time for the upper meter of framework was estimated to be ~ 3 days. This is consistent with findings from multiple experiments on Checker Reef, a patch reef in Kaneohe Bay, by Tribble et al. (1988) and Tribble (1990), where mean residence times averaged ~ 2.5 days based on various methods including tracers (radon and salinity), hydrostatic pressure measurements,

and wave pumping models. The range of residence times in the upper meter of the framework was 1–4.5 days depending on the method. An average DIC of $2.384 \text{ mmol}\cdot\text{kg}^{-1}$ was taken from the data reported for the upper 1 m of framework on Checker Reef (Tribble et al. 1990; Tribble 1990) and extrapolated to the framework of the crestal portion of the barrier reef, which yielded an export of DIC to the surface water of $1.45 \times 10^9 \text{ mol C}\cdot\text{yr}^{-1}$. A DIC of $1.973 \text{ mmol}\cdot\text{kg}^{-1}$ (as previously discussed) was used to calculate a flux from the surface water into the framework of $1.20 \times 10^9 \text{ mol C}\cdot\text{yr}^{-1}$, creating a net flux of $2.5 \times 10^8 \text{ mol C}\cdot\text{yr}^{-1}$ out of the framework.

The final surface water flux due to physical processes is air-sea CO_2 gas exchange. This accounted for $8.03 \times 10^6 \text{ mol C}\cdot\text{yr}^{-1}$ out of the surface water into the atmosphere, equaling to an areal flux of $0.80 \text{ mol C}\cdot\text{m}^2\cdot\text{yr}^{-1}$. The model assumes a U_{10} wind speed of $5.2 \text{ m}\cdot\text{s}^{-1}$, based on the average speed measured in Kaneohe Bay from 2008-2014 (updated from Drupp et al. 2013, Terlouw et al., in prep). A piston velocity (k_{600}) was calculated based on the wind speed using the parameterization from Ho et al. (2006) and Equation 4.2.

$$k_{600} = 0.266 \times (U_{10})^2 \quad (4.2)$$

The overall exchange was calculated using Equation 4.3.

$$F = k\alpha(p\text{CO}_{2\text{sw}} - p\text{CO}_{2\text{air}}) \quad (4.3)$$

where k has been modified to ambient temperature and salinity conditions and α is the solubility of CO_2 in seawater (Wanninkhof 1992; Drupp et al. 2011; Massaro et al. 2012). The $p\text{CO}_2$ of seawater was $440 \text{ }\mu\text{atm}$ - the mean value measured at the CRIMP-2 location (Drupp et al. 2013) - and the $p\text{CO}_{2\text{air}}$ of the atmosphere was $399 \text{ }\mu\text{atm}$ (Terlouw et al., in prep). Our estimate is in line with other measurements made both for Kaneohe Bay and other coral reef ecosystems (see Table 4.3). The gas exchange rates previously reported by Drupp et al. (2013) are slightly higher because the $p\text{CO}_2$ measurements were made on the backreef where $p\text{CO}_{2\text{sw}}$ is higher than the

average for the reef. Using a slightly lower $p\text{CO}_{2\text{sw}}$ for the average reef surface water results in a lower $\Delta p\text{CO}_2$. An additional check on the average $p\text{CO}_{2\text{sw}}$ used in *CRESCAM* was performed by calculating the CO_2 -carbonic acid system (from $p\text{CO}_2$ and DIC), which yielded values of $\text{pH}=7.99$ (total scale) and total alkalinity (A_T) = $2.242 \text{ mmol}\cdot\text{kg}^{-1}$. These values are consistent with measurements made on the Kaneohe reef flat (Shamberger et al. 2011; Drupp et al. 2013) and lend support to the values adopted in *CRESCAM*.

Table 4.3: Annualized air-sea gas exchange fluxes for several coral reef ecosystems.

Site	Flux ($\text{mol C}\cdot\text{m}^{-2}\cdot\text{yr}^{-1}$)	Reference
<i>CRESCAM</i> model	0.8	This study
Kaneohe Bay - Southern Sector (2005-2008)	1.80	(Massaro et al. 2012)
Kaneohe Bay - CRIMP-2 (2008-2011)	1.15	(Drupp et al. 2013)
Kaneohe Bay - entire bay	1.45	(Fagan and Mackenzie 2007)
Hog Reef, Bermuda	1.2	(Bates et al. 2001)
Okinawa Reef flat, Japan	1.8	(Ohde and Van Woesik 1999)

4.4.1.2 Biogeochemical processes

The remaining processes affecting fluxes for the reef flat surface water are biogeochemical in nature, as opposed to physical forcings. Gross photosynthesis ($\text{CF}_{1:2}$) and respiration ($\text{CF}_{2:1}$) represent the largest biologically controlled fluxes altering the DIC pool in the surface waters. The model does not attempt to separate the effects of pelagic photosynthesis or respiration from the benthic processes, so all rates used include both water column and benthic processes (see Ver et al. 1999). In the most recent publication on gross photosynthesis and respiration for the Kaneohe Bay barrier reef ecosystem, Falter et al. (2008) reported estimates of $440 \text{ mmol}\cdot\text{m}^{-2}\cdot\text{d}^{-1}$ and $435 \text{ mmol}\cdot\text{m}^{-2}\cdot\text{d}^{-1}$, respectively, calculated from measurements made at one location on the reef. These values were used as an initial starting point in *CRESCAM*. The photosynthetic rate was then adjusted to achieve model balance in terms of other fluxes to 520

$\text{mmol}\cdot\text{m}^{-2}\cdot\text{d}^{-1}$ ($6.2\text{ g C}\cdot\text{m}^{-2}\cdot\text{d}^{-1}$) for a P/R autotrophic system relationship of 1.2. These specific area rates equate to annual fluxes for the entire reef of $\text{CF}_{1:2} = 1.89 \times 10^{10}\text{ mol C}\cdot\text{yr}^{-1}$ and $\text{CF}_{2:1} = 1.59 \times 10^{10}\text{ mol C}\cdot\text{yr}^{-1}$.

The photosynthetic rate adapted for the model and reported by Kinsey (1979) falls between the values of $5.9\text{ g C}\cdot\text{m}^{-2}\cdot\text{d}^{-1}$, for the Kaneohe barrier reef, and $7.0\text{ g C}\cdot\text{m}^{-2}\cdot\text{d}^{-1}$, for general reef communities. An extensive list of community metabolic rates in coral reef systems is presented in Kinsey (1985), in which gross photosynthesis ranged from $2\text{--}19\text{ g C}\cdot\text{m}^{-2}\cdot\text{d}^{-1}$ for “complete reef systems” and “reef –flat coral/algal zones,” with a mean of $7.45\text{ g C}\cdot\text{m}^{-2}\cdot\text{d}^{-1}$. The gross respiration used in *CRESCAM*, $435\text{ mmol}\cdot\text{m}^{-2}\cdot\text{d}^{-1}$ ($5.2\text{ g C}\cdot\text{m}^{-2}\cdot\text{d}^{-1}$), falls in the range - and is comparable to the mean - of respiration rate ($2.3\text{--}17\text{ g C}\cdot\text{m}^{-2}\cdot\text{d}^{-1}$; mean of $6.8\text{ g C}\cdot\text{m}^{-2}\cdot\text{d}^{-1}$) for “complete reef systems” and “reef – flat coral/algal zones” reported by Kinsey (1985).

There is some debate over whether the Kaneohe Bay barrier reef is net autotrophic or net heterotrophic (e.g. Shamberger et al. 2011), but for this model it is considered to be net autotrophic. Atkinson and Falter (2003) report most reef systems have a P/R of $\sim 1\text{--}1.1$, but areas abundant in algae and exposed to continuous seawater flow (like the Kaneohe barrier reef) can have a P/R greater than 1. In addition, Kinsey (1985) reported P/R ratios of between $1\text{--}1.6$ for reef-flat coral/algal zones, and Kinsey (1979) determined a P/R for a central Kaneohe Bay patch reef of 1.2. Coral coverage on the barrier reef is $\sim 20\text{--}30\%$, and much of the reef flat is dominated by turf grass and algae (Falter et al. 2008; Shamberger et al. 2011), so it fits in Kinsey’s category of “reef-flat coral/algal zone.” Shamberger et al. (2011) showed the reef switching between net autotrophy and net heterotrophy with a P/R of ~ 1 , but the study was performed in an area of higher than average coral coverage on a very short time scale and is unlikely to be representative of the entire reef. Thus, the calculated net autotrophy used in *CRESCAM* for the crestal Kaneohe

Bay barrier reef, both in terms of information on the net trophic status of world reefs and specifically determined for the Kaneohe Bay barrier reef, is considered to be a reasonable estimate.

The final biogeochemical processes altering surface water DIC are biogenic calcification and dissolution from chemical bioerosion. Although Kaneohe Bay surface waters are supersaturated with respect to aragonite ($\Omega_{ar} \sim 3$), and hence also calcite (including up to 3–4 mol% $MgCO_3$), abiotic precipitation in sandy reef sediments and in near surface framework is insignificant compared to biogenic calcification. Aragonite and calcite are unlikely to be found as direct abiotic precipitates because of inhibition from high seawater magnesium concentrations (Berner et al. 1978). Biogenic gross calcification was estimated to be $250 \text{ mmol CaCO}_3 \cdot \text{m}^{-2} \cdot \text{d}^{-1}$ ($9 \text{ kg CaCO}_3 \cdot \text{m}^{-2} \cdot \text{yr}^{-1}$) based on net ecosystem calcification (NEC) rates determined by Shamberger et al. (2011) via the alkalinity anomaly technique (Smith and Key 1975). During the study by Shamberger et al. (2011), NEC ranged from $108\text{--}371 \text{ mmol CaCO}_3 \cdot \text{m}^{-2} \cdot \text{d}^{-1}$ ($4\text{--}13.5 \text{ kg CaCO}_3 \cdot \text{m}^{-2} \cdot \text{yr}^{-1}$). Kinsey (1985) reported an average net gain of CaCO_3 for reef flats of $4 \text{ kg CaCO}_3 \cdot \text{m}^{-2} \cdot \text{yr}^{-1}$. While the Kaneohe reef flat NEC estimate is slightly higher than many systems listed in Kinsey (1985), Smith et al. (1981) estimate a CaCO_3 accumulation of $8.9 \text{ kg} \cdot \text{m}^{-2} \cdot \text{yr}^{-1}$ for reefs in central Kaneohe Bay, and Kinsey (1979) measured rates of $10\text{--}12 \text{ kg} \cdot \text{m}^{-2} \cdot \text{yr}^{-1}$ in Kaneohe patch reefs, which are expected to be higher due to a lower export rate than the barrier reef.

The calcification rate of $250 \text{ mmol CaCO}_3 \cdot \text{m}^{-2} \cdot \text{d}^{-1}$ in *CRESCAM* for the crestal portion of the Kaneohe Bay barrier reef yields an annual flux of $9.13 \times 10^8 \text{ mol C} \cdot \text{yr}^{-1}$ for the entire reef flat. This total was partitioned to the model's reef framework in the same relative abundances as the mineral phases present in the permeable sediments (Section 4.3.1.3), where calcite, aragonite,

and Mg-calcite are found in relative proportions of 13%, 63%, and 24%, respectively. Individual fluxes calculated for each framework component are detailed in Table A.1.

Gross calcification is offset slightly by bioerosion, which is the summation of the processes of chemical dissolution and physical destruction of reef framework via a variety of grazing and reef-boring organisms such as echinoids, fish, sponges, and euendolithic algae. These organisms contribute to the mechanical and chemical breakdown of the existing carbonate structures resulting in both particulate inorganic carbon (PIC) and DIC. In *CRESCAM*, the released DIC is returned to the surface water, and the PIC is transported to the permeable sediments, as well as exported off the reef. The erosional process which returns DIC to the water column is referred to as chemical bioerosion (e.g. Tribollet and Golubic 2005; Andersson and Gledhill 2013). The process of mechanical bioerosion producing PIC will be discussed in Section 4.4.3. Tribollet (2008) and Tribollet et al. (2009) measured bioerosional dissolution rates, on blocks of *Porites sp.* coral substrates, due to euendolithic algae ranging from 0.1-1.4 kg $\text{CaCO}_3 \cdot \text{m}^{-2} \cdot \text{yr}^{-1}$ on the Great Barrier Reef (GBR) and 0.31 kg $\text{CaCO}_3 \cdot \text{m}^{-2} \cdot \text{yr}^{-1}$ in Kaneohe Bay. The highest rates occurred on oligotrophic reefs, as compared to inshore reefs where higher rates of sedimentation and turbidity limit the photosynthetic ability of the algae. Fang et al. (2013) measured bioerosion rates – both mechanical and chemical - of an excavating sponge, *Cliona orientalis*, under varying temperature and pCO_2 scenarios. Under the experimental conditions representative of present day - very similar to the conditions on the Kaneohe barrier reef ($\text{pCO}_2 = 455 \mu\text{atm}$ and temperature = 24-26 °C) - chemical bioerosion by the sponges was 0.29 kg $\text{CaCO}_3 \cdot \text{m}^{-2} \cdot \text{yr}^{-2}$. The chemical bioerosion rate increased with increasing pCO_2 while the mechanical erosion rate remained almost constant under the various treatments. Fang et al. (2013) suggest increasing ocean pCO_2 may lead to a shift of erosional processes, from being

mechanically dominated to chemically dominated under future emissions scenarios, as lower pH conditions make it relatively easier for bioeroding organisms to breakdown carbonate substrates. In *CRESCAM*, a bioerosion rate from eunendolithic algae and sponges of $0.60 \text{ kg} \cdot \text{m}^{-2} \cdot \text{yr}^{-1}$ was estimated by combining the rates for individual organisms from Tribollet (2008), Tribollet et al. (2009), and Fang et al. (2013) to obtain a total ecosystem rate.

The breakdown of substrates from these boring organisms (microborers) creates both PIC (“chips”) and DIC. Production of DIC is estimated as 2-75% of the total bored materials with 25-98% being released as chips. For *CRESCAM* we chose a release of 40% as DIC (60% resulting in chips). According to Fang et al. (2013) approximately 40% of net erosion of *C. orientalis* is due to chemical bioerosion. Further discussion regarding the choice of this value can be found in Section 4.4.2. The total flux of DIC to the surface water due to chemical bioerosion was estimated as $2.28 \times 10^7 \text{ mol C} \cdot \text{yr}^{-1}$. As previously discussed, this total flux was apportioned according to the relative abundance of carbonate mineral phases in the sediments and framework (Sections 4.3.1.2 and 4.3.1.3).

4.4.2 Permeable sediments domain

4.4.2.1 Physical Processes

The main flux controlled by physical processes in the mass balance of the oxic (C_3) and anoxic porewater reservoirs (C_{17}) is the transport of anoxic porewater DIC to the shallower oxic layer because of the gradient in DIC between these two reservoirs ($\Delta\text{DIC} = 0.20 \text{ mmol} \cdot \text{kg}^{-1}$). Due to the relatively slower rate of advection in the deeper layer, molecular diffusion, calculated from Fick’s 1st Law, plays an increasingly more important role (albeit still less important than advection) in the transport of DIC from the anoxic to the oxic sediment layer. The flux can be calculated as the combination of the Fickian diffusion and the advective rate in Equation 4.4,

$$CF_{173} = -D \frac{\partial C_T}{\partial z} + uDIC \quad (4.4)$$

where $-D \frac{\partial C_T}{\partial z}$ is the diffusional flux, D , is the diffusion coefficient of HCO_3^- in units of $10^{-5} \text{ cm}^2 \cdot \text{s}^{-1}$ and is equal to 1.335, at $T = 25^\circ\text{C}$ (Berner 1980), and $\frac{\partial C_T}{\partial z}$ is the concentration gradient between the oxic and anoxic layers and $uDIC$ is the net advection. The concentration of DIC in the anoxic layer was taken as $2.35 \text{ mmol} \cdot \text{kg}^{-1}$ (Drupp et al., in review; Chapter 3) and the Fickian molecular diffusion transport was calculated to be $2.22 \times 10^{-3} \text{ mol C} \cdot \text{yr}^{-1}$. For the purposes of mass balance, an average residence time of 112 hrs (4.6 d) was assumed. This residence time is similar to the residence time of the upper meter of the reef framework previously reported by Tribble (1990). The DIC advective flux was then calculated to be $3.28 \times 10^6 \text{ mol C} \cdot \text{yr}^{-1}$. Even with a relatively long residence time, advection was still three orders of magnitude larger than molecular diffusion, although considerably less than the difference between the advection and diffusion rates for the surface water-oxic porewater exchange. The total exchange was the sum of the advective and diffusive fluxes, $3.29 \times 10^6 \text{ mol C} \cdot \text{yr}^{-1}$.

The other primary physical process controlling the sediment reservoirs and fluxes is the sedimentation of particulate inorganic carbon (PIC) and subsequent burial of sediments into the anoxic and deeper layers of the sediment column. The rates of these processes are dependent on both the bioerosion rates and the export of PIC from the reef. Approximately 90% of coral reef sediments are produced by reef eroders (Hubbard et al. 1990). As discussed in Section 4.4.1.2, *CRESCAM* assumes that 60% of the erosion of reef framework due to boring organisms, such as sponges and euendolithic algae, results in the production of “chips” or PIC, contributing $3.42 \times 10^7 \text{ mol C} \cdot \text{yr}^{-1}$ to the sediments.

In addition, mechanical erosion - due to the grazing of organisms such as echinoids and fish, as well as physical breakdown from waves – also produces PIC. A total mechanical erosion rate (from abiotic physical breakdown and grazing organisms) was based on data from Tribollet et al. (2006) and Fang et al. (2013) and estimated to be $3.5 \text{ kg CaCO}_3 \cdot \text{m}^{-2} \cdot \text{yr}^{-1}$ equivalent to an annual rate of $3.32 \times 10^8 \text{ mol C} \cdot \text{yr}^{-1}$ when extrapolated over the reef framework area. When combined with the PIC produced by microborers, the total PIC production is estimated as $3.66 \times 10^8 \text{ mol C} \cdot \text{yr}^{-1}$. Consistent with this value, Tribollet et al. (2002) estimated a mean grazing rate of $2.78 \text{ kg CaCO}_3 \cdot \text{m}^{-2} \cdot \text{yr}^{-1}$ from a study at six sites on the GBR and determined that approximately 70% of the total bioerosion was due to grazing. In *CRESCAM*, mechanical erosion accounts for approximately 85% of total reef erosion. *CRESCAM* uses a slightly higher rate than the literature values because it combines grazing and boring with abiotic physical breakdown of the reef substrates.

A portion of the PIC produced by erosion is exported off the reef flat, while the remainder is deposited to the sediments. *CRESCAM* assumes an export rate of ~30%, with 70% of the eroded PIC accumulating in the sediments. Export rates of PIC from reef flats are poorly constrained in the literature, but Hubbard et al. (1990) report that more than half of all PIC production remains on the reef flat. The total mechanical erosion and export rates in *CRESCAM* were chosen to fit constraints of organic burial rates and total sedimentation rates. The sedimentation of organic carbon was set to be ~3 wt% of total sedimentation to the upper sediment layer, with a burial of 0.98 wt% organic carbon to the deeper anoxic sediments. These values were estimated based on analysis of a sediment core from the CRIMP-2 location (Drupp et al., in review; Chapter 3). The PIC sedimentation rate is equal to $\sim 3.75 \text{ cm} \cdot \text{yr}^{-1}$ ($2.56 \times 10^8 \text{ mol CaCO}_3 \cdot \text{yr}^{-1}$). Roy (1970) estimated a carbonate sedimentation rate (from reef produced PIC) of

2.9 cm·yr⁻¹ for the Kaneohe Bay central lagoon based on sediment core data, so it is reasonable to estimate that the sedimentation on the reef would be higher. Sedimentation rates were partitioned into the carbonate reservoirs based on the relative abundances of the mineral phases as previously described. The mass balance for each oxic carbonate sediment reservoir (C₅, C₆, and C₇) was defined for steady-state as

$$P_x + FE_x = D_x + B_x + E_x \quad (4.5)$$

where x is the mineral phase, P is precipitation, FE is framework mechanical erosion (PIC production), D is dissolution, B is burial to the anoxic layer, and E is export off the reef (set to 30% of the mechanical erosion rate). Rearranging Equation 4.5, a burial rate was calculated

$$B_x = P_x + FE_x - D_x - E_x \quad (4.6)$$

Burial of organic carbon from the oxic to anoxic layer was simply the difference between the sedimentation rate of OC from the surface water and the oxic layer respiration rate. In the anoxic layer, organic carbon burial was the difference between the supply from above and the respiration rate. In the anoxic carbonate sediments

$$B_x = P_x + T_x - D_x \quad (4.7)$$

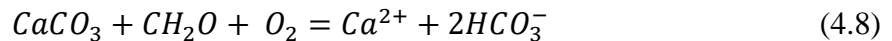
where B is now burial rate to the deeper sediments (>1 m depth), and T is the transfer of sediment from the oxic layer into the anoxic layer.

4.4.2.2 Biogeochemical Processes

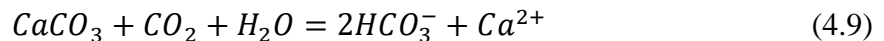
The permeable sediments include two layers of the sandy sediments: oxic and anoxic. The porewater biogeochemistry in each layer is primarily determined by the type of microbial respiration (e.g., aerobic respiration vs. sulfate reduction). Metabolic dissolution of carbonates is driven by microbial respiration and is an important factor in the biogeochemistry of this

environment (e.g., Moulin et al., 1985; Morse and Mackenzie, 1990; Mackenzie and Andersson, 2011; Drupp et al., in review; Chapter 3).

The limited marine carbon system data available from permeable reef environments of Kaneohe Bay (Drupp et al. in review; Chapter 3; Tribble 1990; Tribble 1993) suggest that most of the dissolution occurring in the sediments and framework is metabolically controlled via Equation 4.8.



where CH₂O is organic matter, and there is a 1:1 molar relationship between the dissolution of CaCO₃ and the consumption of organic matter via oxic respiration. This process also leads to a 1:1 ratio of total alkalinity and DIC produced by dissolution (e.g. Moulin et al. 1985). In addition to metabolic dissolution, environmental dissolution – dissolution due to thermodynamic undersaturation of a carbonate mineral phase (Equation 4.9) in the surface waters – can also control sediment dissolution rates (Andersson and Gledhill 2013).



If operative, environmental dissolution would lead to an increase in total alkalinity of twice that of the DIC produced by respiration. However, measurements in the surface water (Section 4.4.1) suggest the surface seawater over the reef is supersaturated with respect to both calcite (and low Mg-calcite) and aragonite, and close to saturation with most high Mg-calcite phases, making it highly unlikely that environmental dissolution is *currently* playing an active role in sediment biogeochemistry. Because of this, we assume that microbial respiration combined with metabolic dissolution is the dominant factor, and in the initial steady-state of *CRESCAM*, all organic matter respiration is nearly balanced by an equivalent amount of carbonate dissolution in a 1:0.85 (i.e., $\Delta TA:\Delta DIC = 0.85$) molar ratio. This ratio is observed in various carbonate sediment porewater

studies reported by Moulin et al. (1985) and Morse and Mackenzie (1990). Drupp et al. (in review; Chapter 3) reported a $\Delta TA:\Delta DIC$ of 0.80 in the porewater at the CRIMP-2 location. In addition, because there is some burial of organic matter into the deeper sediments, respiration cannot exceed the sedimentation rate of organic carbon, imposing an upper limit to the rates of respiration and dissolution. Porewater samples from the sediments at the CRIMP-2 location (Drupp et al., in review; see Chapter 3) are supersaturated with respect to calcite and aragonite, even down to a depth of 60 cm, so dissolution of both substrates is set initially to zero in the oxic layer. The porewater is undersaturated with respect to >15 mol% $MgCO_3$. Dissolution rates were calculated using Equation 4.10 (Walter and Morse 1985; Andersson et al. 2005; Andersson et al. 2006; Morse et al. 2006).

$$R_D = k(1 - \Omega)^n \times M \times A_{RS} \times I_P \times I_O \quad (4.10)$$

where k and n are the rate constant, in $\mu\text{mol}\cdot\text{g}^{-1}\cdot\text{hr}^{-1}$, and the reaction order, respectively, from Walter and Morse (1985). M is the available mass (reservoir size) and A_{RS} is the reactive surface area available for dissolution. I_P and I_O are inhibition coefficients from dissolved phosphate and dissolved organic matter (DOM) in the porewater ($I = R/R_0$, R = rate with phosphate or DOM present and R_0 = rate with no phosphate or DOM). The inhibition coefficients were adapted from experimental data of Berner et al. (1978) for aragonite precipitation, but phosphate and DOM are known to inhibit dissolution processes as well (e.g. Berner et al. 1978; Morse 1983; Mucci 1986; Burton and Walter 1990). Because laboratory dissolution rates can often be orders of magnitude higher than those measured in the field, reactive surface area and the inhibition coefficients were used as limiting factors to maintain the calculated dissolution rate nearly equal to a respiration rate. The k from Walter and Morse (1985) is in units of mol per mass per time and does not specifically require a reactive surface area correction. However, laboratory experiments are

typically performed with fine grained substrates kept in suspension, thereby maximizing available surface area; in the natural environment, larger grain sizes and the heterogeneity of particle sizes prevent the entire mass from being available for dissolution.

The phosphate inhibition factor was calculated to be 0.26, based on an assumed $[\text{PO}_4^{3-}]$ of 2.5 μM (Fogaren et al. 2013) and the DOM inhibition factor was 0.3 assuming a $\text{DOM} = 1.8 \text{ mg C}\cdot\text{L}^{-1}$ (Fogaren, pers. comm.). A reactive surface area of 25% was used (Walter and Morse 1985; Andersson et al. 2006). The saturation state (Ω) of pore water collected at CRIMP-2 (Drupp et al., in review; Chapter 3) ranged from 0.4-1 in the upper 20 cm of the sediments, using the stoichiometric solubility of Plummer and Mackenzie (1974). *CRESCAM* assumed an average Ω , with respect to 15% Mg-calcite, of 0.8 for a dissolution rate of $4.38 \times 10^6 \text{ mol}\cdot\text{yr}^{-1}$.

Precipitation rates, R_p , were calculated using a rate constant, k , and reaction order, n , from Zhong and Mucci (1989). Due to the preferential and relatively rapid rate of precipitation of aragonite in magnesium rich waters over calcite (Berner et al. 1978; Morse 1983; Mucci 1986), calcite precipitation was assumed to be zero. This assumption is confirmed by the lack of calcite cementation in sandy sediments. Mg-calcite precipitation is also set to zero because the porewaters are undersaturated with respect to this mineral phase - assuming an average composition of 15 mol% MgCO_3 and stoichiometric solubility products from Plummer and Mackenzie (1974) and Thorstenson and Plummer (1977) - so abiotic precipitation should not occur. Aragonite precipitation is calculated using Equation 4.11,

$$R_p = k(\Omega - 1)^n \times M \times A_{RS} \times I_p \times I_o \quad (4.11)$$

where M is now the mass of DIC in the porewater (C_3). A rate constant, k , and reaction order, n , from Zhong and Mucci (1989) were used. A_{RS} was taken as 25% (Walter and Morse 1985; Morse and Mackenzie 1990; Andersson et al. 2006). Phosphate and DOM inhibition coefficients

were the same as those employed for dissolution. An aragonite saturation state of 2.68, adapted from porewater samples obtained from the CRIMP-2 location (Drupp et al., in review; Chapter 3), was used to estimate a precipitation rate of $4.63 \times 10^4 \text{ mol C} \cdot \text{yr}^{-1}$. The total mass balance for the oxic porewater reservoir is

$$\begin{aligned} dC_3(t)/dt = & CF_{13}(t) + CF_{43}(t) + CF_{53}(t) + CF_{63}(t) + CF_{73}(t) + CF_{173}(t) - \\ & CF_{31}(t) - CF_{35}(t) - CF_{36}(t) - CF_{37}(t) \end{aligned} \quad (4.12)$$

The rate of change of porewater DIC, $dC_3(t)/dt$, equals 0 at the initial steady-state so

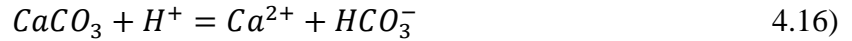
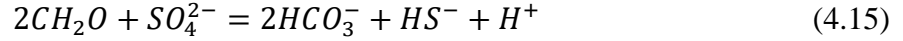
$$\begin{aligned} CF_{13}(t) + CF_{43}(t) + CF_{53}(t) + CF_{63}(t) + CF_{73}(t) + CF_{173}(t) = \\ CF_{31}(t) + CF_{35}(t) + CF_{36}(t) + CF_{37}(t) \end{aligned} \quad (4.13)$$

This equation can be written as

$$U_{in} + R + D_C + D_A + D_{Mg} + U_{an} = U_{out} + P_C + P_A + P_{Mg} \quad (4.14)$$

where U_{in} is the advective carbon flux from the surface water; U_{an} is the advective/diffusive flux up from the anoxic layer (Equation 4.4); U_{out} is the advective flux out of the sediments; R is oxic respiration, and D_x and P_x are dissolution and precipitation of the various carbonates represented as C, A, and Mg for the mineral phases calcite, aragonite, and Mg-calcite, respectively.

Anoxic sediment processes were calculated in a similar manner as those for the oxic layer. Even at the deeper depths, the porewaters collected at CRIMP-2 were not undersaturated with respect to calcite or aragonite, so dissolution could only occur within the high Mg-calcite reservoir (Drupp et al., in review; Chapter 3). This dissolution rate, however, is controlled by the reduction of organic matter through sulfate reduction (rather than by oxic respiration), where a 1:2 relationship between dissolution and respiration exists. This relationship is described by the sum of Equations 4.15 and 4.16, to produce Equation 4.17,



where one mole of $CaCO_3$ is dissolved for every two moles of organic matter consumed via sulfate reduction. The respiration rate in the organic carbon reservoir was set at 2.31×10^6 mol $C \cdot yr^{-1}$ in order to be approximately two times greater than Mg-calcite dissolution (Equations 4.15-4.17). Mg-calcite dissolution was calculated to be 1.04×10^6 mol $C \cdot yr^{-1}$ (see Equation 4.10). As in the oxic layer, the precipitation flux of calcite is considered to be zero. Aragonite precipitation is minor and estimated to be 6.5×10^4 mol $C \cdot yr^{-1}$.

4.4.3 Reef framework domain

Processes within the reef framework are calculated in a similar manner as those in the permeable sediment reservoirs, but because the framework is 95% of the crestal reef area, the magnitude of the fluxes and their impact on the reef biogeochemistry are much greater. The mass balance of the carbonate framework can be written as

$$dC_x(t)/dt = CF_{1x}(t) + CF_{11x}(t) - CF_{x1}(t) - CF_{xy}(t) - CF_{x11}(t) - CF_{xB}(t) \quad (4.18)$$

where x is the reef framework mineral phase, and y is the corresponding mineral phase reservoir in the permeable sediments. Porewater is considered supersaturated with respect to calcite, so dissolution is zero, but due to magnesium inhibition (e.g. Morse 1983), calcite is not expected to precipitate abiotically. The rate of aragonite precipitation within the pore fluids was calculated according to Equation 4.11 and was equivalent to 7.71×10^6 mol $C \cdot yr^{-1}$, using $\Omega=2.9$ (Tribble 1990). The rate of dissolution of Mg-calcite was determined using Equation 4.10, and with Ω estimated to be 0.87, yielding a rate of 1.24×10^8 mol $C \cdot yr^{-1}$. A respiration rate of 1.34×10^8 mol $C \cdot yr^{-1}$ was estimated by constraining organic matter burial within the framework (4.98×10^6 mol

C·yr⁻¹) to ~1 wt% of total burial. Similarly to the burial rates previously described for the sediment reservoirs, framework burial rates can be calculated from

$$CF_{xB}(t) = CF_{Ix}(t) + CF_{I1x}(t) - CF_{x1}(t) - CF_{xy}(t) - CF_{x11}(t) \quad (4.19)$$

where x is the mineral phase and y is the corresponding phase in the sediments. This equation is the difference between the positive fluxes (framework accretion) of calcification and abiotic precipitation and the negative fluxes (framework erosion) of bio/mechanical erosion and dissolution.

Now that we have constructed the model *CRESCAM*, we can investigate solutions to the hypotheses presented at the beginning of this chapter. The broader implications of the effects of future rising atmospheric CO₂, temperature, and ocean acidification on the Kaneohe Bay barrier reef ecosystem can be evaluated through the results of *CRESCAM*.

4.5 Model Forcings

After solving the initial quasi-steady-state solution for *CRESCAM*, the model was perturbed or “forced” by a series of forcing mechanisms using the Representative Concentration Pathway (RCP) emissions scenarios developed for the Intergovernmental Panel on Climate Change (IPCC) 5th Assessment Report (Intergovernmental Panel on Climate Change 2013). The forcing mechanisms include the future time course of atmospheric pCO₂, temperature, and open ocean DIC (Figure 4.7a, b, c). The RCP scenarios are based on four potential changes in global radiative climatic forcing by 2100, relative to 1765. The scenarios are known as RCP 2.6, RCP 4.5, RCP 6.0, and RCP 8.5, where the number (e.g., 2.6) is the global radiative forcing (W·m²) in the year 2100. Anthropogenic CO₂ emissions scenarios were then calculated for the planet to reach each radiative forcing value, along with cumulative atmospheric CO₂ concentrations and temperature anomalies relative to the year 2000 (Figure 4.6a, b). RCP 2.6 is a mitigation scenario

where both anthropogenic CO₂ emissions and atmospheric CO₂ peak mid-century and decline through the 21st century to the year 2100. This is the so-called “best-case” scenario, which has an average temperature anomaly by 2100 of less than two degrees Celsius. RCP 4.5 and 6.0 are “stabilization” emissions scenarios, which involve a continued increase in CO₂ emissions and atmospheric concentrations during the 21st century before stabilizing around 2100. These scenarios are similar to the Special Report Emissions Scenarios (SRES) ES B1 and B2 scenarios from the IPCC 3rd Assessment Report (AR) (Intergovernmental Panel on Climate Change 2001). In contrast, RCP 8.5 is most similar to the “business as usual” SRES A1F1 and IS92A scenarios (IPCC Intergovernmental Panel on Climate Change, 1996; 2001), whereby atmospheric CO₂ continues to accelerate and does not stabilize until ~2200.

For *CRESCAM*, the atmospheric CO₂ concentrations and temperature anomalies from 2015 to 2100 were obtained from the Coupled Model Intercomparison Project (CMIP) 5 model outputs (accessed from Climate Explorer, <http://climexp.knmi.nl/>). Temperature anomalies were recalculated relative to 2014-2015 and applied to an initial reef surface water temperature of 25.0 °C. This temperature is close to the average annual temperature of Kaneohe Bay reef surface waters (Drupp et al., 2013). Atmospheric CO₂ concentrations and temperature anomalies extracted from the CMIP5 models were specific to the Hawaiian Island region (21-22 °N and 156-158 °W). The values were obtained as yearly averages and subsequently interpolated linearly at intervals of 0.001 years – the interval at which the forcings were applied during the *CRESCAM* simulations. The DIC concentrations of the open ocean source waters (Figure 4.7c) were calculated using the two CO₂-carbonic acid system parameters of pCO₂ and TA. Using the various RCP scenarios, increasing atmospheric CO₂ concentrations were obtained and TA was held constant to make the calculations. In addition, instantaneous equilibrium between the

atmosphere and the ocean was assumed (Kleypas et al. 1999; Ver et al. 1999; Andersson et al. 2005). For the standard model run (Section 4.5) and each specialized case study (Section 4.6), four *CRESCAM* model outputs were obtained – one for each RCP scenario.

4.6 Results and Discussion of the Standard Run

Each set of external forcings, based on the four RCP emissions and temperature scenarios, was applied to *CRESCAM*. The model has numerous parameters that can be altered (e.g., coral calcification response to temperature change) to investigate how the system will respond under a range of potential future conditions. The initial (i.e., first run) values for these parameters, discussed in this section (and in Section 4.4), comprise the “standard run.” Table 4.11 summarizes the changes in various output fluxes and model parameters (e.g., DIC, pH, bioerosion) under each RCP scenario for the standard model run. Individual model parameters were then varied, usually one at a time, to create multiple “case studies” based on various possible future conditions of atmospheric CO₂, temperature, and open ocean DIC and to account for the uncertainty in how some of the processes will respond to changing temperature and CO₂. The results and discussion of the case studies, and a comparison with the standard run, are presented in Section 4.7.

4.6.1 *Surface water response to increased atmospheric CO₂*

DIC in the reef surface water increases with rising atmospheric CO₂ – and hence DIC of open ocean waters - and temperature of the external source waters. In the RCP 2.6 simulation, DIC in the external waters begins to decrease concomitantly with the decline in atmospheric pCO₂ around mid-century. Although DIC, pCO₂, pH, and Ω do not fully recover to their initial 2015 values by the end of the simulation, RCP 2.6 is the only forcing scenario that results in a

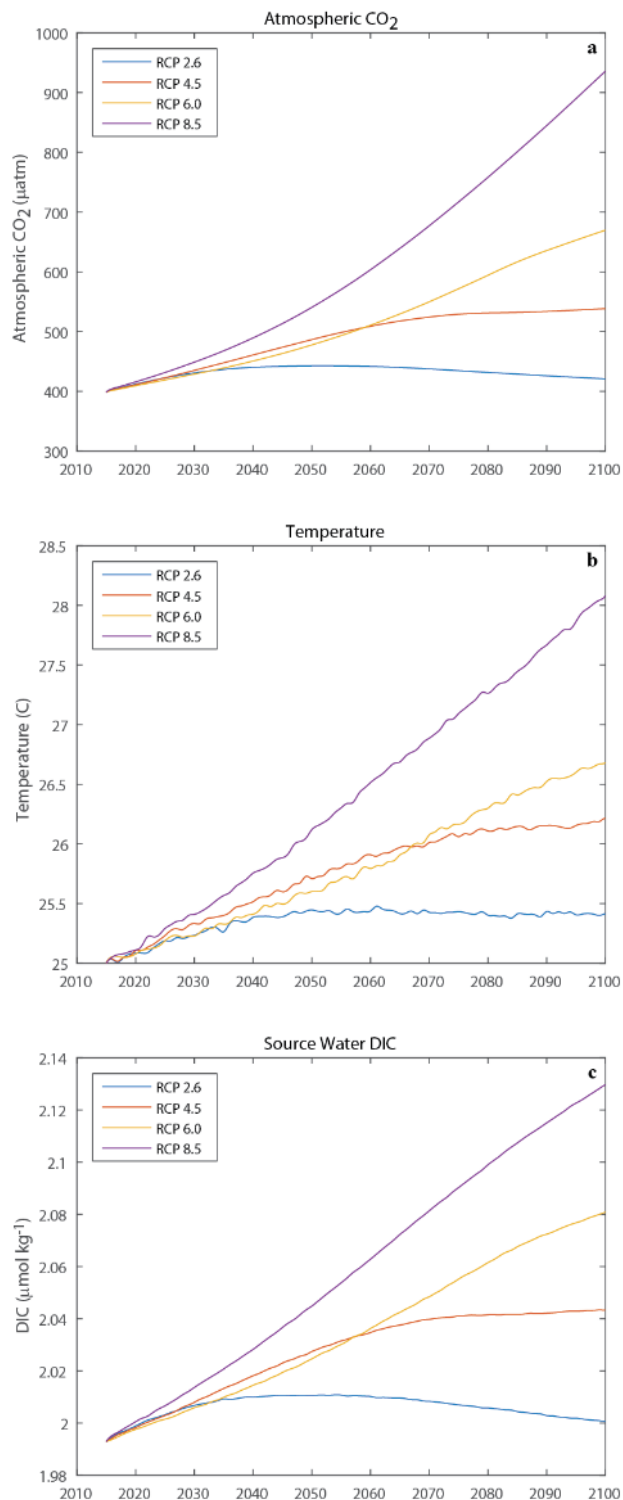


Figure 4.6: Atmospheric CO₂ concentrations (a), temperature (b), and source water DIC (c) are shown for each RCP emissions scenario. RCP 2.6 is a mitigation scenario where CO₂ emissions peak and begin to decline around mid-century. RCP 8.5 is the “business as usual” scenario. Note that the temperature anomalies from each RCP have been applied to an initial starting temperature of 25 °C in 2015 and source water DIC refers to the open ocean offshore of the Kaneohe Bay barrier reef.

decline in reef surface water DIC at any time prior to at 2100. In the standard run, surface water TA is held constant - so that there is no aqueous carbon system buffering feedback – which induces a significant drop in pH and Ω and an increase in $p\text{CO}_2$ of reef surface waters. Holding TA constant for marine surface waters is an assumption embedded in most models that calculate the pH of surface waters under rising atmospheric CO_2 levels because it is assumed that there is no significant dissolution of CaCO_3 in these waters under rising atmospheric CO_2 and declining pH (Kleypas et al. 1999; Orr et al. 2005; Silverman et al. 2009). This assumption is discussed via several case studies in Section 4.7.1. Table 4.4 and Figure 4.7 present the CO_2 -carbonic acid system parameters for the reef flat surface waters under each RCP scenario, as well as the final output value for the year 2100. For the three non-mitigation emissions scenarios, the reef surface water decreases in pH by 0.1 - 0.34 units, an increase in acidity (i.e., $[\text{H}^+]$) of ~30 - 120%.

Despite the substantial increase in acidity, and the boundary conditions of no change in TA, the saturation state of the surface water with respect to aragonite does not fall below one under any of the simulated emissions scenarios. This result suggests that widespread environmental dissolution of aragonitic sediments and structures is unlikely to become the norm on the reef flat, even under the worst case scenarios. In reality, TA in the reef surface water is likely to increase, a scenario that is explained in Section 4.7.1. Although reef surface waters do not become undersaturated with respect to aragonite, the substantial decrease in Ω and pH will almost certainly have deleterious effects on coral calcification (e.g., Kleypas et al., 1999; Silverman et al., 2007; Feely et al., 2009; Silverman et al., 2009; Andersson and Gledhill, 2013; see Section 4.6.1.3 for further details on biogenic calcification and NECP).

Although aragonite substrates are not undergoing environmental dissolution in the surface water, many compositions of Mg-calcite are undersaturated by the end of the century in

the *CRESCAM* standard runs. At the start of the simulations, the water column was close to thermodynamic equilibrium ($\Omega=1$) with a Mg-calcite containing ~14-15 mol% MgCO_3 (i.e., all compositions >15 mol% MgCO_3 are subject to environmental dissolution). Under RCP 4.5, 6.0, and 8.5, by the end of the century, environmental dissolution is predicted to affect compositions greater than 14%, 13%, and 12%, respectively.

Table 4.5 and Figure 4.8 show the surface water Ω for Mg-calcite compositions ranging from 11-18 mol% MgCO_3 . The composition (mol % MgCO_3) of the Mg-calcite substrate in metastable equilibrium with the surface water in 2100 progressively decreases under each RCP scenario. This predicted change has significant consequences for the overall reef accretion/erosion balance, will lead to dissolution of substrates previously unaffected, and will include nearly all compositions of “high Mg-calcite,” which represent a potentially significant portion (~25%) of the reef framework and binding/cement structure.

In addition to changes in the surface water chemistry due to increasing open ocean source water DIC, the effects of porewater dissolution (and changes in porewater chemistry) and the flux of carbon out of the sediments into the surface water, will be discussed in Section 4.7.1.

Table 4.4: CO_2 -carbonic acid system parameters of *CRESCAM* for the reef surface water in 2015 and 2100, under the various IPCC RCP emissions scenarios. Atmospheric CO_2 concentrations and temperature anomalies are progressively higher under each emission scenario. pH and Ω are expected to decrease substantially under each scenario.

Surface Water	DIC ($\mu\text{mol}\cdot\text{kg}^{-1}$)	pH	pCO_2 (μatm)	Ω_{arag}	$\Omega_{15\%\text{Mg-calc}}$	$[\text{H}^+]$ % Change
2015	1973	8.00	440	3.03	0.90	
2100 RCP 2.6	1981	7.98	464	2.97	0.88	4%
2100 RCP 4.5	2024	7.89	601	2.56	0.76	30%
2100 RCP 6.0	2062	7.80	762	2.20	0.65	59%
2100 RCP 8.5	2112	7.66	1093	1.76	0.51	119%

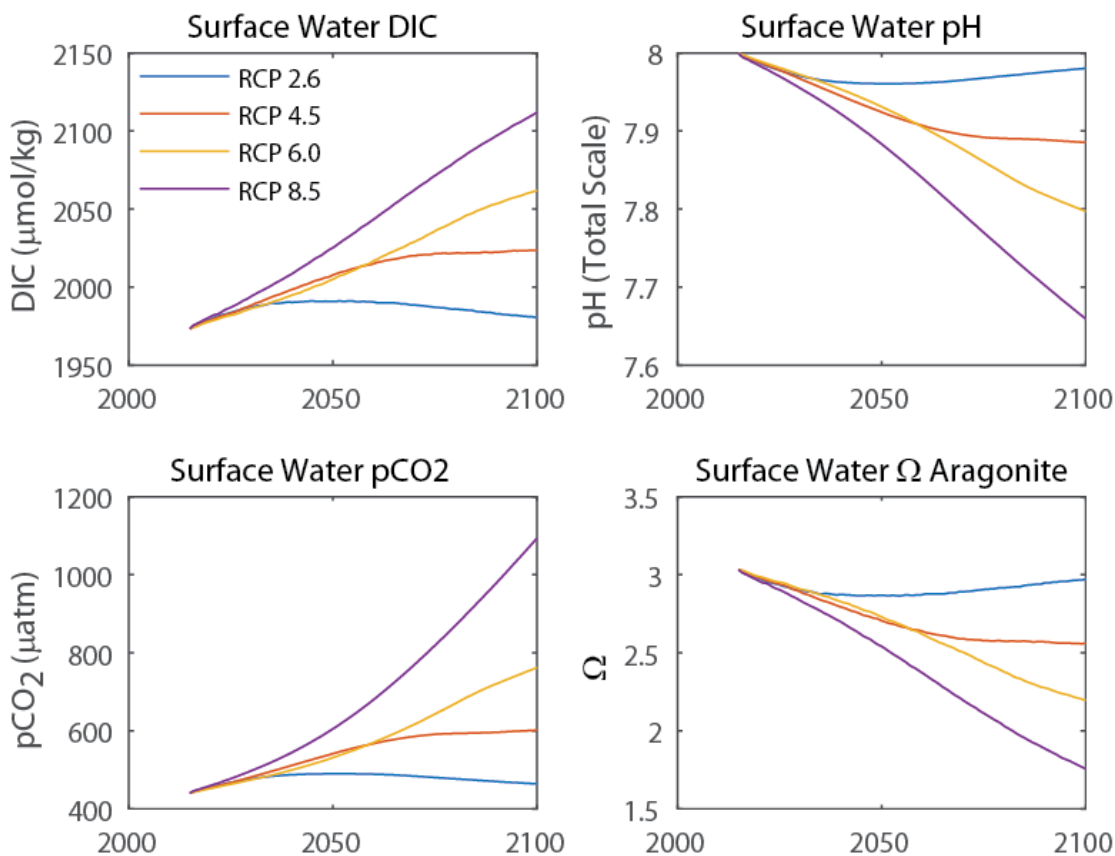


Figure 4.7: Surface water CO₂-carbonic acid system outputs from *CRESCAM* for the period 2015 to 2100 using the four RCP scenarios as forcings. RCP 2.6, the “mitigation” scenario, predicts a decline in CO₂ emissions by mid-century. This decline is reflected in the surface water carbonic acid system chemistry.

Table 4.5: Surface water Ω with respect to Mg-calcite compositions of varying mol % MgCO₃ predicted by *CRESCAM*. Mg-calcite compositions are presented from most soluble (18%) to least soluble (11%) under each RCP scenario. The thick black line demarcates the composition in metastable thermodynamic equilibrium with the seawater at the end of the century (note that the actual composition in equilibrium with the seawater falls somewhere between the two columns; e.g., 14.5%), and the seawater is supersaturated with respect to the compositions that are italicized.

Surface Water	18%	17%	16%	15%	14%	13%	12%	11%
2015	0.59	0.65	0.76	0.90	<i>1.08</i>	<i>1.28</i>	<i>1.53</i>	<i>1.84</i>
2100 RCP 2.6	0.58	0.64	0.74	0.88	<i>1.05</i>	<i>1.25</i>	<i>1.50</i>	<i>1.79</i>
2100 RCP 4.5	0.50	0.55	0.63	0.76	0.90	<i>1.07</i>	<i>1.28</i>	<i>1.54</i>
2100 RCP 6.0	0.43	0.47	0.54	0.65	0.77	0.92	<i>1.10</i>	<i>1.32</i>
2100 RCP 8.5	0.34	0.37	0.43	0.51	0.61	0.73	0.87	<i>1.05</i>

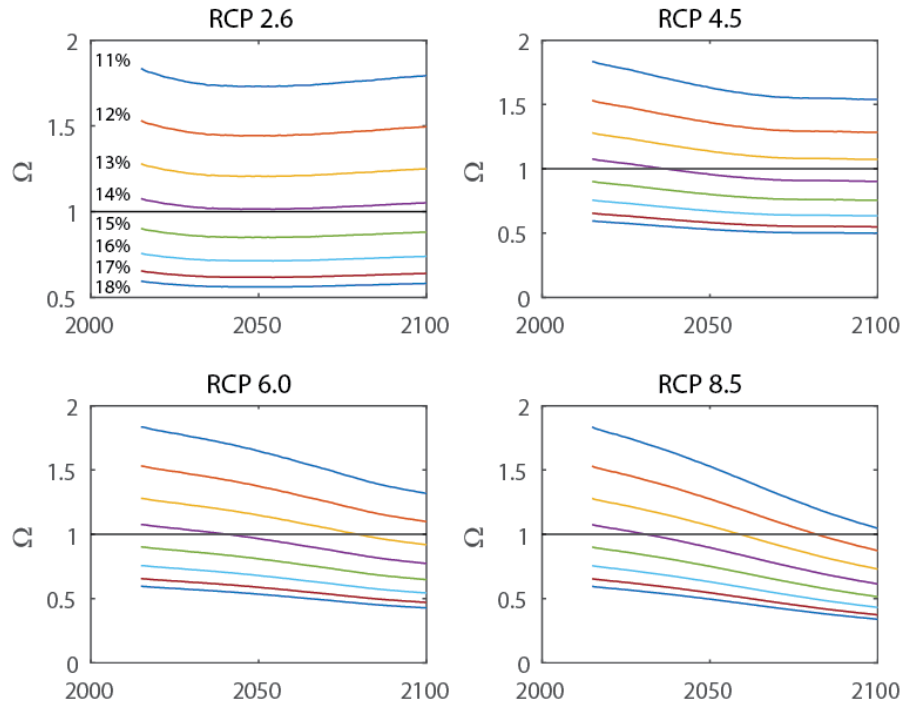


Figure 4.8: Saturation state calculations in *CRESCAM* from 2015-2100 under four RCP emissions scenarios for Mg-calcite ranging in composition from 11-18 mol% MgCO_3 . The horizontal black line is $\Omega=1$, where above the line, the seawater is supersaturated with respect to the mineral phase and below it is undersaturated. Substrates of compositions below $\Omega=1$ are subject to environmental dissolution. By the end of the century under RCP 8.5, reef surface waters are undersaturated with respect to all Mg-calcite compositions except for ~11 mol%, as contrasted with compositions of >15 mol% MgCO_3 in 2015.

4.6.2 Porewater CO_2 -carbonic acid system chemistry

The next major domain to be considered is the permeable sediment porewater system. In the oxic porewater layer (0-20 cm sediment depth), DIC and pCO_2 increase while pH decreases from 2015 to 2100 (Figure 4.9 and Table 4.6). As observed in field studies of the CO_2 -carbonic acid system in carbonate sediment porewaters, the initial $\Delta\text{TA}:\Delta\text{DIC}$ was set to 0.85, assuming that aerobic respiration of organic matter was primarily driving dissolution of carbonate mineral phases (e.g., Moulin et al., 1985; Morse and Mackenzie, 1990; Mackenzie and Andersson, 2011, Drupp et al., in review; Chapter 3). The ratio of 0.85 is comparable to that found in the sandy sediments of the backreef (Drupp et al., in review and Chapter 3) and in other carbonate sediments in Bermuda and the Bay of Calvi (Moulin et al. 1985; Morse and Mackenzie 1990;

Mackenzie and Andersson 2011). The $\Delta\text{TA}:\Delta\text{DIC}$ ratio reflects the microbial and geochemical processes occurring in the porewater that ultimately control the release or uptake of TA and DIC. Morse and Mackenzie (1990) showed that carbonate dissolution is mainly driven by remineralization of organic matter (i.e., metabolic dissolution), rather than carbonate reaction kinetics. When the remineralization of organic matter occurs via aerobic respiration, and all the metabolically produced CO_2 is used in the dissolution of carbonate minerals, TA and DIC are released into the porewater in a nearly 1:1 ratio (see Section 4.4.2.2). In reality, the ratio could be slightly more or slightly less, depending on other factors such as sediment grain size, residence time of the porewater, and other microbial processes, including denitrification and sulfate reduction (Sansone et al., 1988; Tribble et al., 1990; Bouillon et al., 2007; Drupp et al., in review; Chapter 3, Section 4.2). Larger sediment grain sizes (e.g., sand vs. silt) may dissolve more slowly due to a more limited surface area for reaction (e.g., Walter and Morse, 1985). Thus, $\Delta\text{TA}:\Delta\text{DIC}$ ratio = 0.85 is a reasonable ratio to use to approximate the TA concentration of the porewater from the DIC. Because the ratio was set at 0.85:1 (Drupp et al., 2015; Chapter 3), the saturation state decreases ($\Delta\text{TA}:\Delta\text{DIC} < 0.95$ leads to a decrease in Ω) due to a rise in $[\text{H}^+]$, and a decrease in pH.

Under this scenario of $\Delta\text{TA}:\Delta\text{DIC} = 0.85$, Ω decreases slightly within the porewater from 2015 to 2100 despite the TA released from carbonate mineral dissolution, as Ω will always decrease if $\Delta\text{TA}:\Delta\text{DIC} < 0.95$. Dissolution of Mg-calcites greater than 14 mol% MgCO_3 occurs throughout the simulation under *all* RCP forcings. The pH and Ω values reported by Drupp et al., (in review; Chapter 3) for the porewater at the CRIMP-2 buoy site located on the backreef of the Kaneohe Bay barrier reef are lower than the average reef values used in *CRESCAM* because the average pH of the reef crest surface water (the porewater source) is higher than the pH of

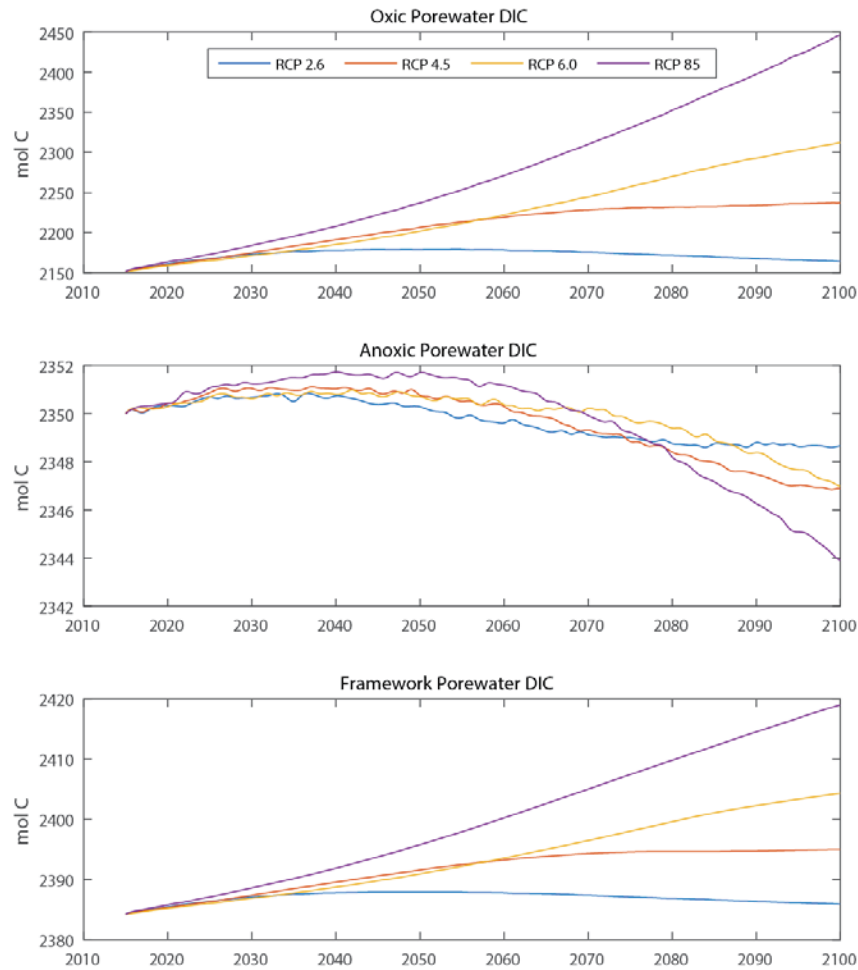


Figure 4.9: DIC concentrations from 2015 to 2100 for each of *CRESCAM*'s three porewater reservoirs. DIC peaks and begins to decline mid-century under RCP 2.6 in both the oxic porewater and framework porewater. The DIC concentrations of the anoxic porewater box peak, and then decline, at various times through the century depending on the emissions scenario.

seawater on the backreef (Shamberger et al. 2011). Aragonite saturation states at the CRIMP-2 location are as low as ~ 1.25 in the oxic layer (Chapter 3 Drupp et al., 2015), so a decrease of ~ 0.3 as calculated in the *CRESCAM* standard run would likely cause some degree of undersaturation of the porewater with respect to aragonite at some locations on the reef (i.e., backreef vs. forereef), resulting in environmental and microbial dissolution of the mineral.

Porewater Ω is partially dependent on whether the microbial processes that control $\Delta TA:\Delta DIC$

ratios remain the same or change over time. If the ratio $\Delta\text{TA}:\Delta\text{DIC}$ remains less than 0.95, Ω will continue to decrease. In the oxic layer, where aerobic respiration dominates, it is unlikely that $\Delta\text{TA}:\Delta\text{DIC}$ would ever exceed 1, as all metabolically produced CO_2 is consumed stoichiometrically in carbonate mineral dissolution reactions (Moulin et al., 1985; Sansone et al., 1988; Tribble, 1990; Morse et al., 2006; Andersson and Gledhill, 2013; Andersson et al., 2013, Drupp et al., in review). Even if surface source waters do not become undersaturated with respect to aragonite or Mg-calcite, an overall lower Ω due to OA will reduce the amount of CO_2 that must be produced via microbial respiration in the sediments before the porewater reaches undersaturation. This will lead to less CaCO_3 accumulation in the sediments and higher rates of dissolution (controlled in *CRESCAM* by Ω) because the initial porewater pH and Ω , after being advected into the sediments from the surface, will decline as surface waters acidify into the future (Andersson 2015).

The temporal evolution of the dissolution rate of Mg-calcite within the oxic sediments from 2015 to 2100 is shown in Figure 4.10. The initial rate of $\sim 2.5 \text{ g CaCO}_3 \cdot \text{m}^{-2} \cdot \text{d}^{-1}$ is similar to the rates reported by Cyronak et al. (2013a) for sandy carbonate sediments in which porewater advective processes play a major role. This initial dissolution rate results in a release of $\sim 50 \text{ mmol TA} \cdot \text{m}^{-2} \cdot \text{d}^{-1}$ into the overlying water column, however, this flux increases surface water TA by only $\sim 1\text{-}2 \text{ } \mu\text{mol} \cdot \text{kg}^{-1}$. Sandy sediments are the dominant sediment reservoir of CaCO_3 on many reefs – sometimes accounting for as much as 90% of the carbonate sediment mass (Cyronak et al., 2013a) – but for the reef flat as modeled in *CRESCAM*, they make up only about 5% of the total area. However, the total percentage area of sandy sediments for the *entire* barrier reef system is considerably higher. Even if we adopted in *CRESCAM* a sediment area of 70%, which may be more accurate for the entire reef system, rather than just the barrier reef, the

amount of TA increase in the surface water would still only equal $\sim 15 \mu\text{mol}\cdot\text{kg}^{-1}$, which is sufficient to raise saturation state by only ~ 0.2 units. However, the addition is calculated for the entire day, and with the reef free water column being flushed multiple times per day, the TA flux will not lead to any significant accumulation of alkalinity in the surface water.

Under RCP 8.5, the dissolution rate of Mg-calcite (Figure 4.10) in the oxic layer porewater-sediment system could exceed $8 \text{ g CaCO}_3 \cdot \text{m}^{-2} \cdot \text{d}^{-1}$ by 2100. This is the equivalent of an addition of $\sim 4 \mu\text{mol}\cdot\text{kg}^{-1} \cdot \text{d}^{-1}$ of TA to the surface water, which is still a negligible amount in terms of altering the surface water carbon chemistry. It is also important to note that the dissolution rate is calculated here by assuming that *all* Mg-calcite is of a 15 mol% MgCO_3 composition. This may overestimate the dissolution rate slightly, as some phases of Mg-calcite (11-13%) may not begin dissolving under the various emissions scenarios. Regardless, it is clear from these model simulation outputs, that the dissolution of sediments is unlikely to have any significant effect in offsetting the decrease in pH experienced by the surface water under rising OA from 2015 to 2100 (see also Ver et al., 1999; Andersson et al., 2003; Mackenzie, 2003).

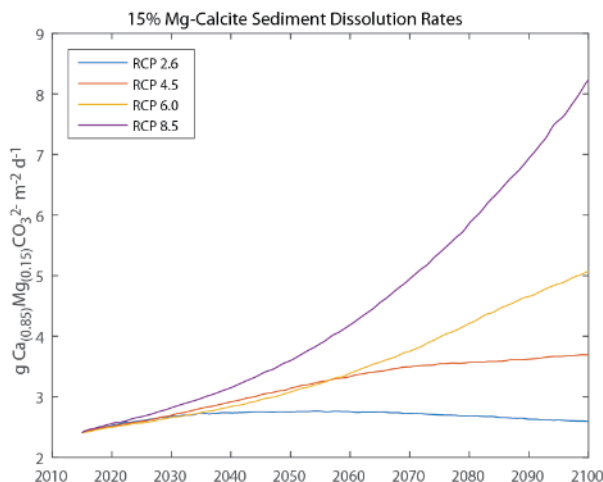


Figure 4.10: Oxic-layer sediment gross dissolution rates of Mg-calcite calculated using the model *CRESCAM* for the Kaneohe Bay barrier reef flat from 2015 to 2100.

Based on observational evidence and theoretical calculations involving carbonate sediment-porewater systems containing a multi-mineral assemblage of metastable carbonate phases, Andersson et al. (2005, 2006) and Morse et al. (2006) showed that the CO₂-carbonic acid system of porewater can remain well-buffered during dissolution reactions. This is due to the stepwise dissolution of Mg-calcite compositions of varying MgCO₃ mol %. Provided there are no kinetic inhibitions, the first composition to dissolve is the one at metastable equilibrium with the porewater. After this phase dissolves completely, pH and Ω decrease, and the next most soluble Mg-calcite phase begins to dissolve. This process may continue to occur in a stepwise fashion until the solubility of aragonite is reached, at which point both this phase and possibly a Mg-calcite equivalent in stability to aragonite can start to dissolve. In *CRESCAM* an average Mg-calcite of 15 mol% MgCO₃ represents the *entire* Mg-calcite reservoir. This reservoir does not completely dissolve by 2100 so the porewater remains fairly well buffered. Although in reality various Mg-calcite phases would dissolve sequentially, resulting in drops in pH and Ω as predicted by Andersson et al. (2005, 2006) and Morse et al. (2006). If the average Mg-calcite composition for the reef is actually higher than 15 mol % then greater dissolution would be expected and vice versa.

In *CRESCAM*, the *overall* accumulation (or loss) of solid phase carbonate mineral substrates on the reef flat is referred to as net ecosystem carbonate production (NECP), which is defined here as the balance of coral calcification, bioerosion, mechanical erosion, sediment import/export and precipitation and dissolution in the porewater (where (+) is net accumulation and (-) is net loss).

$$\text{NECP} = \text{G} + \text{P} - \text{B} - \text{D} - \text{MEE} \quad (4.20)$$

where G is gross coral calcification, P is precipitation in the sediments and framework, B is bioerosion, D is dissolution of carbonate minerals, and MEE is the mechanical erosion of reef materials which are exported off the reef to the inner lagoon (note that mechanical erosion where the particles are then deposited in the reef sediments does not change the overall carbonate balance of the ecosystem). For the *CRESCAM* standard run, $NECP$ in the oxic sediment layer decreases while the $NECP$ in both the anoxic sediment layer and the framework increase (become less negative). In the oxic layer, Ω is driven down from the aerobic oxidation of organic matter and production of CO_2 . Any reduction in the pH of the surface source water will have an additive effect on decreasing Ω when combined with aerobic respiration, and eventually *both* environmental and metabolic dissolution could become the baseline conditions in the sediments.

In the anoxic porewater layer (20-100 cm sediment depth), Ω increased slightly because $\Delta TA:\Delta DIC$ was set at 1.2:1 (see Section 4.4.3; Tribble et al., 1990). This was the ratio previously observed under conditions of sulfate reduction by Sansone and colleagues for Checker Reef, Kaneohe Bay, Hawai'i (Sansone et al. 1988; Morse and Mackenzie 1990; Sansone et al. 1990; Tribble et al. 1990). This process produces TA via Mg -calcite dissolution and production of HS^- while buffering pH. It should be noted that sulfate reduction will always result in the production of alkalinity, even if it is not coupled to carbonate dissolution (Stoessell 1992). As in the oxic layer, it would be expected that once the Mg -calcite reservoir was completely dissolved, a drop in pH would occur until aragonite began dissolving, resulting in a new equilibrium state (Andersson et al. 2005; Morse et al. 2006).

The anoxic porewater pH decreased in each scenario, with RCP 8.5 producing the largest change from 7.90 to 7.85. DIC in the anoxic layer follows a parabolic trend, increasing from the onset of the simulation before eventually reaching a maximum value and subsequently declining

through 2100 (see Figure 4.9 and Table 4.7). The NECP in the anoxic layer (and framework, see below) increases solely due to the initial conditions of $\Delta\text{TA}:\Delta\text{DIC} > 0.95$, despite the changes in DIC and pH. This estimation of TA is a major limitation of *CRESCAM* and can only fully be resolved by building a coupled DIC and TA or DIC and $[\text{H}^+]$ scheme into the model architecture. In order to evaluate how NECP might change in these reservoirs over time, a variety of case studies were performed, where $\Delta\text{TA}:\Delta\text{DIC}$ for each reservoir was altered at the onset of the model (see Section 4.7.3). However, the change in NECP in the anoxic sediment layer was very small (only 6% under RCP 8.5), so even under conditions of slightly decreasing Ω , the anoxic sediment layer is unlikely to contribute much to the overall change in NECP for the entire system.

The framework porewater $\Delta\text{TA}:\Delta\text{DIC}$ was also set equal to 1.2, as it was assumed that most of the interstitial porewater was suboxic and the dominant microbial process was sulfate reduction, similar to the processes reported for the framework of Checker Reef in Kaneohe Bay (Sansone et al. 1988; Sansone et al. 1990; Tribble et al. 1990). This resulted in slight increases in Ω (a maximum of 0.15 and 0.03 increases for aragonite and 15% Mg-calcite under RCP 8.5, see Table 4.8). Similar to the anoxic sediments, the addition of TA (from both carbonate dissolution and HS^- production) buffered the porewater so that pH only decreased by 0.01–0.04 units, and DIC increased by 2% in even the worst case forcing scenario. Interestingly, the rate of dissolution of 15% Mg-calcite within the framework declined substantially more (relative to its initial value) than the rate of 15% Mg-calcite biogenic calcification in the surface water. This resulted in a greater imbalance between the two rates at the end of the simulation than at the beginning, causing the Mg-calcite framework reservoir to grow in size despite a decrease in the rate of biogenic calcification.

Initially, the interior framework porewater was net dissolving (negative NECP; note that this does not include biogenic calcification on the surface). Under every forcing scenario in the standard run, framework NECP increased (became less negative) as carbonate precipitation increased and dissolution decreased due to the change in Ω . Despite this, the framework porewater remained net dissolving over the length of the simulation. Because the NECP of the interior framework is of the same order of magnitude as biogenic calcification and bioerosion fluxes, changes in the framework porewater Ω significantly impact the overall NECP for the system. Under the initial conditions in 2015, interior framework NECP is 15% of the total NECP.

Table 4.6: CO₂-carbonic acid system parameters of *CRESCAM* for the oxic layer (0-20 cm) sediment-porewater system in 2015 and 2100, under the various IPCC RCP emissions scenarios.

Porewater (0-20 cm)	DIC ($\mu\text{mol}\cdot\text{kg}^{-1}$)	pH	pCO₂ (μatm)	Ω_{arag}	$\Omega_{15\%Mg\text{-calc}}$	[H⁺] % Change
2015	2152	7.90	613	2.68	0.80	
2100 RCP 2.6	2164	7.89	634	2.68	0.79	3%
2100 RCP 4.5	2237	7.85	727	2.62	0.77	13%
2100 RCP 6.0	2312	7.81	823	2.54	0.75	23%
2100 RCP 8.5	2447	7.74	1045	2.43	0.71	45%

Table 4.7: CO₂-carbonic acid system parameters of *CRESCAM* for the anoxic layer (20-100 cm) sediment-porewater system in 2015 and 2100, under the various IPCC RCP emissions scenarios.

Porewater (20-100 cm)	DIC ($\mu\text{mol}\cdot\text{kg}^{-1}$)	pH	pCO ₂ (μatm)	Ω_{arag}	$\Omega_{15\%Mg\text{-calc}}$	[H ⁺] % Change
2015	2350	7.90	676	2.91	0.86	
2100 RCP 2.6	2349	7.89	688	2.91	0.86	1%
2100 RCP 4.5	2347	7.88	710	2.92	0.86	4%
2100 RCP 6.0	2347	7.87	723	2.93	0.86	6%
2100 RCP 8.5	2344	7.85	764	2.96	0.87	11%

Table 4.8: CO₂-carbonic acid system parameters of *CRESCAM* for the framework-porewater system in 2015 and 2100, under the various IPCC RCP emissions scenarios.

Framework Porewater	DIC ($\mu\text{mol}\cdot\text{kg}^{-1}$)	pH	pCO ₂ (μatm)	Ω_{arag}	$\Omega_{15\%Mg\text{-calc}}$	[H ⁺] % Change
2015	2384	7.89	695	2.92	0.87	
2100 RCP 2.6	2386	7.89	706	2.93	0.87	1%
2100 RCP 4.5	2395	7.88	728	2.97	0.88	4%
2100 RCP 6.0	2404	7.87	741	3.00	0.89	5%
2100 RCP 8.5	2419	7.85	781	3.07	0.90	9%

4.6.3 Net Ecosystem Carbonate Production (NECP)

The NECP of the Kaneohe Bay barrier reef is dominated by biogenic calcification in the water column and the interior framework processes of precipitation and dissolution. Table 4.9 presents the initial NECP-related parameters in 2015 and in 2100 under each IPCC RCP forcing scenario. Under RCP 2.6, gross water column calcification decreases to a minimum of 9.02×10^8

mol C·yr⁻¹ in 2034, when atmospheric CO₂ peaks, before increasing to an end-century value 2% greater than in 2015. NECP increases by ~ 3% to 7.91×10⁸ mol C·yr⁻¹ (9.0 mmol C·m⁻²·yr⁻¹) by 2100. RCP 4.5 results in essentially no change in NECP, while RCP 6.0 and 8.5 cause NECP to decline by ~ 7% and 17%, respectively. Although the surface water never becomes undersaturated with respect to calcite, aragonite, and even some compositions of Mg-calcite (see Table 4.5), the decrease in Ω in every scenario, except RCP 2.6, results in a decrease in gross water column biogenic calcification (e.g., corals and coralline algae). In addition, rising seawater pCO₂ causes an increase in bioerosion (Figure 4.11), as anticipated from the work of Tribollet et al. (2006, 2009), further reducing water column NECP (toward net dissolution). The increase in NECP under RCP 2.6 is a result of the positive response of biogenic calcification to increasing temperature, which initially outweighs its negative response to a decreasing Ω , in this scenario. This outcome is dependent on how corals will react to rising temperatures, and various coral species on the Kaneohe Bay reef as well as different reef locations globally will not all respond in the same manner. Eventually, however, the adverse effect of lowering Ω becomes stronger than the (initially) beneficial effect of rising temperatures, and biogenic calcification decreases as shown in the RCP 6.0 and 8.5 scenarios. It is not well known how calcifying organisms will respond to a combination of increased temperature and decreased pH, and it is possible that the combination of stressors could lead to reduced calcification at temperatures and pH levels that, alone, would not be deleterious (Agegian 1985; Agegian and Mackenzie 1989; Gattuso et al. 1999; Langdon and Atkinson 2005; Hoegh-Guldberg et al. 2007; Silverman et al. 2007; Pandolfi et al. 2011; Gattuso et al. 2015).

The temperatures used in the standard *CRESCAM* run are on the low-end of the ranges predicted for each RCP scenario. In *CRESCAM*, 28 °C is set as the maximum temperature

threshold before calcification begins to decline. However, using the curvilinear temperature-calcification equation adapted from Agegian and Mackenzie (1989, see also Andersson et al., 2005) results in a temperature difference above or below 28 °C to be equal in its effect on calcification (e.g., 26 or 30 degrees result in the same decrease in calcification relative to the 28 degree threshold). This is likely not the case as calcification will probably decrease very rapidly - due to coral bleaching - once temperatures cross the maximum sustainable critical temperature for corals to thrive (e.g., Clausen and Roth, 1975; Coles and Jokiel, 1978; Marshall and Clode, 2004; Langdon and Atkinson, 2005; Silverman et al., 2007; Pandolfi et al., 2011). In addition, as summer temperatures continue to exceed historical maximums as a result of global climate change (Intergovernmental Panel on Climate Change 2013), the potential for long-term bleaching increases (Silverman et al. 2007). Temperatures on the barrier reef have exceeded 28°C for portions of both the 2014 and 2015 summers, so exceeding the maximum calcification temperature thresholds is likely for at least portions of the year. As previously mentioned, this response is highly dependent on the reef location and coral species that comprise it. *CRESCAM* does not account for bleaching on either a long-term or seasonal scale in the standard run.

Along with temperature and pH effects on calcification, increases in pCO₂ are generally expected to enhance bioerosion (Tribollet et al. 2002; Tribollet and Golubic 2005; Tribollet et al. 2009; Wisshak et al. 2012; Wisshak et al. 2013; Andersson and Gledhill 2013; Fang et al. 2013; Barkley et al. 2015; Silbiger and Donahue 2015). This is due to multiple factors: A less-dense coral skeleton due to OA is easier for bioeroding organisms to breakdown; and the lowered pH increases bioerosional processes by enhancing the efficiency of biochemical dissolution by organisms such as *Cliona orientalis* and euendolithic algae (Tribollet et al. 2009; Wisshak et al. 2012; Wisshak et al. 2013; Fang et al. 2013; Silbiger et al. 2014; Barkley et al. 2015). Barkley et

al. (2015) measured bioerosion on reef flats of Palau with varying water column pH levels and found that bioerosion was consistently higher in low pH waters (values similar to those expected by 2100) than in the higher pH waters. Bioerosional fluxes in *CRESCAM* increase under all scenarios, including RCP 2.6, and nearly doubles from present-day conditions under RCP 8.5. The bioerosion rates are the same order of magnitude as sediment NECP and could potentially become the most important factor - other than biogenic calcification – contributing to the reef’s overall carbonate balance (Barkley et al. 2015). In addition, weakened coral skeletons from OA are more susceptible to increased mechanical erosion, further altering the carbonate balance of the barrier reef ecosystem.

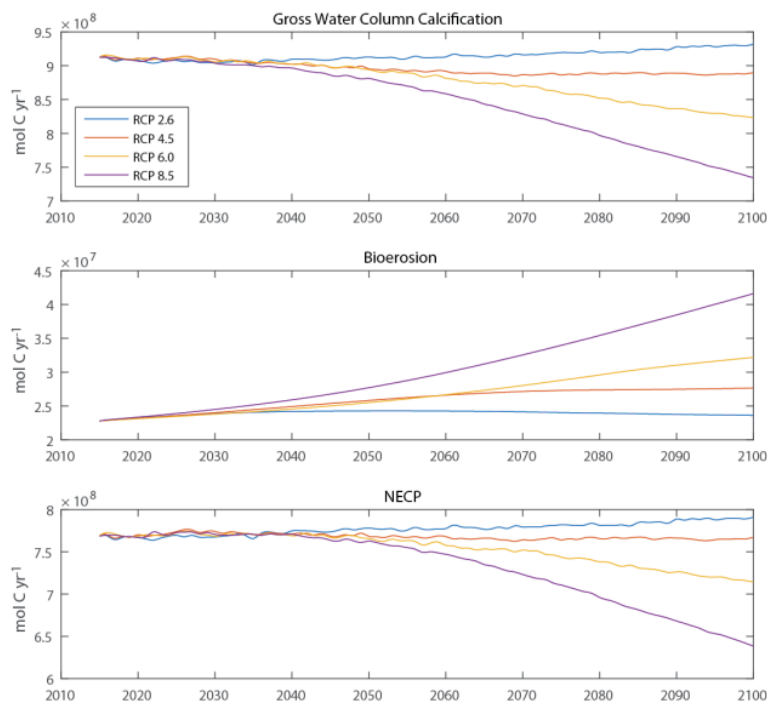


Figure 4.11: Water column gross calcification, bioerosion, and NECP fluxes from 2015 to 2100. The fluxes respond to changes in seawater DIC, pH, $p\text{CO}_2$, and Ω over this period of time. NECP is expected to decline under RCP 6.0 and 8.5 by as much as 15%. Increased bioerosion of carbonate substrates exposed to surface and porewater moves the system significantly towards a net erosional state, and gross water column calcification declines as Ω decreases under RCP 6.0 and RCP 8.5 emissions scenarios.

Table 4.9: NECP and related parameters at the start (2015) and end (2100) of the four *CRESCAM* simulations. Increased acidity negatively affects gross calcification, while enhancing bioerosion. Increases in anoxic and framework porewater Ω result in enhanced precipitation and lower dissolution, increasing NECP. All values are in mol C·yr⁻¹ unless otherwise indicated. Negative values indicate net loss via dissolution, while positive values indicate net gain via calcification and/or precipitation.

	Gross Surface Calcification	Bioerosion	Oxic Sediment NECP	Anoxic Sediment NECP	Interior Framework NECP	NECP	NECP Change	Gross Surface Calcification Change	NECP mmol C·m⁻²·hr⁻¹
2015	9.13E+08	-2.28E+07	- 4.34E+06	- 9.79E+05	-1.16E+08	7.69E+08			8.8
2100 RCP 2.6	9.32E+08	-2.36E+07	- 4.68E+06	- 9.97E+05	-1.11E+08	7.91E+08	3%	2%	9.0
2100 RCP 4.5	8.89E+08	-2.76E+07	- 6.69E+06	- 9.87E+05	-8.74E+07	7.67E+08	0%	-3%	8.8
2100 RCP 6.0	8.23E+08	-3.22E+07	- 9.21E+06	- 9.46E+05	-6.64E+07	7.15E+08	-7%	-10%	8.2
2100 RCP 8.5	7.34E+08	-4.16E+07	- 1.50E+07	- 9.16E+05	-3.82E+07	6.39E+08	-17%	-20%	7.3

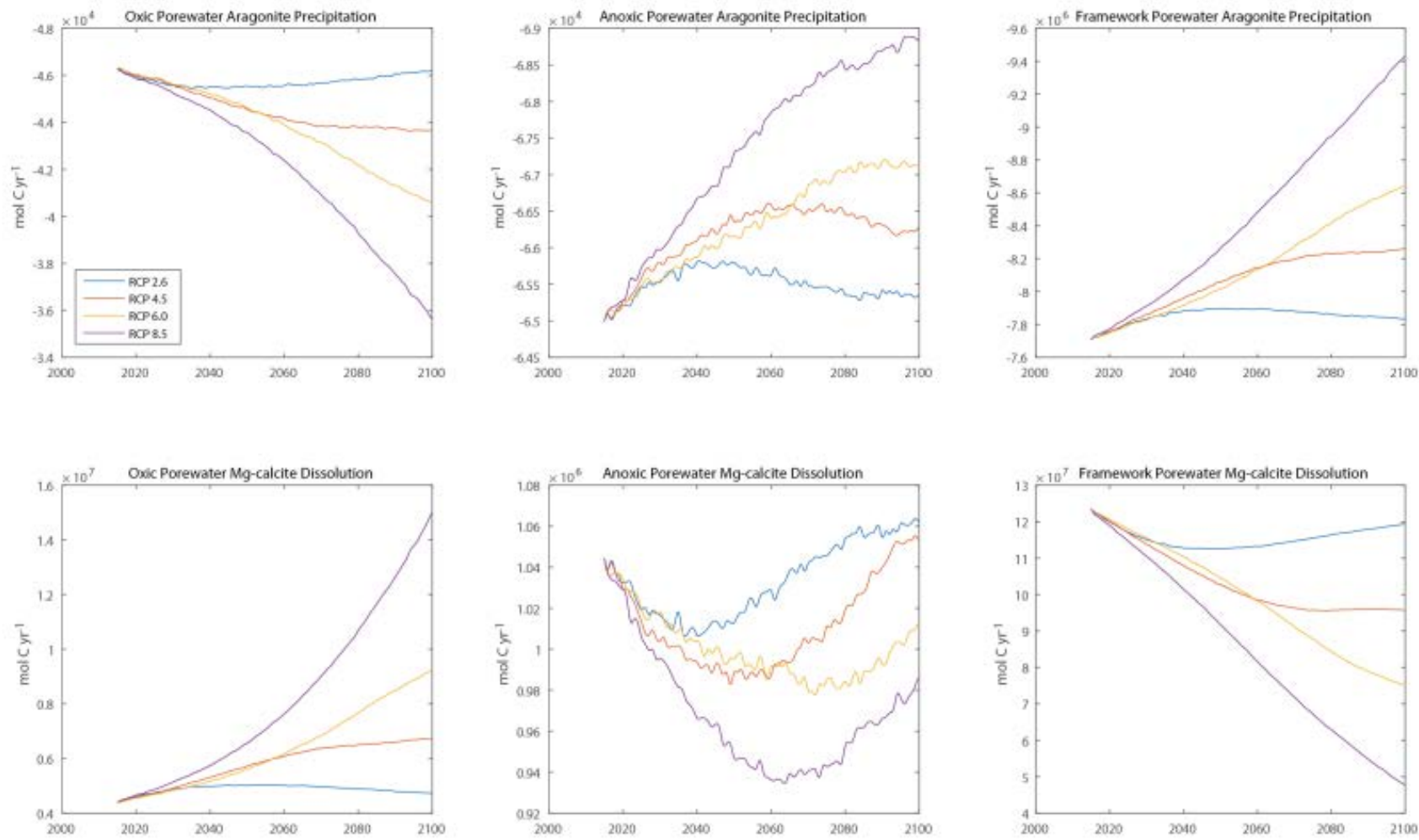


Figure 4.12: Precipitation of aragonite and dissolution of Mg-calcite in the three porewater reservoirs of the oxic, anoxic, and framework domains from 2015 to 2100.

4.6.4 Ocean-Atmosphere CO₂ Exchange

For the three larger RCP emissions scenarios, the numerical results of *CRESCAM* show that the Kaneohe Bay barrier reef surface water remains a source of CO₂ to the atmosphere from 2015 to 2100 because pCO₂ accumulation accelerates faster in the seawater than in the air (Figure 4.14). *CRESCAM* assumes that there will be no change in average wind speed, which controls air-sea flux rates, over the century. The surface water source strengthens throughout the century, with CO₂ efflux becoming as much as four times stronger by the end of the century for emissions scenario RCP 8.5. Under RCP 2.6, CO₂ efflux reaches its peak in 2054, before slowly decreasing over the remainder of the century (Figure 4.14).

It is the lack of any buffering feedback on the CO₂-carbonic acid system from TA release from the sediments or framework via carbonate dissolution (TA is held constant) during this time period, along with rising temperatures, that results in pCO₂ increasing at a more rapid rate in the water column than the atmosphere (see Figure 4.13). This occurs despite the decrease in NEC and increase in NEP, both of which should result in a drawdown of pCO₂, further evidence that short surface water residence times can significantly negate biogeochemical changes occurring over the reef flat. Decreasing NEC on the reef flat would likely lead to a smaller TA depletion, relative to the source waters, as seawater flows across the reef and TA is removed during biogenic calcification. This feature is not captured in the *CRESCAM* standard run because reef surface water TA is held constant, but its importance is discussed in Section 4.7.1 in a case study and sensitivity analysis dealing with changing the TA content of the surface waters.

At the start of the *CRESCAM* runs, the net-annualized areal CO₂ exchange was +0.80 mol C·m²·yr⁻¹, slightly less than the +1.15 mol C·m²·yr⁻¹ reported by Drupp et al. (2013) at the CRIMP-2 location (see Table 4.3). By 2100, the projected net-annualized areal CO₂ fluxes increased to +0.84, +1.23, +1.80, and +3.08 mol C·m²·yr⁻¹ for RCP 2.6, 4.5, 6.0, and 8.5,

respectively (Figure 4.14). However, under the RCP 2.6 scenario, the air-sea gas exchange rate is expected to return to its initial 2015 values sometime after 2100, provided that atmospheric CO₂ (and hence surface water DIC) continues to decrease. While these flux rates are similar to those reported for other studies and locations in Kaneohe Bay (e.g., Fagan and Mackenzie, 2007; Drupp et al., 2011; Massaro et al., 2012; Drupp et al., 2013), it is important to note that net autotrophy is increasing on the reef, which, as previously mentioned, lowers pCO₂ and can even affect the direction of gas flux (Andersson et al., 2003, 2005; Drupp et al., 2011). The rate of photosynthetic increase as modeled in *CRESCAM* is likely close to the maximum change possible, and thus the standard run flux rates are probably conservative estimates.

In contrast to the air-sea CO₂ exchange numerical results obtained from *CRESCAM* for the Kaneohe Bay barrier reef, Massaro et al. (2012) concluded that the waters of Southern Kaneohe Bay (about three km southeast of the barrier reef and close to a fringing reef) would decrease in CO₂ source strength with rising atmospheric CO₂, and decreased calcification and heterotrophy. This was based on a 2.5-year continuous temporal study of CO₂ biogeochemical dynamics and air-sea exchange in the Southern Kaneohe Bay waters. The authors posited that the bay waters would eventually become a *sink* of CO₂ from the atmosphere at some undetermined point in the future. Furthermore, Massaro et al. (2012) report that changes in air-sea CO₂ gas exchange are ultimately controlled by changes in the source water DIC, biogeochemical processes on the reef, and the seawater residence time (e.g., Andersson et al., 2005; Andersson et al., 2006). The fact that the *CRESCAM* standard run does not agree with the prediction of Massaro et al. illustrates the importance of understanding fully the positive and negative feedbacks resulting from changes in the biogeochemistry of reef ecosystems when evaluating the future course of air-sea CO₂ exchange on a reef. In light of this conclusion, several case study

model runs were performed using CRESCAM to examine the effects of various feedback mechanisms on the air-sea CO₂ exchange and are discussed in Section 4.7.2.

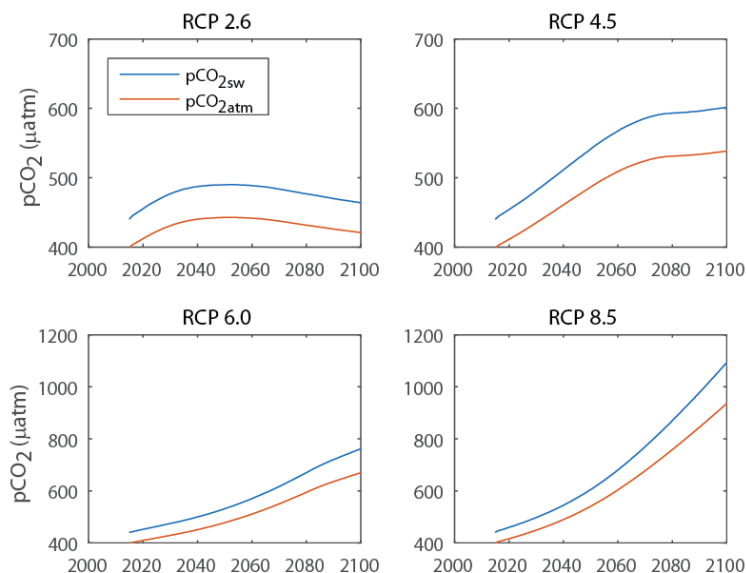


Figure 4.13: pCO₂ in the surface seawater and atmosphere under each RCP scenario from 2015 to 2100. The pCO₂ in the seawater increases faster than in the atmosphere resulting in a larger $\Delta p\text{CO}_2$ and an increase in air-sea CO₂ gas exchange.

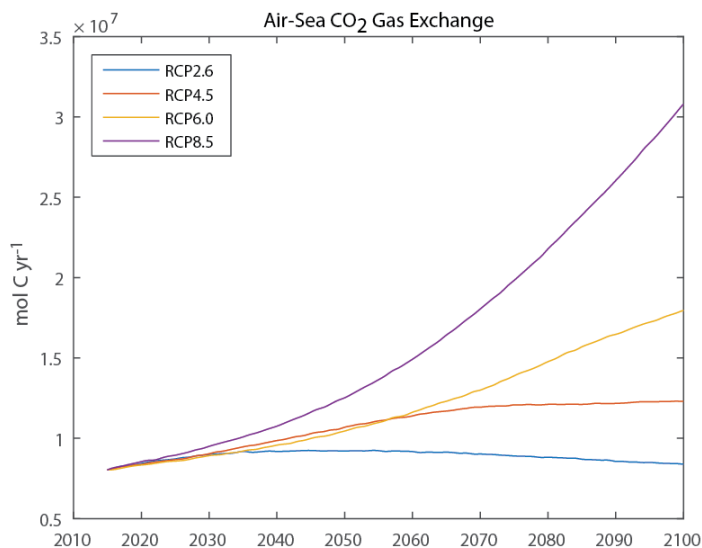


Figure 4.14: Air-sea CO₂ exchange for each forcing scenario from 2015 to 2100. CO₂ evasion is presented as annual fluxes. The source strength of the surface water increases under RCP 4.5, 6.0, and 8.5 as $\Delta p\text{CO}_2$ ($p\text{CO}_{2\text{sw}} - p\text{CO}_{2\text{air}}$) grows larger.

4.6.5 Net Ecosystem Production (NEP)

We now consider the net ecosystem production (NEP) of the Kaneohe Bay barrier reef ecosystem as modeled in *CRESCAM* and its changes over time from 2015 to 2100. In *CRESCAM*, net ecosystem production is calculated as the difference between photosynthesis (both pelagic and benthic) and total ecosystem respiration - the sum of *all* respiration in the surface water, sediment, and framework boxes (Figure 4.15 and Table 4.10). NEP represents the total amount of organic carbon available for storage or export for the barrier reef. The standard run of *CRESCAM* assumes that nutrients, like nitrogen and phosphorus, are not limiting plant growth, and their concentrations do not change over time. This is not the case in reality because either nitrogen or phosphorus is likely the limiting factor for photosynthesis on the reef (e.g., Atkinson and Falter, 2003; Drupp et al., 2011). In addition, the standard run assumes that both photosynthesis and respiration (Figure 4.16) will increase at the same rate with respect to temperature change (i.e., a doubling of the rate for every 10 °C increase, $Q_{10}=2$). The effects of changing nutrient and organic carbon inputs to the reef and further aspects of the temperature forcing on NEP are discussed in Section 4.7.4 through the use of sensitivity analysis and different case studies.

NEP increases under each RCP forcing scenario, by 3-16%, as both the photosynthetic and respiration rates increase with temperature. In Section 4.7.4, the effect of temperature change on photosynthesis, respiration, and NEP will be discussed through a series of case studies. However, an increase in NEP of 10% was assumed in simulations by Andersson et al. (2013), so we are confident that our predicted outputs (3-16%) are in line with other model estimates for changes in NEP by 2100. The increase in NEP results in TOC (Figure 4.17) accumulating in the water column and increased sedimentation of organic carbon to the upper sediments and framework, although in all three sediment/framework reservoirs, organic carbon was found to

decrease over time because increases in sediment-porewater respiration, as a result of temperature change, outpaced the supply of OC to the sediments.

DIC changes in the porewater, relative to the surface water, are controlled primarily by the respiration of the sedimented organic carbon, subsequent carbonate mineral dissolution, and the rate of organic carbon burial from above. In the oxic sediment layer, TOC decreases despite the increase in sedimentation from enhanced photosynthesis, and, under RCP 2.6 and 4.5, TOC only stabilizes once temperature (and respiration rates) level off during the latter half of the century. The continued respiration produces $p\text{CO}_2$, which elevates DIC concentrations and drives carbonate dissolution (Moulin et al., 1985; Morse and Mackenzie, 1990; A. J. Andersson et al., 2005; Mackenzie and Andersson, 2011, Drupp et al., in review). An often overlooked, or ignored, consequence of rising temperatures and changes in NEP is the change in organic carbon burial, as decreased TOC in the upper sediments clearly has implications for the carbon cycle in the deeper sediments.

Porewater respiration fluxes and DIC concentrations (see Figure 4.18 Figure 4.19) initially increase in the anoxic layer but peak between ~2040 and 2065, depending on the forcing scenario, then decline through the end of the century. This is in contrast to the respiration rates in the oxic porewater layer and in the framework porewater, which increase over the entire simulation (Figure 4.18). The initial increase in the anoxic layer respiration is driven by the rising temperature. However, as seen in Figure 4.19, the flux of OC to the anoxic layer steadily decreases. By mid-century, the lack of OC becomes the limiting factor for the sediment microbial respiration, resulting in decreased respiration rates and porewater DIC concentrations. Organic carbon burial below one meter of sediment depth decreases by as much as 15% (RCP 8.5). It is worth noting that this substantial decrease occurs despite a rise in NEP and TOC in the

surface water. If photosynthesis does not increase, the burial of organic carbon will decrease by an even greater amount.

Organic carbon in the framework responds to the forcing mechanisms in the same manner as in the oxic sediment layer. As respiration rates increase due to rising temperatures, the reservoir size is diminished over the simulation despite the increased rate of sedimentation of OC. The enhanced respiration in the framework counteracts the rise in surface NEP (surface water photosynthesis – surface water respiration). Sediment and framework respiration is a significant contributor to the overall organic carbon budget, reducing the overall NEP by 45% as compared to the NEP calculated for just the surface water. As previously discussed, organic carbon burial below one meter of depth decreases as the OC is consumed faster than it is replenished.

Overall, the change in NEP, whether it is positive or negative, will have a significant effect on the carbonate system of the reef and whether the reef suffers a deficit in CaCO_3 , because NEP is second only to NECP in terms adding or removing DIC via biogeochemical processes on the reef.

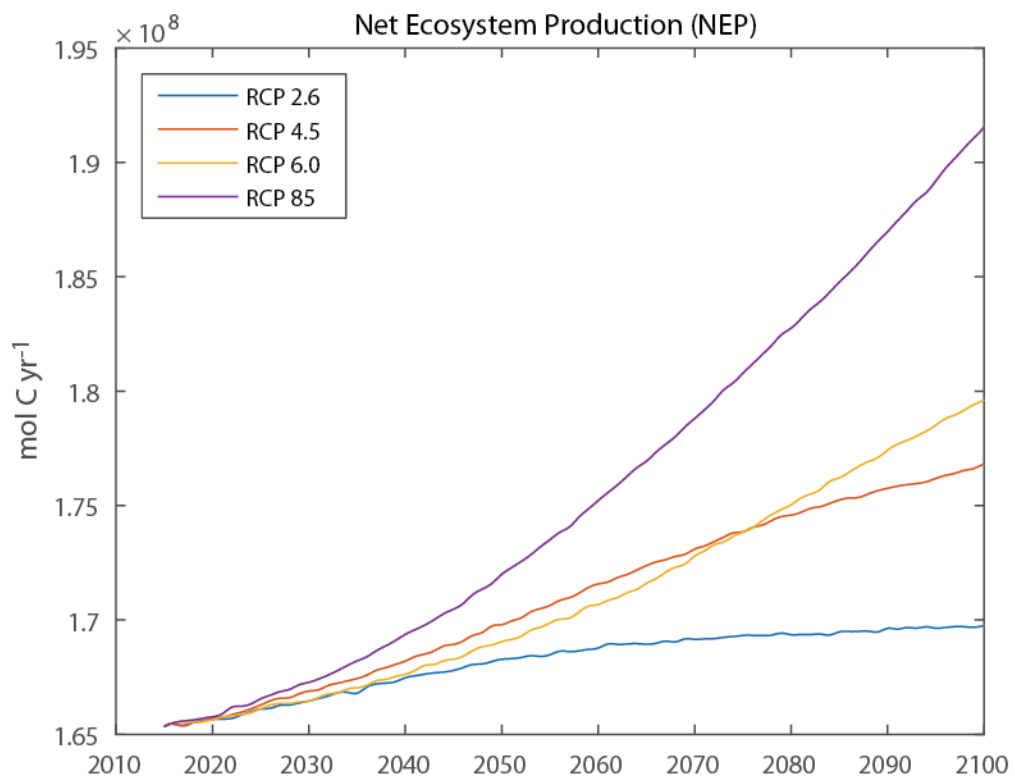


Figure 4.15: Net ecosystem production (NEP) from 2015 to 2100 increases under *CRESCAM*'s standard run as temperature change increases photosynthetic and respiration rates in the surface water and sediment-porewater systems.

Table 4.10: Photosynthesis, respiration, and NEP at the start (2015) and end (2100) of the four *CRESCAM* RCP simulations. Increased temperature positively affects both processes. Despite the rise in respiration in the sediment-porewater systems, the ecosystem remains net autotrophic (+ NEP). All values are shown in mol C·yr⁻¹ unless otherwise indicated.

	Surface Photosynthesis	Surface Respiration	Porewater Respiration	NEP	NEP (mmol C·m ⁻² ·d ⁻¹)	NEP Change
2015	1.89E+09	1.59E+09	1.42E+08	1.65E+08	45.30	
2100 RCP 2.6	1.95E+09	1.64E+09	1.43E+08	1.70E+08	46.50	3%
2100 RCP 4.5	2.06E+09	1.74E+09	1.46E+08	1.77E+08	48.44	7%
2100 RCP 6.0	2.13E+09	1.80E+09	1.50E+08	1.80E+08	49.21	9%
2100 RCP 8.5	2.35E+09	2.00E+09	1.56E+08	1.92E+08	52.48	16%

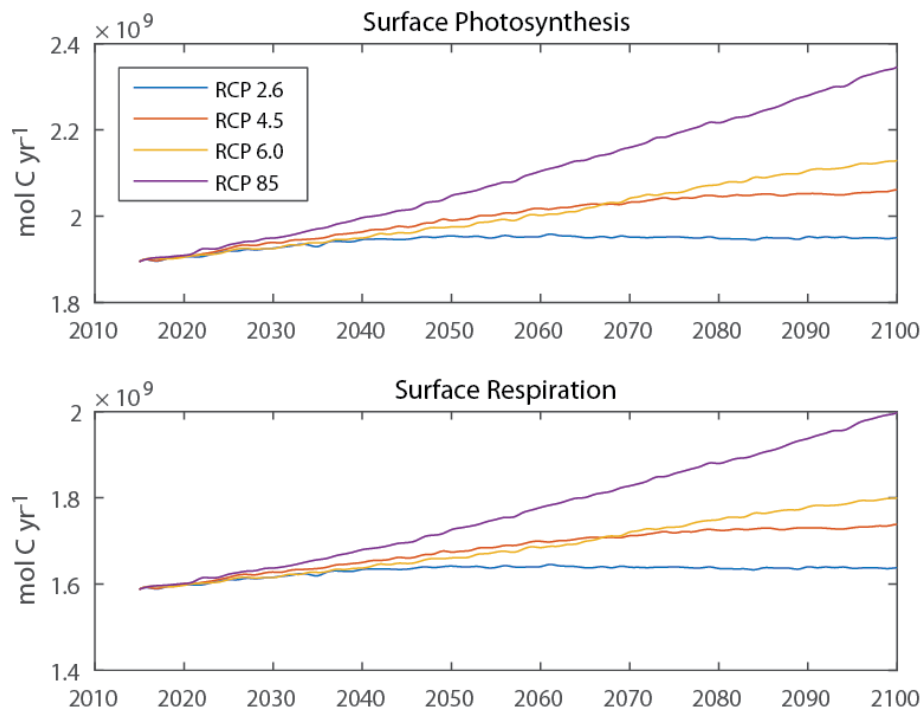


Figure 4.16: Surface water photosynthesis and respiration rates from 2015 to 2100. Both rates increase with rising temperatures under all four RCP forcing scenarios, although the rates level off around mid-century under RCP 2.6 as temperatures in this scenario stabilize.

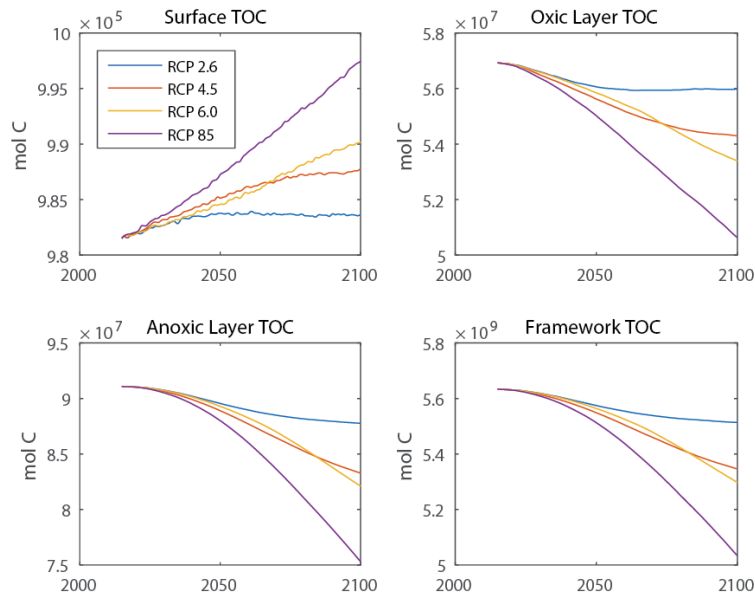


Figure 4.17: TOC in each seawater and sediment reservoir under the four RCP forcing scenarios from 2015 to 2100. TOC in the surface water increases due to rising photosynthesis. Despite increased delivery rates of TOC to the sediments, TOC in each sediment-porewater system decreases over time as respiration rates increase faster than sedimentation of TOC.

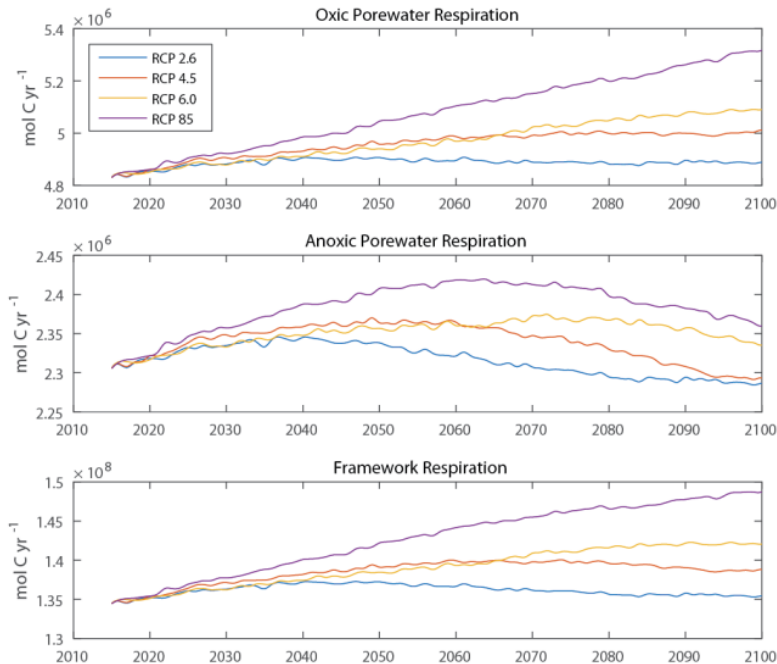


Figure 4.18: Respiration rates for the oxic and anoxic sediment-porewater domains and the framework-porewater system under the four RCP scenarios from 2015 to 2100. Each reservoir exhibits an increase in rates as temperature rises. The oxic layer domain and framework domain rates increase continuously, unlike the anoxic-layer domain where respiration peaks mid-century and begins to decline through 2100.

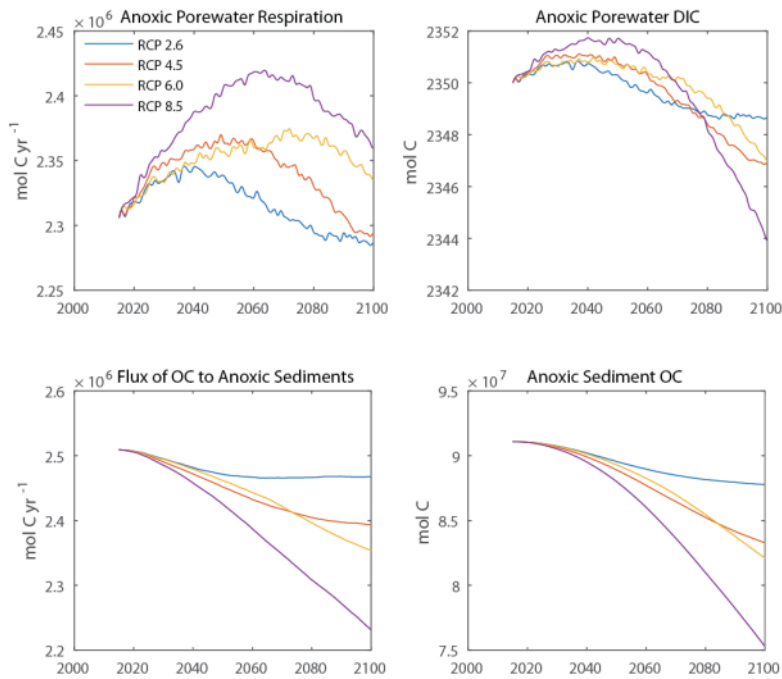


Figure 4.19: Respiration rates (a), DIC (b), organic carbon flux (c), and reservoir size (d) in the anoxic sediment layer domain from 2015 to 2100. Respiration and DIC peak mid-century before decreasing as a result of the competing effects of rising temperatures and decreased OC burial (c) from the upper sediments. The decrease in deep sediment OC results in a significant decrease in burial to deeper depths of the sediment column below one meter.

Table 4.11: Summary table of overall change of important processes and parameters in *CRESCAM* by 2100 under each RCP forcing scenario. The arrow indicates only whether the final value in 2100 is greater or less than the initial value in 2015. For TOC, the arrows refer to the change in TOC in the surface water, oxic-layer sediment-porewater, anoxic-layer sediment-porewater, and framework-porewater reservoirs, respectively.

	DIC	pH	NECP	Bioerosion	NEP	Air-Sea Exchange	TOC
RCP 2.6	↑	↓	↑	↑	↑	↑	↑↓ ↓ ↓ ↓
RCP 4.5	↑	↓	=	↑	↑	↑	↑↓ ↓ ↓ ↓
RCP 6.0	↑	↓	↓	↑	↑	↑	↑↓ ↓ ↓ ↓
RCP 8.5	↑	↓	↓	↑	↑	↑	↑↓ ↓ ↓ ↓

4.7 Case Studies

Various case studies of important parameters considered most essential or not well constrained in CRESCAM were investigated using the technique of sensitivity analysis by altering their values often one at a time (e.g., Hamby, 1994; Dubus and Brown, 2002; Andersson, 2006). These parameters were initially assessed qualitatively to exert the most influence on model results. The analysis includes: altering $\Delta\text{TA}:\Delta\text{DIC}$ ratios in the porewater systems; allowing surface water TA to change over time; utilizing different Q_{10} values for photosynthesis; and changing organic matter and nitrogen inputs to the reef. The list of case studies is shown in Table 4.12. Throughout the discussion, the case studies will be referred to by the code in the left hand column of Table 4.12.

Table 4.12: List of case studies and the changes made to various parameters within the model as compared to the standard run.

Case Study	Changes	Standard Run
A1	Surface $\Delta\text{TA}:\Delta\text{DIC} = 0.15$	Constant TA
A2	Surface $\Delta\text{TA}:\Delta\text{DIC} = 0.25$	Constant TA
A3	Surface $\Delta\text{TA}:\Delta\text{DIC} = 0.75$	Constant TA
B1	Photosynthetic $Q_{10} = 1.5$	$Q_{10} = 2$
A2B1	Photosynthetic $Q_{10} = 1.5$, Surface $\Delta\text{TA}:\Delta\text{DIC} = 0.25$	Constant TA, $Q_{10} = 2$
A3B1	Photosynthetic $Q_{10} = 1.5$, Surface $\Delta\text{TA}:\Delta\text{DIC} = 0.75$	Constant TA, $Q_{10} = 2$
C1	Oxic porewater $\Delta\text{TA}:\Delta\text{DIC} = 1$	$\Delta\text{TA}:\Delta\text{DIC} = 0.85$
D1	Framework porewater $\Delta\text{TA}:\Delta\text{DIC} = 0.92$	$\Delta\text{TA}:\Delta\text{DIC} = 1.2$
E1	OC flux increased 25%	OC flux constant
E2	OC flux increased 50%	OC flux constant
E3	OC flux increased 100%	OC flux constant
F1	Nitrogen loading doubled	Constant nitrogen
E1F1	OC flux increased 25%, nitrogen doubled	OC flux and nitrogen constant
E3F1	OC flux increased 100%, nitrogen doubled	OC flux and nitrogen constant

4.7.1 Case Study 1: Changing TA in the surface water

Although TA was held constant in the reef surface water in the standard CRESCAM run – and while this may occur in the open ocean on the time scale of a century – it is likely that TA will change in response to changing biogeochemical processes and mechanisms on the reef flat that result from rising DIC and decreasing pH and Ω . Changes in reef calcification rates and NECP will have an effect on the depletion (or enrichment) of TA as water flows over the barrier reef ecosystem. A decrease in coral calcification, as is expected under lower pH conditions, will result in higher remaining concentrations of TA, as less TA is removed from the source water during transit across the reef (Smith and Key 1975; Massaro et al. 2012; Andersson and Gledhill 2013; Andersson et al. 2013).

As anticipated, allowing the TA of the surface water to change over time had a dramatic effect on water column carbon chemistry. In the case study analysis of changing TA, TA was set to vary as a function of DIC with further addition of these parameters to the system in $\Delta\text{TA}:\Delta\text{DIC}$ ratios of 0.15, 0.25, and 0.75 (e.g., an increase in DIC of $1 \mu\text{mol}\cdot\text{kg}^{-1}$ would result in an increase in TA of 0.15, 0.25, or $0.75 \mu\text{mol}\cdot\text{kg}^{-1}$). Table 4.13 presents the final (year 2100) TA of the surface water under the varying scenarios. The increase in average surface water TA due to a decline in NECP helps to buffer partially the seawater pH and slow the rise in pCO_2 (e.g., Andersson et al., 2013). This partial pH buffering is shown in Figure 4.20 and results in significant changes to the air-sea CO_2 exchange (see Section 4.7.2).

The effect on pH is strongest under scenario A3, where the $\Delta\text{TA}:\Delta\text{DIC}$ ratio equals 0.75. However, this scenario would also result in the reef undergoing net carbonate dissolution (negative NECP) as the final TA of $2342 \mu\text{mol}\cdot\text{kg}^{-1}$ is higher than that of the source waters ($2290 \mu\text{mol}\cdot\text{kg}^{-1}$). If the source waters TA remained constant, this increase in TA could be produced by

a net dissolution rate equivalent to $\sim 15 \text{ mmol C} \cdot \text{m}^{-2} \cdot \text{hr}^{-1}$. None of the *CRESCAM* simulations resulted in net dissolution on the reef, but there is still a large amount of uncertainty as to how NEP and NECP will respond to changing OA. As previously discussed, *CRESCAM* utilizes the lower end of the predicted IPCC temperature ranges for 2015 to 2100 and does not address the problem of coral mortality due to bleaching, so it is possible that NECP on this time frame could fall even lower than predicted in our model runs. However, even a reduction in gross coral calcification by 50% when temperature thresholds are exceeded (see also Silverman et al., 2009) would not cause NECP to become negative.

In addition, Shamberger et al. (2011) reported nighttime net dissolution on the Kaneohe Bay barrier reef flat with TA values exceeding $2300 \mu\text{mol} \cdot \text{kg}^{-1}$ (greater than the source water), so there is a real possibility that the barrier reef flat could reach a level of pCO_2 and low enough NECP that net dissolution becomes the baseline condition. Nighttime net dissolution has been reported at many reef locations (e.g., Kinsey, 1985; Frankignoulle et al., 1996; Silverman et al., 2007) and it is widely predicted that many reefs may reach a general state of net dissolution/erosion by the end of the century (Kleypas et al. 2006; Silverman et al. 2009; Andersson et al. 2009; Silbiger et al. 2014; Silverman et al. 2014; Eyre et al. 2014; Silbiger and Donahue 2015).

Table 4.14 shows the offsetting effect of increasing surface water TA as the percent difference between the reduction in pH by 2100 under each case study/RCP scenario and the reduction in pH of the standard run. Andersson et al. (2013) predicted partial offset changes in pH between $\sim 12\text{-}24\%$ on a Bermuda coral reef under several scenarios of changing NEC and NEP by 2100. *CRESCAM* outputs are close to this range for all forcing scenarios under case studies A1 and A2. A $\Delta\text{TA}:\Delta\text{DIC}$ of 0.75 would result in $>60\%$ offset in the pH changes under all non-mitigation

emissions scenarios. It is important to note that an offset in pH of 60% would come at the expense of live coral coverage and reef stability, as the offset cannot be reached by sediment dissolution alone.

Table 4.13: Surface water TA at the end of each RCP forcing scenario under various $\Delta\text{TA}:\Delta\text{DIC}$ ratios used in *CRESCAM*. The value in parentheses is the $\Delta\text{TA}:\Delta\text{DIC}$ ratio that was used in the model run.

	TA ($\mu\text{mol}\cdot\text{kg}^{-1}$) (standard)	TA ($\mu\text{mol}\cdot\text{kg}^{-1}$) A1 (0.15)	TA ($\mu\text{mol}\cdot\text{kg}^{-1}$) A2 (0.25)	TA ($\mu\text{mol}\cdot\text{kg}^{-1}$) A3 (0.75)
2015	2242	2242	2242	2242
2100 RCP 2.6	2242	2243	2244	2247
2100 RCP 4.5	2242	2250	2254	2278
2100 RCP 6.0	2242	2255	2264	2306
2100 RCP 8.5	2242	2263	2276	2342

Table 4.14: The percent offset in pH values for each sensitivity analysis of the case study relative to the standard run in the final year 2100 of the different RCP emissions scenarios.

	TA:DIC = 0.15	TA:DIC = 0.25	TA:DIC = 0.75
RCP 2.6	10%	16%	47%
RCP 4.5	13%	21%	60%
RCP 6.0	14%	23%	64%
RCP 8.5	15%	24%	64%

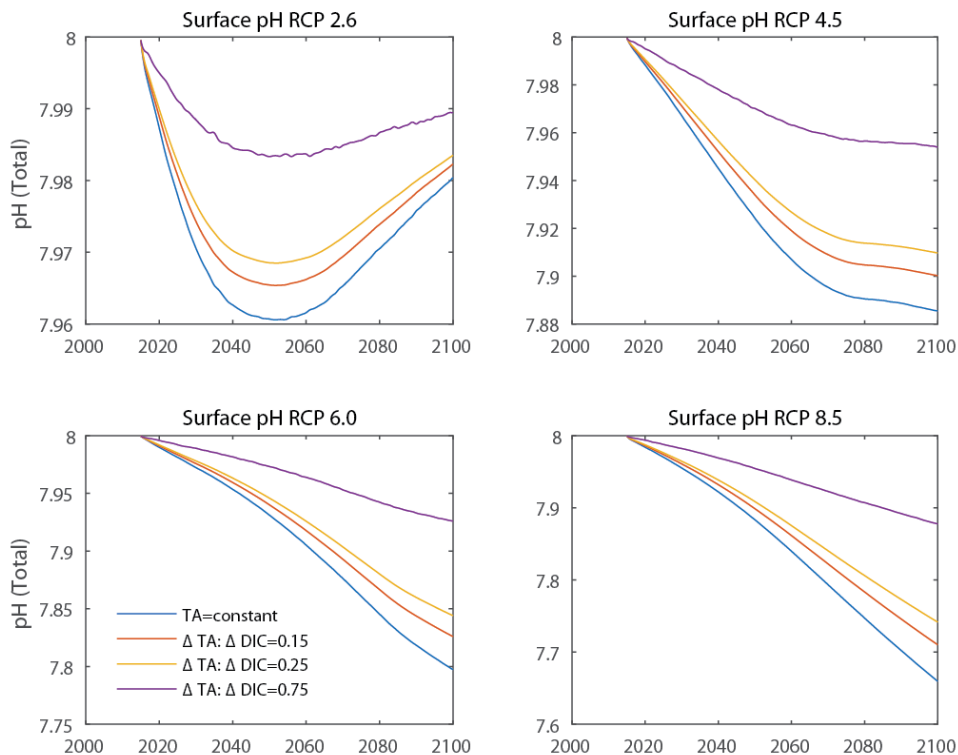


Figure 4.20: Surface water pH from 2015 to 2100 under the various surface $\Delta\text{TA}:\Delta\text{DIC}$ ratios. Increased TA concentrations buffer the surface water at higher pH values. Note that the pH range on the y-axis is different for each plot.

4.7.2 Case Study 2: Air-Sea CO_2 Gas Exchange

The case study involving changing surface water TA showed that the rate of atmospheric pCO_2 increase outpaces that of the seawater increase, despite declining pH and Ω and rising seawater pCO_2 . This result is different from the standard run - where seawater pCO_2 increases more rapidly than atmospheric - and leads to a “crossover” where the surface water switches from acting as a source of CO_2 to the atmosphere to a sink. Figure 4.21 shows the air-sea gas exchange for each sensitivity analysis of the case study under all four RCP scenarios. Under RCP 2.6, the reef flat remains a source of CO_2 to the atmosphere throughout the simulation, but under the other three RCP scenarios there is a crossover to a sink for case studies A2 and A3. The

crossover occurs earlier in the century with higher CO₂ emissions to the atmosphere from anthropogenic sources. Under RCP 8.5 and a $\Delta TA:\Delta DIC$ of 0.25, the surface water is predicted to switch to a sink of CO₂ from the atmosphere by 2076. While the reef flat surface water does not switch to a sink under RCP 6.0, it approaches the crossover by the end of the century and would be projected to switch shortly after 2100. The A3 case study produced a crossover by the year 2047, 2050, and 2037 under RCP 4.5, 6.0, and 8.5, respectively. This result supports the conclusion of Massaro et al. (2012) for Southern Kaneohe Bay of a future switchover of CO₂ exchange direction, and the SOCM results of Andersson et al. (2005, 2006) for the global coastal ocean. A switch from source to sink behavior may not have a large effect on the overall reef carbon balance of the Kaneohe Bay barrier reef ecosystem because air-sea gas exchange is small relative to other fluxes, and residence time is short enough that excess carbon, that would have otherwise degassed, will mostly be transported off the reef as DIC. However, this may result in more CO₂ accumulation in the inner Kaneohe Bay lagoon. On other reefs, where residence time is much longer and degassing is a large factor in sustaining pH and pCO₂ at levels that encourage reef accretion, a switch to sink behavior could have significant implications on biogenic calcification rates and NECP.

Changes in respiration and photosynthesis will also strongly influence the direction of air-sea gas exchange and are discussed in Section 4.7.4. In the standard run and the previously described case studies, NEP increases over the length of the simulation as both photosynthesis and respiration respond positively to rising temperatures. As previously mentioned, it is not well-known how NEP will change under future conditions of high temperature and OA, although Mackey et al. (2013) showed that photosynthetic rates of *Synechococcus* - which is found in abundance in Kaneohe Bay - increase with rising

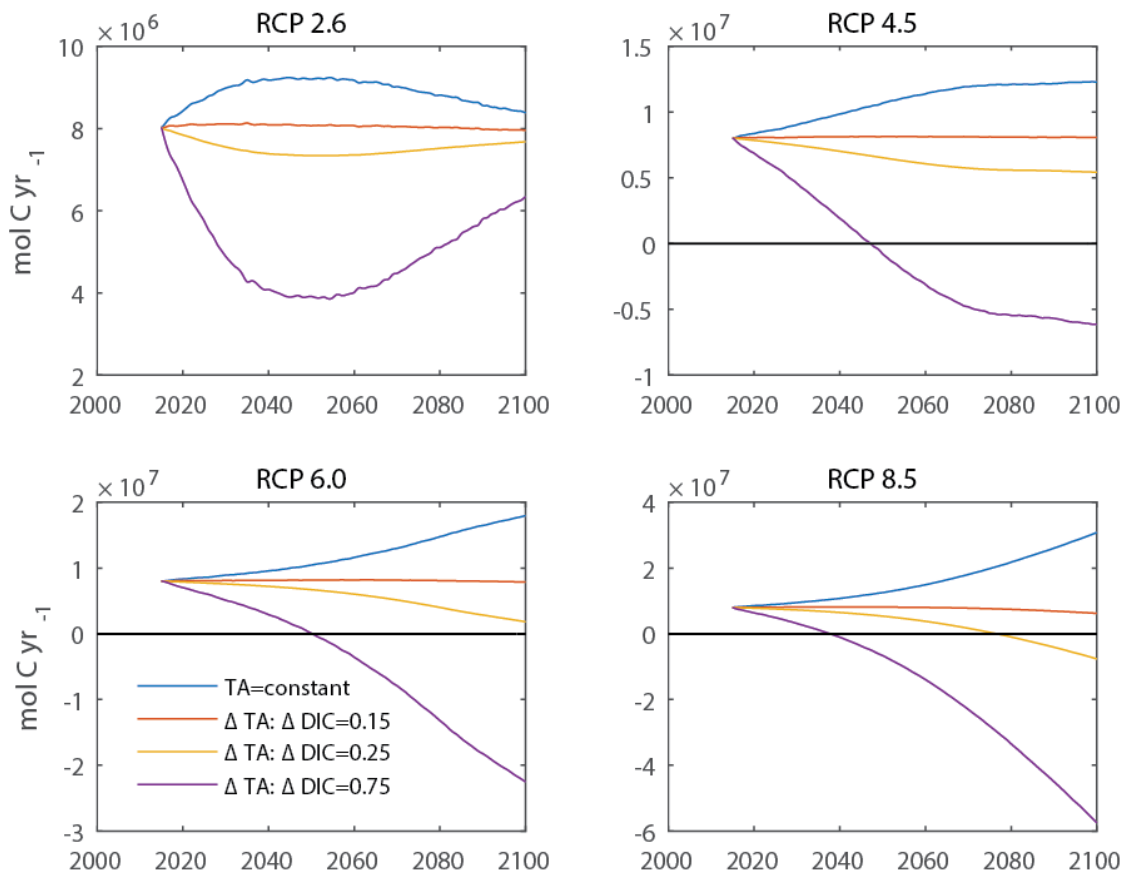


Figure 4.21: Air-sea CO_2 gas exchange under the various surface water $\Delta\text{TA}:\Delta\text{DIC}$ ratios from 2015 to 2100. The buffering effect on the CO_2 -carbonic acid system of increased TA leads to a “crossover” in some scenarios where the surface water switches from being a source of CO_2 to the atmosphere to a sink. The horizontal black line represents the crossover from source to sink.

temperatures. The amount of increase and the maximum growth temperature were dependent on the strain, but samples from Palau and Tahiti – the only Pacific sites studied – had maximum growth temperatures of $24\text{ }^\circ\text{C}$ and $>27\text{ }^\circ\text{C}$, respectively. These temperature thresholds are well within the predicted range of temperatures under at least RCP 6.0 and 8.5. A vast majority of the photosynthetic activity on the reef flat is associated with corals and coralline algae, which are also expected to increase their photosynthesis under rising temperatures and pCO_2 (Langdon and Atkinson 2005). It is likely that photosynthetic rates on the reef will first respond positively to rising temperatures before leveling off or, depending on coral mortality, even declining, while

respiration will almost certainly continue to increase with rising temperatures and a continuous supply of DOC. This scenario would lead to a decline in NEP by the end of the century.

If NEP were to decrease, $p\text{CO}_2$ on the reef would increase and contribute to a stronger seawater source, potentially counteracting some of the effect of increasing TA concentrations and vice versa. To elucidate further these effects, an additional parameter, the photosynthetic Q_{10} , was decreased and surface water $\Delta\text{TA}:\Delta\text{DIC}$ ratios were set at 0.25 and 0.75. The $\Delta\text{TA}:\Delta\text{DIC}$ values were chosen because both of these ratios resulted in the reef water becoming a sink under certain RCP scenarios. The photosynthetic Q_{10} was reduced to 1.5, while the respiration Q_{10} was left equal to 2. Under this scenario, respiration would increase as a function of temperature at a faster rate than photosynthesis, resulting in a decline in NEP. It is important to note that, even under the largest temperature change (RCP 8.5), the ecosystem never became net heterotrophic (negative NEP) even though NEP decreased by ~50%. Table 4.15 shows the air-sea flux under each of these model runs by 2100. It is clear that decreasing NEP mitigates some of the effect of changing TA (i.e., increases the source strength of the reef surface water). This effect is much stronger under the $\Delta\text{TA}:\Delta\text{DIC} = 0.25$ scenario, where decreasing NEP increases air-sea flux nearly 40%. Under the $\Delta\text{TA}:\Delta\text{DIC} = 0.75$ scenario, the large change in TA overwhelms any effect of increasing $p\text{CO}_2$ due to changing NEP, resulting in an increase in source strength of only 1-3%. These outputs clearly show how strongly the CO_2 source or sink behavior of coral reef ecosystems depends on how NEP and NECP will respond to changing future temperatures and OA conditions (e.g., Gattuso et al., 1995; Andersson and Mackenzie, 2004).

Table 4.15: Air-sea CO₂ gas exchange rates under various *CRESCAM* simulations. Each row shows the flux in 10⁶ mol C·yr⁻¹ in the year 2100 under the various RCP scenarios for each case study. The percentages in parentheses are the difference between the flux in combined case study (changing both TA:ΔDIC and Q₁₀) and the flux where Q₁₀ was not changed (i.e., the adjacent column to the left). The NEP % change column is the change in NEP relative to 2015 when the photosynthetic Q₁₀ was changed to 1.5. All values in 10⁶ mol C·yr⁻¹.

	Constant TA	ΔTA:ΔDIC = 0.25	ΔTA:ΔDIC = 0.25 Q _{10 photo} = 1.5	ΔTA:ΔDIC = 0.75	ΔTA:ΔDIC = 0.75 Q _{10 photo} = 1.5	NEP % Change
2015	8.03	8.03	8.03	8.03	8.03	
RCP 2.6	8.38	7.68	7.78 (1%)	6.34	6.39 (1%)	-5%
RCP 4.5	12.26	5.44	5.84 (7%)	-6.14	-5.98 (3%)	-17%
RCP 6.0	17.85	1.83	2.55 (39%)	-22.52	-22.28 (1%)	-26%
RCP 8.5	30.45	-7.64	-5.74 (25%)	-57.45	-56.91 (1%)	-49%

4.7.3 Case Study 3: Sediment and Framework Porewaters

Because TA was calculated based on changes in DIC, several ΔTA:ΔDIC ratios were also employed to evaluate the effects of different porewater microbial and biogeochemical processes on the sediment-porewater system carbon budget. When the ΔTA:ΔDIC ratio in the oxic porewater was set to 1, compared to the default of 0.85, porewater chemistry changed considerably. Under all non-mitigation emissions scenarios, the overall decline in pH was less than half relative to the standard scenario (see Figure 4.22). When ΔTA:ΔDIC is greater than 0.95, saturation state increases (see Figure 4.23), leading to a decrease in Mg-calcite dissolution and an increase in aragonite precipitation (NECP increases). Changes in the NECP of the oxic layer sediment-porewater system are presented in Table 4.16 for both the standard run and scenario B1. While this scenario is likely unrealistic – as many studies show dissolution and declining Ω in the upper sediments (e.g., Moulin et al., 1985; Morse and Mackenzie, 1990; Morse et al., 2006; Cyronak et al., 2013a; Cyronak et al., 2013b; Drupp et al., in review; Chapter 3) - it serves as a valid comparison to illustrate how sensitive the sediment-porewater system is to small changes in biogeochemical (e.g., microbial) processes. This result fits well with the

assertion by Morse and Mackenzie (1990) that porewater CO_2 -carbonic acid system chemistry is mostly controlled by microbial processes involving oxidation of organic matter, production of CO_2 , and precipitation/dissolution of carbonate phases. In addition, dissolution rates are very sensitive to changes in Ω (Andersson et al. 2005) and that assertion is reflected in the *CRESCAM* model outputs.

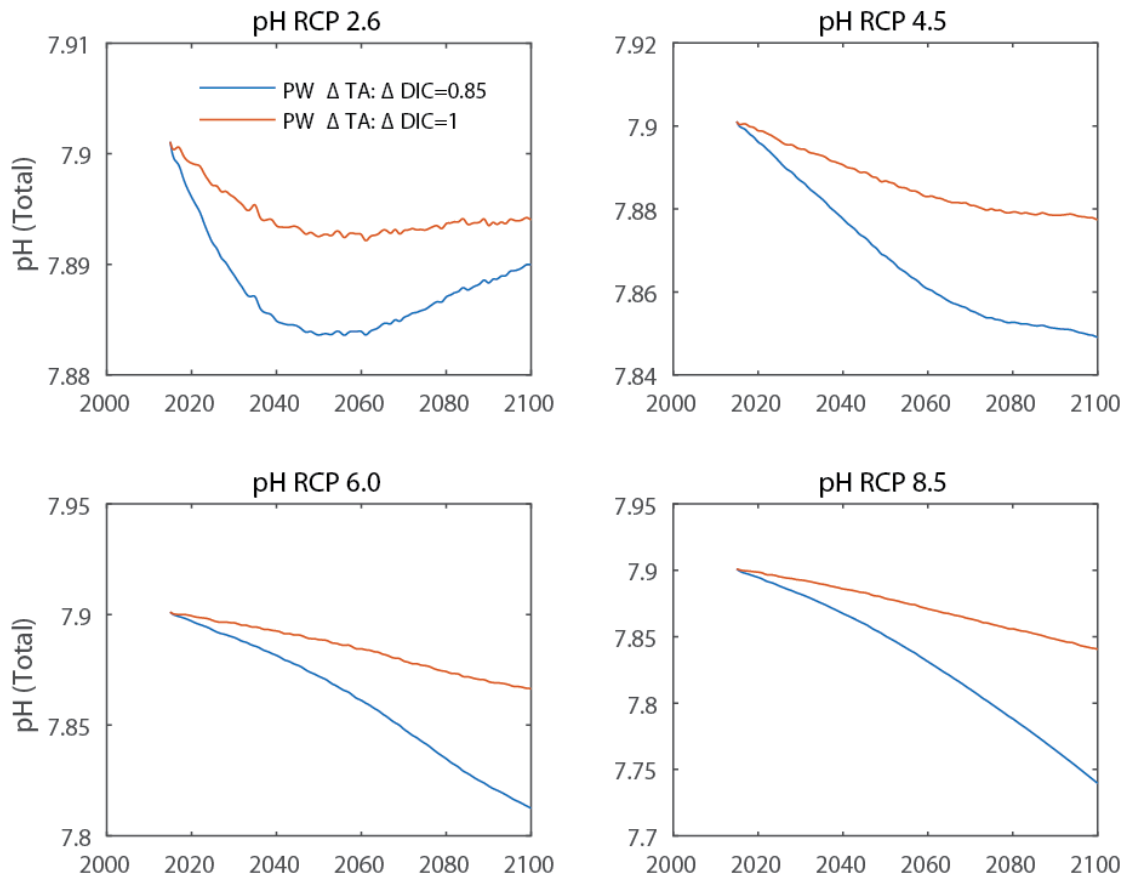


Figure 4.22: pH numerical outputs from 2015 to 2100 from the standard *CRESCAM* run (blue) and a case study where the $\Delta\text{TA}:\Delta\text{DIC}$ ratio of the oxic porewater was set to 1 (red). The higher ratio leads to more TA being released into the porewater and results in a partial buffering effect on the pH.

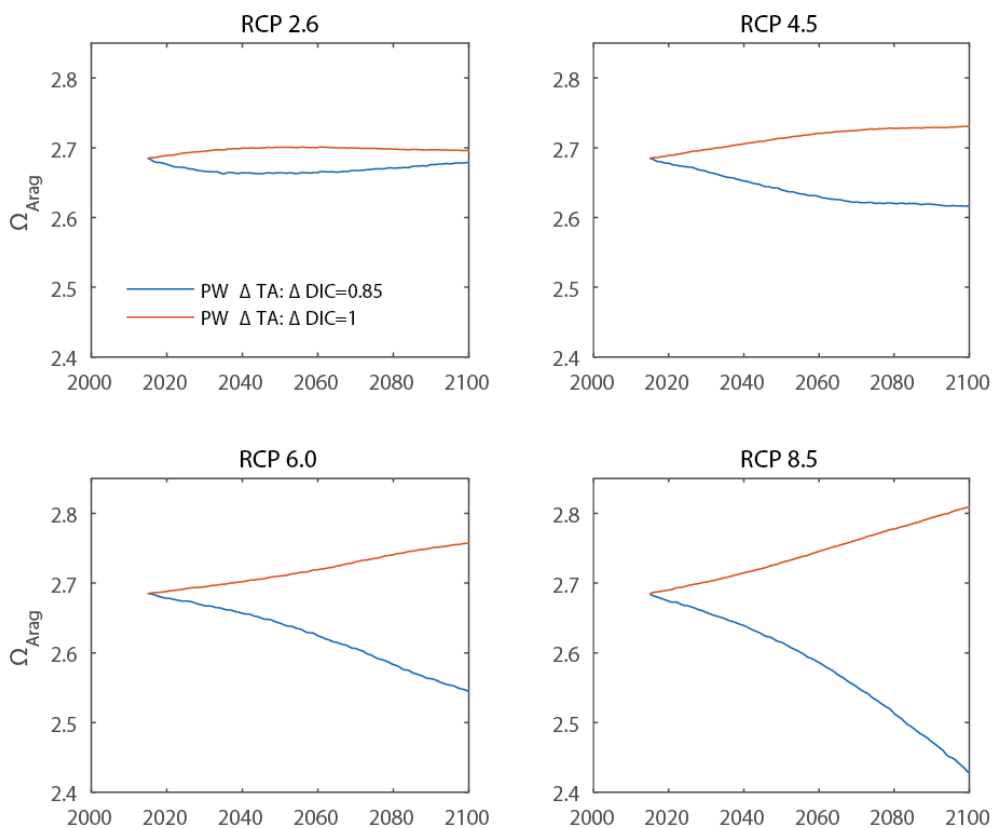


Figure 4.23: Aragonite saturation state of the oxic porewater from 2015 to 2100 under the standard *CRESCAM* run (blue) and a case study where $\Delta TA:\Delta DIC$ was set to 1 (green). A $\Delta TA:\Delta DIC$ ratio greater than 0.95 leads to an increase in saturation state, where a ratio less than 0.95 leads to a decrease.

Table 4.16: NECP in the oxic layer sediments for the *CRESCAM* standard run and the $\Delta TA:\Delta DIC = 1$ analysis. Note that values are in $10^6 \text{ mol C}\cdot\text{yr}^{-1}$ and negative values indicate net dissolution. A $\Delta TA:\Delta DIC$ ratio greater than 0.95, as is the case in the sensitivity analysis, causes Ω to increase, leading to declines in carbonate dissolution and increases in carbonate precipitation. Overall this has the effect of increasing NECP. The percent change is the increase in NECP, relative to the standard run, where $\Delta TA:\Delta DIC$ in the oxic porewater is set to 1.

$10^6 \text{ mol C}\cdot\text{yr}^{-1}$	$\Delta TA:\Delta DIC = 0.85$	$\Delta TA:\Delta DIC = 1$	Percent Change
2015	-4.34	-4.34	
RCP 2.6	-4.68	-4.30	8%
RCP 4.5	-6.69	-3.88	42%
RCP 6.0	-9.21	-3.48	62%
RCP 8.5	-14.96	-2.97	80%

Despite the large changes in local NECP that result from altering the $\Delta\text{TA}:\Delta\text{DIC}$, the oxic-layer porewater chemistry and any release of TA appear to have no influence on the chemistry of the overlying seawater, where carbon system parameters (e.g., Ω , DIC, pH) do not change under various oxic-layer porewater scenarios. As previously discussed in Section 4.6.2 – and it cannot be overemphasized – there is simply not enough TA released into the surface water, from the relatively small area of sandy sediments on the Kaneohe Bay barrier reef, to increase the surface water TA concentration by any appreciable amount. In addition, because the residence time of surface water is so short, additional TA, produced from geochemical changes in the sediments, is removed from the system rapidly. Therefore, dissolution of the barrier reef sandy sediments is not expected to represent a large source of alkalinity to the water column. These results are in line with those of other studies regarding buffering effects of sediment dissolution on reef surface waters (e.g., Andersson et al., 2006; Morse et al., 2006; Andersson and Mackenzie, 2011). However, changes in sediment dissolution do affect the overall net ecosystem carbonate production (NECP) of the reef system.

The effects of changes in the framework-porewater CO_2 -carbonic acid system parameters were also examined by altering the $\Delta\text{TA}:\Delta\text{DIC}$ within the framework. While the ratio of 1.2 is a reasonable and proven estimate for this system (Tribble et al. 1990), a ratio of 0.92 was employed in a case study to examine the effects, if any, of a decreasing Ω on the framework reservoir and the overlying water column. The change caused the framework NECP to decrease, as the Mg-calcite dissolution rate increased and the aragonite precipitation rate decreased. Despite the order of magnitude change in framework NECP (up to 80% decrease under RCP 8.5), due primarily to enhanced Mg-calcite dissolution and subsequent release of TA out of the framework, the overlying water column chemistry remained unaffected. However, this large

decline in framework NECP led to a significant difference in the decline in overall reef NECP over the century relative to the standard run, as seen in Table 4.17.

The results of the porewater sensitivity analyses show that, contrary to the conclusions of studies such as Barnes and Cuff (2000) and Halley and Yates (2000), carbonate mineral dissolution in reef sediments will buffer corals from increasing CO₂ concentrations, this scenario seems unlikely for the Kaneohe Bay barrier reef ecosystem. The modeled crestal portion of the reef does not release sufficient alkalinity into the overlying waters through dissolution of carbonate substrates in the sediments and framework to have any significant effect on the surface water carbon chemistry; thus, this lack of alkalinity buffer to mitigate the effects of OA on the major framework building corals and coralline algae is absent. However, we point out that this may not be the case for other reefs because the strength of the buffering effect is also highly dependent on the residence time of the surface water on the reef, just as residence time was shown to be a crucial factor in carbonate dissolution for the coastal ocean (Andersson et al. 2003). Reef environments with much longer residence time may accumulate enough TA to display *partially* offsetting effects on pH and Ω similar to those demonstrated by Andersson et al. (2013). The results of the *CRESCAM* numerical outputs show that, despite the limited impact on the surface water chemistry, changes in dissolution rates clearly have a significant impact on the accumulation of carbonate on a reef, regardless of changes in biogenic calcification rates. The process of dissolution is far more sensitive to OA than biogenic calcification and changes in dissolution rates could be the ultimate control on whether reefs remain net accreting or become net eroding (Eyre et al. 2014). This is regardless of whether or not carbonate dissolution produces sufficient TA to mitigate partially changes in pH. It is clear that we must understand

more fully the biogeochemical and physical (e.g., flushing rates) processes occurring within the sediments and framework in order to predict accurately future NECP for reef systems.

Table 4.17: NECP of the overall system under the standard run (column 2) and sensitivity analysis (column 3) where the TA:DIC ratio in the framework was lowered from 1.2 to 0.92. The percentage in parentheses is the change in NECP relative to 2015 for each scenario. Dissolution in the framework has a significant effect on the overall NECP of the reef system. All values in $10^8 \text{ mol C}\cdot\text{yr}^{-1}$

	$\Delta\text{TA}:\Delta\text{DIC} =$ 1.2	$\Delta\text{TA}:\Delta\text{DIC} =$ 0.92
2015	7.69	7.69
RCP 2.6 2100	7.91(3%)	7.89 (3%)
RCP 4.5 2100	7.67 (0%)	7.21 (-6%)
RCP 6.0 2100	7.15 (-7%)	6.14 (-20%)
RCP 8.5 2100	6.39 (-17%)	4.98 (-35%)

4.7.4 Case Study 4: Analysis of NEP

NEP clearly exerts a strong influence on the carbon budget of the Kaneohe Bay barrier reef ecosystem and on other reefs. The standard *CRESCAM* runs, as well as the previously discussed case studies, all relied on changes in temperature and the photosynthetic/respiration response to temperature as the driving force behind changing NEP. The Kaneohe Bay barrier reef is influenced very little by terrestrial runoff, unlike reefs and waters of the southern and northern sectors of the bay (Tomlinson and De Carlo 2003; Ringuet and Mackenzie 2005; De Carlo et al. 2007; Hoover and Mackenzie 2009), and we expect there to be fairly little change in nitrogen or organic matter loading of the barrier reef waters as this century progresses, despite any changes in land use that may occur along the central bay coast. However, many patch and fringing reefs within Kaneohe Bay and inner reefs of the Great Barrier Reef in Australia, for example, are expected to be heavily impacted by land use change over the coming decades.

Therefore, a case study involving several sensitivity analyses was run using *CRESCAM* under conditions of increasing nitrogen and organic carbon fluxes, thereby affecting both gross photosynthesis and respiration and, ultimately, sedimentation and potential sequestration or remineralization of organic carbon in the reef sediments and framework. In the first set of model runs, the concentration of organic carbon transported onto the reef by 2100 was increased by 25% (E1), 50% (E2), and 100% (E3) over its flux in 2015. Organic carbon was assumed to increase linearly over the century to reach the final values. A doubling of nitrate loading (F1) to the reef waters by 2100 was assumed in the second set of model runs. Organic carbon was increased via the CF_{O_2} flux (open ocean to reef). Although the OC in this model run is meant to be a result of land use change and terrestrial runoff, the model does not distinguish between sources of OC and, therefore, increasing CF_{O_2} is a valid approach to achieve the desired end result. The effect of nitrogen on photosynthesis was controlled with the fN term in the photosynthesis equation employed in *CRESCAM* (i.e., doubling nitrogen will double the photosynthetic rate, assuming that nitrogen is the limiting nutrient).

Under each OC loading scenario (and each RCP emissions scenario), gross respiration exceeded gross photosynthesis by 2100, causing a switch from positive to negative NEP at some point during the century. The pH declined slightly more than in the standard run, falling an additional 0.03-0.05 units due to the higher levels of pCO_2 . When the OC flux was increased by 100% over the standard simulation, the source strength was enhanced, and air-sea gas exchange approximately doubled. As previously discussed, a decrease in NEP leads to an increased CO_2 source strength of the surface waters but also to a greater decline in pH. Higher concentrations of surface TOC lead to increased sedimentation and enhanced sediment/framework respiration of organic matter, driving further undersaturation of the porewater with respect to carbonate

minerals. However, even under the most extreme scenario – RCP 8.5 with a 100% increase in OC – the porewater *still* never becomes undersaturated with respect to aragonite. This is further evidence that there is virtually no feasible model scenario for the Kaneohe Bay barrier reef in which sedimentary aragonite would undergo bulk dissolution.

In the second set of model runs, where nitrogen loading was doubled, photosynthesis was effectively doubled, leading to an increase in OC in both the surface water, sediments, and framework as sedimentation of OC increased. This is the opposite result to the outcome of the previously described OC loading scenario. In addition, the elevated production of OC actually resulted in the system sustaining higher rates of respiration than in the standard scenarios. Despite the rise in respiration in the sediments, NEP increased nearly an order of magnitude as the two processes rapidly diverged. NEP was nearly $400 \text{ mmol C} \cdot \text{m}^{-2} \cdot \text{d}^{-1}$ by the end of the simulation under RCP 8.5 (as compared to $52 \text{ mmol C} \cdot \text{m}^{-2} \cdot \text{d}^{-1}$ in the standard scenario). Depending on the emissions scenarios, a drawdown in water column pCO_2 of between 50-100 μatm due to increased productivity caused a reversal in the direction of the air-sea gas exchange. Final gas exchange fluxes were on the order of $-2 \times 10^6 \text{ mol C} \cdot \text{yr}^{-1}$ for this model run. Drupp et al. (2011) reported this same result in the southern sector of Kaneohe Bay, where the direction of gas exchange in the surface waters reversed following large storm events due to a temporary increase (as much as 25x above baseline) in nitrate concentrations from terrestrial input and a large photosynthetic-driven drawdown of pCO_2 .

It is clear that large changes in organic matter or inorganic nutrient fluxes can have a substantial effect on the reef environment. However, it is unlikely that land use change would alter only OC or nitrate, as in the previous model runs, so a combination of both changes was utilized in a third set of sensitivity analyses. Again, the OC flux was increased by 25% (E1F1)

and 100% (E3F1) over the simulation. In both cases, nitrogen loading was also doubled. As expected, the results fell in between those of the previous two simulations, because the effect of OC was somewhat mitigated by the concomitant change in nitrogen loading. NEP increased under all emissions scenarios for these simulations, increasing nearly an order of magnitude when OC was increased only by 25% (see Table 4.18). Under scenario E3F1, the air-sea CO₂ flux increased in source strength, but decreased under E1F1. In the latter scenario, under RCPs 2.6 and 4.5, the surface water switched to being a sink of CO₂ from the atmosphere because the limited increases in temperature and the subsequent effect on respiration were not enough to counteract the drawdown of pCO₂ from enhanced photosynthesis.

An unexpected consequence of the large increase in OC and nitrogen fluxes was the effects on the NECP within the anoxic sediments and framework. The large increase in surface TOC (as a result of both the OC flux and increased productivity) led to higher rates of sedimentation so that the sediment environments could sustain much higher rates of respiration as compared to other scenarios. The production of metabolic CO₂ and alkalinity, due to the $\Delta\text{TA}:\Delta\text{DIC}$ ratio of 1.2, was enough to cause the NECP in the anoxic sediments to become positive (i.e., precipitation exceeding dissolution) under all RCP scenarios. Enough alkalinity was added back into the water that by 2100, under RCP 8.5, the anoxic porewater was in metastable equilibrium with 15% Mg-calcite. This was the only case study where such a change in NECP occurred. Under RCP 8.5, even the framework NECP became positive. This outcome was predicted by Morse and Mackenzie (1990), who showed that increased organic matter and sulfate reduction in the sediment-porewater system would raise saturation states of the porewater with respect to the various carbonate phases. As discussed in Section 4.7.3, changes in the framework NECP are large enough to alter the overall reef NECP (unlike the anoxic system), as

shown in Table 4.19. In all emissions scenarios except for RCP 8.5, the changes in the framework are large enough to actually cause an increase in overall reef NECP. The increase in sedimentation and porewater respiration also increased dissolution in the oxic-layer. These model runs further serve to show the importance of OC fluxes and concentrations on early diagenetic processes within the sediments and framework.

The framework NECP results further show that it is critical that we understand the metabolic processes occurring within the reef ecosystem. Small changes in alkalinity production coupled with porewater respiration have the potential to change completely the carbon balance of reefs because the overwhelming majority of the carbon in reefs is stored in the sediment/framework reservoirs. In addition to porewater processes, understanding how photosynthesis and respiration will react to changing temperatures is of equal importance, as shown by the model runs altering Q_{10} and the nitrogen balance.

Table 4.18: NEP under various scenarios of increasing organic carbon and nitrogen loading to the reef. 100% OC refers to the sensitivity analysis where OC flux onto the reef was doubled over the century and 2x N refers to the simulation where nitrogen loading was doubled by 2100.

NEP ($\text{mmol}\cdot\text{m}^{-2}\cdot\text{d}^{-1}$)	Standard Run	100% OC	2x N	100% OC 2x N	25% OC 2x N
2015	45	45	45	45	45
RCP 2.6 2100	47	-204	359	109	297
RCP 4.5 2100	48	-210	372	113	307
RCP 6.0 2100	49	-215	378	115	312
RCP 8.5 2100	52	-226	400	121	330

Table 4.19: NECP of the overall reef system under the standard run and the case study where OC and N were doubled over the length of the simulation, leading to changes in productivity and respiration throughout the system. The percentages in parentheses are the percent change in NECP by 2100 relative to the initial value in 2015. NECP values are in $10^8 \text{ mol C}\cdot\text{yr}^{-1}$.

NECP ($10^8 \text{ mol C}\cdot\text{yr}^{-1}$)	Standard Run	100% OC 2x N
2015	7.69	7.69
RCP 2.6 2100	7.91 (3%)	8.58 (12%)
RCP 4.5 2100	7.67 (0%)	8.31 (8%)
RCP 6.0 2100	7.15 (-7%)	7.82 (2%)
RCP 8.5 2100	6.39 (-17%)	7.02 (-9%)

4.8 Conclusions

The results of the *CRESCAM* simulations show that the Kaneohe Bay barrier reef ecosystem will be affected substantially by increasing ocean acidification and rising temperatures through a variety of processes. Biogenic calcification by corals and other calcifying organisms is expected to decrease significantly, while bioerosion increases, leading to a decrease in NECP and carbonate accumulation on the barrier reef. Despite these changes and enhanced carbonate dissolution rates in some sediment domains, it is unlikely that the barrier reef will reach a state of net erosion (negative NECP) by the end of the century, even under the worst case scenarios for temperature, CO₂ emissions, and land use changes. Dissolution and precipitation of carbonate substrates within the sediments are highly dependent on microbial processes and the respiration of organic matter, via oxic respiration or various anoxic processes such as sulfate reduction and denitrification. Oxic respiration of organic matter in the sediments, which may increase with enhanced NEP in the surface water (and increased sedimentation of OC) or changes in terrestrial nutrient loading, is expected to lower pH and Ω , resulting in more sedimentary carbonate dissolution. However, the release of excess TA from dissolution will not be enough to significantly buffer changes in surface water pH as a result of ocean acidification. In the anoxic and framework porewaters, processes such as sulfate reduction can increase pH and

Ω , and *CRESCAM* demonstrates that increased sedimentation of organic carbon to these domains will result in higher rates of carbonate precipitation. The future of the magnitude and direction of air-sea CO₂ gas exchange is also highly dependent on changes in the NEP and NEC of the barrier reef system. A decrease in NEC, resulting in higher concentrations of TA on the reef, or an increase in NEP from enhanced photosynthesis, would decrease the source strength of the surface water and in some cases (e.g., RCP 8.5) may result in the surface waters switching from acting a source of CO₂ to a sink.

The various case studies and sensitivity analyses employed in *CRESCAM* show that the biogeochemistry of the reef will change greatly depending on how certain processes react to changing temperature and pH. The case studies also serve to illustrate the importance of fully understanding and constraining the many physical and biogeochemical parameters and processes on coral reefs if we hope to make better predictions about the future of these ecosystems. The process of carbonate dissolution appears to be much more sensitive to OA than calcification and thus increases in dissolution, coupled with the likely decreases in calcification, could serve to significantly alter the carbon balance of the barrier reef.

The *CRESCAM* architecture can be applied to any reef system where the biogeochemical and physical parameters are available. While some of the results of *CRESCAM* for the Kaneohe Bay barrier reef do not fully agree with other modeling studies for global reefs, it is important to recognize that every reef system is different and will respond to OA and temperature change in entirely different, sometimes counterintuitive, ways depending on physical characteristics such as the amount of sediment and its mineralogy, the residence time and circulation of the reef system, and the impact of land use changes and terrestrial runoff. The relatively short residence time of the surface waters of the Kaneohe Bay barrier reef may serve to limit some of the

declining open ocean pH as the reef is rapidly flushed and $p\text{CO}_2$ may not build up to the same levels as on a reef with a residence time of several days. While global reef estimates and models are valuable, we would caution against applying the results of any global model to a single reef ecosystem (and vice versa). Nevertheless it is apparent that future OA and temperature change as a result of anthropogenic CO_2 emissions is certain to alter significantly the carbon biogeochemistry of coral reef ecosystems.

4.9 References

- Agegian CR (1985) *The Biogeochemical Ecology of Porolithon Gardineri* (Foslie). University of Hawai'i
- Agegian CR, Mackenzie FT (1989) Calcareous organisms and sediment mineralogy on a mid-depth bank in the Hawaiian Archipelago. *Pacific Sci* 43:56–66.
- Andersson A, Mackenzie F (2004) Shallow-water oceans: a source or sink of atmospheric CO₂? *Front Ecol.* 2:348–353.
- Andersson A, Mackenzie F, Ver L (2003) Solution of shallow-water carbonates: An insignificant buffer against rising atmospheric CO₂. *Geology* 31:513–516.
- Andersson AJ (2006) *Biogeochemical Consequences of Rising Atmospheric CO₂ and Ocean Acidification in the Global Coastal Ocean and Carbonate Ecosystems*. University of Hawai'i
- Andersson AJ (2015) A fundamental paradigm for coral reef carbonate sediment dissolution. *Front Mar Sci* 2:1–8. doi: 10.3389/fmars.2015.00052
- Andersson AJ, Gledhill D (2013) Ocean acidification and coral reefs: effects on breakdown, dissolution, and net ecosystem calcification. *Ann Rev Mar Sci* 5:321–48. doi: 10.1146/annurev-marine-121211-172241
- Andersson AJ, Kuffner IB, Mackenzie FT, et al (2009) Net Loss of CaCO₃ from a subtropical calcifying community due to seawater acidification: mesocosm-scale experimental evidence. *Biogeosciences* 6:1811–1823. doi: 10.5194/bg-6-1811-2009
- Andersson AJ, Mackenzie FT (2011) Ocean acidification: setting the record straight. *Biogeosciences Discuss* 8:6161–6190.
- Andersson AJ, Mackenzie FT, Lerman A (2005) Coastal Ocean and Carbonate Systems in the High CO₂ World of the Anthropocene. *Am J Sci* 305:875–918.
- Andersson AJ, Mackenzie FT, Lerman A (2006) Coastal ocean CO₂–carbonic acid–carbonate sediment system of the Anthropocene. *Global Biogeochem Cycles* 20:GB1S92. doi: 10.1029/2005GB002506
- Andersson AJ, Yeakel KL, Bates NR, de Putron SJ (2013) Partial offsets in ocean acidification from changing coral reef biogeochemistry. *Nat Clim Chang* 4:56–61. doi: 10.1038/nclimate2050
- Atkinson MJ, Falter JL (2003) Biogeochemistry of coral reefs. In: Black KD, Shimmield GB (eds) *Biogeochemistry of Marine Systems*. Blackwell Publishing Ltd., pp 40–64
- Barkley HC, Cohen AL, Golbuu Y, et al (2015) Changes in coral reef communities across a natural gradient in seawater pH. *Sci Adv* 1:E1500328.
- Barnes DJ, Cuff C (2000) Solution of reef rock buffers seawater against rising atmospheric CO₂. In: Hopley D, Al. E (eds) *Proceedings of the 9th International Coral Reef Symposium* 2. Indonesia, p 248
- Bates NR, Samuels L, Merlivat L (2001) Biogeochemical and physical factors influencing seawater f CO₂ and air-sea CO₂ exchange on the Bermuda coral reef. *Limnol Oceanogr*

46:833–846. doi: 10.4319/lo.2001.46.4.0833

- Bathen KH (1968) A Descriptive Study Of The Physical Oceanography Of Kaneohe Bay, Oahu, Hawai'i. University of Hawai'i
- Berner RA (1980) Early Diagenesis: A Theoretical Approach. Princeton University Press, Princeton, NJ
- Berner RA, Westrich JT, Graber R, et al (1978) Inhibition of aragonite precipitation from supersaturated seawater; a laboratory and field study. *Am J Sci* 278:816–837.
- Bouillon S, Dehairs F, Velimirov B, et al (2007) Dynamics of organic and inorganic carbon across contiguous mangrove and seagrass systems (Gazi Bay, Kenya). *J Geophys Res Biogeosciences* 112:1–14. doi: 10.1029/2006JG000325
- Burton EA, Walter LM (1990) The role of pH in phosphate inhibition of calcite and aragonite precipitation rates in seawater. *Geochim Cosmochim Acta* 54:797–808.
- Clausen CD, Roth A (1975) Effect of temperature and temperature adaptation on calcification rate in the hermatypic coral *Pocillopora damicornis*. *Mar Biol* 33:93–100.
- Climate Explorer CMIP 5 Scenario Runs. <http://climexp.knmi.nl/>.
- Coles S, Jokiel PL (1978) Synergistic effects of temperature, salinity, and light on hermatypic coral *Montipora verrucosai*. *Mar Biol* 49:187–195.
- Cox E, Ribes M, Kinzie RA I (2006) Temporal and spatial scaling of planktonic responses to nutrient inputs into a subtropical embayment. *Mar Ecol Prog Ser* 324:19–35. doi: 10.3354/meps324019
- Cyronak T, Santos IR, Eyre BD (2013a) Permeable coral reef sediment dissolution driven by elevated p CO₂ and pore water advection. *Geophys Res Lett* 40:4876–4881. doi: 10.1002/grl.50948
- Cyronak T, Santos IR, McMahon A, Eyre BD (2013b) Carbon cycling hysteresis in permeable carbonate sands over a diel cycle : Implications for ocean acidification. *Limnol Oceanogr* 58:131–143. doi: 10.4319/lo.2013.58.1.0131
- De Carlo EH, Hoover DJ, Young CW, et al (2007) Impact of storm runoff from tropical watersheds on coastal water quality and productivity. *Appl Geochemistry* 22:1777–1797. doi: 10.1016/j.apgeochem.2007.03.034
- Dickson AG, Millero FJ (1987) A comparison of the equilibrium constants for the dissociation of carbonic acid in seawater media. *Deep Sea Res* 34:1733–1743.
- Drupp PS, De Carlo EH, Mackenzie FT, et al (2011) Nutrient Inputs, Phytoplankton Response, and CO₂ Variations in a Semi-Enclosed Subtropical Embayment, Kaneohe Bay, Hawai'i. *Aquat Geochemistry* 17:473–498. doi: 10.1007/s10498-010-9115-y
- Drupp PS, De Carlo EH, Mackenzie FT, et al (2013) Comparison of CO₂ Dynamics and Air–Sea Gas Exchange in Differing Tropical Reef Environments. *Aquat Geochemistry* 19:371–397. doi: 10.1007/s10498-013-9214-7
- Drupp PS, De Carlo EH, Mackenzie FT Porewater CO₂-Carbonic Acid System Chemistry in Permeable Carbonate Reef Sands, *in review at Marine Chemistry*
- Dubus IG, Brown CD (2002) Organic Compounds in the Environment. *J Environ Qual* 31:227–

240.

- Eyre BD, Andersson AJ, Cyronak T (2014) Benthic coral reef calcium carbonate dissolution in an acidifying ocean. *Nat Clim Chang* 4:969–976. doi: 10.1038/nclimate2380
- Fagan KE, Mackenzie FT (2007) Air–sea CO₂ exchange in a subtropical estuarine-coral reef system, Kaneohe Bay, Oahu, Hawai‘i. *Mar Chem* 106:174–191. doi: 10.1016/j.marchem.2007.01.016
- Falter JL, Lowe RJ, Atkinson MJ, et al (2008) Continuous measurements of net production over a shallow reef community using a modified Eulerian approach. *J Geophys Res* 113:C07035. doi: 10.1029/2007JC004663
- Falter JL, Sansone FJ (2000) Shallow pore water sampling in reef sediments. *Coral Reefs* 19:93–97. doi: 10.1007/s003380050233
- Fang JKH, Mello-Athayde M a, Schönberg CHL, et al (2013) Sponge biomass and bioerosion rates increase under ocean warming and acidification. *Glob Chang Biol* 19:3581–3591. doi: 10.1111/gcb.12334
- Feely R, Doney S, Cooley S (2009) Ocean Acidification: Present Conditions and Future Changes in a High- CO₂ World. *Oceanography* 22:36–47. doi: 10.5670/oceanog.2009.95
- Fogaren KE, Sansone FJ, De Carlo EH (2013) Porewater temporal variability in a wave-impacted permeable nearshore sediment. *Mar Chem* 149:74–84. doi: 10.1016/j.marchem.2012.12.005
- Fram JP, Pawlak GR, Sansone FJ, et al (2014) Miniature thermistor chain for determining surficial sediment porewater advection. *Limnol Oceanogr Methods* 12:155–165. doi: 10.4319/lom.2014.12.155
- Frankignoulle M, Gattuso J-P, Biondo R, et al (1996) Carbon fluxes in coral reefs . II. Eulerian study of inorganic carbon dynamics and measurement of air-sea CO₂ exchanges.
- Garrels R, Wollast R (1978) Discussion of article “Equilibrium Criteria for Two-Component Solids Reacting with Fixed Composition in an Aqueous Phase - Example: the Magnesian Calcites” by D.C. Thorstenson and L. Niel Plummer. *Am J Sci* 1469.
- Gattuso J, Pichon M, Frankignoulle M (1995) Biological control of air-sea CO₂ fluxes: effect of photosynthetic and calcifying marine organisms and ecosystems. *Mar Ecol Prog Ser* 129:307–312.
- Gattuso J-P, Allemand D, Frankignoulle M (1999) Photosynthesis and Calcification at Cellular, Organismal and Community Levels in Coral Reefs: A Review on Interactions and Control by Carbonate Chemistry. *Am Zool* 39:160–183.
- Gattuso J-P, Magnan A, Bille R, et al (2015) Contrasting futures for ocean and society from different anthropogenic CO₂ emissions scenarios. *Science* (80-) 349:45–56. doi: 10.1126/science.aac4722
- Halley RB, Yates KK (2000) Will reef sediments buffer corals from increased global CO₂. In: Hopley D, Al. E (eds) *Proceedings of the 9th International Coral Reef Symposium*. Indonesia, p 248
- Hamby DM (1994) A Review of Techniques for Parameter Sensitivity Analysis of Environmental Models. *Environ Monit Assess* 32:135–154.

- Hebert AB, Sansone FJ, Pawlak GR (2007) Tracer dispersal in sandy sediment porewater under enhanced physical forcing. *Cont Shelf Res* 27:2278–2287. doi: 10.1016/j.csr.2007.05.016
- Ho DT, Law CS, Smith MJ, et al (2006) Measurements of air-sea gas exchange at high wind speeds in the Southern Ocean: Implications for global parameterizations. *Geophys Res Lett* 33:L16611. doi: 10.1029/2006GL026817
- Hoegh-Guldberg O, Mumby PJ, Hooten AJ, et al (2007) Coral reefs under rapid climate change and ocean acidification. *Science* (80-) 318:1737–1742.
- Hoover DJ, Mackenzie FT (2009) Fluvial Fluxes of Water, Suspended Particulate Matter, and Nutrients and Potential Impacts on Tropical Coastal Water Biogeochemistry: Oahu, Hawai‘i. *Aquat Geochemistry* 15:547–570. doi: 10.1007/s10498-009-9067-2
- Hubbard DK, Miller AI, Scaturro D (1990) Production and cycling of calcium carbonate in a shelf-edge reef system (St. Croix, United States, Virgin Islands) -application to the nature of reef systems in the fossil record. *J Sediment Petrol* 60:335–360.
- Intergovernmental Panel on Climate Change (2013) *Climate Change 2013: The Physical Science Basis. Contribution of Working Group I to the Fifth Assessment Report of the Intergovernmental Panel on Climate Change*. Cambridge University Press, Cambridge, United Kingdom and New York, NY, USA
- Intergovernmental Panel on Climate Change (2001) *Climate Change 2001: The Scientific Basis- Contribution of Working Group I to the Third Assessment Report of the Intergovernmental Panel on Climate Change*. Cambridge University Press, Cambridge, United Kingdom and New York, NY, USA
- Intergovernmental Panel on Climate Change (1996) *Climate Change 1995: The Science of Climate Change, Contribution of Working Group I to the Second Assessment Report of the Intergovernmental Panel on Climate Change*. Cambridge University Press, Cambridge, United Kingdom and New York, NY, USA
- Jury C, Thomas F, Atkinson M, Toonen R (2013) Buffer Capacity, Ecosystem Feedbacks, and Seawater Chemistry under Global Change. *Water* 5:1303–1325. doi: 10.3390/w5031303
- Keeling CD (2004) Seasonal and long-term dynamics of the upper ocean carbon cycle at Station ALOHA near Hawai‘i. *Global Biogeochem Cycles* 18:GB4006. doi: 10.1029/2004GB002227
- Kinsey DW (1985) Metabolism, Calcification and Carbon Production. *Proc 5th Int Coral Reef Congr* 4:505–526.
- Kinsey DW (1979) *Carbon Turnover and Accumulation by Coral Reefs*. University of Hawai‘i
- Kleypas JA, Buddemeier RW, Archer D, et al (1999) Geochemical Consequences of Increased Atmospheric Carbon Dioxide on Coral Reefs. *Science* (80-) 284:118–120.
- Kleypas JA, Feely RA, Fabry VJ, et al (2006) *Impacts of Ocean Acidification on Coral Reefs and Other Marine Calcifiers : A Guide for Future Research*, report of a workshop held 18-20 April 2005, St. Petersburg, FL, sponsored by NSF, NOAA, and the U.S. Geological Survey.
- Langdon C, Atkinson MJ (2005) Effect of elevated CO₂ on photosynthesis and calcification of corals and interactions with seasonal change in temperature/irradiance and nutrient enrichment. *J Geophys Res Ocean* 110:C09S07.

- Lavigne H, Andersson AJ, Gattuso J (2011) Seawater carbonate chemistry with R: Om.
- Lavigne H, Gattuso J (2011) Seawater carbonate chemistry with R.
- Lerman A, Mackenzie FT, Garrels RM (1975) Modeling of geochemical cycles. Phosphorus as an example. *Geol Soc Am Mem* 142:205–218.
- Lerman A, Mackenzie FT. (1975) Rates of Dissolution of Aluminosilicates in Seawater. *Earth Planet Sci Lett* 25:82–88. doi: 10.1016/j.vepar.2012.12.037
- Lewis E, Wallace DWR (1998) Program developed for CO₂ system calculations. In: ORNL/CDIAC-105. Carbon Dioxide Information Analysis Center, Oak Ridge National Laboratory, Oak Ridge, TN,
- Lowe RJ, Falter JL, Monismith SG, Atkinson MJ (2009a) Wave-Driven Circulation of a Coastal Reef–Lagoon System. *J Phys Oceanogr* 39:873–893. doi: 10.1175/2008JPO3958.1
- Lowe RJ, Falter JL, Monismith SG, Atkinson MJ (2009b) A numerical study of circulation in a coastal reef-lagoon system. *J Geophys Res* 114:C06022. doi: 10.1029/2008JC005081
- Mackenzie FT (2003) Carbonate Mineralogy and Geochemistry. In: Middleton GV (ed) *Encyclopedia of Sediments and Sedimentary Rocks*. Kluwer Academic Publishers, Boston, pp 93–100
- Mackenzie FT, Andersson AJ (2011) Biological control on diagenesis: influence of bacteria and relevance to ocean acidification. In: Reitner J, Thiels V (eds) *Encyclopedia of Geobiology*. Springer Verlag, Dordrecht, The Netherlands,
- Mackenzie FT, De Carlo EH, Lerman A (2011) Coupled C, N, P, and O Biogeochemical Cycling at the Land-Ocean Interface. In: Wolanski E, McLusky D (eds) *Treatise on Estuarine and Coastal Science, Vol 5*. Waltham: Academic Press, pp 317–342
- Mackey KRM, Paytan A, Caldeira K, et al (2013) Effect of Temperature on Photosynthesis and Growth in Marine *Synechococcus* spp. *Plant Physiol* 163:815–829. doi: 10.1104/pp.113.221937
- Marshall ATA, Clode P (2004) Calcification rate and the effect of temperature in a zooxanthellate and an azooxanthellate scleractinian reef coral. *Coral Reefs* 23:218–224. doi: 10.1007/s00338-004-0369-y
- Massaro RFS, De Carlo EH, Drupp PS, et al (2012) Multiple Factors driving Variability of CO₂ Exchange Between the Ocean and Atmosphere in a Tropical Coral Reef Environment. *Aquat Geochemistry* 18:357–386. doi: 10.1007/s10498-012-9170-7
- Mehrbach C, Culberso CH, Hawley JE, Pytkowic RM (1973) Measurement of apparent dissociation constants of carbonic-acid in seawater at atmospheric pressure. *Limnol Oceanogr* 18:897–907.
- Morse JW (1983) The kinetics of calcium carbonate dissolution and precipitation. In: Reeder RJ (ed) *Carbonates: mineralogy and chemistry*. Mineralogical Society of America, Reviews in Mineralogy, pp 227–264
- Morse JW, Andersson AJ, Mackenzie FT (2006) Initial responses of carbonate-rich shelf sediments to rising atmospheric pCO₂ and “ocean acidification”: Role of high Mg-calcites. *Geochim Cosmochim Acta* 70:5814–5830. doi: 10.1016/j.gca.2006.08.017
- Morse JW, Mackenzie FT (1990) *Geochemistry of Sedimentary Carbonates*. Elsevier,

Amsterdam, The Netherlands

- Moulin E, Jordens A, Wollast R (1985) Influence of the Aerobic Bacterial Respiration on the Early Dissolution of Carbonates in Coastal Sediments. In: Progress in Belgian Oceanographic Research. p 13
- Mucci A (1986) Growth kinetics and composition of magnesian calcite overgrowths precipitated from seawater. Quantitative influence of orthophosphate ions. *Geochim Cosmochim Acta* 50:2255–2265.
- Ohde S, Van Woesik R (1999) Carbon dioxide flux and metabolic processes of a coral reef, Okinawa. *Bull Mar Sci* 65:681–686.
- Orr JC, Fabry VJ, Aumont O, et al (2005) Anthropogenic ocean acidification over the twenty-first century and its impact on calcifying organisms. *Nature* 437:681–686. doi: 10.1038/nature04095
- Pandolfi JM, Connolly SR, Marshall DJ, Cohen AL (2011) Projecting coral reef futures under global warming and ocean acidification. *Science* 333:418–22. doi: 10.1126/science.1204794
- Plummer LN, Mackenzie FT (1974) Predicting Mineral Solubility From Rate Data: Application to the Dissolution of Magnesian Calcite. *Am J Sci* 274:61–83.
- Precht E, Huettel M (2004) Rapid wave-driven advective pore water exchange in a permeable coastal sediment. *J Sea Res* 51:93–107. doi: 10.1016/j.seares.2003.07.003
- Redfield A (1934) On the proportions of organic derivatives in seawater and their relation to the composition of plankton.pdf. In: Daniel RJ (ed) James Johnstone Memorial Volume. University Press of Liverpool, pp 176–192
- Ringuet S, Mackenzie FT (2005) Controls on nutrient and phytoplankton dynamics during normal flow and storm runoff conditions, southern Kaneohe Bay, Hawai‘i. *Estuaries* 28:327–337. doi: 10.1007/BF02693916
- Roy KJ (1970) Change in Bathymetric Configuration, Kaneohe Bay, Oahu, 1882-1969. Honolulu, HI
- Sansone FJ, Tribble G, Andrews CC, Chanton JP (1990) Anaerobic diagenesis within Recent, Pleistocene, and Eocene marine carbonate frameworks. *Sedimentology* 37:997–1009.
- Sansone FJ, Tribble GW, Buddemeier RW, Andrews CC (1988) Time and Space Scales of Anaerobic Diagenesis within a Coral Reef Framework. *Proc 6th Int Coral Reef Symp Aust* 3:367–372.
- Shamberger KEF, Feely RA, Sabine CL, et al (2011) Calcification and organic production on a Hawaiian coral reef. *Mar Chem* 127:64–75. doi: 10.1016/j.marchem.2011.08.003
- Shum KT (1993) The Effects of Wave-Induced Pore Water Circulation on the Transport of Reactive Solutes Below a Rippled Sediment Bed. *J Geophys Res Ocean* 98:10289–10301.
- Silbiger N, Guadayol Ò, Thomas F, Donahue M (2014) Reefs shift from net accretion to net erosion along a natural environmental gradient. *Mar Ecol Prog Ser* 515:33–44. doi: 10.3354/meps10999
- Silbiger NJ, Donahue MJ (2015) Secondary calcification and dissolution respond differently to future ocean conditions. *Biogeosciences* 12:567–578. doi: 10.5194/bg-12-567-2015

- Silverman J, Lazar B, Cao L, et al (2009) Coral reefs may start dissolving when atmospheric CO₂ doubles. *Geophys Res Lett* 36:L05606. doi: 10.1029/2008GL036282
- Silverman J, Lazar B, Erez J (2007) Effect of aragonite saturation, temperature, and nutrients on the community calcification rate of a coral reef. *J Geophys Res* 112:C05004. doi: 10.1029/2006JC003770
- Silverman J, Schneider K, Kline DI, et al (2014) Community calcification in Lizard Island, Great Barrier Reef: A 33 year perspective. *Geochim Cosmochim Acta*. doi: 10.1016/j.gca.2014.09.011
- Smith S V., Key GS (1975) Carbon Dioxide and Metabolism in Marine Environments. *Limnol Oceanogr* 20:493–495.
- Smith S V., Kimmerer W, Laws E (1981) Kaneohe Bay sewage diversion experiment: perspectives on ecosystem responses to nutritional perturbation.
- Stoessell RK (1992) Effects of Sulfate Reduction on CaCO₃ Dissolution and Precipitation in Mixing-Zone Fluids. *J Sediment Petrol* 62:873–880.
- Suzumura M, Miyajima T, Hata H, et al (2002) Cycling of phosphorus maintains the production of microphytobenthic communities in carbonate sediments of a coral reef. *Limnol Oceanogr* 47:771–781. doi: 10.4319/lo.2002.47.3.0771
- Taguchi S (1982) Seasonal study of fecal pellets and discarded houses of appendicularia in a subtropical inlet, Kaneohe Bay, Hawai‘i. *Estuarine, Coastal, Shelf Sci* 14:545–555.
- Tanaka K, Mackenzie FT (2005) Ecosystem behavior of southern Kaneohe Bay, Hawai‘i: A statistical and modelling approach. *Ecol Modell* 188:296–326. doi: 10.1016/j.ecolmodel.2005.02.018
- Thorstenson DC, Plummer LN (1977) Equilibrium Criteria for Two-Component Solids Reacting with Fixed Composition in an Aqueous Phase - Example: The Magnesian Calcites. *Am J Sci* 277:1203–1223.
- Tomlinson MS, De Carlo EH (2003) The Need For High Resolution Time Series Data To Characterize Hawaiian Streams. *J Am Water Resour Assoc* 39:113–123.
- Tribble GW (1990) Early Diagenesis in a Coral Reef Framework. University of Hawai‘i
- Tribble GW (1993) Organic Matter Oxidation and Aragonite Diagenesis in a Coral Reef. *SEPM J Sediment Res Vol.* 63:523–527. doi: 10.1306/D4267B45-2B26-11D7-8648000102C1865D
- Tribble GW, Sansone FJ, Li Y, et al (1988) Material Fluxes from a Reef Framework. *Proc 6th Int Coral Reef Symp Aust* 2:577–582.
- Tribble GW, Sansone FJ, Smith S V. (1990) Stoichiometric modeling of carbon diagenesis within a coral reef framework. *Geochim Cosmochim Acta* 54:2439–2449.
- Tribollet A (2008) Dissolution of dead corals by euendolithic microorganisms across the northern Great Barrier Reef (Australia). *Microb Ecol* 55:569–80. doi: 10.1007/s00248-007-9302-6
- Tribollet A, Decherf G, Hutchings PA, Peyrot-Clausade M (2002) Large-scale spatial variability in bioerosion of experimental coral substrates on the Great Barrier Reef (Australia): importance of microborers. *Coral Reefs* 21:424–432. doi: 10.1007/s00338-002-0267-0

- Tribollet A, Godinot C, Atkinson M, Langdon C (2009) Effects of elevated pCO₂ on dissolution of coral carbonates by microbial euendoliths. *Global Biogeochem Cycles* 23:n/a–n/a. doi: 10.1029/2008GB003286
- Tribollet A, Golubic S (2005) Cross-shelf differences in the pattern and pace of bioerosion of experimental carbonate substrates exposed for 3 years on the northern Great Barrier Reef, Australia. *Coral Reefs* 24:422–434. doi: 10.1007/s00338-005-0003-7
- Tribollet A, Langdon C, Golubic S, Atkinson M (2006) Endolithic Microflora Are Major Primary Producers in Dead Carbonate Substrates of Hawaiian Coral Reefs. *J Phycol* 42:292–303. doi: 10.1111/j.1529-8817.2006.00198.x
- Ver LM, Mackenzie FT, Lerman A (1999) Biogeochemical Responses of the Carbon Cycle to Natural and Human Perturbations: Past, Present, and Future. *Am J Sci* 299:762–801.
- Walter LM, Morse JW (1985) The dissolution kinetics of shallow marine carbonates in seawater: A laboratory study. *Geochim Cosmochim Acta* 49:1503–1515.
- Wanninkhof R (1992) Relationship between wind speed and gas exchange. *J Geophys Res* 97:7373–7382.
- Wisshak M, Schonberg CHL, Form A, Freiwald A (2012) Ocean Acidification Accelerates Reef Bioerosion. *PLoS One* 7:2–9. doi: 10.1371/Citation
- Wisshak M, Schönberg CHL, Form A, Freiwald A (2013) Effects of ocean acidification and global warming on reef bioerosion—lessons from a clonoid sponge. *Aquat Biol* 19:111–127. doi: 10.3354/ab00527
- Zhong S, Mucci A (1989) Calcite and aragonite precipitation from seawater solutions of various salinities: precipitation rates and overgrowth compositions. *Chem Geol* 78:283–299.

Chapter 5 CONCLUSIONS

5.1 Summary of Results

This dissertation uses several research techniques to elucidate the marine CO₂-carbonic acid system, specifically on coral reefs, and how coral reef carbon biogeochemistry will change under future conditions of rising atmospheric CO₂ and temperature. Through our long-term monitoring efforts we have shown that coral reef environments are much more variable than previously thought in their CO₂ chemistry (e.g., pCO₂, Ω, pH) on both the short and long term than previously thought (Drupp et al. 2011; Shamberger et al. 2011; Massaro et al. 2012; Drupp et al. 2013). The direction of CO₂ flux into (sink) or out of (source) Hawaiian reef waters is dependent on multiple factors such as temperature, land/ocean interactions, pelagic/benthic photosynthesis and respiration, and residence time.

The barrier reef of Kaneohe Bay (CRIMP-2 site) is primarily a source of CO₂ to the atmosphere due to the production of CO₂ from positive net ecosystem calcification. Remineralization of organic matter from land runoff is the primary reason for the slightly elevated levels of pCO₂ at the Ala Wai location relative to the open ocean. While the seawater pCO₂ is lower at Ala Wai than CRIMP-2, Ala Wai still remains a source of CO₂ to the atmosphere. The Kilo Nalu location, which has little terrestrial input and a short residence time, was essentially at equilibrium with the atmosphere over the length of the study period. Air-sea CO₂ exchange, at all locations, displayed a seasonality driven by both changes in temperature and biological activity, whereby the Ala Wai and Kilo Nalu locations transitioned to sinks in the winter (and sources in the summer). CRIMP-2 never became a net sink for any extended period of time, even during the winter, but its source strength was reduced during the winter months.

The monitoring effort described in this dissertation also showed that only continual, long-term, high-resolution CO₂ monitoring will result in a thorough and correct understanding of the tropical nearshore reef (and likely most coastal regions) CO₂ system, including air-sea gas exchange. This monitoring approach is the only way to capture both the short-term (hours-days) and long-term (months-years) changes that occur in the reef ecosystem. De Carlo et al. (2013) compared CO₂ flux calculations derived from weekly measurements of pCO₂ at Point B off the coast of Villefranche in the Mediterranean Sea with those from Kilo Nalu - our least variable site and recalculated Kilo Nalu fluxes as if measurements had been made daily, weekly, and monthly, as opposed to every three hours. This comparison showed that sampling weekly or monthly can change the calculated annualized flux by at least 1-2 orders of magnitude. The work presented in Chapter 2 (see also Drupp et al. 2011; Massaro et al. 2012; Drupp et al. 2013) has shown that the only way to accurately characterize air-sea CO₂ exchange in dynamic reef or coastal environments is through high-resolution monitoring.

While air-sea CO₂ exchange is an important component for understanding the processes affecting the CO₂ chemistry of coral reefs, as well as determining the carbon budget of these ecosystems, the sediment-porewater and porewater-surface water interactions that occur in reef systems can transfer carbon in much greater quantities than can air-sea exchange. This work establishes a critical baseline that is necessary to begin investigating nearshore, permeable sediment-porewater chemistry and its relationship to the overlying water column. This relationship has implications for how the coral reef sediments will react to the increasing ocean acidification that is expected both locally and globally over the next century, as modeled for the Kaneohe Bay barrier reef in Chapter 4. Sediment-porewater analyses at Ala Wai and CRIMP-2, to a depth of 60 cm, showed evidence of carbonate dissolution coupled with aerobic respiration

within the oxic layer at a nearly 1:1 ratio (i.e., each mole of CO₂ produced via respiration dissolved one mole of CaCO₃). Changes in TA, DIC, and sulfate, relative to the overlying water column, suggest that sulfate reduction and potentially denitrification, control the porewater CO₂ chemistry below the oxic layer (~12-20 cm). Porewater $\Delta\text{TA}:\Delta\text{DIC}$ values through the sediment were similar to those observed in other carbonate sediments (e.g., Ristvet 1978; Moulin et al. 1985; Tribble et al. 1990; Burdige and Zimmerman 2002; Bouillon et al. 2007), despite a significantly shorter porewater residence times at our study locations, due to the large physical differences in permeability, grain size, and porosity at our sample locations,

Despite elevated pCO₂ levels and decreased pH, the porewaters at CRIMP-2 and Ala Wai were never undersaturated with respect to aragonite, although Ω_{Ar} decreased to as low as ~1.2 in the deeper samples. However, the porewater was consistently undersaturated with respect to 15% Mg-calcite, suggesting that the elevated TA observed in the porewater was at least partially the result of Mg-calcite dissolution (some TA would also be produced via sulfate reduction). Detrital remains of Mg-calcite-producing organisms such as *Amphiroa sp.* and *Lithothamnion sp.* are likely the dissolving phases, as these organisms are common on Hawaiian reefs (Agegian and Mackenzie 1989). Currently, carbonate mineral dissolution is controlled by metabolic dissolution, whereby microbes increase pCO₂ levels during the respiration of organic matter and lower the pH and Ω . However, future OA could cause surface waters to become undersaturated with respect to phases such as high Mg-calcites (>12 mol%), resulting in environmental dissolution (this process was further investigated through a biogeochemical model in Chapter 4). Porewater TA and DIC data from Chapter 3 (Section 3.4.2) show that an addition of only 100-150 $\mu\text{mol}\cdot\text{kg}^{-1}$ of DIC is needed to reach a state of environmental dissolution of aragonite in the sediments at CRIMP-2 and Ala Wai. This DIC increase is well within the ranges predicted by the

IPCC for surface seawater due to rising anthropogenic CO₂ emissions. The DIC change necessary for environmental dissolution to occur is also within the predicted ranges of DIC for the Kaneohe Bay barrier reef from *CRESCAM*. If the overlying water column at CRIMP-2 or Ala Wai (or any reef system) becomes corrosive to these substrates, environmental dissolution, along with the already occurring metabolic dissolution, could further deplete the CaCO₃ budget of the reef.

Sandy, permeable sands are more heavily influenced by the overlying water column chemistry than are finer grained, low permeability sediments due to increased advection and short porewater residence times (Shum 1993; Falter and Sansone 2000; Boudreau et al. 2001; Huettel and Webster 2001; Precht and Huettel 2004; Fogaren et al. 2013; Fram et al. 2014). Because the porewater in permeable sands is being flushed at a much faster rate than the diffusional rates found in fine-grained sediments, TA and DIC are constantly delivered to the overlying water from the sediments. In addition, the short residence time leads to porewater chemistry that more closely resembles the surface water, especially under conditions of rapid advection (e.g., high wind or wave activity), and porewaters can serve as an important source of TA and DIC to the water column due to the active flushing. Rapid advection also replenishes the dissolved oxygen in the porewater and allows dissolved oxygen to penetrate to deeper sediment-porewater depths, sustaining oxic respiration in a fashion similar to the resupply mechanism of oxygen and nutrients in seagrass beds through the plant roots (e.g., Morse et al. 1987; Burdige and Zimmerman 2002; Burdige et al. 2008). Periods of high wave activity (e.g., storms, swells, or high winds) lead to a flushing of the porewater down to at least 20-30 cm sediment depth at CRIMP-2 and Ala Wai (Drupp et al. in review). Despite the relatively low concentrations of TA and DIC, compared to fine-grained sediments, the physical characteristics of highly permeable

sediments ensure that the sands are very biogeochemically active due to vigorous turnover of the porewater and rapid resupply of oxygen and organic carbon (OC) from the surface.

The porewater data and the CO₂ monitoring data were used to constrain the sediment-domain parameters in the biogeochemical box model, *CRESCAM*. This model, specific to the Kaneohe Bay barrier reef flat, showed that even under the worst case conditions of rising OA and temperature, the reef flat was unlikely to become net erosional (net loss of CaCO₃) by 2100. The model also showed that the porewater carbon chemistry is strongly controlled by microbial respiration and the release of TA through carbonate dissolution and sulfate reduction. In addition, despite the potential for increased sediment carbonate mineral dissolution, the release of TA from the porewater to the overlying water column is insufficient to cause any significant pH buffering in the surface water and elevates the surface water TA concentration by only ~1-2 μmol·kg⁻¹. This is partially due to the rapid rate of porewater advection, which deprives the sediment-porewater system of the time required to accumulate TA via microbial respiration and subsequent carbonate dissolution. The short residence time of the reef surface water also quickly removes any additional water column TA from the reef flat.

Changes in NEC and NEP in response to changing seawater chemistry and temperature control the magnitude and direction of the local air-sea CO₂ flux. If the average TA on the reef increases from present day conditions, due to a combination of decreased biogenic calcification and enhanced carbonate dissolution and bioerosion, the reef surface water has the potential to switch from being a source of CO₂ to a sink. This reversal in the direction of CO₂ exchange would further compound the effects of increased seawater CO₂, as it eliminates one of the potential mechanisms for CO₂ removal from the system. Biogenic calcification is expected to decrease over the century because of declining pH and Ω and - along with an increase in

bioerosion and dissolution - is expected to lower the overall NECP of the reef ecosystem by as much as 20% below 2015 conditions. Future changes in NECP are also directly related to any land-use changes that may affect the organic carbon and/or nutrient balance of the reef flat. While the latter two potential changes are unlikely, because the reef flat is fairly isolated from terrestrial input due to the hydrodynamics of the lagoon, increases in overall NEP from additional nutrient subsidies could cause enhanced dissolution in the oxic sediments due to higher rates of sedimentation of OC. However, the increase in OC to the anoxic sediment and framework domains may have the opposite effect. Rapid sulfate reduction from the additional input of OC will increase TA and raise the saturation state of the porewaters with respect to carbonate minerals, which would promote carbonate precipitation. These intricate, sometimes counterintuitive, and often ignored aspects of reef and sediment carbonate biogeochemistry can have profound effects on the overall accretion or erosion status of a reef system and must be included when considering the future conditions of the reef ecosystem under anthropogenic change.

Coral reef environments are highly dynamic systems that are controlled by many factors that can be difficult to quantify without extensive study. While there is utility in using simplified general models and predictions for coral reefs under rising OA, the inherent variability in different reef settings throughout the tropical ocean requires that these systems must be treated on an individual basis to assess accurately the local effects of changing CO₂-carbonic acid system chemistry.

5.2 References

- Agegian CR, Mackenzie FT (1989) Calcareous organisms and sediment mineralogy on a mid-depth bank in the Hawaiian Archipelago. *Pacific Sci* 43:56–66.
- Boudreau BP, Huettel M, Forster S, et al (2001) Permeable Marine Sediments : Overturning an Old Paradigm. *EOS Trans Am Geophys Union* 82:133–140.
- Bouillon S, Dehairs F, Velimirov B, et al (2007) Dynamics of organic and inorganic carbon across contiguous mangrove and seagrass systems (Gazi Bay, Kenya). *J Geophys Res Biogeosciences* 112:1–14. doi: 10.1029/2006JG000325
- Burdige DJ, Zimmerman RC (2002) Impact of seagrass density on carbonate dissolution in Bahamian sediments. *Limnol Oceanogr* 47:1751–1763.
- Burdige DJ, Zimmerman RC, Hu X (2008) Rates of carbonate dissolution in permeable sediments estimated from pore-water profiles: The role of sea grasses. *Limnol Oceanogr* 53:549–565. doi: 10.4319/lo.2008.53.2.0549
- De Carlo EH, Mousseau L, Passafiume O, et al (2013) Carbonate Chemistry and Air–Sea CO₂ Flux in a NW Mediterranean Bay Over a Four-Year Period: 2007–2011. *Aquat Geochemistry* 19:399–442. doi: 10.1007/s10498-013-9217-4
- Drupp PS, De Carlo EH, Mackenzie FT, et al (2011) Nutrient Inputs, Phytoplankton Response, and CO₂ Variations in a Semi-Enclosed Subtropical Embayment, Kaneohe Bay, Hawai‘i. *Aquat Geochemistry* 17:473–498. doi: 10.1007/s10498-010-9115-y
- Drupp PS, De Carlo EH, Mackenzie FT, et al (2013) Comparison of CO₂ Dynamics and Air–Sea Gas Exchange in Differing Tropical Reef Environments. *Aquat Geochemistry* 19:371–397. doi: 10.1007/s10498-013-9214-7
- Drupp PS, De Carlo EH, Mackenzie FT Porewater CO₂-Carbonic Acid System Chemistry in Permeable Carbonate Sands.
- Falter JL, Sansone FJ (2000) Shallow pore water sampling in reef sediments. *Coral Reefs* 19:93–97. doi: 10.1007/s003380050233
- Fogaren KE, Sansone FJ, De Carlo EH (2013) Porewater temporal variability in a wave-impacted permeable nearshore sediment. *Mar Chem* 149:74–84. doi: 10.1016/j.marchem.2012.12.005
- Fram JP, Pawlak GR, Sansone FJ, et al (2014) Miniature thermistor chain for determining surficial sediment porewater advection. *Limnol Oceanogr Methods* 12:155–165. doi: 10.4319/lom.2014.12.155
- Huettel M, Webster IT (2001) Porewater flow in permeable sediments. In: Boudrea BP, Jorgensen BB (eds) *The benthic boundary layer: Transport processes and biogeochemistry*. Oxford University Press, pp 144–179
- Massaro RFS, De Carlo EH, Drupp PS, et al (2012) Multiple Factors driving Variability of CO₂ Exchange Between the Ocean and Atmosphere in a Tropical Coral Reef Environment. *Aquat Geochemistry* 18:357–386. doi: 10.1007/s10498-012-9170-7

- Morse JW, Zullig JJ, Iverson RL, et al (1987) The influence of seagrass beds on carbonate sediments in the Bahamas. *Mar Chem* 22:71–83.
- Moulin E, Jordens A, Wollast R (1985) Influence of the Aerobic Bacterial Respiration on the Early Dissolution of Carbonates in Coastal Sediments. In: *Progress in Belgian Oceanographic Research*. p 13
- Precht E, Huettel M (2004) Rapid wave-driven advective pore water exchange in a permeable coastal sediment. *J Sea Res* 51:93–107. doi: 10.1016/j.seares.2003.07.003
- Ristvet B (1978) Reverse Weather Reactions Within Recent Nearshore Marine Sediments, Kaneohe Bay, Oahu. University of Hawai'i
- Shamberger KEF, Feely RA, Sabine CL, et al (2011) Calcification and organic production on a Hawaiian coral reef. *Mar Chem* 127:64–75. doi: 10.1016/j.marchem.2011.08.003
- Shum KT (1993) The Effects of Wave-Induced Pore Water Circulation on the Transport of Reactive Solutes Below a Rippled Sediment Bed. *J Geophys Resarch Ocean* 98:10289–10301.
- Tribble GW, Sansone FJ, Smith S V. (1990) Stoichiometric modeling of carbon diagenesis within a coral reef framework. *Geochim Cosmochim Acta* 54:2439–2449.

Appendix MODEL CODE AND CALCULATIONS

This appendix contains the MatLab code, forcing data, mass balance and flux equations, and initial steady state reservoir and flux calculations used to create and run the Coral Reef Ecosystem and Sediment Carbonate Model (*CRESCAM*). The full description of the model, including detailed a detailed description of the initial steady state solution can be found in Chapter 4.

A.1 MATLAB Code

The following program code was written in MatLab and can be executed as a m-file. In addition to the code, an RCP forcing file (A.1.4-A.1.7) is required to perturb the model.

A.1.1 Initial Steady State Reservoir and Flux Calculations Code

```
%-----  
% Matlab code for Coral Reef Ecosystem Carbon Model (CRESCAM)  
% standard scenario, year 2015-2100  
% created by Patrick Drupp 2014  
% This file calculates the initial steady state values of the C1-C17  
% reservoirs and all the accompanying steady state fluxes  
% Three m-files and a forcing file are required:  
% 1. CRESCAM_initialss.m  
% 2. CRESCAM.m  
% 3. CRESCAMdiff.m  
%-----  
  
%-----  
% CRESCAM_initialss.m  
%-----  
close all  
clc  
clear all  
  
global R0 k F0;  
%-----  
%Define reef parameters used in calculating reservoir sizes and fluxes  
%-----  
  
%define initial temperature (celsius), salinity, and density (kg/m^3)  
T0=25;  
S0=35;  
den1=999.842594+T0*(6.793952*10^-2)+T0^2*(-9.09529*10^-3)+...  
    T0^3*(1.001685*10^-4);  
den2=den1+T0^4*(-1.120083*10^-6)+T0^5*(6.536332*10^-9);
```

```

den3=den2+S0*(0.824493+T0*(-4.0899*10^-3)+T0^2*(7.6438*10^-5)+...
T0^3*(-8.2467*10^-7)+T0^4*(5.3875*10^-9));
densi ty=den3+S0^(3/2)*(-5.72466*10^-3+T0*1.0227*10^-4+T0^2*...
(-1.6546*10^-6))+S0^2*(4.8314*10^-4);

%define size parameters of reef in m, m^2, or m^3
w=2000;
l=5000;
z=2;
a=w*l; %m^2
v=w*l*z; %m^3
surf_mass=v*densi ty;

%define relative carbonate mineral abundances on reef
cal c_abund=0.13;
arag_abund=0.63;
mgcal c_abund=0.24;

%define sediment and framework porosities (from Drupp et al. (2015)
%and Tribble(1990)),
%define areal coverage (from NOAA benthic mapping) and reservoir depths
permsedpor=0.52;
frameworkpor=0.50;
areal_perm_sed=0.05;
areal_framework=1-areal_perm_sed;
oxi c_depth=0.2;
anoxi c_depth=1-oxi c_depth;
fw_depth=1;

%define porewater volumes (m^3) and masses (kg)
pw_vol=a*oxi c_depth*areal_perm_sed*permsedpor;
pw_mass=pw_vol*densi ty;

pwan_vol=a*anoxi c_depth*areal_perm_sed*permsedpor;
pwan_mass=pwan_vol*densi ty;

pfw_vol=a*fw_depth*areal_framework*frameworkpor;
pfw_mass=pfw_vol*densi ty;

%define mineral densities (g/cm^3) and sediment mass (kg)
cal c_dens=2.71;
arag_dens=2.93;
mgcal c_dens=2.71;
sed_densi ty=cal c_abund*cal c_dens+arag_abund*arag_dens+mgcal c_abund...
*mgcal c_dens;

sedmass=w*l*oxi c_depth*sed_densi ty*1e6*(1-permsedpor)*areal_perm_sed;
anoxsedmass=w*l*anoxi c_depth*sed_densi ty*1e6*(1-permsedpor)*areal_perm_sed;

%-----
%define initial carbon reservoirs (R0) in mols C
%-----
%where Ri = Ci at time t=0

```

```

%C1- Surface Water DIC
%from Drupp et al. (2013) and Shamberger et al. (2011)
DICsurf=1973.44052127512e-6;
R1=surf_mass*DICsurf;

%C2- Surface TOC
%pelagic DOC (mol/m^3) calculated from DON from Smith et al. (1981)
%and Cox et al. (2006)
%using Redfield (1934) ratio of 106:16
DON=6.2e-3;
DOC=DON*6.625;
%POC (mol/m^3) from Cox et al. (2006) and Atkinson and Falter (2003)
POC=0.008;
R2=(DOC+POC)*v;

%C3- Oxic Porewater DIC (0-20cm)
%DIC (mol/kg) from Drupp et al., 2015 Porewater study
DICoxi_cpw=0.00215163423109156;
R3=pw_mass*DICoxi_cpw;

%C4- Oxic Sediment OM
%(OM from Drupp et al. (2015) and Atkinson and Falter(2003)
wtOC=0.005;
R4=sedmass*wtOC/12.01;

%C5- Oxic Sediment Calcite
ICwt=0.1145; %Drupp et al. (2015)
R5=sedmass*calc_abund*ICwt/12.01;

%C6- Oxic Sediment Aragonite
R6=sedmass*arag_abund*ICwt/12.01;

%C7- Oxic Sediment Mg- Calcite
R7=sedmass*mgcalc_abund*ICwt/12.01;

%C8- Calcite Reef Framework
%where 100.1 is calcite molar weight
R8=w*1*fw_depth*areal_framework*calc_dens*1e6...
*(1-frameworkpor)*calc_abund/100.1;

%C9- Aragonite Reef Framework
%where 100.1 is aragonite molar weight
R9=w*1*fw_depth*areal_framework*arag_dens*1e6...
*(1-frameworkpor)*arag_abund/100.1;

%C10- Calcite Reef Framework
%where 97.7 is 15% Mg- calcite molar weight
R10=w*1*fw_depth*areal_framework*mgcalc_dens*1e6...
*(1-frameworkpor)*mgcalc_abund/97.7;

%C11- Reef Framework Porewater
%(DICfw in mol/kg from Tribble et al (1990))
DICfw=2384.24255801791e-6;
R11=pwfw_mass*DICfw;

```

```

%C12- Reef Framework OM
wtOMfw=0.005; %Tribble et al. (1990)
R12=w*I*fw_depth*areal_framework*(1-frameworkpor)*sed_density*1e6*wtOMfw...
/12.01;

%C13- Anoxic Sed OM
wtOManox=0.002; %Drupp et al. (2015)
R13=anoxsedmass*wtOManox/12.01;

%C14- Anoxic Sed Calcite
R14=anoxsedmass*Icwt*calc_abund/12.01;

%C15- Anoxic Sed Aragonite
R15=anoxsedmass*Icwt*arag_abund/12.01;

%C16- Anoxic Sed Mg-Calcite
R16=anoxsedmass*Icwt*mgcalc_abund/12.01;

%C17- Anoxic Porewater DIC (20-100cm)
DICanox=2350e-6; %Drupp et al. (2015)
R17=pwan_mass*DICanox;

%-----
%initial steady state fluxes (mol C/yr)
%-----
% RCFij=CFij at t=0

%CF0:1 open ocean import of DIC
speed=0.15; %current speed (m/s) from Lowe et al. (2009)
RT=w/speed/3600/24; %residence time in days
DICext=0.00199289917770423; %from Shamberger et al. (2011)
% DICext=0.00198445865642911; %testing 7/4/15
RCF01=v/RT*365*density*DICext;

%CF0:2 open ocean import of TOC
DONext=6.09948900470243; %mmol N/m^3 Smith et al. (1981)
POCext=75.4420777695913/12.01/1000; %mg C/m^3 to mol C/m^3 Cox et al. (2006)
DOCext=DONext*6.625/1000; %Redfield ratio, DOCext in mol C/m^3
RCF02=v/RT*365*(DOCext+POCext);

%CF1:0 surface water export of DIC off the reef
DICint=0.00197344052127512; %Shamberger et al. (2011) and Drupp et al. (2013)
% DICint=0.001965; %testing 7/4/15
RCF10=v/RT*365*density*DICint;

%CF1:A atmospheric exchange -Drupp et al. (2013)
u10=5.19292253475285; %m/s
k600=0.266*u10^2; %Ho et al. (2006)
%schmidt from Wanninkhof (1992) s=35
schmidt=2073.1-(125.62*T0)+(3.6276*T0^2)-0.043219*T0^3;
%ambient k in m/hr
k=k600*(schmidt/600)^-0.5/100;
co2sol=exp(93.4517*(100/(T0+273.15))-60.2409+23.3585...

```

```

*log((T0+273.15)/100)+S0*(0.023517-0.023656*((T0+273.15)/100)...
+0.0047036*((T0+273.15)/100)*((T0+273.15)/100));
%pCO2 in uatm
pCO2sw=440.1118344492954;
pCO2air=399;
delpCO2=pCO2sw-pCO2air;
RCF1A=k*co2sol*density*delpCO2*1e-6*24*365*a;

%CF1: 2 %photosynthesis
%from Falter et al. (2004) in mol C/m2/d
photo=0.519090542510258;
RCF12=photo*a*365;

% CF1: 3 advection(m/hr) of surface DIC into permeable sediments
adv=0.03;
RTpw=oxic_depth/adv;
RCF13=pw_mass/RTpw*8760*DICsurf;

%Calcification in mol CaCO3/m2/yr (from Shamberger et al. (2011))
calcrate=0.25;
NECinit=calcrate*365*a;

%calcification is divided amongst fw minerals based on relative abundance

%CF1: 8, 9, 10 calcite, aragonite, mg-calcite calcification
RCF18=NECinit*calc_abund;
RCF19=NECinit*arag_abund;
RCF110=NECinit*mgcalc_abund;

%CF1: 11 surface water DIC advection into framework
%RT in days from Tribble (1990)
RTfw=2.91236395906563;
RCF111=w*1*fw_depth*areal_framework*frameworkpor*density*DICsurf/RTfw*365;

%CF2: 0 export of TOC
DONint=6.3; %mmol N/m^3 Smith et al. (1981)
POCint=100.146149384765/12.01/1000; %mg C/m^3 to mol C/m^3 Cox et al. (2006)
DOCint=DONint*6.625/1000; %Redfield ratio, DOCext in mol C/m^3
RCF20=v/RT*365*(DOCint+POCint);

%CF2: 1 surface water respiration (TOC TO DIC) from Falter et al. (2004)
resp=0.435;
RCF21=resp*a*365;

%CF2: 4 sedimentation of TOC to sediments
POCsed=483; %mg/m2/day from Taguchi (1982)
RCF24=POCsed/1000/12.01*a*areal_perm_sed*365;

%CF2: 12 sedimentation of TOC to framework
RCF212=POCsed/1000/12.01*a*areal_framework*365;

%CF3: 1 advection of DIC out of sediments
DICpw=2151.63423109156e-6; %Drupp et al. (2015)
RCF31=pw_mass/RTpw*8760*DICpw;

```

```

%initial steady state precipitation/dissolution is determined by Om
%if Om>1 precipitation will occur, if Om<1 dissolution will occur

%CF3:5 precip of calcite
% despite Om>1, aragonite is preferentially precipitated over calcite due
% to Mg inhibition
RCF35=0;

%CF5:3 diss of calcite
RCF53=0;

%CF3:6 precip of aragonite
% Om_arag>1 so precip occurs
Omarag_init_oxi c=2.68445267396941; %Drupp et al. (2015)
Rate_constant_arag=10^1.09; %umol/m2/hr
DICresoxi c=R3*12.01; %grams of DIC
narag=2.36;
P04oxi c=2.5; %uM
P04i nhi boxi c=0.9711*exp(-0.52*P04oxi c); %Berner et al. (1978)
DOMoxi c=1.8; %mg C/L
DOMi nhi boxi c=-0.2462*DOMoxi c+0.7879; %Berner et al. (1978)
RCF36=Rate_constant_arag*(Omarag_init_oxi c-1)^narag*DICresoxi c...
*8760*1e-6*P04i nhi boxi c*DOMi nhi boxi c;

%CF6:3 dissolution of aragonite
RCF63=0;

%CF3:7 precip of mg-calcite
RCF37=0;

%CF7:3 dissolution of mg-calcite in oxic sediments
% Om_mgcal<1 so diss occurs
Ommgcal_c_init_oxi c=0.7976471505796423; %Drupp et al. (2015)
Rate_constant_mgcal c=10^2.32; %umol/g/hr
Mgcal cresoxi c=R7*97.7; %grams of Mg-calc
Ars=0.25;
nmgcal c=3.55;
P04oxi c=2.5; %uM
P04i nhi boxi c=0.9711*exp(-0.52*P04oxi c); %Berner et al. (1978)
DOMoxi c=1.8; %mg C/L
DOMi nhi boxi c=-0.2462*DOMoxi c+0.7879; %Berner et al. (1978)
RCF73=Rate_constant_mgcal c*(1-Ommgcal_c_init_oxi c)^nmgcal c*Mgcal cresoxi c...
*Ars*8760*1e-6*P04i nhi boxi c*DOMi nhi boxi c;

%CF4:3 respiration of organic matter in sediments
RCF43=4830298.826048818;

%CF4:13 burial of OM to anoxic layer
RCF413=RCF24-RCF43;

%erosional processes of the reef framework
%kg CaCO3/m2/yr based on Tribollet et al. (2006) and Fang et al. (2013)

```

```

boring_rate=0.60;
chips=0.6; %percent that is left as chips (Andersson and Gledhill (2013))
total_dissolved=w*1*areal_framework*boring_rate*(1-chips)*1000/100.1;

%total dissolved reef is divided based on relative abundances of minerals
RCF81=total_dissolved*calc_abund;
RCF91=total_dissolved*arag_abund;
RCF101=total_dissolved*mgcalc_abund;

%mechanical erosion
grazing_rate=3.5; %kg CaCO3/m2/yr Tribollet et al. (2006, 2008)
total_mechanical=(grazing_rate+boring_rate*chips)*w*1*...
    areal_framework*1000/100.1;
%partition based on relative abundances of minerals
RCF85=total_mechanical*calc_abund;
RCF96=total_mechanical*arag_abund;
RCF107=total_mechanical*mgcalc_abund;

%assuming that 70% of the eroded material is sedimented out and 30% is
%exported off the reef
RCF50=RCF85*0.3;
RCF60=RCF96*0.3;
RCF70=RCF107*0.3;

%CF5, 6, 7: 14, 15, 16 burial is defined as B=P+FE-D-E where P is precipitation,
%FE is framework erosion, D is dissolution, and E is export off the reef

RCF514=RCF35+RCF85-RCF53-RCF50;
RCF615=RCF36+RCF96-RCF63-RCF60;
RCF716=RCF37+RCF107-RCF73-RCF70;

% precip/dissolution of calcite framework from the porewater
% despite Om>1, aragonite is preferentially precipitated over calcite due
% to Mg inhibition
RCF811=0;
RCF118=0;

% precip of arag framework from the porewater
% Om of arag is >1 so precipitation occurs
Omarag_init_fw=2.915757048552778; %Tribble (1990)
Rate_constant_arag=10^1.09; %umol/m2/hr
DICresfw=R11*12.01; %grams of DIC
narag=2.36;
P04fw=2.5; %uM
P04inibfw=0.9711*exp(-0.52*P04fw); %Berner et al. (1978)
DOMfw=1.5; %mg C/L
DOMinibfw=-0.2462*DOMfw+0.7879; %Berner et al. (1978)
RCF119=Rate_constant_arag*(Omarag_init_fw-1)^narag*DICresfw...
    *8760*1e-6*P04inibfw*DOMinibfw;

%diss of arag framework in the porewater
RCF911=0;

% dissolution of mg-calc framework from the porewater

```

```

% Om of mg-calc is <1 so dissolution occurs
Ommgcalc_init_fw=0.8663759745563439; %Tribble(1990)
Rate_constant_mgcalc=10^2.32; %umol/g/hr
Mgcalcresfw=R10*97.7; %grams of Mg-calc
Ars=0.25;
nmgcalc=3.55;
P04fw=2.5; %uM
P04inhibfw=0.9711*exp(-0.52*P04fw); %Berner et al. (1978)
DOMfw=1.5; %mg C/L
DOMinhibfw=-0.2462*DOMfw+0.7879; %Berner et al. (1978)
RCF1011=Rate_constant_mgcalc*(1-Ommgcalc_init_fw)^nmgcalc*Mgcalcresfw...
    *Ars*8760*1e-6*P04inhibfw*DOMinhibfw;
%precip of mg-calc from framework porewater
RCF1110=0;

% CF11:1 reef framework porewater advection to surface water
RTfw=2.91236395906563; %days from Tribble (1990)
RCF11_1=pfw_mass*DICfw/RTfw*365;

%burial of framework is B=calcification+P-CE-ME-D, where CE and ME are
%chemical and mechanical bioerosion
%CF8: B burial of calcite framework
RCF8B=RCF18+RCF118-RCF81-RCF85-RCF811;

%CF9: B burial of aragonite framework
RCF9B=RCF19+RCF119-RCF91-RCF96-RCF911;

%CF10: B burial of Mg-calcite framework
RCF10B=RCF110+RCF1110-RCF101-RCF107-RCF1011;

%CF12: 11 framework respiration of OM was set to 1.32e8 based on a ~1%
%burial rate, constrained by sedimentation and dissolution of Mg-calcite
RCF1211=134463202.4025807;

%CF12: B burial of framework OM
RCF12B=RCF212-RCF1211;

%CF14: 17 and CF17: 14 precip/dissolution of calcite in anoxic sediment
%despite Om>1 calcite precip does not occur due to Mg inhibition
RCF1417=0;
RCF1714=0;

%CF17: 15 precip of aragonite in anoxic sediments
%Om>1 so precipitation occurs
Omarag_init_anox=2.90586125199625; %Tribble (1990)
Rate_constant_arag=10^1.09; %umol/m2/hr
DICresanox=R17*12.01; %grams of DIC
narag=2.36;
P04anox=5.5; %uM
P04inhibanox=0.9711*exp(-0.52*P04anox); %Berner et al. (1978)
DOManox=1.6; %mg C/L
DOMinhibanox=-0.2462*DOManox+0.7879; %Berner et al. (1978)
RCF1715=Rate_constant_arag*(Omarag_init_anox-1)^narag*DICresanox...
    *8760*1e-6*P04inhibanox*DOMinhibanox;

```

```

%CF15: 17 dissolution of aragonite in anoxic sediments
RCF1517=0;

%CF16: 17 dissolution of mg-calcite in anoxic sediments
%Om<1 so dissolution occurs
Ommgcal c_init_anox=0.8634355824716051; %Tribble(1990)
Rate_constant_mgcal c=10^2.32; %umol/g/hr
Mgcal cresanox=R16*97.7; %grams of Mg-calc
Ars=0.25;
nmgcal c=3.55;
P04anox=5.5; %uM
P04inhibanox=0.9711*exp(-0.52*P04anox); %Berner et al.(1978)
DOManox=1.6; %mg C/L
DOMinhibanox=-0.2462*DOManox+0.7879; %Berner et al.(1978)
RCF1617=Rate_constant_mgcal c*(1-Ommgcal c_init_anox)^nmgcal c*Mgcal cresanox...
    *Ars*8760*1e-6*P04inhibanox*DOMinhibanox;

%CF17: 16 precip of mg-calcite in anoxic sediments
RCF1716=0;

%CF13: 17 respiration of OM in the anoxic sediments based on 0.2 wt% of
%total carbonate burial and 2x mg-calcite dissolution
RCF1317=2305635.792969301;

RCF13B=RCF413-RCF1317;

%burial from the anoxic layer where B=burial from oxic+P-D
%CF14: B burial of calcite
RCF14B=RCF514+RCF1714-RCF1417;
%CF15: B burial of aragonite
RCF15B=RCF615+RCF1715-RCF1517;
%CF16: B burial of mg-calcite
RCF16B=RCF716+RCF1716-RCF1617;

%CF17: 3 exchange of anoxic porewater with oxic layer porewater
adv_anox=0.710028986047654; %cm/hr
RTanox=anoxic_depth*100/adv_anox; %hrs
DICanox=2350e-6; %mol/kg
delDIC=DICanox-DICoxcpw;
diff=1.335e-9; %m2/s from Berner(1980) diffusivity coefficient of bicarb
%Fick's First Law
FFL=diff*permsedpor*delDIC/1*density;
%diffusional flux
Fickdiff=FFL*w*1*areal_perm_sed*3600*8760;
%advective flux
advflux=pwan_mass*delDIC/RTanox*8760;
RCF173=Fickdiff+advflux;

%-----
% k values from steady state reservoirs and flux
%-----

k10=RCF10/R1;

```

k13=RCF13/R1;
k18=RCF18/R1;
k19=RCF19/R1;
k110=RCF110/R1;
k111=RCF111/R1;
k20=RCF20/R2;
k21=RCF21/R2;
k24=RCF24/R2;
k212=RCF212/R2;
k31=RCF31/R3;
k43=RCF43/R4;
k413=RCF413/R4;
k53=RCF53/R5;
k514=RCF514/R5;
k50=RCF50/R5;
k63=RCF63/R6;
k615=RCF615/R6;
k60=RCF60/R6;
k73=RCF73/R7;
k716=RCF716/R7;
k70=RCF70/R7;
k81=RCF81/R8;
k85=RCF85/R8;
k811=RCF811/R8;
k8B=RCF8B/R8;
k91=RCF91/R9;
k96=RCF96/R9;
k911=RCF911/R9;
k9B=RCF9B/R9;
k101=RCF101/R10;
k107=RCF107/R10;
k1011=RCF1011/R10;
k10B=RCF10B/R10;
k11_1=RCF11_1/R11;
k1211=RCF1211/R12;
k12B=RCF12B/R12;
k1317=RCF1317/R13;
k13B=RCF13B/R13;
k1417=RCF1417/R14;
k14B=RCF14B/R14;
k1517=RCF1517/R15;
k15B=RCF15B/R15;
k1617=RCF1617/R16;
k16B=RCF16B/R16;
k173=RCF173/R17;
k35=RCF35/R3;
k36=RCF36/R3;
k37=RCF37/R3;
k1714=RCF1714/R17;
k1715=RCF1715/R17;
k1716=RCF1716/R17;
k118=RCF118/R11;
k119=RCF119/R11;
k1110=RCF1110/R11;

```

%define initial reservoir, initial flux and rate constant matrices
R0=[R1 R2 R3 R4 R5 R6 R7 R8 R9 R10 R11 R12 R13 R14 R15 R16 R17];

FO=[RCF01 RCF02 RCF10 RCF1A RCF12 RCF13 RCF18 RCF19 RCF110 RCF111 RCF20...
    RCF21 RCF24 RCF212 RCF31 RCF43 RCF413 RCF53 RCF514 RCF50 RCF63...
    RCF615 RCF60 RCF73 RCF716 RCF70 RCF81 RCF85 RCF811 RCF8B RCF91 RCF96...
    RCF911 RCF9B RCF101 RCF107 RCF1011 RCF10B RCF11_1 RCF1211 RCF12B...
    RCF1317 RCF13B RCF1417 RCF14B RCF1517 RCF15B RCF1617 RCF16B RCF173...
    RCF35 RCF36 RCF37 RCF1714 RCF1715 RCF1716 RCF118 RCF119 RCF1110];

k=[k10 k13 k18 k19 k110 k111 k20 k21 k24 k212 k31...
    k43 k413 k53 k514 k50 k63 k615 k60 k73 k716 k70 k81 k85 k811...
    k8B k91 k96 k911 k9B k101 k107 k1011 k10B k11_1...
    k1211 k12B k1317 k13B k1417 k14B k1517...
    k15B k1617 k16B k173 k35 k36 k37 k1714 k1715 k1716 k118 k119 k1110];

save('CRESCAM_InitSS_Var', 'R0', 'k', 'FO');

% -----
% end of file CRESCAM_initialss.m
% -----

```

A.1.2 CRESCAM.m Run File

```

% -----
% Matlab code for Coral Reef Ecosystem Carbon Model (CRESCAM)
% standard scenario, year 2015-2100
% created by Patrick Drupp 2014, based on SOCM code from Andersson, 2005

% Three m-files and a forcing file are required:
% 1. CRESCAM_initialss.m
% 2. CRESCAM.m
% 3. CRESCAMdiff.m
% -----

% -----
% CRESCAM.m
% -----

% -----
% Define and load variables
% -----

close all
clc
clear all

global R0 f OM OM_pw OM_pwan OM_fw G sat_pw sat_pwan sat_fw;

```

```

% -----
% Load initial reservoirs, fluxes, k values
% Choose RCP forcing scenario to load forcing file
% -----
load (' CRESCAM_forcings_RCP26', ' forcing26')
f=forcing26;
x=1;

% load (' CRESCAM_forcings_RCP45', ' forcing45')
% f=forcing45;
% x=2;

% load (' CRESCAM_forcings_RCP60', ' forcing60')
% f=forcing60;
% x=3;

% load (' CRESCAM_forcings_RCP85', ' forcing85')
% f=forcing85;
% x=4;

load(' CRESCAM_Ini tSS_var', ' R0', ' k', ' FO');
G=[]; OM=[]; OM_pw=[]; OM_pwan=[]; OM_fw=[];
sat_pw=[]; sat_pwan=[]; sat_fw=[];

% -----
% Solve ODE defined in CRESCAMdiff.m using a stiff solver ODE15s
% -----
tspan=(2015:0.01:2100);
options=odeset(' MaxStep', 0.01, ' MaxOrder', 1);
[t, C]=ode15s(@CRESCAMdiff, tspan, R0, options);

% -----
% define reservoir variables and plot reservoirs
% -----
C1=C(:, 1); C2=C(:, 2); C3=C(:, 3); C4=C(:, 4); C5=C(:, 5); C6=C(:, 6);
C7=C(:, 7); C8=C(:, 8); C9=C(:, 9); C10=C(:, 10); C11=C(:, 11); C12=C(:, 12);
C13=C(:, 13); C14=C(:, 14); C15=C(:, 15); C16=C(:, 16); C17=C(:, 17);

Flux=G(:, 19:1:68);

figure(1)
subplot(4, 3, 1), plot(t, C1); title(' C1 DIC')
subplot(4, 3, 2), plot(t, C2); title(' C2 TOC')
subplot(4, 3, 3), plot(t, C3); title(' C3 Porewater DIC')
subplot(4, 3, 4), plot(t, C4); title(' C4 Sediment OM')
subplot(4, 3, 5), plot(t, C5); title(' C5 Sediment Calcite')
subplot(4, 3, 6), plot(t, C6); title(' C6 Sed Arag')
subplot(4, 3, 7), plot(t, C7); title(' C7 Sed Mg- Calcite')
subplot(4, 3, 8), plot(t, C8); title(' C8 FW Calcite')
subplot(4, 3, 9), plot(t, C9); title(' C9 FW Arag')
subplot(4, 3, 10), plot(t, C10); title(' C10 FW Mg- Calcite')
subplot(4, 3, 11), plot(t, C11); title(' C11 FW Porewater')
subplot(4, 3, 12), plot(t, C12); title(' C12 FW OM')

```

figure(2)

```
subplot(3, 2, 1), plot(t, C13); title(' C13 Anox OM' )  
subplot(3, 2, 2), plot(t, C14); title(' C14 Anox Calcite' )  
subplot(3, 2, 3), plot(t, C15); title(' C15 Anox Arag' )  
subplot(3, 2, 4), plot(t, C16); title(' C16 Anox Mg- Calcite' )  
subplot(3, 2, 5), plot(t, C17); title(' C17 Anox Porewater' )
```

figure(3)

```
subplot(4, 3, 1), plot(t, Flux(:, 5), t, Flux(:, 12)); title(' Photo/Resp' )  
subplot(4, 3, 2), plot(t, Flux(:, 4)); title(' CF1A Atmosphere Exchange' )  
subplot(4, 3, 3), plot(t, Flux(:, 1)); title(' CF01 Ocean Import of DIC' )  
subplot(4, 3, 4), plot(t, Flux(:, 15), t, Flux(:, 6)); title(' Porewater Adv' )  
subplot(4, 3, 5), plot(t, Flux(:, 21)); title(' CF63 Aragonite Precip' )  
subplot(4, 3, 6), plot(t, Flux(:, 24)); title(' CF73 Mg- calcite Dissolution' )  
subplot(4, 3, 7), plot(t, Flux(:, 33)); title(' CF911 FW Aragonite Precip' )  
subplot(4, 3, 8), plot(t, Flux(:, 37)); title(' CF10: 11 FW Mg- calcite Diss' )  
subplot(4, 3, 9), plot(t, Flux(:, 46)); title(' CF15: 17 Anoxic Aragonite Precip' )  
subplot(4, 3, 10), plot(t, Flux(:, 48)); title(' CF16: 17 Anoxic Mg- calcite Diss' )  
subplot(4, 3, 11), plot(t, Flux(:, 16)); title(' Sediment Respiration' )  
subplot(4, 3, 12), plot(t, Flux(:, 42)); title(' Anoxic Sed Respiration' )
```

figure(4)

```
subplot(3, 3, 1), plot(t, Flux(:, 7)); title(' Calcite Calcification' )  
subplot(3, 3, 2), plot(t, Flux(:, 8)); title(' Aragonite Calcification' )  
subplot(3, 3, 3), plot(t, Flux(:, 9)); title(' Mg- calcite Calcification' )  
subplot(3, 3, 4), plot(t, Flux(:, 27)); title(' Calcite Chemical Bioerosion' )  
subplot(3, 3, 5), plot(t, Flux(:, 31)); title(' Aragonite Chemical Bioerosion' )  
subplot(3, 3, 6), plot(t, Flux(:, 35)); title(' Mg- calcite Chemical Bioerosion' )  
subplot(3, 3, 7), plot(t, Flux(:, 28)); title(' Calcite Mechanical Erosion' )  
subplot(3, 3, 8), plot(t, Flux(:, 32)); title(' Aragonite Mechanical Erosion' )  
subplot(3, 3, 9), plot(t, Flux(:, 36)); title(' Mg- calcite Mechanical Erosion' )
```

figure(5)

```
subplot(3, 2, 1), plot(t, G(:, 74)); title(' Surf 0m Calcite' )  
subplot(3, 2, 2), plot(t, G(:, 75)); title(' Surf 0m Aragonite' )  
subplot(3, 2, 3), plot(t, G(:, 76)); title(' Surf 0m 15% Mg- calc' )  
subplot(3, 2, 4), plot(t, G(:, 71)); title(' Surface pH' )  
subplot(3, 2, 5), plot(t, G(:, 72), t, G(:, 102)); title(' pCO2sw and pCO2atm' )  
subplot(3, 2, 6), plot(t, G(:, 70)); title(' Surface DIC' )
```

figure(6)

```
subplot(2, 2, 1), plot(t, G(:, 83), t, G(:, 84)); title(' PW 0m Arag/Mg- calcite' )  
subplot(2, 2, 2), plot(t, G(:, 79)); title(' PW pH' )  
subplot(2, 2, 3), plot(t, G(:, 80)); title(' PW pCO2' )  
subplot(2, 2, 4), plot(t, G(:, 78)); title(' PW DIC' )
```

figure(7)

```
subplot(2, 2, 1), plot(t, G(:, 91), t, G(:, 92)); title(' Anox PW 0m Arag/Mg- cal' )  
subplot(2, 2, 2), plot(t, G(:, 87)); title(' Anoxic PW pH' )  
subplot(2, 2, 3), plot(t, G(:, 88)); title(' Anoxic PW pCO2' )  
subplot(2, 2, 4), plot(t, G(:, 86)); title(' Anoxic PW DIC' )
```

figure(8)

```
subplot(2, 2, 1), plot(t, G(:, 99), t, G(:, 100)); title(' FW 0m Arag/Mg- cal' )
```

```

subplot(2, 2, 2), plot(t, G(:, 95)); title(' FW pH')
subplot(2, 2, 3), plot(t, G(:, 96)); title(' FW pCO2')
subplot(2, 2, 4), plot(t, G(:, 94)); title(' FW DIC')

if x==1;
    rcp26=v2struct(res, flux, surf, pw, pwan, fw, force);
    save(' CRESCAM_ODE15s_RCP26', ' G');
    save(' RCP26_structure', ' rcp26');
else if x==2;
    rcp45=v2struct(res, flux, surf, pw, pwan, fw, force);
    save(' CRESCAM_ODE15s_RCP45', ' G');
    save(' RCP45_structure', ' rcp45');
else if x==3;
    rcp60=v2struct(res, flux, surf, pw, pwan, fw, force);
    save(' CRESCAM_ODE15s_RCP6', ' G');
    save(' RCP60_structure', ' rcp60');
else if x==4;
    rcp85=v2struct(res, flux, surf, pw, pwan, fw, force);
    save(' CRESCAM_ODE15s_RCP85', ' G');
    save(' RCP85_structure', ' rcp85');
end
end
end
end

% -----
% end CRESCAM m
% -----

```

A.1.3 CRESCAMdiff.m Solver File

```
%-----  
% Matlab code for Coral Reef Ecosystem Carbon Model (CRESCAM)  
% standard scenario, year 2015-2100  
% created by Patrick Drupp 2014, based on SOCM code from Andersson, 2005  
  
% Three m-files and a forcing file are required:  
% 1. CRESCAM_initialss.m  
% 2. CRESCAM.m  
% 3. CRESCAMdiff.m  
%-----  
  
%-----  
%CRESCAMdiff.m  
%-----  
  
function yt = CRESCAMdiff(t,y)  
  
global R0 k f OM OM_pw OM_pwan OM_fw G sat_pw sat_pwan sat_fw;  
  
%-----  
%define anthropogenic forcings from forcing file  
%-----  
% for use with 0.001 year resolution forcings (default)  
tt=t*1000;  
tr=round(tt);  
r=find(f(:,1)==tr/1000);  
  
Tc=f(r,4); pCO2atm=f(r,3); DICocean=f(r,2); fN=f(r,5); fT=f(r,6);  
dAdt=f(r,7); fOM=f(r,8); fOM25=f(r,9); fOM50=f(r,10); fN2=f(r,11);  
fbleach=f(r,12);  
  
t  
%-----  
%First Order Steady State Fluxes  
%-----  
CF10=k(1)*y(1); %export off reef  
  
CF13=k(2)*y(1); %advection into porewater  
% CF18=k(3)*y(1); %calcification (calcite)  
% CF19=k(4)*y(1); %calcification (aragonite)  
% CF110=k(5)*y(1); %calcification (15% Mg-calcite)  
CF111=k(6)*y(1); %advection into framework porewater  
  
CF20=k(7)*y(2); %export off reef  
% CF21=k(8)*y(2); %respiration  
CF24=k(9)*y(2); %sedimentation to sediments  
CF212=k(10)*y(2); %sedimentation to framework  
  
CF31=k(11)*y(3); %advection out of porewater
```

```

% CF43=k(12)*y(4);      %OM sediment respiration
CF413=k(13)*y(4);      %OM burial to anoxic layer

% CF53=k(14)*y(5);      %sed calcite dissolution
CF514=k(15)*y(5);      %calcite burial to anoxic
CF50=k(16)*y(5);        %sed calcite export off reef

% CF63=k(17)*y(6);      %sed arag dissolution
CF615=k(18)*y(6);      %arag burial to anoxic
CF60=k(19)*y(6);        %sed arag export off reef

% CF73=k(20)*y(7);      %sed Mg-calcite dissolutoin
CF716=k(21)*y(7);      %Mg-calcite burial to anoxic
CF70=k(22)*y(7);        %sed Mg-calcite export off reef

% CF81=k(23)*y(8);      %chemical bioerosion of calcite framework
CF85=k(24)*y(8);        %mechanical erosion of calcite fw
% CF811=k(25)*y(8);     %dissolution of interior calcite framework
CF8B=k(26)*y(8);        %burial of calcite framework

% CF91=k(27)*y(9);      %chemical bioerosion of arag fw
CF96=k(28)*y(9);        %mechanical erosion of arag fw
% CF911=k(29)*y(9);     %diss of interior arag fw
CF9B=k(30)*y(9);        %burial of arag fw

% CF101=k(31)*y(10);    %chemical bioerosion of mg-calcite fw
CF107=k(32)*y(10);      %mechanical erosion of mg-calcite fw
% CF1011=k(33)*y(10);   %diss of interior mg-calcite fw
CF10B=k(34)*y(10);      %burial of mg-calcite fw

CF11_1=k(35)*y(11);     %advection of fw porewater to surface

% CF1211=k(36)*y(12);   %respiration of fw organic matter
CF12B=k(37)*y(12);      %burial of fw organic matter

% CF1317=k(38)*y(13);   %dissolution of anoxic layer organic matter
CF13B=k(39)*y(13);      %burial of organic matter

% CF1417=k(40)*y(14);   %dissolution of anoxic layer calcite
CF14B=k(41)*y(14);      %burial of calcite

% CF1517=k(42)*y(15);   %dissolution of anoxic layer arag
CF15B=k(43)*y(15);      %burial of arag

% CF1617=k(44)*y(16);   %dissolution of anoxic layer mg-calcite
CF16B=k(45)*y(16);      %burial of mg-calcite

CF173=k(46)*y(17);      %pw DIC exchange from anoxic to oxic layer

%-----
% initial physical state of surface seawater
%-----
T=Tc+273. 15;

```

```

S=35;

den1=999.842594+Tc*(6.793952*10^-2)+Tc^2*(-9.09529*10^-3)...
    +Tc^3*(1.001685*10^-4);
den2=den1+Tc^4*(-1.120083*10^-6)+Tc^5*(6.536332*10^-9);
den3=den2+S*(0.824493+Tc*(-4.0899*10^-3)+Tc^2*(7.6438*10^-5)...
    +Tc^3*(-8.2467*10^-7)+Tc^4*(5.3875*10^-9));
density=den3+S^(3/2)*(-5.72466*10^-3+Tc*1.0227*10^(-4)...
    +Tc^2*(-1.6546*10^-6))+S^2*(4.8314*10^-4);

%-----
%Calculate CO2-system parameters in surface water from TA and DIC
%Note that surface water TA is held constant
%-----

dic=y(1)/(5000*2000*2*density);
alk=2242.065257307470000e-6;

% % next three lines are for allowing TA to change during the simulation
% alk_i=2242.065257307470000e-6;
% dic_i=1973.44052127512e-6;
% alk=0.75*dic+(alk_i-0.75*dic_i);

% Calculating CaCO3 saturation state (0m) in surface water from TA and DIC
Kh=exp(93.4517.*(100./T)-60.2409+23.3585.*log(T./100)...
    +S.*(0.023517-0.023656.*(T./100)+0.0047036.*(T./100).^2));
K1=10^(-3633.86./T+61.2172-9.67770.*log(T)+0.011555.*S-0.0001152.*S^2);
K2=10^(-471.78./T-25.9290+3.16967.*log(T)+0.01781.*S-0.0001122.*S^2);
Kw=exp(-13847.26./T+148.9652-23.6521*log(T)...
    +(118.67./T-5.977+1.0495*log(T)).*S.^0.5-0.01615.*S);
kb1=-8966.9-2890.53.*S.^0.5-77.942.*S;
kb2=kb1+1.728.*S.^1.5-0.0996.*S.^2;
kb3=kb2./T;
kb4=kb3+148.0248+137.1942.*S.^0.5+1.62142.*S;
kb5=kb4+(-24.4344-25.085.*S.^0.5-0.2474*35)*log(T);
kb6=kb5+0.053105.*S.^0.5.*T;
Kb=exp(kb6);
bor = 1.*(416.*(S/35.))*.1e-6;
ca=0.0102821.*S/35;
mg=0.0528171.*S/35;

Kspc=10^(-171.9065-0.077993*T+2839.319/T+71.595*log10(T)...
    +(-0.77712+0.0028426*T+178.34/T)*S.^0.5-0.07711*S+0.0041249*S^1.5);
Kspa=10^(-171.945-0.077993*T+2903.293/T+71.595*log10(T)...
    +(-0.068393+0.0017276*T+88.135/T)*S.^0.5-0.10018*S+0.0059415*S^1.5);

p5 = -1.;
p4 = -alk-Kb-K1;
p3 = dic*K1-alk*(Kb+K1)+Kb*bor+Kw-Kb*K1-K1*K2;
tmp = dic*(Kb*K1+2.*K1*K2)-alk*(Kb*K1+K1*K2)+Kb*bor*K1;
p2 = tmp+(Kw*Kb+Kw*K1-Kb*K1*K2);
tmp = 2.*dic*Kb*K1*K2-alk*Kb*K1*K2+Kb*bor*K1*K2;
p1 = tmp+(Kw*Kb*K1+Kw*K1*K2);
p0 = Kw*Kb*K1*K2;
p = [p5 p4 p3 p2 p1 p0];

```

```

r_C1 = roots(p);
h = max(real(r_C1));
hco3 = di c/(1+h/K1+K2/h);
C03 = di c/(1+h/K2+h*h/K1/K2);

%activity coefficients (Millero 1998)
gCa=0.198;
gMg=0.203;
gC03=0.043;
aCa=gCa*ca;
aMg=gMg*mg;
aC03=gC03*C03;

% Plummer and Mackenzie (1974) solubilities from IAP18-IAP11
IAP=[10^-7.4208, ...
      10^-7.4695, ...
      10^-7.5396, ...
      10^-7.6229, ...
      10^-7.7071, ...
      10^-7.7894, ...
      10^-7.8745, ...
      10^-7.9606];

OMEGAcAl=ca*C03/Kspc;
OMEGAaAr=ca*C03/Kspa;
OMEGAmg=[aCa^0.82*aMg^0.18*aC03/IAP(1)...
          aCa^0.83*aMg^0.17*aC03/IAP(2)...
          aCa^0.84*aMg^0.16*aC03/IAP(3)...
          aCa^0.85*aMg^0.15*aC03/IAP(4)...
          aCa^0.86*aMg^0.14*aC03/IAP(5)...
          aCa^0.87*aMg^0.13*aC03/IAP(6)...
          aCa^0.88*aMg^0.12*aC03/IAP(7)...
          aCa^0.89*aMg^0.11*aC03/IAP(8)];
OM=[OMEGAcAl OMEGAaAr OMEGAmg(4)];

pHtotal = -log10(h);
C02star= h*hco3/K1;
fC02sw = C02star/Kh*1.e6;
HC03 = hco3*1.e6;
C03 = C03*1.e6;
DIC = di c*1.e6;
TA = al k*1.e6;
B=(-1636.75+12.0408.*T-0.0327957.*T.^2+3.16528e-5.*T.^3)*10^-6;
cvc=(57.7-0.118.*T)*10^-6;
R=8.314;
pC02= fC02sw/(exp(1*(B+2*cvc)/R.*T));

%-----
%Calculate CO2-system parameters in porewater from TA and DIC
%-----

%Oxic porewater: 0-20 cm in sediments
al k_i_pw=2378e-6;
di c_i_pw=2151.63423109156e-6;

```

```

di c_pw=y(3)/5.32138390408158E+07;
al k_pw=0.85*di c_pw+(al k_i_pw-0.85*di c_i_pw);

q5 = -1.;
q4 = -al k_pw- Kb- K1;
q3 = di c_pw*K1- al k_pw*(Kb+K1)+Kb*bor+Kw- Kb*K1- K1*K2;
tmp = di c_pw*(Kb*K1+2.*K1*K2)- al k_pw*(Kb*K1+K1*K2)+Kb*bor*K1;
q2 = tmp+(Kw*Kb+Kw*K1- Kb*K1*K2);
tmp = 2.*di c_pw*Kb*K1*K2- al k_pw*Kb*K1*K2+Kb*bor*K1*K2;
q1 = tmp+(+Kw*Kb*K1+Kw*K1*K2);
q0 = Kw*Kb*K1*K2;
q = [q5 q4 q3 q2 q1 q0];
r_pw = roots(q);
h_pw = max(real(r_pw));
hco3_pw = di c_pw/(1+h_pw/K1+K2/h_pw);
co3_pw = di c_pw/(1+h_pw/K2+h_pw*h_pw/K1/K2);
aCO3_pw=gCO3*co3_pw;

OMEGAc_al_pw=ca*co3_pw/Kspc;
OMEGAara_pw=ca*co3_pw/Kspa;
OMEGAmg_pw=[aCa^0.82*aMg^0.18*aCO3_pw/IAP(1)...
aCa^0.83*aMg^0.17*aCO3_pw/IAP(2)...
aCa^0.84*aMg^0.16*aCO3_pw/IAP(3)...
aCa^0.85*aMg^0.15*aCO3_pw/IAP(4)...
aCa^0.86*aMg^0.14*aCO3_pw/IAP(5)...
aCa^0.87*aMg^0.13*aCO3_pw/IAP(6)...
aCa^0.88*aMg^0.12*aCO3_pw/IAP(7)...
aCa^0.89*aMg^0.11*aCO3_pw/IAP(8)];
OM_pw=[OMEGAc_al_pw OMEGAara_pw OMEGAmg_pw(4)];

pHtotal_pw=-log10(h_pw);
CO2star_pw= h_pw*hco3_pw/K1;
fCO2_pw = CO2star_pw/Kh*1.e6;
HCO3_pw = hco3_pw*1.e6;
CO3_pw = co3_pw*1.e6;
DIC_pw = di c_pw*1.e6;
TA_pw = al k_pw*1.e6;
pCO2_pw = fCO2_pw/(exp(1*(B+2*cvc)/R.*T));

% Anoxic porewater: 20-100 cm in sediments
al k_i_pwan=2588e-6;
di c_i_pwan=2350e-6;

di c_pwan=y(17)/2.1285535616E+08;
al k_pwan=1.2*di c_pwan+(al k_i_pwan- (1.2*di c_i_pwan));

w5 = -1.;
w4 = -al k_pwan- Kb- K1;
w3 = di c_pwan*K1- al k_pwan*(Kb+K1)+Kb*bor+Kw- Kb*K1- K1*K2;
tmp = di c_pwan*(Kb*K1+2.*K1*K2)- al k_pwan*(Kb*K1+K1*K2)+Kb*bor*K1;
w2 = tmp+(Kw*Kb+Kw*K1- Kb*K1*K2);
tmp = 2.*di c_pwan*Kb*K1*K2- al k_pwan*Kb*K1*K2+Kb*bor*K1*K2;
w1 = tmp+(+Kw*Kb*K1+Kw*K1*K2);

```

```

w0 = Kw*Kb*K1*K2;
w = [w5 w4 w3 w2 w1 w0];
r_pwan = roots(w);
h_pwan = max(real(r_pwan));
hco3_pwan = di_c_pwan/(1+h_pwan/K1+K2/h_pwan);
co3_pwan = di_c_pwan/(1+h_pwan/K2+h_pwan*h_pwan/K1/K2);
aCO3_pwan=gCO3*co3_pwan;

OMEGAcAl_pwan=ca*co3_pwan/Kspc;
OMEGAara_pwan=ca*co3_pwan/Kspa;
OMEGAmg_pwan=[ aCa^0.82*aMg^0.18*aCO3/IAP(1)...
aCa^0.83*aMg^0.17*aCO3_pwan/IAP(2)...
aCa^0.84*aMg^0.16*aCO3_pwan/IAP(3)...
aCa^0.85*aMg^0.15*aCO3_pwan/IAP(4)...
aCa^0.86*aMg^0.14*aCO3_pwan/IAP(5)...
aCa^0.87*aMg^0.13*aCO3_pwan/IAP(6)...
aCa^0.88*aMg^0.12*aCO3_pwan/IAP(7)...
aCa^0.89*aMg^0.11*aCO3_pwan/IAP(8) ];
OM_pwan=[ OMEGAcAl_pwan OMEGAara_pwan OEGAmg_pwan(4) ];

pHtotal_pwan=-log10(h_pwan);
CO2star_pwan= h_pwan*hco3_pwan/K1;
fCO2_pwan = CO2star_pwan/Kh*1.e6;
HCO3_pwan = hco3_pwan*1.e6;
CO3_pwan = co3_pwan*1.e6;
DIC_pwan = di_c_pwan*1.e6;
TA_pwan = al_k_pwan*1.e6;
pCO2_pwan = fCO2_pwan/(exp(1*(B+2*cvc)/R.*T));

% Framework porewater
al_k_i_fw=2621.51580782553e-6;
di_c_i_fw=2384.24255801791e-6;

di_c_fw=y(11)/(2000*5000*0.95*0.5*density);
al_k_fw=1.2*di_c_fw+(al_k_i_fw-(1.2*di_c_i_fw));

e5 = -1.;
e4 = -al_k_fw-Kb-K1;
e3 = di_c_fw*K1-al_k_fw*(Kb+K1)+Kb*bor+Kw-Kb*K1-K1*K2;
tmp = di_c_fw*(Kb*K1+2.*K1*K2)-al_k_fw*(Kb*K1+K1*K2)+Kb*bor*K1;
e2 = tmp+(Kw*Kb+Kw*K1-Kb*K1*K2);
tmp = 2.*di_c_fw*Kb*K1*K2-al_k_fw*Kb*K1*K2+Kb*bor*K1*K2;
e1 = tmp+(Kw*Kb*K1+Kw*K1*K2);
e0 = Kw*Kb*K1*K2;
e = [e5 e4 e3 e2 e1 e0];
r_fw = roots(e);
h_fw = max(real(r_fw));
hco3_fw = di_c_fw/(1+h_fw/K1+K2/h_fw);
co3_fw = di_c_fw/(1+h_fw/K2+h_fw*h_fw/K1/K2);
aCO3_fw=gCO3*co3_fw;

OMEGAcAl_fw=ca*co3_fw/Kspc;
OMEGAara_fw=ca*co3_fw/Kspa;
OMEGAmg_fw=[ aCa^0.82*aMg^0.18*aCO3_fw/IAP(1)...

```

```

aCa^0.83*aMg^0.17*aCO3_fw/IAP(2)...
aCa^0.84*aMg^0.16*aCO3_fw/IAP(3)...
aCa^0.85*aMg^0.15*aCO3_fw/IAP(4)...
aCa^0.86*aMg^0.14*aCO3_fw/IAP(5)...
aCa^0.87*aMg^0.13*aCO3_fw/IAP(6)...
aCa^0.88*aMg^0.12*aCO3_fw/IAP(7)...
aCa^0.89*aMg^0.11*aCO3_fw/IAP(8)];
OM_fw=[OMEGAcalfw OMEGAarawf OMEGAmg_fw(4)];

pHtotal_fw=-log10(h_fw);
CO2star_fw= h_fw*hco3_fw/K1;
fCO2_fw = CO2star_fw/Kh*1.e6;
HCO3_fw = hco3_fw*1.e6;
CO3_fw = co3_fw*1.e6;
DIC_fw = dic_fw*1.e6;
TA_fw = alk_fw*1.e6;
pCO2_fw = fCO2_fw/(exp(1*(B+2*cvc)/R.*T));

%-----
%Special Flux Cases: This section is for fluxes that do not
%follow the simple CFij=ki*j*Ci 1st order formula.
%-----
T0=25;

%ocean import of organic carbon - zero order flux
CF02=2.20865780938767e9; %standard run
% CF02=f0M25; %25 percent increase in om by 2100
% CF02=f0M50; %50 percent increase in om by 2100
% CF02=f0M; %doubling of organic matter by 2100

%Photosynthesis standard run
CF12=1.89468048016244e9.*fN.*fT;

% Photosynthesis sensitivity runs and case studies

%no temperature dependence
% CF12=1.89468048016244e9.*fN;

% sensitivity analysis of a different photosynthetic Q10 (fT)
% fT2 = 1.5.^((Tc-25)./10);
% CF12=1.89468048016244e9.*fN.*fT2;

%doubling of nitrate by 2100
% CF12=1.89468048016244e9.*fN2.*fT;

%no temperature dependence but double nitrate
% CF12=1.89468048016244e9.*fN2;

%Respiration
CF21=k(8)*y(2).*fT;

%open ocean import of DIC
v=2000*5000*2;

```

```

RT=2000/0.15/3600/24/365;
CF01=DI Cocean*v*densi ty/RT;

CF43=k(12)*y(4). *fT;
CF1211=k(36)*y(12). *fT;
CF1317=k(38)*y(13). *fT;

%Biogenic Calcification - Omega and Temperature Dependences

%Linear calcification-Omega dependence (Gattuso et al. 1999)
LRom_cal0=21.3*4.601640838167461+12; LRom_cal=21.3*OM(1)+12;
LRom_ara0=21.3*3.033100165919164+12; LRom_ara=21.3*OM(2)+12;
LRom_mgca0=21.3*0.901242822504544+12; LRom_mgca=21.3*OM(3)+12;

%Curvilinear calcification-Omega dependence (Gattuso et al. 1998)
% CRom_cal=228*(1-exp(-4.601640838167461/0.69))-128;
% CRom_cal=228*(1-exp(-OM(1)/0.69))-128;
% CRom_ara=228*(1-exp(-3.033100165919164/0.69))-128;
% CRom_ara=228*(1-exp(-OM(2)/0.69))-128;
% CRom_mgca=228*(1-exp(-0.901242822504544/0.69))-128;
% CRom_mgca=228*(1-exp(-OM(3)/0.69))-128;

% Linear calcification-temp dependence
% LRt0=100; LRt=28*(Tc-T0)+100;

% Negative parabolic calcification-temp dependence 28 degree max threshold
% Standard Run
PRt0=88.12;
PRt=100-1.32.*(Tc-28).^2;

% % for sensitivity analysis of 27 degrees max threshold
% PRt0=94.72;
% PRt=100-1.32.*(Tc-27).^2;

% Calcification and temperature dependence used in flux equations
f1=LRom_cal/LRom_cal0;
f2=LRom_ara/LRom_ara0;
f3=LRom_mgca/LRom_mgca0;
% f1=CRom_cal/CRom_cal0;
% f2=CRom_ara/CRom_ara0;
% f3=CRom_mgca/CRom_mgca0;

% f4=LRt/LRt0;
f4=PRt/PRt0;

CF18=k(3)*y(1)*f1*f4;
CF19=k(4)*y(1)*f2*f4;
CF110=k(5)*y(1)*f3*f4;

% with bleaching and 50% reduction in coral calc. above 27.5 degrees
% CF18=k(3)*y(1)*f1*f4*fbleach;
% CF19=k(4)*y(1)*f2*f4*fbleach;
% CF110=k(5)*y(1)*f3*f4*fbleach;

```

```

%-----
% Porewater dissolution and precipitation calculations
%-----
% Porewater-permeable oxic sediment system
% Inhibition coefficients
P04_pw=2.5; %uM
P04i_nhi_b_pw=0.9711*exp(-0.52*P04_pw); %Berner et al. (1978)
DOM_pw=1.8; %mg C/L
DOMi_nhi_b_pw=-0.2462*DOM_pw+0.7879; %Berner et al. (1978)

P04_fw=2.5; %uM
P04i_nhi_b_fw=0.9711*exp(-0.52*P04_fw); %Berner et al. (1978)
DOM_fw=1.5; %mg C/L
DOMi_nhi_b_fw=-0.2462*DOM_fw+0.7879; %Berner et al. (1978)

P04_pwan=5.5; %uM
P04i_nhi_b_pwan=0.9711*exp(-0.52*P04_pwan); %Berner et al. (1978)
DOM_pwan=1.6; %mg C/L
DOMi_nhi_b_pwan=-0.2462*DOM_pwan+0.7879; %Berner et al. (1978)

kp=[10^-0.29 10^1.09 10^-0.29]; np=[2.8 2.36 2.8];
kd=[10^2.82 10^2.89 10^2.32]; nd=[2.86 2.48 3.55];

if OM_pw(1)>1
    Di_ssc=0; PPTc=(kp(1)*(OM_pw(1)-1)^np(1))*1E-6*8760*y(3)*12.01...
        *P04i_nhi_b_pw*DOMi_nhi_b_pw;
else
    PPTc=0; Di_ssc=(kd(1)*(1-OM_pw(1))^nd(1))*1E-6*8760*y(5)*100.1...
        *0.25*P04i_nhi_b_pw*DOMi_nhi_b_pw;
end

if OM_pw(2)>1
    Di_ssa=0; PPTa=(kp(2)*(OM_pw(2)-1)^np(2))*1E-6*8760*y(3)*12.01...
        *P04i_nhi_b_pw*DOMi_nhi_b_pw;
else
    PPTa=0; Di_ssa=(kd(2)*(1-OM_pw(2))^nd(2))*1E-6*8760*y(6)*100.1...
        *0.25*P04i_nhi_b_pw*DOMi_nhi_b_pw;
end

if OM_pw(3)>1
    Di_ssm=0; PPTm=(kp(3)*(OM_pw(3)-1)^np(3))*1E-6*8760*y(3)*12.01...
        *P04i_nhi_b_pw*DOMi_nhi_b_pw;
else
    PPTm=0; Di_ssm=(kd(3)*(1-OM_pw(3))^nd(3))*1E-6*8760*y(7)*97.7...
        *0.25*P04i_nhi_b_pw*DOMi_nhi_b_pw;
end

b=size(sat_pw,1);
if b==0
    sat_pw(b+1,:)= [tr PPTc PPTa PPTm Di_ssm];
else
    if tr<sat_pw(b,1)
        bb= sat_pw(:,1)<tr;

```

```

    sat_pw=sat_pw(bb,:);
    ij=size(sat_pw,1);
    sat_pw(ij+1,:)=[tr PPTc PPTa PPTm Di ssm];
elseif tr==sat_pw(b,1)
    sat_pw(b,:)=[tr PPTc PPTa PPTm Di ssm];
else
    sat_pw(b+1,:)=[tr PPTc PPTa PPTm Di ssm];
end
end
end

CF53i=0; CF63i=k(48)*R0(3);
CF73i=k(20)*R0(7);
PPTci=sat_pw(1,2); PPTai=sat_pw(1,3);
PPTmi=sat_pw(1,4); Di ssmi=sat_pw(1,5);

CF53=0;
CF63=(- CF63i +(PPTai - PPTa)+Di ssa);
CF73=- (PPTm- PPTmi - CF73i - Di ssm+Di ssmi);

% Porewater-permeable anoxic sediment system
if OM_pwan(1)>1
    Di ssc_pwan=0; PPTc_pwan=(kp(1)*(OM_pwan(1)-1)^np(1))*1E-6*8760*...
    *y(17)*12.1*P04i nhi b_pwan*DOMi nhi b_pwan;
else
    PPTc_pwan=0; Di ssc_pwan=(kd(1)*(1-OM_pwan(1))^nd(1))*1E-6*8760*...
    y(14)*100.1*0.25*P04i nhi b_pwan*DOMi nhi b_pwan;
end

if OM_pwan(2)>1
    Di ssa_pwan=0; PPTa_pwan=(kp(2)*(OM_pwan(2)-1)^np(2))*1E-6*8760*...
    y(17)*12.01*P04i nhi b_pwan*DOMi nhi b_pwan;
else
    PPTa_pwan=0; Di ssa_pwan=(kd(2)*(1-OM_pwan(2))^nd(2))*1E-6*8760*...
    y(15)*100.1*0.25*P04i nhi b_pwan*DOMi nhi b_pwan;
end

if OM_pwan(3)>1
    Di ssm_pwan=0; PPTm_pwan=(kp(3)*(OM_pwan(3)-1)^np(3))*1E-6*8760*...
    y(17)*12.01*P04i nhi b_pwan*DOMi nhi b_pwan;
else
    PPTm_pwan=0; Di ssm_pwan=(kd(3)*(1-OM_pwan(3))^nd(3))*1E-6*8760*...
    y(16)*97.7*0.25*P04i nhi b_pwan*DOMi nhi b_pwan;
end

c=size(sat_pwan,1);
if c==0
    sat_pwan(c+1,:)=[tr PPTc_pwan PPTa_pwan PPTm_pwan Di ssm_pwan];
else
    if tr<sat_pwan(c,1)
        cc = sat_pwan(:,1)<tr;
        sat_pwan=sat_pwan(cc,:);
        jk=size(sat_pwan,1);
        sat_pwan(jk+1,:)=[tr PPTc_pwan PPTa_pwan PPTm_pwan Di ssm_pwan];
    elseif tr==sat_pwan(c,1)

```

```

    sat_pwan(c,:)=[tr PPTc_pwan PPTa_pwan PPTm_pwan Di ssm_pwan];
else
    sat_pwan(c+1,:)=[tr PPTc_pwan PPTa_pwan PPTm_pwan Di ssm_pwan];
end
end

CF1417i=0; CF1517i=k(51)*R0(17); CF1617i=k(44)*R0(16);
PPTci_pwan=sat_pwan(1,2); PPTai_pwan=sat_pwan(1,3);
PPTmi_pwan=sat_pwan(1,4); Di ssmi_pwan=sat_pwan(1,5);

CF1417=0;
CF1517=(-CF1517i+(PPTai_pwan-PPTa_pwan)+Di ssa_pwan);
CF1617=- (PPTm_pwan-PPTmi_pwan-CF1617i-Di ssm_pwan+Di ssmi_pwan);

% Porewater-Framework system
if OM_fw(1)>1
    Di ssc_fw=0; PPTc_fw=(kp(1)*(OM_fw(1)-1)^np(1))*1E-6*8760*y(11)*12.01...
        *P04i nhi b_fw*DOMi nhi b_fw;
else
    PPTc_fw=0; Di ssc_fw=(kd(1)*(1-OM_fw(1))^nd(1))*1E-6*8760*y(8)*100.1...
        *0.25*P04i nhi b_fw*DOMi nhi b_fw;
end

if OM_fw(2)>1
    Di ssa_fw=0; PPTa_fw=(kp(2)*(OM_fw(2)-1)^np(2))*1E-6*8760*y(11)*12.01...
        *P04i nhi b_fw*DOMi nhi b_fw;
else
    PPTa_fw=0; Di ssa_fw=(kd(2)*(1-OM_fw(2))^nd(2))*1E-6*8760*y(9)*100.1...
        *0.25*P04i nhi b_fw*DOMi nhi b_fw;
end

if OM_fw(3)>1
    Di ssm_fw=0; PPTm_fw=(kp(3)*(OM_fw(3)-1)^np(3))*1E-6*8760*y(11)*12.01...
        *P04i nhi b_fw*DOMi nhi b_fw;
else
    PPTm_fw=0; Di ssm_fw=(kd(3)*(1-OM_fw(3))^nd(3))*1E-6*8760*y(10)*97.7...
        *0.25*P04i nhi b_fw*DOMi nhi b_fw;
end

d=size(sat_fw,1);
if d==0
    sat_fw(d+1,:)=[tr PPTc_fw PPTa_fw PPTm_fw Di ssm_fw];
else
    if tr<sat_fw(d,1)
        dd= sat_fw(:,1)<tr;
        sat_fw=sat_fw(dd,:);
        kl=size(sat_fw,1);
        sat_fw(kl+1,:)=[tr PPTc_fw PPTa_fw PPTm_fw Di ssm_fw];
    elseif tr==sat_fw(d,1)
        sat_fw(d,:)=[tr PPTc_fw PPTa_fw PPTm_fw Di ssm_fw];
    else
        sat_fw(d+1,:)=[tr PPTc_fw PPTa_fw PPTm_fw Di ssm_fw];
    end
end
end

```

```

CF811i=0; CF911i=k(54)*R0(11);
CF1011i=k(33)*R0(10);
PPTci_fw=sat_fw(1,2); PPTai_fw=sat_fw(1,3);
PPTmi_fw=sat_fw(1,4);
Dissmi_fw=sat_fw(1,5);
CF1011i=Dissmi_fw;

CF811=0;
CF911=(-CF911i+(PPTai_fw-PPTa_fw)+Dissa_fw);
CF1011=- (PPTm_fw-PPTmi_fw-CF1011i-Dissm_fw+Dissmi_fw);

%-----
% Chemical Bioerosion of Reef Framework
%-----
% Linear bioerosion-pCO2 relationship
RpC02=0.429*440.1118344492954+138.57; RpC02=0.429*pC02+138.57;

f5=RpC02./RpC020;

CF81=k(23)*y(8)*f5;
CF91=k(27)*y(9)*f5;
CF101=k(31)*y(10)*f5;

%-----
% Reef surface water-atmospheric gas exchange
%-----
Atm0=399; Atm=pC02atm; %pC02 in uatm
Ro=9; d=4;

%CF1: A atmospheric exchange - Values from Drupp et al. (2013)
u10=5.19292253475285; %m/s
k600=0.266*u10^2; %Ho et al. (2006)
%schmidt from Wanninkhof (1992) s=35
schmidt=2073.1-(125.62*Tc)+(3.6276*Tc^2)-0.043219*Tc^3;
%ambient k in m/hr
k_amb=k600*(schmidt/600)^-0.5/100;
co2sol=exp(93.4517*(100/(Tc+273.15))-60.2409+23.3585...
*log((Tc+273.15)/100)+S*(0.023517-0.023656*((Tc+273.15)/100)...
+0.0047036*((Tc+273.15)/100)*((Tc+273.15)/100));
del pC02=pC02-pC02atm;
CF1A=k_amb*co2sol*density*del pC02*1e-6*24*365*2000*5000;

%-----
% Differential Equations (Mass Balance)
%-----
yt = [CF01+CF21+CF31+CF81+CF91+CF101+CF11_1-CF10-CF1A-CF12-CF13-CF18-...
CF19-CF110-CF111,...
CF02+CF12-CF20-CF21-CF24-CF212,...
CF13+CF43+CF53+CF63+CF73+CF173-CF31,...
CF24-CF43-CF413,...
CF85-CF53-CF514-CF50,...
CF96-CF63-CF615-CF60,...
CF107-CF73-CF716-CF70,...

```

```

CF18- CF81- CF85- CF811- CF8B, ...
CF19- CF91- CF96- CF911- CF9B, ...
CF110- CF101- CF107- CF1011- CF10B, ...
CF111+CF811+CF911+CF1011+CF1211- CF11_1, ...
CF212- CF1211- CF12B, ...
CF413- CF1317- CF13B, ...
CF514- CF1417- CF14B, ...
CF615- CF1517- CF15B, ...
CF716- CF1617- CF16B, ...
CF1317+CF1417+CF1517+CF1617- CF173]';

% -----
% Output parameters to be saved to matrix G
% -----
i=size(G, 1);
if i==0
    G(i+1,:)=[tr y' CF01 CF02 CF10 CF1A CF12 CF13 CF18 CF19 CF110 CF111...
              CF20 CF21 CF24 CF212...
              CF31 CF43 CF413 CF53 CF514 CF50 CF63 CF615 CF60 CF73 CF716 CF70...
              CF81 CF85 CF811 CF8B CF91 CF96 CF911 CF9B CF101 CF107 CF1011...
              CF10B CF11_1 CF1211 CF12B CF1317 CF13B CF1417 CF14B CF1517 CF15B...
              CF1617 CF16B CF173...
              TA DIC pHtotal pCO2 fCO2sw OM TA_pw DIC_pw pHtotal_pw pCO2_pw...
              fCO2_pw OM_pw TA_pwan DIC_pwan pHtotal_pwan pCO2_pwan...
              fCO2_pwan OM_pwan TA_fw DIC_fw pHtotal_fw pCO2_fw...
              fCO2_fw OM_fw dCdt Atm f1 f2 f3 f4 f5 Tc DI Cocean...
              OMEGAmg OMEGAmg_pw OMEGAmg_pwan OMEGAmg_fw];
else
    if tr<G(i, 1);
        ii= G(:, 1)<tr;
        G=G(ii, :);
        ij=size(G, 1);
        G(ij+1,:)=[tr y' CF01 CF02 CF10 CF1A CF12 CF13 CF18 CF19 CF110...
                  CF111 CF20 CF21 CF24 CF212...
                  CF31 CF43 CF413 CF53 CF514 CF50 CF63 CF615 CF60 CF73 CF716 CF70...
                  CF81 CF85 CF811 CF8B CF91 CF96 CF911 CF9B CF101 CF107 CF1011...
                  CF10B CF11_1 CF1211 CF12B CF1317 CF13B CF1417 CF14B CF1517 CF15B...
                  CF1617 CF16B CF173...
                  TA DIC pHtotal pCO2 fCO2sw OM TA_pw DIC_pw pHtotal_pw pCO2_pw...
                  fCO2_pw OM_pw TA_pwan DIC_pwan pHtotal_pwan pCO2_pwan...
                  fCO2_pwan OM_pwan TA_fw DIC_fw pHtotal_fw pCO2_fw...
                  fCO2_fw OM_fw dCdt Atm f1 f2 f3 f4 f5 Tc DI Cocean...
                  OMEGAmg OMEGAmg_pw OMEGAmg_pwan OMEGAmg_fw];
    elseif tr==G(i, 1)
        G(i,:)=[tr y' CF01 CF02 CF10 CF1A CF12 CF13 CF18 CF19 CF110...
               CF111 CF20 CF21 CF24 CF212...
               CF31 CF43 CF413 CF53 CF514 CF50 CF63 CF615 CF60 CF73 CF716 CF70...
               CF81 CF85 CF811 CF8B CF91 CF96 CF911 CF9B CF101 CF107 CF1011...
               CF10B CF11_1 CF1211 CF12B CF1317 CF13B CF1417 CF14B CF1517 CF15B...
               CF1617 CF16B CF173...
               TA DIC pHtotal pCO2 fCO2sw OM TA_pw DIC_pw pHtotal_pw pCO2_pw...
               fCO2_pw OM_pw TA_pwan DIC_pwan pHtotal_pwan pCO2_pwan...
               fCO2_pwan OM_pwan TA_fw DIC_fw pHtotal_fw pCO2_fw...
               OMEGAmg OMEGAmg_pw OMEGAmg_pwan OMEGAmg_fw];
    end
end

```

```
fCO2_fw OM_fw dCdt Atm f1 f2 f3 f4 f5 Tc DIcocean...
OMEGAng OMEGAng_pw OMEGAng_pwan OMEGAng_fw];
```

```
else
```

```
G(i+1,:)= [tr y' CF01 CF02 CF10 CF1A CF12 CF13 CF18 CF19 CF110...
           CF111 CF20 CF21 CF24 CF212...
           CF31 CF43 CF413 CF53 CF514 CF50 CF63 CF615 CF60 CF73 CF716 CF70...
           CF81 CF85 CF811 CF8B CF91 CF96 CF911 CF9B CF101 CF107 CF1011...
           CF10B CF11_1 CF1211 CF12B CF1317 CF13B CF1417 CF14B CF1517 CF15B...
           CF1617 CF16B CF173...
           TA DIC pHtotal pCO2 fCO2sw OM TA_pw DIC_pw pHtotal_pw pCO2_pw...
           fCO2_pw OM_pw TA_pwan DIC_pwan pHtotal_pwan pCO2_pwan...
           fCO2_pwan OM_pwan TA_fw DIC_fw pHtotal_fw pCO2_fw...
           fCO2_fw OM_fw dCdt Atm f1 f2 f3 f4 f5 Tc DIcocean...
           OMEGAng OMEGAng_pw OMEGAng_pwan OMEGAng_fw];
```

```
end
```

```
end
```

```
return;
```

```
% -----
% end of file CRESCAMdiff.m
% -----
```

A.1.4 RCP 2.6 Forcing File

Year	DIC (mol kg ⁻¹)	pCO ₂ (µatm)	Temp (°C)	fN	fT	dAdt	fOM	fOM25	fOM50	fN2
2015	0.001993	399.00	25.00	1	1.000	0.00	2.21E+09	2.21E+09	2.21E+09	1.000
2016	0.001995	402.97	25.03	1	1.002	3.97	2.23E+09	2.22E+09	2.22E+09	1.012
2017	0.001996	405.25	25.01	1	1.001	2.28	2.26E+09	2.22E+09	2.23E+09	1.024
2018	0.001997	407.53	25.05	1	1.003	2.28	2.29E+09	2.23E+09	2.25E+09	1.035
2019	0.001998	409.80	25.08	1	1.005	2.27	2.31E+09	2.23E+09	2.26E+09	1.047
2020	0.001999	412.07	25.08	1	1.006	2.27	2.34E+09	2.24E+09	2.27E+09	1.059
2021	0.002000	414.33	25.08	1	1.006	2.26	2.36E+09	2.25E+09	2.29E+09	1.071
2022	0.002001	416.52	25.09	1	1.006	2.19	2.39E+09	2.25E+09	2.30E+09	1.082
2023	0.002002	418.60	25.13	1	1.009	2.09	2.42E+09	2.26E+09	2.31E+09	1.094
2024	0.002002	420.60	25.16	1	1.011	2.00	2.44E+09	2.27E+09	2.33E+09	1.106
2025	0.002003	422.52	25.19	1	1.013	1.91	2.47E+09	2.27E+09	2.34E+09	1.118
2026	0.002004	424.35	25.19	1	1.013	1.83	2.49E+09	2.28E+09	2.35E+09	1.129
2027	0.002005	426.10	25.21	1	1.015	1.75	2.52E+09	2.29E+09	2.36E+09	1.141
2028	0.002006	427.75	25.21	1	1.014	1.66	2.55E+09	2.29E+09	2.38E+09	1.153
2029	0.002006	429.31	25.22	1	1.015	1.56	2.57E+09	2.30E+09	2.39E+09	1.165
2030	0.002007	430.78	25.23	1	1.016	1.47	2.60E+09	2.31E+09	2.40E+09	1.176
2031	0.002007	432.16	25.25	1	1.018	1.38	2.62E+09	2.31E+09	2.42E+09	1.188
2032	0.002008	433.44	25.27	1	1.019	1.27	2.65E+09	2.32E+09	2.43E+09	1.200
2033	0.002008	434.59	25.30	1	1.021	1.16	2.68E+09	2.33E+09	2.44E+09	1.212
2034	0.002009	435.65	25.29	1	1.020	1.06	2.70E+09	2.33E+09	2.46E+09	1.224
2035	0.002009	436.63	25.26	1	1.018	0.98	2.73E+09	2.34E+09	2.47E+09	1.235
2036	0.002009	437.52	25.33	1	1.023	0.89	2.75E+09	2.35E+09	2.48E+09	1.247
2037	0.002009	438.33	25.36	1	1.025	0.81	2.78E+09	2.35E+09	2.49E+09	1.259
2038	0.002010	439.06	25.35	1	1.024	0.73	2.81E+09	2.36E+09	2.51E+09	1.271
2039	0.002010	439.69	25.35	1	1.025	0.63	2.83E+09	2.36E+09	2.52E+09	1.282
2040	0.002010	440.22	25.38	1	1.027	0.53	2.86E+09	2.37E+09	2.53E+09	1.294
2041	0.002010	440.66	25.39	1	1.028	0.43	2.88E+09	2.38E+09	2.55E+09	1.306
2042	0.002010	441.02	25.39	1	1.028	0.37	2.91E+09	2.38E+09	2.56E+09	1.318
2043	0.002010	441.35	25.39	1	1.027	0.32	2.94E+09	2.39E+09	2.57E+09	1.329
2044	0.002011	441.62	25.38	1	1.027	0.27	2.96E+09	2.40E+09	2.59E+09	1.341
2045	0.002011	441.86	25.39	1	1.027	0.24	2.99E+09	2.40E+09	2.60E+09	1.353
2046	0.002011	442.08	25.41	1	1.029	0.22	3.01E+09	2.41E+09	2.61E+09	1.365
2047	0.002010	442.28	25.43	1	1.030	0.20	3.04E+09	2.42E+09	2.62E+09	1.376
2048	0.002011	442.46	25.42	1	1.030	0.17	3.07E+09	2.42E+09	2.64E+09	1.388
2049	0.002011	442.60	25.44	1	1.031	0.14	3.09E+09	2.43E+09	2.65E+09	1.400
2050	0.002011	442.70	25.45	1	1.031	0.10	3.12E+09	2.44E+09	2.66E+09	1.412
2051	0.002011	442.75	25.44	1	1.031	0.05	3.14E+09	2.44E+09	2.68E+09	1.424
2052	0.002011	442.76	25.43	1	1.030	0.01	3.17E+09	2.45E+09	2.69E+09	1.435
2053	0.002011	442.73	25.44	1	1.031	-0.03	3.20E+09	2.46E+09	2.70E+09	1.447
2054	0.002011	442.66	25.41	1	1.029	-0.07	3.22E+09	2.46E+09	2.72E+09	1.459
2055	0.002011	442.55	25.42	1	1.030	-0.11	3.25E+09	2.47E+09	2.73E+09	1.471
2056	0.002010	442.41	25.45	1	1.032	-0.14	3.27E+09	2.47E+09	2.74E+09	1.482
2057	0.002010	442.25	25.43	1	1.030	-0.16	3.30E+09	2.48E+09	2.75E+09	1.494
2058	0.002010	442.08	25.43	1	1.030	-0.17	3.33E+09	2.49E+09	2.77E+09	1.506
2059	0.002010	441.89	25.43	1	1.030	-0.19	3.35E+09	2.49E+09	2.78E+09	1.518
2060	0.002010	441.67	25.44	1	1.031	-0.21	3.38E+09	2.50E+09	2.79E+09	1.529

2061	0.002010	441.42	25.48	1	1.034	-0.25	3.40E+09	2.51E+09	2.81E+09	1.541
2062	0.002010	441.13	25.45	1	1.032	-0.29	3.43E+09	2.51E+09	2.82E+09	1.553
2063	0.002010	440.80	25.44	1	1.031	-0.33	3.46E+09	2.52E+09	2.83E+09	1.565
2064	0.002010	440.43	25.44	1	1.031	-0.37	3.48E+09	2.53E+09	2.85E+09	1.576
2065	0.002010	440.01	25.42	1	1.029	-0.42	3.51E+09	2.53E+09	2.86E+09	1.588
2066	0.002009	439.54	25.42	1	1.029	-0.47	3.53E+09	2.54E+09	2.87E+09	1.600
2067	0.002009	439.05	25.44	1	1.031	-0.49	3.56E+09	2.55E+09	2.88E+09	1.612
2068	0.002009	438.54	25.42	1	1.029	-0.51	3.59E+09	2.55E+09	2.90E+09	1.624
2069	0.002008	438.02	25.44	1	1.031	-0.52	3.61E+09	2.56E+09	2.91E+09	1.635
2070	0.002008	437.48	25.43	1	1.030	-0.54	3.64E+09	2.57E+09	2.92E+09	1.647
2071	0.002008	436.92	25.42	1	1.030	-0.56	3.66E+09	2.57E+09	2.94E+09	1.659
2072	0.002008	436.34	25.42	1	1.029	-0.58	3.69E+09	2.58E+09	2.95E+09	1.671
2073	0.002008	435.76	25.43	1	1.030	-0.58	3.72E+09	2.59E+09	2.96E+09	1.682
2074	0.002007	435.18	25.43	1	1.030	-0.58	3.74E+09	2.59E+09	2.98E+09	1.694
2075	0.002007	434.60	25.43	1	1.030	-0.59	3.77E+09	2.60E+09	2.99E+09	1.706
2076	0.002007	434.00	25.42	1	1.030	-0.60	3.79E+09	2.60E+09	3.00E+09	1.718
2077	0.002007	433.38	25.41	1	1.029	-0.61	3.82E+09	2.61E+09	3.01E+09	1.729
2078	0.002006	432.78	25.41	1	1.029	-0.60	3.85E+09	2.62E+09	3.03E+09	1.741
2079	0.002006	432.19	25.43	1	1.030	-0.59	3.87E+09	2.62E+09	3.04E+09	1.753
2080	0.002006	431.62	25.40	1	1.028	-0.57	3.90E+09	2.63E+09	3.05E+09	1.765
2081	0.002006	431.06	25.40	1	1.028	-0.56	3.92E+09	2.64E+09	3.07E+09	1.776
2082	0.002005	430.51	25.39	1	1.028	-0.55	3.95E+09	2.64E+09	3.08E+09	1.788
2083	0.002005	429.96	25.39	1	1.028	-0.55	3.98E+09	2.65E+09	3.09E+09	1.800
2084	0.002005	429.41	25.38	1	1.027	-0.55	4.00E+09	2.66E+09	3.11E+09	1.812
2085	0.002004	428.86	25.41	1	1.029	-0.56	4.03E+09	2.66E+09	3.12E+09	1.824
2086	0.002004	428.30	25.41	1	1.029	-0.56	4.05E+09	2.67E+09	3.13E+09	1.835
2087	0.002004	427.73	25.41	1	1.029	-0.57	4.08E+09	2.68E+09	3.14E+09	1.847
2088	0.002004	427.14	25.41	1	1.029	-0.58	4.11E+09	2.68E+09	3.16E+09	1.859
2089	0.002003	426.57	25.39	1	1.027	-0.58	4.13E+09	2.69E+09	3.17E+09	1.871
2090	0.002003	426.00	25.43	1	1.030	-0.56	4.16E+09	2.70E+09	3.18E+09	1.882
2091	0.002003	425.46	25.42	1	1.029	-0.54	4.18E+09	2.70E+09	3.20E+09	1.894
2092	0.002002	424.94	25.43	1	1.030	-0.52	4.21E+09	2.71E+09	3.21E+09	1.906
2093	0.002002	424.43	25.42	1	1.029	-0.51	4.24E+09	2.72E+09	3.22E+09	1.918
2094	0.002002	423.93	25.43	1	1.030	-0.50	4.26E+09	2.72E+09	3.24E+09	1.929
2095	0.002002	423.43	25.41	1	1.028	-0.50	4.29E+09	2.73E+09	3.25E+09	1.941
2096	0.002002	422.93	25.41	1	1.029	-0.50	4.31E+09	2.73E+09	3.26E+09	1.953
2097	0.002001	422.43	25.42	1	1.029	-0.50	4.34E+09	2.74E+09	3.27E+09	1.965
2098	0.002001	421.92	25.41	1	1.029	-0.51	4.37E+09	2.75E+09	3.29E+09	1.976
2099	0.002001	421.40	25.40	1	1.028	-0.52	4.39E+09	2.75E+09	3.30E+09	1.988
2100	0.002001	420.90	25.42	1	1.029	-0.51	4.42E+09	2.76E+09	3.31E+09	2.000

A.1.5 RCP 4.5 Forcing File

Year	DIC (mol kg⁻¹)	pCO₂ (µatm)	Temp (°C)	fN	fT	dAdt	fOM	fOM25	fOM50	fN2
2015	0.001993	399.00	25.00	1	1.000	0.00	2.21E+09	2.21E+09	2.21E+09	1.000
2016	0.001994	402.18	25.04	1	1.003	3.18	2.23E+09	2.22E+09	2.22E+09	1.012
2017	0.001996	404.41	25.02	1	1.001	2.23	2.26E+09	2.22E+09	2.23E+09	1.024
2018	0.001996	406.64	25.05	1	1.004	2.23	2.29E+09	2.23E+09	2.25E+09	1.035
2019	0.001997	408.88	25.06	1	1.004	2.24	2.31E+09	2.23E+09	2.26E+09	1.047

2020	0.001998	411.13	25.11	1	1.007	2.25	2.34E+09	2.24E+09	2.27E+09	1.059
2021	0.001999	413.38	25.11	1	1.007	2.25	2.36E+09	2.25E+09	2.29E+09	1.071
2022	0.002000	415.64	25.13	1	1.009	2.26	2.39E+09	2.25E+09	2.30E+09	1.082
2023	0.002001	417.94	25.16	1	1.011	2.30	2.42E+09	2.26E+09	2.31E+09	1.094
2024	0.002002	420.27	25.19	1	1.014	2.34	2.44E+09	2.27E+09	2.33E+09	1.106
2025	0.002003	422.66	25.23	1	1.016	2.38	2.47E+09	2.27E+09	2.34E+09	1.118
2026	0.002004	425.08	25.27	1	1.019	2.42	2.49E+09	2.28E+09	2.35E+09	1.129
2027	0.002005	427.54	25.29	1	1.020	2.46	2.52E+09	2.29E+09	2.36E+09	1.141
2028	0.002006	430.02	25.28	1	1.020	2.48	2.55E+09	2.29E+09	2.38E+09	1.153
2029	0.002007	432.52	25.32	1	1.022	2.50	2.57E+09	2.30E+09	2.39E+09	1.165
2030	0.002008	435.05	25.33	1	1.023	2.52	2.60E+09	2.31E+09	2.40E+09	1.176
2031	0.002009	437.59	25.33	1	1.023	2.54	2.62E+09	2.31E+09	2.42E+09	1.188
2032	0.002010	440.13	25.37	1	1.026	2.54	2.65E+09	2.32E+09	2.43E+09	1.200
2033	0.002011	442.66	25.38	1	1.027	2.53	2.68E+09	2.33E+09	2.44E+09	1.212
2034	0.002012	445.21	25.39	1	1.027	2.54	2.70E+09	2.33E+09	2.46E+09	1.224
2035	0.002013	447.77	25.40	1	1.028	2.56	2.73E+09	2.34E+09	2.47E+09	1.235
2036	0.002014	450.36	25.43	1	1.030	2.59	2.75E+09	2.35E+09	2.48E+09	1.247
2037	0.002015	452.96	25.47	1	1.033	2.61	2.78E+09	2.35E+09	2.49E+09	1.259
2038	0.002016	455.59	25.48	1	1.034	2.62	2.81E+09	2.36E+09	2.51E+09	1.271
2039	0.002017	458.22	25.50	1	1.035	2.63	2.83E+09	2.36E+09	2.52E+09	1.282
2040	0.002018	460.84	25.52	1	1.036	2.63	2.86E+09	2.37E+09	2.53E+09	1.294
2041	0.002019	463.48	25.55	1	1.039	2.63	2.88E+09	2.38E+09	2.55E+09	1.306
2042	0.002020	466.09	25.56	1	1.039	2.62	2.91E+09	2.38E+09	2.56E+09	1.318
2043	0.002021	468.68	25.57	1	1.040	2.58	2.94E+09	2.39E+09	2.57E+09	1.329
2044	0.002022	471.23	25.61	1	1.043	2.56	2.96E+09	2.40E+09	2.59E+09	1.341
2045	0.002023	473.78	25.60	1	1.042	2.55	2.99E+09	2.40E+09	2.60E+09	1.353
2046	0.002024	476.33	25.62	1	1.044	2.55	3.01E+09	2.41E+09	2.61E+09	1.365
2047	0.002025	478.88	25.66	1	1.047	2.55	3.04E+09	2.42E+09	2.62E+09	1.376
2048	0.002026	481.44	25.67	1	1.048	2.56	3.07E+09	2.42E+09	2.64E+09	1.388
2049	0.002026	483.99	25.73	1	1.052	2.55	3.09E+09	2.43E+09	2.65E+09	1.400
2050	0.002027	486.54	25.71	1	1.050	2.54	3.12E+09	2.44E+09	2.66E+09	1.412
2051	0.002028	489.06	25.73	1	1.052	2.53	3.14E+09	2.44E+09	2.68E+09	1.424
2052	0.002029	491.54	25.74	1	1.052	2.48	3.17E+09	2.45E+09	2.69E+09	1.435
2053	0.002030	493.93	25.78	1	1.056	2.40	3.20E+09	2.46E+09	2.70E+09	1.447
2054	0.002031	496.24	25.79	1	1.056	2.31	3.22E+09	2.46E+09	2.72E+09	1.459
2055	0.002031	498.47	25.80	1	1.057	2.23	3.25E+09	2.47E+09	2.73E+09	1.471
2056	0.002032	500.65	25.83	1	1.059	2.17	3.27E+09	2.47E+09	2.74E+09	1.482
2057	0.002033	502.77	25.83	1	1.059	2.12	3.30E+09	2.48E+09	2.75E+09	1.494
2058	0.002034	504.85	25.86	1	1.061	2.08	3.33E+09	2.49E+09	2.77E+09	1.506
2059	0.002034	506.88	25.90	1	1.064	2.04	3.35E+09	2.49E+09	2.78E+09	1.518
2060	0.002035	508.87	25.91	1	1.065	1.99	3.38E+09	2.50E+09	2.79E+09	1.529
2061	0.002036	510.80	25.90	1	1.064	1.93	3.40E+09	2.51E+09	2.81E+09	1.541
2062	0.002036	512.65	25.92	1	1.066	1.85	3.43E+09	2.51E+09	2.82E+09	1.553
2063	0.002037	514.40	25.92	1	1.066	1.75	3.46E+09	2.52E+09	2.83E+09	1.565
2064	0.002037	516.06	25.95	1	1.068	1.66	3.48E+09	2.53E+09	2.85E+09	1.576
2065	0.002038	517.63	25.97	1	1.070	1.56	3.51E+09	2.53E+09	2.86E+09	1.588
2066	0.002038	519.10	25.98	1	1.070	1.47	3.53E+09	2.54E+09	2.87E+09	1.600
2067	0.002039	520.49	25.98	1	1.070	1.39	3.56E+09	2.55E+09	2.88E+09	1.612
2068	0.002039	521.82	25.98	1	1.070	1.33	3.59E+09	2.55E+09	2.90E+09	1.624
2069	0.002040	523.09	25.98	1	1.070	1.27	3.61E+09	2.56E+09	2.91E+09	1.635

2070	0.002040	524.30	26.01	1	1.073	1.21	3.64E+09	2.57E+09	2.92E+09	1.647
2071	0.002040	525.45	26.02	1	1.073	1.15	3.66E+09	2.57E+09	2.94E+09	1.659
2072	0.002040	526.51	26.04	1	1.075	1.06	3.69E+09	2.58E+09	2.95E+09	1.671
2073	0.002040	527.46	26.06	1	1.077	0.95	3.72E+09	2.59E+09	2.96E+09	1.682
2074	0.002041	528.30	26.08	1	1.078	0.84	3.74E+09	2.59E+09	2.98E+09	1.694
2075	0.002041	529.03	26.06	1	1.076	0.73	3.77E+09	2.60E+09	2.99E+09	1.706
2076	0.002041	529.64	26.08	1	1.078	0.62	3.79E+09	2.60E+09	3.00E+09	1.718
2077	0.002041	530.14	26.08	1	1.078	0.50	3.82E+09	2.61E+09	3.01E+09	1.729
2078	0.002041	530.55	26.11	1	1.080	0.41	3.85E+09	2.62E+09	3.03E+09	1.741
2079	0.002041	530.88	26.12	1	1.081	0.33	3.87E+09	2.62E+09	3.04E+09	1.753
2080	0.002041	531.14	26.11	1	1.080	0.25	3.90E+09	2.63E+09	3.05E+09	1.765
2081	0.002042	531.32	26.11	1	1.080	0.18	3.92E+09	2.64E+09	3.07E+09	1.776
2082	0.002041	531.49	26.13	1	1.082	0.17	3.95E+09	2.64E+09	3.08E+09	1.788
2083	0.002042	531.70	26.12	1	1.081	0.21	3.98E+09	2.65E+09	3.09E+09	1.800
2084	0.002042	531.94	26.13	1	1.082	0.24	4.00E+09	2.66E+09	3.11E+09	1.812
2085	0.002042	532.20	26.15	1	1.083	0.26	4.03E+09	2.66E+09	3.12E+09	1.824
2086	0.002042	532.49	26.14	1	1.082	0.28	4.05E+09	2.67E+09	3.13E+09	1.835
2087	0.002042	532.78	26.12	1	1.081	0.29	4.08E+09	2.68E+09	3.14E+09	1.847
2088	0.002042	533.07	26.14	1	1.082	0.29	4.11E+09	2.68E+09	3.16E+09	1.859
2089	0.002042	533.39	26.15	1	1.083	0.32	4.13E+09	2.69E+09	3.17E+09	1.871
2090	0.002042	533.74	26.15	1	1.083	0.35	4.16E+09	2.70E+09	3.18E+09	1.882
2091	0.002042	534.13	26.15	1	1.083	0.39	4.18E+09	2.70E+09	3.20E+09	1.894
2092	0.002042	534.56	26.15	1	1.083	0.43	4.21E+09	2.71E+09	3.21E+09	1.906
2093	0.002043	535.01	26.13	1	1.082	0.45	4.24E+09	2.72E+09	3.22E+09	1.918
2094	0.002043	535.48	26.13	1	1.082	0.47	4.26E+09	2.72E+09	3.24E+09	1.929
2095	0.002043	535.95	26.15	1	1.083	0.48	4.29E+09	2.73E+09	3.25E+09	1.941
2096	0.002043	536.44	26.17	1	1.084	0.48	4.31E+09	2.73E+09	3.26E+09	1.953
2097	0.002043	536.92	26.17	1	1.085	0.48	4.34E+09	2.74E+09	3.27E+09	1.965
2098	0.002043	537.40	26.19	1	1.086	0.48	4.37E+09	2.75E+09	3.29E+09	1.976
2099	0.002043	537.87	26.19	1	1.086	0.47	4.39E+09	2.75E+09	3.30E+09	1.988
2100	0.002043	538.36	26.21	1	1.088	0.49	4.42E+09	2.76E+09	3.31E+09	2.000

A.1.6 RCP 6.0 Forcing File

Year	DIC (mol kg ⁻¹)	pCO ₂ (µatm)	Temp (°C)	fN	fT	dAdt	fOM	fOM25	fOM50	fN2
2015	0.001993	399.00	25.00	1	1.000	0.00	2.21E+09	2.21E+09	2.21E+09	1.000
2016	0.001994	401.42	25.05	1	1.004	2.42	2.23E+09	2.22E+09	2.22E+09	1.012
2017	0.001995	403.43	25.06	1	1.004	2.01	2.26E+09	2.22E+09	2.23E+09	1.024
2018	0.001996	405.43	25.05	1	1.003	1.99	2.29E+09	2.23E+09	2.25E+09	1.035
2019	0.001997	407.40	25.06	1	1.004	1.98	2.31E+09	2.23E+09	2.26E+09	1.047
2020	0.001998	409.36	25.08	1	1.005	1.96	2.34E+09	2.24E+09	2.27E+09	1.059
2021	0.001998	411.30	25.11	1	1.007	1.94	2.36E+09	2.25E+09	2.29E+09	1.071
2022	0.001999	413.22	25.12	1	1.008	1.92	2.39E+09	2.25E+09	2.30E+09	1.082
2023	0.002000	415.14	25.13	1	1.009	1.93	2.42E+09	2.26E+09	2.31E+09	1.094
2024	0.002001	417.08	25.14	1	1.010	1.94	2.44E+09	2.27E+09	2.33E+09	1.106
2025	0.002001	419.04	25.19	1	1.013	1.95	2.47E+09	2.27E+09	2.34E+09	1.118
2026	0.002002	421.00	25.22	1	1.016	1.97	2.49E+09	2.28E+09	2.35E+09	1.129
2027	0.002003	422.98	25.23	1	1.016	1.97	2.52E+09	2.29E+09	2.36E+09	1.141

2028	0.002004	424.95	25.22	1	1.015	1.97	2.55E+09	2.29E+09	2.38E+09	1.153
2029	0.002005	426.92	25.23	1	1.016	1.97	2.57E+09	2.30E+09	2.39E+09	1.165
2030	0.002006	428.88	25.23	1	1.016	1.96	2.60E+09	2.31E+09	2.40E+09	1.176
2031	0.002007	430.83	25.26	1	1.018	1.96	2.62E+09	2.31E+09	2.42E+09	1.188
2032	0.002007	432.81	25.29	1	1.021	1.98	2.65E+09	2.32E+09	2.43E+09	1.200
2033	0.002008	434.83	25.29	1	1.020	2.02	2.68E+09	2.33E+09	2.44E+09	1.212
2034	0.002009	436.92	25.33	1	1.023	2.08	2.70E+09	2.33E+09	2.46E+09	1.224
2035	0.002010	439.07	25.33	1	1.023	2.15	2.73E+09	2.34E+09	2.47E+09	1.235
2036	0.002011	441.29	25.34	1	1.024	2.22	2.75E+09	2.35E+09	2.48E+09	1.247
2037	0.002011	443.57	25.38	1	1.027	2.28	2.78E+09	2.35E+09	2.49E+09	1.259
2038	0.002013	445.90	25.38	1	1.027	2.34	2.81E+09	2.36E+09	2.51E+09	1.271
2039	0.002013	448.28	25.40	1	1.028	2.38	2.83E+09	2.36E+09	2.52E+09	1.282
2040	0.002014	450.70	25.41	1	1.029	2.42	2.86E+09	2.37E+09	2.53E+09	1.294
2041	0.002015	453.15	25.44	1	1.031	2.45	2.88E+09	2.38E+09	2.55E+09	1.306
2042	0.002016	455.65	25.49	1	1.034	2.49	2.91E+09	2.38E+09	2.56E+09	1.318
2043	0.002017	458.18	25.47	1	1.033	2.54	2.94E+09	2.39E+09	2.57E+09	1.329
2044	0.002018	460.76	25.50	1	1.035	2.58	2.96E+09	2.40E+09	2.59E+09	1.341
2045	0.002019	463.41	25.50	1	1.035	2.64	2.99E+09	2.40E+09	2.60E+09	1.353
2046	0.002020	466.12	25.51	1	1.036	2.71	3.01E+09	2.41E+09	2.61E+09	1.365
2047	0.002021	468.91	25.56	1	1.040	2.79	3.04E+09	2.42E+09	2.62E+09	1.376
2048	0.002022	471.77	25.59	1	1.042	2.86	3.07E+09	2.42E+09	2.64E+09	1.388
2049	0.002023	474.69	25.59	1	1.041	2.92	3.09E+09	2.43E+09	2.65E+09	1.400
2050	0.002025	477.67	25.60	1	1.043	2.98	3.12E+09	2.44E+09	2.66E+09	1.412
2051	0.002026	480.70	25.60	1	1.043	3.03	3.14E+09	2.44E+09	2.68E+09	1.424
2052	0.002027	483.78	25.62	1	1.044	3.08	3.17E+09	2.45E+09	2.69E+09	1.435
2053	0.002028	486.92	25.67	1	1.048	3.14	3.20E+09	2.46E+09	2.70E+09	1.447
2054	0.002029	490.10	25.68	1	1.048	3.19	3.22E+09	2.46E+09	2.72E+09	1.459
2055	0.002030	493.34	25.71	1	1.050	3.24	3.25E+09	2.47E+09	2.73E+09	1.471
2056	0.002031	496.64	25.73	1	1.052	3.30	3.27E+09	2.47E+09	2.74E+09	1.482
2057	0.002033	500.02	25.71	1	1.050	3.38	3.30E+09	2.48E+09	2.75E+09	1.494
2058	0.002034	503.48	25.76	1	1.054	3.46	3.33E+09	2.49E+09	2.77E+09	1.506
2059	0.002035	507.02	25.81	1	1.058	3.54	3.35E+09	2.49E+09	2.78E+09	1.518
2060	0.002036	510.63	25.79	1	1.057	3.61	3.38E+09	2.50E+09	2.79E+09	1.529
2061	0.002037	514.31	25.82	1	1.058	3.67	3.40E+09	2.51E+09	2.81E+09	1.541
2062	0.002039	518.03	25.82	1	1.058	3.72	3.43E+09	2.51E+09	2.82E+09	1.553
2063	0.002040	521.80	25.85	1	1.061	3.77	3.46E+09	2.52E+09	2.83E+09	1.565
2064	0.002041	525.62	25.86	1	1.061	3.82	3.48E+09	2.53E+09	2.85E+09	1.576
2065	0.002042	529.49	25.91	1	1.065	3.87	3.51E+09	2.53E+09	2.86E+09	1.588
2066	0.002044	533.40	25.93	1	1.067	3.91	3.53E+09	2.54E+09	2.87E+09	1.600
2067	0.002045	537.38	25.98	1	1.070	3.98	3.56E+09	2.55E+09	2.88E+09	1.612
2068	0.002046	541.44	26.01	1	1.072	4.06	3.59E+09	2.55E+09	2.90E+09	1.624
2069	0.002047	545.59	26.01	1	1.072	4.15	3.61E+09	2.56E+09	2.91E+09	1.635
2070	0.002048	549.82	26.08	1	1.077	4.23	3.64E+09	2.57E+09	2.92E+09	1.647
2071	0.002050	554.13	26.10	1	1.079	4.31	3.66E+09	2.57E+09	2.94E+09	1.659
2072	0.002051	558.49	26.14	1	1.082	4.36	3.69E+09	2.58E+09	2.95E+09	1.671
2073	0.002052	562.87	26.13	1	1.081	4.38	3.72E+09	2.59E+09	2.96E+09	1.682
2074	0.002054	567.27	26.16	1	1.084	4.40	3.74E+09	2.59E+09	2.98E+09	1.694
2075	0.002055	571.70	26.17	1	1.084	4.43	3.77E+09	2.60E+09	2.99E+09	1.706
2076	0.002057	576.15	26.18	1	1.085	4.44	3.79E+09	2.60E+09	3.00E+09	1.718
2077	0.002058	580.61	26.23	1	1.089	4.46	3.82E+09	2.61E+09	3.01E+09	1.729

2078	0.002059	585.10	26.27	1	1.092	4.50	3.85E+09	2.62E+09	3.03E+09	1.741
2079	0.002060	589.65	26.29	1	1.093	4.55	3.87E+09	2.62E+09	3.04E+09	1.753
2080	0.002061	594.26	26.30	1	1.094	4.60	3.90E+09	2.63E+09	3.05E+09	1.765
2081	0.002063	598.92	26.34	1	1.097	4.66	3.92E+09	2.64E+09	3.07E+09	1.776
2082	0.002064	603.54	26.34	1	1.097	4.62	3.95E+09	2.64E+09	3.08E+09	1.788
2083	0.002065	608.02	26.35	1	1.098	4.48	3.98E+09	2.65E+09	3.09E+09	1.800
2084	0.002066	612.36	26.41	1	1.103	4.34	4.00E+09	2.66E+09	3.11E+09	1.812
2085	0.002068	616.57	26.41	1	1.103	4.21	4.03E+09	2.66E+09	3.12E+09	1.824
2086	0.002069	620.65	26.43	1	1.104	4.08	4.05E+09	2.67E+09	3.13E+09	1.835
2087	0.002070	624.58	26.46	1	1.107	3.94	4.08E+09	2.68E+09	3.14E+09	1.847
2088	0.002071	628.38	26.47	1	1.107	3.80	4.11E+09	2.68E+09	3.16E+09	1.859
2089	0.002072	632.06	26.48	1	1.108	3.68	4.13E+09	2.69E+09	3.17E+09	1.871
2090	0.002072	635.65	26.52	1	1.111	3.58	4.16E+09	2.70E+09	3.18E+09	1.882
2091	0.002073	639.14	26.55	1	1.113	3.49	4.18E+09	2.70E+09	3.20E+09	1.894
2092	0.002074	642.60	26.55	1	1.113	3.46	4.21E+09	2.71E+09	3.21E+09	1.906
2093	0.002075	646.06	26.55	1	1.114	3.46	4.24E+09	2.72E+09	3.22E+09	1.918
2094	0.002076	649.52	26.57	1	1.115	3.45	4.26E+09	2.72E+09	3.24E+09	1.929
2095	0.002077	652.95	26.60	1	1.117	3.44	4.29E+09	2.73E+09	3.25E+09	1.941
2096	0.002077	656.36	26.64	1	1.120	3.41	4.31E+09	2.73E+09	3.26E+09	1.953
2097	0.002078	659.75	26.63	1	1.120	3.39	4.34E+09	2.74E+09	3.27E+09	1.965
2098	0.002079	663.11	26.65	1	1.121	3.35	4.37E+09	2.75E+09	3.29E+09	1.976
2099	0.002080	666.42	26.67	1	1.123	3.32	4.39E+09	2.75E+09	3.30E+09	1.988
2100	0.002081	669.72	26.68	1	1.124	3.30	4.42E+09	2.76E+09	3.31E+09	2.000

A.1.7 RCP 8.5 Forcing File

Year	DIC (mol kg⁻¹)	pCO₂ (µatm)	Temp (°C)	fN	fT	dAdt	fOM	fOM25	fOM50	fN2
2015	0.001993	399.00	25.00	1	1.000	0.00	2.21E+09	2.21E+09	2.21E+09	1.000
2016	0.001995	404.33	25.05	1	1.003	5.33	2.23E+09	2.22E+09	2.22E+09	1.012
2017	0.001996	407.10	25.07	1	1.005	2.77	2.26E+09	2.22E+09	2.23E+09	1.024
2018	0.001998	409.93	25.08	1	1.006	2.83	2.29E+09	2.23E+09	2.25E+09	1.035
2019	0.001999	412.82	25.10	1	1.007	2.89	2.31E+09	2.23E+09	2.26E+09	1.047
2020	0.002000	415.78	25.11	1	1.008	2.96	2.34E+09	2.24E+09	2.27E+09	1.059
2021	0.002002	418.80	25.14	1	1.010	3.02	2.36E+09	2.25E+09	2.29E+09	1.071
2022	0.002003	421.86	25.22	1	1.015	3.07	2.39E+09	2.25E+09	2.30E+09	1.082
2023	0.002004	424.99	25.22	1	1.015	3.13	2.42E+09	2.26E+09	2.31E+09	1.094
2024	0.002005	428.20	25.24	1	1.017	3.20	2.44E+09	2.27E+09	2.33E+09	1.106
2025	0.002007	431.47	25.29	1	1.020	3.28	2.47E+09	2.27E+09	2.34E+09	1.118
2026	0.002008	434.83	25.32	1	1.023	3.35	2.49E+09	2.28E+09	2.35E+09	1.129
2027	0.002009	438.24	25.35	1	1.025	3.42	2.52E+09	2.29E+09	2.36E+09	1.141
2028	0.002011	441.72	25.36	1	1.025	3.48	2.55E+09	2.29E+09	2.38E+09	1.153
2029	0.002012	445.25	25.40	1	1.028	3.53	2.57E+09	2.30E+09	2.39E+09	1.165
2030	0.002014	448.83	25.41	1	1.029	3.58	2.60E+09	2.31E+09	2.40E+09	1.176
2031	0.002015	452.47	25.43	1	1.030	3.64	2.62E+09	2.31E+09	2.42E+09	1.188
2032	0.002017	456.18	25.46	1	1.032	3.70	2.65E+09	2.32E+09	2.43E+09	1.200
2033	0.002018	459.96	25.50	1	1.035	3.79	2.68E+09	2.33E+09	2.44E+09	1.212
2034	0.002019	463.85	25.54	1	1.038	3.89	2.70E+09	2.33E+09	2.46E+09	1.224
2035	0.002021	467.85	25.57	1	1.040	4.00	2.73E+09	2.34E+09	2.47E+09	1.235

2036	0.002022	471.96	25.59	1	1.042	4.11	2.75E+09	2.35E+09	2.48E+09	1.247
2037	0.002024	476.18	25.64	1	1.045	4.22	2.78E+09	2.35E+09	2.49E+09	1.259
2038	0.002025	480.51	25.67	1	1.048	4.33	2.81E+09	2.36E+09	2.51E+09	1.271
2039	0.002027	484.93	25.71	1	1.050	4.42	2.83E+09	2.36E+09	2.52E+09	1.282
2040	0.002028	489.44	25.76	1	1.054	4.51	2.86E+09	2.37E+09	2.53E+09	1.294
2041	0.002030	494.03	25.78	1	1.055	4.60	2.88E+09	2.38E+09	2.55E+09	1.306
2042	0.002032	498.73	25.80	1	1.057	4.70	2.91E+09	2.38E+09	2.56E+09	1.318
2043	0.002033	503.53	25.83	1	1.059	4.80	2.94E+09	2.39E+09	2.57E+09	1.329
2044	0.002035	508.43	25.87	1	1.062	4.90	2.96E+09	2.40E+09	2.59E+09	1.341
2045	0.002037	513.46	25.88	1	1.063	5.02	2.99E+09	2.40E+09	2.60E+09	1.353
2046	0.002038	518.61	25.92	1	1.066	5.15	3.01E+09	2.41E+09	2.61E+09	1.365
2047	0.002040	523.90	26.00	1	1.071	5.29	3.04E+09	2.42E+09	2.62E+09	1.376
2048	0.002041	529.32	26.02	1	1.073	5.42	3.07E+09	2.42E+09	2.64E+09	1.388
2049	0.002043	534.88	26.05	1	1.075	5.55	3.09E+09	2.43E+09	2.65E+09	1.400
2050	0.002045	540.54	26.12	1	1.081	5.67	3.12E+09	2.44E+09	2.66E+09	1.412
2051	0.002047	546.32	26.15	1	1.083	5.78	3.14E+09	2.44E+09	2.68E+09	1.424
2052	0.002048	552.21	26.18	1	1.085	5.89	3.17E+09	2.45E+09	2.69E+09	1.435
2053	0.002050	558.21	26.21	1	1.088	6.00	3.20E+09	2.46E+09	2.70E+09	1.447
2054	0.002052	564.31	26.26	1	1.092	6.10	3.22E+09	2.46E+09	2.72E+09	1.459
2055	0.002054	570.52	26.30	1	1.095	6.20	3.25E+09	2.47E+09	2.73E+09	1.471
2056	0.002056	576.84	26.34	1	1.097	6.33	3.27E+09	2.47E+09	2.74E+09	1.482
2057	0.002058	583.30	26.35	1	1.098	6.46	3.30E+09	2.48E+09	2.75E+09	1.494
2058	0.002059	589.91	26.42	1	1.104	6.60	3.33E+09	2.49E+09	2.77E+09	1.506
2059	0.002061	596.65	26.47	1	1.107	6.74	3.35E+09	2.49E+09	2.78E+09	1.518
2060	0.002063	603.52	26.51	1	1.111	6.87	3.38E+09	2.50E+09	2.79E+09	1.529
2061	0.002065	610.52	26.55	1	1.114	7.00	3.40E+09	2.51E+09	2.81E+09	1.541
2062	0.002067	617.61	26.59	1	1.116	7.09	3.43E+09	2.51E+09	2.82E+09	1.553
2063	0.002068	624.76	26.63	1	1.120	7.16	3.46E+09	2.52E+09	2.83E+09	1.565
2064	0.002070	631.99	26.67	1	1.123	7.23	3.48E+09	2.53E+09	2.85E+09	1.576
2065	0.002072	639.29	26.69	1	1.124	7.30	3.51E+09	2.53E+09	2.86E+09	1.588
2066	0.002074	646.65	26.74	1	1.128	7.36	3.53E+09	2.54E+09	2.87E+09	1.600
2067	0.002076	654.10	26.77	1	1.130	7.45	3.56E+09	2.55E+09	2.88E+09	1.612
2068	0.002078	661.64	26.80	1	1.133	7.55	3.59E+09	2.55E+09	2.90E+09	1.624
2069	0.002079	669.30	26.85	1	1.137	7.66	3.61E+09	2.56E+09	2.91E+09	1.635
2070	0.002081	677.08	26.89	1	1.140	7.77	3.64E+09	2.57E+09	2.92E+09	1.647
2071	0.002083	684.95	26.92	1	1.143	7.88	3.66E+09	2.57E+09	2.94E+09	1.659
2072	0.002085	692.90	26.97	1	1.146	7.95	3.69E+09	2.58E+09	2.95E+09	1.671
2073	0.002087	700.89	27.04	1	1.152	7.99	3.72E+09	2.59E+09	2.96E+09	1.682
2074	0.002089	708.93	27.05	1	1.152	8.04	3.74E+09	2.59E+09	2.98E+09	1.694
2075	0.002090	717.02	27.09	1	1.156	8.08	3.77E+09	2.60E+09	2.99E+09	1.706
2076	0.002092	725.14	27.13	1	1.159	8.12	3.79E+09	2.60E+09	3.00E+09	1.718
2077	0.002094	733.31	27.17	1	1.163	8.17	3.82E+09	2.61E+09	3.01E+09	1.729
2078	0.002095	741.52	27.22	1	1.166	8.22	3.85E+09	2.62E+09	3.03E+09	1.741
2079	0.002097	749.80	27.27	1	1.170	8.28	3.87E+09	2.62E+09	3.04E+09	1.753
2080	0.002099	758.18	27.26	1	1.170	8.38	3.90E+09	2.63E+09	3.05E+09	1.765
2081	0.002101	766.64	27.30	1	1.173	8.46	3.92E+09	2.64E+09	3.07E+09	1.776
2082	0.002102	775.17	27.34	1	1.176	8.53	3.95E+09	2.64E+09	3.08E+09	1.788
2083	0.002104	783.75	27.36	1	1.177	8.58	3.98E+09	2.65E+09	3.09E+09	1.800
2084	0.002106	792.37	27.40	1	1.181	8.61	4.00E+09	2.66E+09	3.11E+09	1.812
2085	0.002107	801.02	27.45	1	1.185	8.65	4.03E+09	2.66E+09	3.12E+09	1.824

2086	0.002109	809.71	27.48	1	1.188	8.70	4.05E+09	2.67E+09	3.13E+09	1.835
2087	0.002111	818.42	27.53	1	1.191	8.71	4.08E+09	2.68E+09	3.14E+09	1.847
2088	0.002112	827.16	27.58	1	1.196	8.74	4.11E+09	2.68E+09	3.16E+09	1.859
2089	0.002113	835.96	27.63	1	1.200	8.80	4.13E+09	2.69E+09	3.17E+09	1.871
2090	0.002115	844.80	27.67	1	1.203	8.85	4.16E+09	2.70E+09	3.18E+09	1.882
2091	0.002117	853.73	27.71	1	1.207	8.92	4.18E+09	2.70E+09	3.20E+09	1.894
2092	0.002118	862.73	27.75	1	1.210	9.00	4.21E+09	2.71E+09	3.21E+09	1.906
2093	0.002120	871.78	27.80	1	1.214	9.05	4.24E+09	2.72E+09	3.22E+09	1.918
2094	0.002121	880.86	27.80	1	1.214	9.09	4.26E+09	2.72E+09	3.24E+09	1.929
2095	0.002123	889.98	27.86	1	1.220	9.12	4.29E+09	2.73E+09	3.25E+09	1.941
2096	0.002124	899.12	27.94	1	1.226	9.14	4.31E+09	2.73E+09	3.26E+09	1.953
2097	0.002125	908.29	27.97	1	1.229	9.16	4.34E+09	2.74E+09	3.27E+09	1.965
2098	0.002127	917.47	28.01	1	1.232	9.18	4.37E+09	2.75E+09	3.29E+09	1.976
2099	0.002128	926.67	28.04	1	1.235	9.19	4.39E+09	2.75E+09	3.30E+09	1.988
2100	0.002130	935.87	28.08	1	1.238	9.21	4.42E+09	2.76E+09	3.31E+09	2.000

A.2 Mass Balance Equations

Reef surface water dissolved inorganic carbon

$$dC_1(t)/dt = CF_{01}(t) + CF_{21}(t) + CF_{31}(t) + CF_{81}(t) + CF_{91}(t) + CF_{101}(t) + CF_{111}(t) - CF_{10}(t) - CF_{1A}(t) - CF_{12}(t) - CF_{13}(t) - CF_{18}(t) - CF_{19}(t) - CF_{110}(t) - CF_{111}(t)$$

Reef surface water total organic carbon

$$dC_2(t)/dt = CF_{02}(t) + CF_{12}(t) - CF_{20}(t) - CF_{21}(t) - CF_{24}(t) - CF_{212}(t)$$

Oxic Porewater dissolved inorganic carbon

$$dC_3(t)/dt = CF_{13}(t) + CF_{43}(t) + CF_{53}(t) + CF_{63}(t) + CF_{73}(t) + CF_{173}(t) - CF_{31}(t) - CF_{35}(t) - CF_{36}(t) - CF_{37}(t)$$

Oxic Sediment organic matter

$$dC_4(t)/dt = CF_{24}(t) - CF_{43}(t) - CF_{413}(t)$$

Oxic Sediment calcite

$$dC_5(t)/dt = CF_{35}(t) + CF_{85}(t) - CF_{53}(t) - CF_{514}(t) - CF_{50}(t)$$

Oxic Sediment aragonite

$$dC_6(t)/dt = CF_{36}(t) + CF_{96}(t) - CF_{63}(t) - CF_{615}(t) - CF_{60}(t)$$

Oxic Sediment magnesian-calcite

$$dC_7(t)/dt = CF_{37}(t) + CF_{107}(t) - CF_{73}(t) - CF_{716}(t) - CF_{70}(t)$$

Coral reef calcite framework

$$dC_8(t)/dt = CF_{18}(t) + CF_{118}(t) - CF_{81}(t) - CF_{85}(t) - CF_{811}(t) - CF_{8B}(t)$$

Coral reef aragonite framework

$$dC_9(t)/dt = CF_{19}(t) + CF_{119}(t) - CF_{91}(t) - CF_{96}(t) - CF_{911}(t) - CF_{9B}(t)$$

Coral reef Mg-calcite framework

$$dC_{10}(t)/dt = CF_{110}(t) + CF_{1110}(t) - CF_{101}(t) - CF_{107}(t) - CF_{1011}(t) - CF_{10B}(t)$$

Reef Framework Porewater

$$dC_{11}(t)/dt = CF_{111}(t) + CF_{811}(t) + CF_{911}(t) + CF_{1011}(t) + CF_{1211}(t) - CF_{111}(t) - CF_{118}(t) - CF_{119} - CF_{1110}$$

Reef Framework Organic Matter

$$dC_{12}(t)/dt = CF_{212}(t) - CF_{1211}(t) - CF_{12B}(t)$$

Anoxic Sediment organic matter

$$dC_{13}(t)/dt = CF_{413}(t) - CF_{1317}(t) - CF_{13B}(t)$$

Anoxic Sediment calcite

$$dC_{14}(t)/dt = CF_{514}(t) + CF_{1714}(t) - CF_{1417}(t) - CF_{14B}(t)$$

Anoxic Sediment aragonite

$$dC_{15}(t)/dt = CF_{615}(t) + CF_{1715}(t) - CF_{1517}(t) - CF_{15B}(t)$$

Anoxic Sediment magnesian-calcite

$$dC_{16}(t)/dt = CF_{716}(t) + CF_{1716}(t) - CF_{1617}(t) - CF_{16B}(t)$$

Anoxic Porewater dissolved inorganic carbon

$$dC_{17}(t)/dt = CF_{1317}(t) + CF_{1417}(t) + CF_{1517}(t) + CF_{1617}(t) + CF_{1315}(t) - CF_{173}(t) - CF_{1714}(t) - CF_{1715}(t) - CF_{1716}(t)$$

A.3 Flux Equations

$$k_{i,j} = \frac{CF_{ij,t=0}}{C_{i,t=0}}$$

$$CF_{0:1} = DIC_{ocean} \times FR$$

where FR, flushing rate, equals $V \times \rho / R_T$ and R_T = residence time

$$CF_{0:2} = 2.37 \times 10^9$$

$$CF_{1:0} = k_{1:0} \times C_1(t)$$

$$CF_{1:A} = k_{600} \times \alpha \times (pCO_{2sw} - pCO_{2air})$$

where k_{600} is the CO_2 gas transfer velocity based on wind speed and α is the CO_2 solubility at ambient temperature and salinity

$$CF_{1:2} = CF_{1:2,t=0} \times fN_1 \times fT$$

where $fN_1 = \frac{N_{1,t}}{N_{1,t=0}}$ and $fT_1 = Q_{10}^{(T-T_0)/10}$ and $Q_{10}=2$, so a 10 degree temperature change implies a doubling of the rate

$$CF_{1:3} = k_{1:3} \times C_1(t)$$

$$CF_{1:8} = k_{1:8} \times C_1(t) \times \frac{R_{\Omega t}}{R_{\Omega t=0}} \times \frac{R_{T,t}}{R_{T,t=0}}$$

where R_{Ω} is the effect of Ω on the calcification rate at time, t, relative to time, t=0, and

$$R_{\Omega} = 21.3\Omega + 12$$

and R_T is the effect of temperature on the calcification rate at time, t, relative to time, t=0,

and $R_T = 100 - 1.32\Delta T^2$

$$CF_{1:9} = k_{1:9} \times C_1(t) \times \frac{R_{\Omega t}}{R_{\Omega t=0}} \times \frac{R_{T,t}}{R_{T,t=0}}$$

$$CF_{1:10} = k_{1:10} \times C_1(t) \times \frac{R_{\Omega t}}{R_{\Omega t=0}} \times \frac{R_{T,t}}{R_{T,t=0}}$$

$$CF_{1:11} = k_{1:11} \times C_1(t)$$

$$CF_{2:0} = k_{2:0} \times C_2(t)$$

$$CF_{2:1} = k_{2:1} \times C_2(t) \times fT$$

where $fT_1 = Q_{10}^{(T-T_0)/10}$ and $Q_{10}=2$, so a 10 degree temperature change implies a doubling of the rate

$$CF_{2:4} = k_{sed} \times C_2(t) \times 5\%$$

where k_{sed} is the rate constant for the total rate of sedimentation and 5% is the partitioning to the permeable sediments based on areal coverage

$$CF_{2:12} = k_{sed} \times C_2(t) \times 95\%$$

where k_{sed} is the rate constant for the total rate of sedimentation and 95% is the partitioning to the framework based on areal coverage

$$CF_{3:1} = k_{3:1} \times C_3(t)$$

$$CF_{3:5} = k_{3:5} \times C_3(t) + \Delta P(\Omega_{calcite})$$

where P is precipitation at time, t=0 or t, for the respective mineral phase, \times , and

$$P = k_p(\Omega_{cal} - 1)^{n_p} \times M_{C_3} \times A_{SS} \times A_{RS} \times I_p \times I_o$$

$$\Delta P(\Omega_x) = P_{x,t}(\Omega_x) - P_{x,t=0}(\Omega_x)$$

$$CF_{3:6} = k_{3:6} \times C_3(t) + \Delta P(\Omega_{aragonite})$$

$$CF_{3:7} = k_{3:7} \times C_3(t) + \Delta P(\Omega_{Mg-calcite})$$

$$CF_{4:3} = k_{4:3} \times C_4(t) \times fT$$

$$CF_{4:13} = k_{4:13} \times C_4(t)$$

$$CF_{5:3} = k_{5:3} \times C_5(t) + \Delta D(\Omega_{calcite})$$

where D is the dissolution at time, t=0 or t, for the respective mineral phase and

$$D = k_d(1 - \Omega_{arag})^{n_d} \times M_x \times A_{RS} \times I_p \times I_o$$

$$\Delta D(\Omega_x) = D_{x,t}(\Omega_x) - D_{x,t=0}(\Omega_x)$$

$$CF_{5:14} = k_{5:14} \times C_5(t)$$

$$CF_{5:0} = k_{5:0} \times C_5(t)$$

$$CF_{6:3} = k_{6:3} \times C_6(t) + \Delta D(\Omega_{aragonite})$$

$$CF_{6:15} = k_{6:15} \times C_6(t)$$

$$CF_{6:0} = k_{6:0} \times C_6(t)$$

$$CF_{7:3} = k_{7:3} \times C_7(t) + \Delta D(\Omega_{Mg-calcite})$$

$$CF_{7:16} = k_{7:16} \times C_7(t)$$

$$CF_{7:0} = k_{7:0} \times C_7(t)$$

$$CF_{8:1} = k_{8:1} \times C_8(t) \times \frac{R_{pCO_2,t}}{R_{pCO_2,t=0}}$$

where R_{pCO_2} is the effect of pCO_2 on the chemical bioerosion rate at time, t , relative to time, $t=0$, and $R_{pCO_2} = 0.429 \times pCO_2 + 138.57$

$$CF_{8:5} = k_{8:5} \times C_8(t)$$

$$CF_{8:11} = k_{8:11} \times C_8(t) + \Delta D(\Omega_{calcite})$$

$$CF_{8:B} = k_{8:B} \times C_8(t)$$

$$CF_{9:1} = k_{9:1} \times C_9(t) \times \frac{R_{pCO_2,t}}{R_{pCO_2,t=0}}$$

$$CF_{9:6} = k_{9:6} \times C_9(t)$$

$$CF_{9:11} = k_{9:11} \times C_9(t) + \Delta D(\Omega_{aragonite})$$

$$CF_{9:B} = k_{9:B} \times C_9(t)$$

$$CF_{10:1} = k_{10:1} \times C_{10}(t) \times \frac{R_{pCO_2,t}}{R_{pCO_2,t=0}}$$

$$CF_{10:7} = k_{10:7} \times C_{10}(t)$$

$$CF_{10:11} = k_{10:11} \times C_{10}(t) + \Delta D(\Omega_{Mg-calcite})$$

$$CF_{10:B} = k_{10:B} \times C_{10}(t)$$

$$CF_{11:1} = k_{11:1} \times C_{11}(t)$$

$$CF_{11:8} = k_{11:8} \times C_{11}(t) + \Delta P(\Omega_{calcite})$$

$$CF_{11:9} = k_{11:9} \times C_{11}(t) + \Delta P(\Omega_{aragonite})$$

$$CF_{11:10} = k_{11:10} \times C_{11}(t) + \Delta P(\Omega_{Mg-calcite})$$

$$CF_{12:11} = k_{12:11} \times C_{12}(t) \times fT$$

$$CF_{12:B} = k_{12:B} \times C_{12}(t)$$

$$CF_{13:17} = k_{13:17} \times C_{13}(t) \times fT$$

$$CF_{13:B} = k_{13:B} \times C_{13}(t)$$

$$CF_{14:17} = k_{14:17} \times C_{14}(t) + \Delta D(\Omega_{calcite})$$

$$CF_{14:B} = k_{14:B} \times C_{14}(t)$$

$$CF_{15:17} = k_{15:17} \times C_{15}(t) + \Delta D(\Omega_{aragonite})$$

$$CF_{15:B} = k_{15:B} \times C_{15}(t)$$

$$CF_{16:17} = k_{16:17} \times C_{16}(t) + \Delta D(\Omega_{Mg-calcite})$$

$$CF_{16:B} = k_{16:B} \times C_{16}(t)$$

$$CF_{17:3} = k_{17:3} \times C_{17}(t)$$

$$CF_{17:14} = k_{17:14} \times C_{17}(t) + \Delta P(\Omega_{calcite})$$

$$CF_{17:15} = k_{17:15} \times C_{17}(t) + \Delta P(\Omega_{aragonite})$$

$$CF_{17:16} = k_{17:16} \times C_{17}(t) + \Delta P(\Omega_{Mg-calcite})$$

A.4 Calculations for Initial Carbon Reservoirs

Table A.1: Calculations for the initial carbon reservoir masses on the Kaneohe Bay barrier reef. All densities were calculated assuming a T=25°C and S=35. Reservoir sizes have been rounded for presentation in this table, but significant figures were retained in the actual calculations.

Reservoir	Reservoir Notation	mol C (10 ⁵)	Reference/Comments
Surface Water DIC	1	404	$C_1 = W \times L \times Z \times \text{DIC} \times \rho$ Calculated from DIC=1973 $\mu\text{mol}\cdot\text{kg}^{-1}$ (Shamberger et al. 2011; Drupp et al. 2013) Total reservoir = 2000 m \times 5000 m \times 2 m \times 1973 $\times 10^{-6}$ mol $\cdot\text{kg}^{-1}$ \times 1023 kg $\cdot\text{m}^{-3}$ = 4.04 $\times 10^7$ mol C
Surface Water Organic Carbon (TOC)	2	9.82	$C_2 = V \times [\text{DON}] \times \text{C:N} + V \times [\text{POC}]$ Calculated based on the average DON, 6.2 mmol N $\cdot\text{m}^{-3}$, between the exterior and interior reef flat concentrations used in the flux calculations (Smith et al. 1981; Cox et al. 2006) and assuming a C:N ratio of 106:16 (Redfield 1934). Total reef water volume is 2 $\times 10^7$ m ³ \times 6.2 $\times 10^{-3}$ mol N $\cdot\text{m}^{-3}$ \times 6.625 = 8.22 $\times 10^5$ mol DOC. POC was estimated at 8 mmol C $\cdot\text{m}^{-3}$ (Atkinson and Falter 2003; Cox et al. 2006) thus 2 $\times 10^7$ m ³ \times 0.008 mol C $\cdot\text{m}^{-3}$ = 1.60 $\times 10^5$ mol POC. The total organic carbon is the sum of the DOC + POC, 8.22 $\times 10^5$ mol C + 1.60 $\times 10^5$ mol C = 9.82 $\times 10^5$ mol C.
Oxic Porewater DIC (Permeable Sediments)	3	1.14	$C_3 = V \times \Phi \times A_{\text{ps}} \times \rho \times \text{DIC}$ Calculated for the upper 20cm of the sediment layer with a total volume of 2 $\times 10^6$ m ³ and a porosity of 52% (Morse and Mackenzie 1990; this study). Permeable sediments areal coverage (A_{ps}) was an estimated 5% from the NOAA Benthic Mapping Survey. DIC=2150 $\mu\text{mol kg}^{-1}$ (this study, Morse et al. 1985; Tribble et al. 1990) 2 $\times 10^6$ m ³ \times 0.52 \times 0.05 \times 1023 kg $\cdot\text{m}^{-3}$ \times 2150 $\times 10^{-6}$ mol $\cdot\text{kg}^{-1}$ = 1.14 $\times 10^5$ mol C.
Oxic Sediment Organic Carbon (Permeable Sediments)	4	569	$C_4 = V \times (1-\Phi) \times A_{\text{ps}} \times \rho \times \text{OC}\%$ Calculated based on a sediment volume of 2 $\times 10^6$ m ³ and a 52% porosity. Areal coverage of sandy sediments equals 5%. Sediment density was assumed to be 2.85 $\times 10^6$ g $\cdot\text{m}^{-3}$ (Morse and Mackenzie 1990) with a 0.5% organic matter content (this study, Atkinson and Falter 2003). Thus, (2 $\times 10^6$ m ³ \times (1-0.52) \times 5% \times 2.85 $\times 10^6$ g $\cdot\text{m}^{-3}$ \times 0.5%)/12.01 g $\cdot\text{mol}^{-1}$ C = 5.69 $\times 10^7$ mol C
Oxic Sediment Calcite (Permeable Sediments)	5	1695	$C_5 = V \times (1-\Phi) \times A_{\text{ps}} \times \rho \times A_{\text{c}} \times \text{IC}\%$ Calculated by assuming 13% (A_{c}) abundance of sediment calcite (Morse and Mackenzie 1990) with an average sediment density of 2.85 g $\cdot\text{cm}^{-3}$ and an inorganic carbon weight % of 11.45% (this study). Thus, (2 $\times 10^6$ m ³ \times (1-0.52) \times 5% \times 2.85 $\times 10^6$ g $\cdot\text{m}^{-3}$ \times 13% \times 11.45%)/12.01 g $\cdot\text{mol C} = 1.695\times 10^8$ mol C

Reservoir	Reservoir Notation	mol C (10 ⁵)	Reference/Comments
Oxic Sediment Aragonite (Permeable Sediments)	6	8213	$C_6 = V \times (1-\Phi) \times A_{ps} \times \rho \times A_a \times IC\%$ Calculated by assuming 63% (A_a) abundance of sediment aragonite (Morse and Mackenzie 1990) with an average sediment density of 2.85 g·cm ⁻³ and an inorganic carbon weight % of 11.45% (this study). Thus, $(2 \times 10^6 \text{ m}^3 \times (1-0.52) \times 5\% \times 2.85 \times 10^6 \text{ g} \cdot \text{m}^{-3} \times 63\% \times 11.45\%) / 12.01 \text{ g} \cdot \text{mol C} = 8.21 \times 10^8 \text{ mol C}$
Oxic Sediment Mg-calcite (Permeable Sediments)	7	3129	$C_7 = V \times (1-\Phi) \times A_{ps} \times \rho \times A_{mg} \times IC\%$ Calculated by assuming 24% (A_{mg}) abundance of sediment Mg-calcite (Morse and Mackenzie 1990) with an average sediment density of 2.85 g·cm ⁻³ and an inorganic carbon weight % of 11.45% (this study). Thus, $(2 \times 10^6 \text{ m}^3 \times (1-0.52) \times 5\% \times 2.85 \times 10^6 \text{ g} \cdot \text{m}^{-3} \times 24\% \times 11.45\%) / 12.01 \text{ g} \cdot \text{mol C} = 3.13 \times 10^8 \text{ mol C}$
Calcite Reef Framework	8	167000	$C_8 = V \times (1-\Phi) \times A_{ps} \times \rho \times A_c$ Reef framework from surface to 1m depth. Assumes 95% coral/pavement coverage (NOAA Benthic Mapping Survey) of the barrier reef with a porosity of 50% (Tribble et al. 1990) and a 13% calcite composition. Calcite density is 2.71 g·cm ⁻³ . Thus $(5000 \text{ m} \times 2000 \text{ m} \times 1 \text{ m} \times (1-0.5) \times 95\% \times 2.71 \times 10^6 \text{ g} \cdot \text{m}^{-3} \times 13\%) / 100.1 \text{ g} \cdot \text{mol CaCO}_3 = 1.67 \times 10^{10} \text{ mol C}$
Aragonitic Reef Framework	9	876000	$C_9 = V \times (1-\Phi) \times A_{ps} \times \rho \times A_a$ Reef framework from surface to 1m depth. Assumes 95% coral/pavement coverage (NOAA Benthic Mapping Survey) of the barrier reef with a porosity of 50% (Tribble et al. 1990) and a 63% aragonite composition. Aragonite density is 2.93 g·cm ⁻³ . Thus $(5000 \text{ m} \times 2000 \text{ m} \times 1 \text{ m} \times (1-0.5) \times 95\% \times 2.93 \times 10^6 \text{ g} \cdot \text{m}^{-3} \times 63\%) / 100.1 \text{ g} \cdot \text{mol CaCO}_3 = 8.76 \times 10^{10} \text{ mol C}$
Mg-calcite Reef Framework	10	316000	$C_{10} = V \times (1-\Phi) \times A_{ps} \times \rho \times A_{mg}$ Reef framework from surface to 1m depth. Assumes 95% coral/pavement coverage (NOAA Benthic Mapping Survey) of the barrier reef with a porosity of 50% (Tribble et al. 1990) and a 24% Mg-calcite composition. Mg-calcite density is 2.71 g·cm ⁻³ . Thus $(5000 \text{ m} \times 2000 \text{ m} \times 1 \text{ m} \times (1-0.5) \times 95\% \times 2.71 \times 10^6 \text{ g} \cdot \text{m}^{-3} \times 24\%) / 97.7 \text{ g} \cdot \text{mol CaCO}_3 = 3.16 \times 10^{10} \text{ mol C}$
Reef Framework Porewater	11	116	$C_{11} = V \times \Phi \times A_{ps} \times \rho \times DIC$ Based on a framework porosity of 50% and an areal coverage of 95%. Using a DIC of 2385 $\mu\text{mol} \cdot \text{kg}^{-1}$ (Tribble et al. 1988), $1 \times 10^7 \text{ m}^3 \times 0.50 \times 0.95 \times 1023 \text{ kg} \cdot \text{m}^{-3} \times 2385 \times 10^{-6} \text{ mol} \cdot \text{kg}^{-1} = 1.16 \times 10^7 \text{ mol C}$.

Reservoir	Reservoir Notation	mol C (10 ⁵)	Reference/Comments
Reef Framework OM	12	56300	$C_{12} = V \times (1-\Phi) \times A_{ps} \times \rho \times OC\%$ Based on a framework porosity of 50% and an areal coverage of 95%. Using an OC% of 0.5% and an average framework density of 2.85 g·cm ⁻³ , $1 \times 10^7 \text{ m}^3 \times (1-0.50) \times 0.95 \times 2.85 \times 10^6 \text{ g} \cdot \text{m}^{-3} \times 0.5\% / 12.01 \text{ g} \cdot \text{mol}^{-1} \text{ C} = 5.63 \times 10^9 \text{ mol C}$.
Anoxic Sediment Organic Matter (Permeable Sediments)	13	911	$C_{13} = V \times (1-\Phi) \times A_{ps} \times \rho \times OC\%$ Calculated based on a sediment volume of $8 \times 10^6 \text{ m}^3$ for the 20-100 cm layer and a 52% porosity. Areal coverage of sandy sediments equals 5%. Sediment density was assumed to be $2.85 \times 10^6 \text{ g} \cdot \text{m}^{-3}$ (Morse and Mackenzie 1990) with a 0.2% organic matter content (this study). Thus, $(8 \times 10^6 \text{ m}^3 \times (1-0.52) \times 5\% \times 2.85 \times 10^6 \text{ g} \cdot \text{m}^{-3} \times 0.2\%) / 12.01 \text{ g} \cdot \text{mol}^{-1} \text{ C} = 9.11 \times 10^7 \text{ mol C}$
Anoxic Sediment Calcite (Permeable Sediments)	14	6780	$C_{14} = V \times (1-\Phi) \times A_{ps} \times \rho \times A_c \times IC\%$ Calculated by assuming 13% (A _c) abundance of sediment calcite (Morse and Mackenzie 1990) with an average sediment density of 2.85 g·cm ⁻³ and an inorganic carbon weight % of 11.45% (this study). Thus, $(8 \times 10^6 \text{ m}^3 \times (1-0.52) \times 5\% \times 2.85 \times 10^6 \text{ g} \cdot \text{m}^{-3} \times 13\% \times 11.45\%) / 12.01 \text{ g} \cdot \text{mol}^{-1} \text{ C} = 6.78 \times 10^8 \text{ mol C}$
Anoxic Sediment Aragonite (Sandy Sediments)	15	32900	$C_{15} = V \times (1-\Phi) \times A_{ps} \times \rho \times A_a \times IC\%$ Calculated by assuming 63% (A _a) abundance of sediment aragonite (Morse and Mackenzie 1990) with an average sediment density of 2.85 g·cm ⁻³ and an inorganic carbon weight % of 11.45% (this study). Thus, $(8 \times 10^6 \text{ m}^3 \times (1-0.52) \times 5\% \times 2.85 \times 10^6 \text{ g} \cdot \text{m}^{-3} \times 63\% \times 11.45\%) / 12.01 \text{ g} \cdot \text{mol}^{-1} \text{ C} = 3.29 \times 10^9 \text{ mol C}$
Anoxic Sediment 15% Mg-calcite (Sandy Sediments)	16	12500	$C_{16} = V \times (1-\Phi) \times A_{ps} \times \rho \times A_{mg} \times IC\%$ Calculated by assuming 24% (A _a) abundance of sediment Mg-calcite (Morse and Mackenzie 1990) with an average sediment density of 2.85 g·cm ⁻³ and an inorganic carbon weight % of 11.45% (this study). Thus, $(8 \times 10^6 \text{ m}^3 \times (1-0.52) \times 5\% \times 2.85 \times 10^6 \text{ g} \cdot \text{m}^{-3} \times 24\% \times 11.45\%) / 12.01 \text{ g} \cdot \text{mol}^{-1} \text{ C} = 1.25 \times 10^9 \text{ mol C}$
Anoxic Porewater DIC (Sandy Sediments)	17	5.00	$C_{17} = V \times \Phi \times A_{ps} \times \rho \times DIC$ Calculated for the 20-100 cm of the sediment layer with a total volume of $8 \times 10^6 \text{ m}^3$ and a porosity of 52% (Morse and Mackenzie 1990; this study). Permeable sediments areal coverage (A _{ps}) was an estimated 5% from the NOAA Benthic Mapping Survey. DIC=2350 μmol kg ⁻¹ (this study, Morse et al. 1985; Tribble et al. 1990) $8 \times 10^6 \text{ m}^3 \times 0.52 \times 5\% \times 1023 \text{ kg} \cdot \text{m}^{-3} \times 2350 \times 10^{-6} \text{ mol} \cdot \text{kg}^{-1} = 5.00 \times 10^5 \text{ mol C}$.

A.5 Calculations for Initial Carbon Fluxes

Table A.2: Calculations of carbon fluxes in *CRESCAM*. Note significant figures were retained in order to balance the model in its initial steady-state.

Flux	Flux $CF_{i;j}$	10^7 mol C·yr ⁻¹	Process	Reference/Comments
Open ocean – Surface water	O:1	9650	Physical Exchange	Water exchange was estimated assuming an average current speed of 0.15 m·s ⁻¹ from Lowe et al. (2009a/b) and a reef width of 2000 m, resulting in a flushing rate of 4.83×10 ¹³ kg·yr ⁻¹ . Open ocean DIC was 1993 μmol·kg ⁻¹ (Shamberger et al. 2011; HOT Data). Thus 4.83×10 ¹³ kg·yr ⁻¹ × 1993×10 ⁻⁶ mol·kg ⁻¹ = 9.65×10 ¹⁰ mol C·yr ⁻¹
Surface water – Open ocean	1:O	9553	Physical Exchange	Water exchange was estimated assuming an average current speed of 0.15 m·s ⁻¹ from Lowe et al. (2009a/b) and a reef width of 2000 m, resulting in a flushing rate of 4.83×10 ¹³ kg·yr ⁻¹ . Reef interior DIC was 1973 μmol·kg ⁻¹ (Drupp et al. 2013). Thus 4.83×10 ¹³ kg·yr ⁻¹ × 1973×10 ⁻⁶ mol·kg ⁻¹ = 9.55×10 ¹⁰ mol C·yr ⁻¹
Surface water – Atmosphere	1:A	0.8	Physical Exchange	Calculated using the equation $F = k\alpha(p\text{CO}_{2\text{sw}} - p\text{CO}_{2\text{air}})$, where k is the transfer velocity calculated using the wind speed parameterization of Ho et al. (2006) and $k_{600} = 0.266 \times U10^2$ and an U10 wind speed of 5.2 m·s ⁻¹ (Drupp et al. 2011; Drupp et al. 2013). An average ambient k of 0.072 m·hr ⁻¹ was calculated using the Schmidt number (Massaro et al. 2012). α is the CO ₂ solubility coefficient and is calculated based on the equations in Wanninkhof (1992) assuming an initial temperature and salinity of 25 °C and 35, resulting in an $\alpha = 0.0283$ mol·kg ⁻¹ ·atm ⁻¹ . Average pCO ₂ of the atmosphere and seawater were taken from Drupp et al. (2013). A density of 1023 kg·m ⁻³ and a reef area of 1×10 ⁷ m ² were also used. Thus Flux = 0.072 m·hr ⁻¹ × 0.0283 mol·kg ⁻¹ ·atm ⁻¹ × (440×10 ⁻⁶ atm – 399×10 ⁻⁶ atm) × 1023 kg·m ⁻³ × 1×10 ⁷ m ² × 24 hr·day ⁻¹ × 365 day·yr ⁻¹ = 0.8×10 ⁷ mol C·yr ⁻¹
Surface water DIC - TOC	1:2	189	Photosynthesis	Using a photosynthetic rate of 519 mmol C·m ⁻² ·day ⁻¹ adapted from Falter et al. (2008) yields a total flux of 519×10 ⁻³ mol C·m ⁻² ·day ⁻¹ × 2000 m × 5000 m × 365 days·yr ⁻¹ = 1.89×10 ⁹ mol C·yr ⁻¹

Flux	Flux $CF_{i,j}$	10^7 mol C·yr ⁻¹	Process	Reference/Comments
Surface water – Porewater (Sandy sediments)	1:3	13.8	Advection	Based on an advection rate of 3.0 cm·hr ⁻¹ (Shum 1993; Fram et al. 2014). This results in a porewater residence time of the upper 20 cm of 6.7 hrs. Assuming a porosity of 52% and an areal sand coverage of 5% (NOAA Shallow Water Benthic Habitat Survey) results in a porewater volume of $5.2 \times 10^4 \text{ m}^3$ and a surface water DIC of $0.001973 \text{ mol C} \cdot \text{kg}^{-1}$ the flux = $(5.2 \times 10^4 \text{ m}^3 \times 1023 \text{ kg} \cdot \text{m}^{-3} \times 0.001973 \text{ mol C} \cdot \text{kg}^{-1}) / 6.7 \text{ hrs} \times 8760 \text{ hrs} \cdot \text{yr}^{-1} = 1.38 \times 10^8 \text{ mol C} \cdot \text{yr}^{-1}$
Surface water – Reef Framework (NEC)	1:8, 9, 10	91.3 (11.9, 57.5, 21.9)	Calcification/ Dissolution	An average net calcification rate of $0.25 \text{ mol CaCO}_3 \cdot \text{m}^{-2} \cdot \text{d}^{-1}$ was estimated from Kinsey (1979), Smith et al. (1981), Kinsey (1985), and Shamberger et al. (2011) for an annual rate of $0.25 \text{ mol CaCO}_3 \cdot \text{m}^{-2} \cdot \text{d}^{-1} \times 5000 \text{ m} \times 2000 \text{ m} \times 365 \text{ d} \cdot \text{yr}^{-1} = 9.13 \times 10^8 \text{ mol CaCO}_3 \cdot \text{yr}^{-1}$. This rate was partitioned to each framework reservoir based on the relative abundance of the mineral phase in question (e.g. calcite = 13% $\times 9.13 \times 10^8 \text{ mol CaCO}_3 \cdot \text{yr}^{-1} = 1.19 \times 10^8 \text{ mol CaCO}_3 \cdot \text{yr}^{-1}$)
Surface water – Reef framework porewater	1:11	120	Advection	Based on a residence time in the upper 1 meter of framework of 2.9 days and a porosity of 50% (Tribble et al. 1988; Tribble 1990). The reef framework is assumed to cover 95% of the area of the reef (NOAA Shallow Water Benthic Habitat Survey). Surface DIC is $1973 \mu\text{mol} \cdot \text{kg}^{-1}$, thus $2000 \text{ m} \times 5000 \text{ m} \times 1 \text{ m} \times 50\% \times 95\% \times 1023 \text{ kg} \cdot \text{m}^{-3} \times 1973 \times 10^{-6} \text{ mol} \cdot \text{kg}^{-1} / 2.9 \text{ days} \times 365 \text{ days} \cdot \text{yr}^{-1} = 1.20 \times 10^9 \text{ mol C} \cdot \text{yr}^{-1}$
Open ocean – Total organic carbon (TOC)	O:2	221	Physical Exchange	Open ocean DON $6.1 \text{ mmol} \cdot \text{m}^{-3}$ (Smith et al. 1981; Cox et al. 2006). A C:N of 6.625 was assumed. Thus, $\text{DOC} = 4.73 \times 10^{10} \text{ m}^3 \cdot \text{yr}^{-1} \times 0.0061 \text{ mol N} \cdot \text{m}^{-3} \times 6.625 = 1.41 \times 10^9 \text{ mol C} \cdot \text{yr}^{-1}$. An exterior bay POC of $6.3 \text{ mmol} \cdot \text{m}^{-3}$ (Smith et al. 1981; Cox et al. 2006) was used resulting in POC flux of $2.97 \times 10^8 \text{ mol C} \cdot \text{yr}^{-1}$. Total organic carbon was the sum of DOC + POC = $2.21 \times 10^9 \text{ mol C} \cdot \text{yr}^{-1}$.

Flux	Flux $CF_{i,j}$	10^7 mol C·yr ⁻¹	Process	Reference/Comments
Surface water TOC – open ocean	2:O	237	Physical Exchange	An interior reef DON 6.3 mmol·m ⁻³ (Smith et al. 1981; Cox et al. 2006) was assumed. A C:N of 6.625 was assumed. Thus, DOC = 4.73×10 ¹⁰ m ³ ·yr ⁻¹ × 0.0063 mol N·m ⁻³ × 6.625 = 1.98×10 ⁹ mol C·yr ⁻¹ . An interior reef POC of 8.34 mmol·m ⁻³ (Smith et al. 1981; Cox et al. 2006) was used resulting in POC flux of 3.98×10 ⁸ mol C·yr ⁻¹ . Total organic carbon was the sum of DOC + POC = 2.37×10 ⁹ mol C·yr ⁻¹ .
Surface water TOC – DIC	2:1	159	Respiration	Using a respiration rate of 435 mmol C·m ⁻² ·day ⁻¹ adapted from Falter et al. (2008) yields a total flux of 435×10 ⁻³ mol C·m ⁻² ·day ⁻¹ × 2000 m × 5000 m × 365 days·yr ⁻¹ = 1.59×10 ⁹ mol C·yr ⁻¹
Surface Water TOC – sediments and framework	2:4,1 2	14.7 (0.73, 13.9)	Sedimentatio n	A sedimentation rate of organic carbon of 483 mg·m ⁻² ·d ⁻¹ was adapted from Taguchi (1982). 0.483 g·m ⁻² ·d ⁻¹ × 2000 m × 5000 m/12.01 g C·mol ⁻¹ × 365 d·yr ⁻¹ = 1.47×10 ⁸ mol C·yr ⁻¹ . 5% of the sedimentation went to the permeable sediments and 95% went to the reef framework based on areal coverage.
Porewater DIC (permeable sediments) – Surface water	3:1	15.0	Advection	Based on an advection rate of 3.0 cm·hr ⁻¹ (Shum 1993; Fram et al. 2014). This results in a porewater residence time of the upper 20 cm of 6.7 hrs. Assuming a porosity of 52% and an areal sand coverage of 5% results in a porewater volume of 5.2×10 ⁴ m ³ and a porewater DIC of 0.002150 mol C·kg ⁻¹ the flux = (5.2×10 ⁴ m ³ × 1023 kg·m ⁻³ × 0.002150 mol C·kg ⁻¹)/6.7 hrs × 8760 hrs·yr ⁻¹ = 1.50×10 ⁸ mol C·yr ⁻¹
Oxic porewater – Sediment calcite	3:5	0	Abiotic Precipitation	No calcite precipitation due to inhibition from magnesium ions (Berner et al. 1978), despite the porewater being thermodynamically supersaturated.
Oxic porewater – Sediment aragonite	3:6	0.0046	Abiotic Precipitation	Using $R=10^{1.09}(\Omega-1)^{2.36}$ precipitation equation for aragonite from Zhong and Mucci (1989) so $R=10^{1.09}(\Omega-1)^{2.36} \times M \times I_p \times I_o$, where M is the DIC reservoir mass, I _p and I _o are phosphate and DOM inhibition coefficients of 0.26 and 0.34, respectively, calculated from Berner et al. (1978) 10 ^{1.09} μmol·m ⁻² ·hr ⁻¹ × 1×10 ⁻⁶ mol·μmol ⁻¹ × (2.68-1) ^{2.36} × 1.38×10 ⁶ g C × 0.26 × 0.34 × 8760 hrs·yr ⁻¹ = 4.63×10 ⁴ mol C·yr ⁻¹

Flux	Flux CF_{ij}	10^7 mol $C \cdot yr^{-1}$	Process	Reference/Comments
Oxic porewater – Sediment Mg- calcite	3:7	0	Abiotic Precipitation	There is no high Mg-calcite precipitation as $\Omega < 1$
Sediment organic matter – Oxic porewater	4:3	0.48	Microbial Respiration	Respiration was set assuming a 0.9:1 ratio between TA release from Mg-calcite dissolution (4.38×10^6 mol $C \cdot yr^{-1}$) and DIC production from oxic respiration (Moulin et al. 1985; Morse and Mackenzie 1990, Drupp et al., in review). Respiration = $1.1 \times 4.38 \times 10^6$ mol $C \cdot yr^{-1}$.
Sediment OM – Anoxic sediment OM	4:13	0.25	Burial To Anoxic Layer	The burial rate for the sediment organic matter was defined as the difference between sedimentation and respiration. Thus 7.34×10^6 mol $C \cdot yr^{-1} - 4.83 \times 10^6$ mol $C \cdot yr^{-1} = 2.51 \times 10^6$ mol $C \cdot yr^{-1}$.
Sediment calcite – Oxic porewater	5:3	0	Dissolution	The porewater is supersaturated with respect to calcite so no dissolution occurs.
Sediment calcite – Anoxic sediment calcite	5:14	3.33	Burial To Anoxic Layer	Burial was defined as $B_x = P_x + FE_x - D_x - E_x$, where x is the mineral phase, P is precipitation, FE is the framework erosion (see fluxes 8:5, 9:6, and 10:7), D is the dissolution and E is the export off the reef (30% of erosion, section 4.4.2.1). For calcite, $0 + 4.76 \times 10^7$ mol $C \cdot yr^{-1} - 0 - 1.43 \times 10^7$ mol $C \cdot yr^{-1} = 3.33 \times 10^7$ mol $C \cdot yr^{-1}$
Sediment calcite export - ocean	5:0	1.4	Advection	Export from the reef was defined as 30% of total erosion, so 4.76×10^7 mol $C \cdot yr^{-1} \times 30\% = 1.43 \times 10^7$ mol $C \cdot yr^{-1}$
Sediment aragonite – Oxic porewater	6:3	0	Dissolution	The porewater is supersaturated with respect to aragonite so no dissolution occurs.
Sediment aragonite – Anoxic sediment aragonite	6:15	16.2	Burial	Burial was defined as $B_x = P_x + FE_x - D_x - E_x$, where x is the mineral phase, P is precipitation, FE is the framework erosion (see fluxes 8:5, 9:6, and 10:7), D is the dissolution and E is the export off the reef (30% of erosion, section 4.4.2.1). For aragonite, 4.6×10^4 mol $C \cdot yr^{-1} + 2.31 \times 10^8$ mol $C \cdot yr^{-1} - 0 - 6.92 \times 10^7$ mol $C \cdot yr^{-1} = 1.62 \times 10^8$ mol $C \cdot yr^{-1}$
Sediment aragonite export - ocean	6:0	6.9	Advection	Export from the reef was defined as 30% of total erosion for the mineral phase, so 2.31×10^8 mol $C \cdot yr^{-1} \times 30\% = 6.92 \times 10^7$ mol $C \cdot yr^{-1}$

Flux	Flux $CF_{i,j}$	10^7 mol C·yr ⁻¹	Process	Reference/Comments
Sediment 15% Mg-calcite – Oxic porewater	7:3	0.44	Dissolution	Based on the dissolution equation of $R=10^{2.32}(1-\Omega)^{3.55}$ for 15% Mg-calcite from Walter and Morse (1985), using an average biogenic 15% Mg-calcite for minimally prepared substrates (Plummer and Mackenzie 1974) and $\Omega=0.8$ (Drupp et al., in review). Phosphate and dissolved organic matter inhibition were 0.26 and 0.34, respectively (Bernier et al., 1978, see Section 4.3.2.2). Thus $10^{2.32} \mu\text{mol}\cdot\text{g}^{-1}\cdot\text{hr}^{-1} \times 1 \times 10^{-6} \text{ mol}\cdot\mu\text{mol}^{-1} \times (1-0.8)^{3.55} \times 3.05 \times 10^{10} \text{ g CaCO}_3 \times 0.26 \times 0.34 \times 8760 \text{ hrs}\cdot\text{yr}^{-1} = 4.38 \times 10^6 \text{ mol C}\cdot\text{yr}^{-1}$.
Sediment 15% Mg-calcite – Anoxic sediment 15% Mg-calcite	7:16	5.72	Burial	Burial was defined as $B_x = P_x + FE_x - D_x - E_x$, where \times is the mineral phase, P is precipitation, FE is the framework erosion (see fluxes 8:5, 9:6, and 10:7), D is the dissolution and E is the export off the reef (30% of erosion, section 4.4.2.1). For Mg-calcite, $0 + 8.79 \times 10^7 \text{ mol C}\cdot\text{yr}^{-1} - 0.44 \times 10^7 \text{ mol C}\cdot\text{yr}^{-1} - 8.79 \times 10^7 \text{ mol C}\cdot\text{yr}^{-1} \times 0.3 = 5.72 \times 10^7 \text{ mol C}\cdot\text{yr}^{-1}$.
Sediment Mg-calcite export - ocean	7:0	2.64	Advection	Export from the reef was defined as 30% of total erosion for the mineral phase, so $8.79 \times 10^7 \text{ mol C}\cdot\text{yr}^{-1} \times 30\% = 2.64 \times 10^7 \text{ mol C}\cdot\text{yr}^{-1}$.
Calcite framework to surface water DIC	8:1	0.29	Chemical Bioerosion	A bioerosion rate due to euendolithic algae and boring sponges from Tribollet et al. (2006) and Fang et al. (2013) of $0.6 \text{ kg CaCO}_3\cdot\text{m}^{-2}\cdot\text{yr}^{-1}$ was assumed for the reef framework which has a total area of $9.5 \times 10^6 \text{ m}^2$. 40% of the bioerosion was assumed to result in DIC being released to the water column and 60% was assumed to result in particulate inorganic carbon using estimates from Andersson and Gledhill (2013). 13% of the reef framework is considered calcite, thus $9.5 \times 10^6 \text{ m}^2 \times 13\% \times 600 \text{ g CaCO}_3\cdot\text{m}^{-2}\cdot\text{yr}^{-1} / 100.1 \text{ g CaCO}_3\cdot\text{mol}^{-1} \times 40\% = 2.96 \times 10^6 \text{ mol C}\cdot\text{yr}^{-1}$.

Flux	Flux $CF_{i,j}$	10^7 mol C·yr ⁻¹	Process	Reference/Comments
Calcite framework to sediment calcite	8:5	4.76	Mechanical Erosion	A bioerosion rate due to microborers (previously shown, 8:1), assuming 60% of the dissolution results in “chips” was combined with a bioerosion “grazing” rate (Tribollet et al. 2006; Tribollet 2008) of 3.5 kg CaCO ₃ ·m ⁻² ·yr ⁻¹ . This value includes mechanical erosion by wave activity and was constrained by setting an organic carbon burial weight in the sediments at ~3% (see Section 4.4.2.1). Bioerosion due to grazing results in particulate inorganic carbon available for export to the sediments. Total framework erosion leading to particulate carbon was (3500 g CaCO ₃ ·m ⁻² ·yr ⁻¹ + (600 g CaCO ₃ ·m ⁻² ·yr ⁻¹ × 60%)/100.1 g CaCO ₃ ·mol ⁻¹ × 9.5 × 10 ⁶ m ² = 3.66 × 10 ⁸ mol C·yr ⁻¹ . The model assumes 13% of the framework is calcite so 3.66 × 10 ⁸ mol C·yr ⁻¹ × 13% = 4.76 × 10 ⁷ mol C·yr ⁻¹ .
Calcite framework to framework porewater	8:11	0	Dissolution	The framework porewater is supersaturated with respect to calcite so no dissolution occurs.
Calcite framework to burial	8:B	6.80	Burial	Burial of framework is the sum of all over fluxes involving the framework so Burial = calcification + precipitation – chemical bioerosion – mechanical erosion – dissolution. For calcite, 1.19 × 10 ⁸ mol C·yr ⁻¹ + 0 – 2.96 × 10 ⁶ mol C·yr ⁻¹ – 4.76 × 10 ⁷ mol C·yr ⁻¹ – 0 = 6.80 × 10 ⁷ mol C·yr ⁻¹
Aragonite framework to surface water DIC	9:1	1.43	Chemical Bioerosion	A bioerosion rate due to euendolithic algae and boring sponges from Tribollet et al. (2006) and Fang et al. (2013) of 0.6 kg CaCO ₃ ·m ⁻² ·yr ⁻¹ was assumed for the reef framework which has a total area of 9.5 × 10 ⁶ m ² . 40% of the bioerosion was assumed to result in DIC being released to the water column and 60% was assumed to result in particulate inorganic carbon using estimates from Andersson and Gledhill (2013). 63% of the reef framework is considered aragonite, thus 9.5 × 10 ⁶ m ² × 63% × 600 g CaCO ₃ ·m ⁻² ·yr ⁻¹ /100.1 g CaCO ₃ ·mol ⁻¹ × 40% = 1.43 × 10 ⁷ mol C·yr ⁻¹

Flux	Flux $CF_{i,j}$	10^7 mol C·yr ⁻¹	Process	Reference/Comments
Aragonite framework to sediment aragonite	9:6	23.1	Mechanical Erosion	A bioerosion rate due to microborers (previously shown, 8:1), assuming 60% of the dissolution results in “chips” was combined with a bioerosion “grazing” rate (Tribollet et al. 2006; Tribollet 2008) of 3.5 kg CaCO ₃ ·m ⁻² ·yr ⁻¹ . This value includes mechanical erosion by wave activity and was constrained by setting an organic carbon burial weight in the sediments at ~3% (see Section 4.4.2.1). Bioerosion due to grazing results in particulate inorganic carbon available for export to the sediments. Total framework erosion leading to particulate carbon was (3500 g CaCO ₃ ·m ⁻² ·yr ⁻¹ + (600 g CaCO ₃ ·m ⁻² ·yr ⁻¹ × 60%))/100.1 g CaCO ₃ ·mol ⁻¹ × 9.5 × 10 ⁶ m ² = 3.66 × 10 ⁸ mol C·yr ⁻¹ . The model assumes 63% of the framework is aragonite so 3.66 × 10 ⁸ mol C·yr ⁻¹ × 63% = 2.31 × 10 ⁸ mol C·yr ⁻¹ .
Aragonite framework to framework porewater	9:11	0	Dissolution	The framework porewater is supersaturated with respect to aragonite so no dissolution occurs.
Aragonite framework to burial	9:B	33.7	Burial	Burial of framework is the sum of all over fluxes involving the framework so Burial = calcification + precipitation – chemical bioerosion – mechanical erosion – dissolution. For aragonite, 5.75 × 10 ⁸ mol C·yr ⁻¹ + 7.71 × 10 ⁶ mol C·yr ⁻¹ - 1.43 × 10 ⁷ mol C·yr ⁻¹ - 2.31 × 10 ⁸ mol C·yr ⁻¹ - 0 = 3.37 × 10 ⁸ mol C·yr ⁻¹
Mg-calcite framework to surface water DIC	10:1	0.55	Chemical Bioerosion	A bioerosion rate due to euendolithic algae and boring sponges from Tribollet et al. (2006) and Fang et al. (2013) of 0.6 kg CaCO ₃ ·m ⁻² ·yr ⁻¹ was assumed for the reef framework which has a total area of 9.5 × 10 ⁶ m ² . 40% of the bioerosion was assumed to result in DIC being released to the water column and 60% was assumed to result in particulate inorganic carbon using estimates from Andersson and Gledhill (2013). 24% of the reef framework is considered Mg-calcite, thus 9.5 × 10 ⁶ m ² × 24% × 600 g CaCO ₃ ·m ⁻² ·yr ⁻¹ /100.1 g CaCO ₃ ·mol ⁻¹ × 40% = 5.47 × 10 ⁶ mol C·yr ⁻¹

Flux	Flux CF_{ij}	10^7 mol C·yr ⁻¹	Process	Reference/Comments
Mg-calcite framework to sediment mg-calcite	10:7	8.79	Mechanical Erosion	A bioerosion rate due to microborers (previously shown, 8:1), assuming 60% of the dissolution results in “chips” was combined with a bioerosion “grazing” rate (Tribollet et al. 2006; Tribollet 2008) of 3.5 kg CaCO ₃ ·m ⁻² ·yr ⁻¹ . This value includes mechanical erosion by wave activity and was constrained by setting an organic carbon burial weight in the sediments at ~3% (see Section 4.4.2.1). Bioerosion due to grazing results in particulate inorganic carbon available for export to the sediments. Erosion leading to particulate carbon was (3500 g CaCO ₃ ·m ⁻² ·yr ⁻¹ + (600 g CaCO ₃ ·m ⁻² ·yr ⁻¹ × 60%))/100.1 g CaCO ₃ ·mol ⁻¹ × 9.5 × 10 ⁶ m ² = 3.66 × 10 ⁸ mol C·yr ⁻¹ . The model assumes 24% of the framework is Mg-calcite so 3.66 × 10 ⁸ mol C·yr ⁻¹ × 24% = 8.79 × 10 ⁷ mol C·yr ⁻¹ .
Mg-calcite framework to framework porewater	10:11	12.4	Dissolution	Based on the dissolution equation of $R=10^{2.32}(1-\Omega)^{3.55}$ for 15% Mg-calcite from Walter and Morse (1985), using an average biogenic 15% Mg-calcite for minimally prepared substrates (Plummer and Mackenzie 1974) $\Omega=0.87$, estimated from TA and DIC from Tribble (1990). Phosphate and DOM inhibition were 0.26 and 0.42 (Bernier et al., 1978, see Section 4.4.2.2). Thus $10^{2.32} \mu\text{mol}\cdot\text{g}^{-1}\cdot\text{hr}^{-1} \times 1 \times 10^{-6} \text{ mol}\cdot\mu\text{mol}^{-1} \times (1-0.87)^{3.55} \times 3.09 \times 10^{12} \text{ g CaCO}_3 \times 0.26 \times 0.41 \times 8760 \text{ hrs}\cdot\text{yr}^{-1} = 1.24 \times 10^8 \text{ mol C}\cdot\text{yr}^{-1}$.
Mg-calcite framework to burial	10:B	0.21	Burial	Burial of framework is the sum of all over fluxes involving the framework so Burial = calcification + precipitation – chemical bioerosion – mechanical/bioerosion – dissolution. For Mg-calcite, $2.19 \times 10^8 \text{ mol C}\cdot\text{yr}^{-1} + 0 - 5.47 \times 10^6 \text{ mol C}\cdot\text{yr}^{-1} - 8.79 \times 10^7 \text{ mol C}\cdot\text{yr}^{-1} - 1.24 \times 10^8 \text{ mol C}\cdot\text{yr}^{-1} = 2.11 \times 10^6 \text{ mol C}\cdot\text{yr}^{-1}$
Reef framework porewater to surface water	11:1	145	Advection	Based on a residence time in the upper 1 meter of framework of 2.9 days and a porosity of 50% (Tribble et al. 1988; Tribble 1990). The reef framework is assumed to cover 95% of the area of the reef (NOAA Shallow Water Benthic Habitat Survey). Porewater DIC is 2380 $\mu\text{mol}\cdot\text{kg}^{-1}$, thus $2000 \text{ m} \times 5000 \text{ m} \times 1 \text{ m} \times 50\% \times 95\% \times 1023 \text{ kg}\cdot\text{m}^{-3} \times 2384 \times 10^{-6} \text{ mol}\cdot\text{kg}^{-1} / 2.9 \text{ days} \times 365 \text{ days}\cdot\text{yr}^{-1} = 1.45 \times 10^9 \text{ mol C}\cdot\text{yr}^{-1}$

Flux	Flux $CF_{i,j}$	10^7 mol C·yr ⁻¹	Process	Reference/Comments
Reef framework porewater to calcite framework	11:8	0	Abiotic Precipitation	No calcite precipitation due to inhibition from magnesium ions (Berner et al. 1978), despite the porewater being thermodynamically supersaturated.
Reef framework porewater to aragonite framework	11:9	0.77	Abiotic Precipitation	Using $R=10^{1.09}(\Omega-1)^{2.36}$ precipitation equation for aragonite from Zhong and Mucci (1989) so $R=10^{1.09}(\Omega-1)^{2.36} \times M \times I_p \times I_o$, where M is the DIC reservoir mass, and I_p and I_o are phosphate and DOM inhibition coefficients of 0.26 and 0.42, respectively, calculated from Berner et al. (1978). $\Omega=2.9$ was estimated from (Tribble 1990; Tribble 1993). $10^{1.09} \mu\text{mol}\cdot\text{m}^{-2}\cdot\text{hr}^{-1} \times 1 \times 10^{-6} \text{ mol}\cdot\mu\text{mol}^{-1} \times (2.9-1)^{2.36} \times 1.39 \times 10^8 \text{ g C} \times 0.26 \times 0.42 \times 8760 \text{ hrs}\cdot\text{yr}^{-1} = 7.71 \times 10^6 \text{ mol C}\cdot\text{yr}^{-1}$
Reef framework porewater to Mg-calcite framework	11:1 0	0	Abiotic Precipitation	There is no high Mg-calcite precipitation as $\Omega < 1$.
Framework OC to framework porewater	12:1 1	13.4	Respiration	A respiration rate of $1.34 \times 10^8 \text{ mol C}\cdot\text{yr}^{-1}$ was set by constraining organic carbon burial to ~1% of total burial (see Section 4.4.3), and assuming a $\Delta\text{TA}:\Delta\text{DIC}$ of 1.2:1. The upper limit of respiration was $1.39 \times 10^8 \text{ mol C}\cdot\text{yr}^{-1}$ which is equal to the sedimentation rate. The respiration to dissolution ratio is 1.2 and is expected to be between 1:1 and 2:1 because of the mix of oxic respiration and sulfate reduction (see Section 4.4.3). Tribble et al. (1988) measured a respiration in the framework of Checker Reef, a patch reef, in Kaneohe Bay to be 25% of the water column gross photosynthesis (GP). Our rate represents only 7% of water column GP, but sedimentation of OC, the limiting factor, is likely less on the barrier reef than it is on the interior of Checker Reef.
Framework OC to burial	12:B	0.50	Burial	The burial of organic matter within the reef framework was the difference between the sedimentation rate of OC and the respiration rate, thus $1.39 \times 10^8 \text{ mol C}\cdot\text{yr}^{-1} - 1.34 \times 10^8 \text{ mol C}\cdot\text{yr}^{-1} = 4.99 \times 10^6 \text{ mol C}\cdot\text{yr}^{-1}$. This represents a burial of wt. 1.2% OC relative to the burial rates of the carbonate framework.

Flux	Flux CF_{ij}	10^7 mol C·yr ⁻¹	Process	Reference/Comments
Anoxic sediment OC to anoxic porewater	13:1 7	0.23	Respiration	A respiration rate of 2.31×10^6 mol C·yr ⁻¹ was estimated by assuming a burial of wt. ~0.2% organic carbon relative to the total carbonate sediment burial, with the remaining OC being respired.
Anoxic sediment OC to burial	13:B	0.02	Burial	Overall burial is the difference between the burial from the oxic layer and the respiration rate so 2.50×10^6 mol C·yr ⁻¹ - 2.31×10^6 mol C·yr ⁻¹ = 1.87×10^5 mol C·yr ⁻¹ . This is equal to a wt. 0.1% OC burial.
Anoxic sediment calcite to anoxic porewater	14:1 7	0	Dissolution	There is no dissolution of calcite because $\Omega > 1$.
Anoxic sediment calcite to burial	14:B	3.33	Burial	The burial of the anoxic carbonate sediments is calculated as the sum of the burial from the oxic layer plus precipitation minus dissolution. For calcite, 3.33×10^7 mol C·yr ⁻¹ was the burial rate from the oxic layer, and no precipitation or dissolution occurred.
Anoxic sediment aragonite to anoxic porewater	15:1 7	0	Dissolution	There is no dissolution of aragonite because $\Omega > 1$.
Anoxic sediment aragonite to burial	15:B	16.2	Burial	The burial of the anoxic carbonate sediments is calculated as the sum of the burial from the oxic layer plus precipitation minus dissolution. For aragonite, 1.62×10^8 mol C·yr ⁻¹ + 6.5×10^4 mol C·yr ⁻¹ - 0 = 1.62×10^8 mol C·yr ⁻¹
Anoxic sediment Mg-calcite to anoxic porewater	16:1 7	0.10	Dissolution	Based on the dissolution equation of $R = 10^{2.32}(1 - \Omega)^{3.55}$ for 15% Mg-calcite from Walter and Morse (1985), using an average biogenic 15% Mg-calcite for minimally prepared substrates (Plummer and Mackenzie 1974) $\Omega = 0.86$, estimated from TA and DIC from Tribble (1990). Phosphate and dissolved organic matter inhibition were 0.06 and 0.40, respectively (Berner et al. 1978). Thus $10^{2.32} \mu\text{mol} \cdot \text{g}^{-1} \cdot \text{hr}^{-1} \times 10^{-6} \text{mol} \cdot \mu\text{mol}^{-1} \times (1 - 0.86)^{3.55} \times 1.22 \times 10^{12} \text{g CaCO}_3 \times 0.06 \times 0.40 \times 8760 \text{hrs} \cdot \text{yr}^{-1} = 1.04 \times 10^6 \text{mol C} \cdot \text{yr}^{-1}$.

Flux	Flux $CF_{i,j}$	10^7 mol C·yr ⁻¹	Process	Reference/Comments
Anoxic sediment Mg-calcite to burial	16:B	5.6	Burial	The burial of the anoxic carbonate sediments is calculated as the sum of the burial from the oxic layer plus precipitation minus dissolution. For Mg-calcite, 5.7×10^7 mol C·yr ⁻¹ + 0 - 1.10×10^6 mol C·yr ⁻¹ = 5.59×10^7 mol C·yr ⁻¹ .
Anoxic porewater DIC to oxic porewater DIC	17:3	0.33	Advection/ Diffusion	A combination of Fickian Diffusion over the entire porewater gradient was used along with advective transport. A residence time of 4.6 days, slightly longer, but comparable to residence times of porewater in the more permeable reef framework measured by Tribble (1990). A diffusion coefficient of 1.34×10^{-9} m ² ·s ⁻¹ (Berner 1980) was used and the DIC gradient was 2.35 mmol·kg ⁻¹ - 2.15 mmol·kg ⁻¹ over 0.8 m. The advective flux was 3.28×10^6 mol C·yr ⁻¹ plus the diffusion flux of 2.22×10^3 mol C·yr ⁻¹ equals a total transport of 3.29×10^6 mol C·yr ⁻¹ .
Anoxic porewater – anoxic sediment calcite	17:1 4	0	Abiotic Precipitation	No calcite precipitation due to inhibition from magnesium ions (Berner et al. 1978), despite the porewater being thermodynamically supersaturated.
Anoxic porewater – anoxic sediment aragonite	17:1 5	0.007	Abiotic Precipitation	Using $R=10^{1.09}(\Omega-1)^{2.36}$ precipitation equation for aragonite from Zhong and Mucci (1989) so $R=10^{1.09}(\Omega-1)^{2.36} \times M \times I_p \times I_o$, where M is the DIC reservoir mass, and I_p and I_o are phosphate and DOM inhibition coefficients of 0.06 and 0.40, respectively, calculated from Berner et al. (1978). $\Omega=2.9$ was estimated from (Tribble, 1990; Tribble, 1993; Drupp et al., in review). $10^{1.09} \mu\text{mol} \cdot \text{m}^{-2} \cdot \text{hr}^{-1} \times 1 \times 10^{-6} \text{ mol} \cdot \mu\text{mol}^{-1} \times (2.9-1)^{2.36} \times 6.01 \times 10^6 \text{ g C} \times 0.06 \times 0.40 \times 8760 \text{ hrs} \cdot \text{yr}^{-1} = 6.5 \times 10^4 \text{ mol C} \cdot \text{yr}^{-1}$
Anoxic porewater – anoxic sediment Mg-calcite	17:1 6	0	Abiotic Precipitation	There is no precipitation of Mg-calcite because $\Omega < 1$.

A.6 References

- Andersson AJ, Gledhill D (2013) Ocean acidification and coral reefs: effects on breakdown, dissolution, and net ecosystem calcification. *Ann Rev Mar Sci* 5:321–48. doi: 10.1146/annurev-marine-121211-172241
- Atkinson MJ, Falter JL (2003) Biogeochemistry of coral reefs. In: Black KD, Shimmiel GB (eds) *Biogeochemistry of Marine Systems*. Blackwell Publishing Ltd., pp 40–64
- Berner RA (1980) *Early Diagenesis: A Theoretical Approach*. Princeton University Press, Princeton, NJ
- Berner RA, Westrich JT, Graber R, et al (1978) Inhibition of aragonite precipitation from supersaturated seawater; a laboratory and field study. *Am J Sci* 278:816–837.
- Cox E, Ribes M, Kinzie RA I (2006) Temporal and spatial scaling of planktonic responses to nutrient inputs into a subtropical embayment. *Mar Ecol Prog Ser* 324:19–35. doi: 10.3354/meps324019
- Drupp PS, De Carlo EH, Mackenzie FT, et al (2011) Nutrient Inputs, Phytoplankton Response, and CO₂ Variations in a Semi-Enclosed Subtropical Embayment, Kaneohe Bay, Hawai‘i. *Aquat Geochemistry* 17:473–498. doi: 10.1007/s10498-010-9115-y
- Drupp PS, De Carlo EH, Mackenzie FT, et al (2013) Comparison of CO₂ Dynamics and Air–Sea Gas Exchange in Differing Tropical Reef Environments. *Aquat Geochemistry* 19:371–397. doi: 10.1007/s10498-013-9214-7
- Drupp PS, De Carlo EH, Mackenzie FT Porewater CO₂-Carbonic Acid System Chemistry in Permeable Carbonate Reef Sands, *in review at Marine Chemistry*
- Falter JL, Lowe RJ, Atkinson MJ, et al (2008) Continuous measurements of net production over a shallow reef community using a modified Eulerian approach. *J Geophys Res* 113:C07035. doi: 10.1029/2007JC004663
- Fang JKH, Mello-Athayde M a, Schönberg CHL, et al (2013) Sponge biomass and bioerosion rates increase under ocean warming and acidification. *Glob Chang Biol* 19:3581–3591.
- Fram JP, Pawlak GR, Sansone FJ, et al (2014) Miniature thermistor chain for determining surficial sediment porewater advection. *Limnol Oceanogr Methods* 12:155–165.
- Ho DT, Law CS, Smith MJ, et al (2006) Measurements of air-sea gas exchange at high wind speeds in the Southern Ocean: Implications for global parameterizations. *Geophys Res Lett* 33:L16611. doi: 10.1029/2006GL026817
- Kinsey DW (1979) *Carbon Turnover and Accumulation by Coral Reefs*. University of Hawai‘i
- Kinsey DW (1985) Metabolism, Calcification and Carbon Production. *Proc 5th Int Coral Reef Congr* 4:505–526.
- Lowe RJ, Falter JL, Monismith SG, Atkinson MJ (2009a) Wave-Driven Circulation of a Coastal Reef–Lagoon System. *J Phys Oceanogr* 39:873–893. doi: 10.1175/2008JPO3958.1
- Lowe RJ, Falter JL, Monismith SG, Atkinson MJ (2009b) A numerical study of circulation in a coastal reef-lagoon system. *J Geophys Res* 114:C06022. doi: 10.1029/2008JC005081
- Massaro RFS, De Carlo EH, Drupp PS, et al (2012) Multiple Factors driving Variability of CO₂ Exchange Between the Ocean and Atmosphere in a Tropical Coral Reef Environment.

- Aquat Geochemistry 18:357–386. doi: 10.1007/s10498-012-9170-7
- Morse J, Zullig J, Bernstein L, et al (1985) Chemistry of calcium carbonate-rich shallow water sediments in the Bahamas. *Am J Sci* 285:147–185.
- Morse JW, Mackenzie FT (1990) *Geochemistry of Sedimentary Carbonates*. Elsevier, Amsterdam, The Netherlands
- Moulin E, Jordens A, Wollast R (1985) Influence of the Aerobic Bacterial Respiration on the Early Dissolution of Carbonates in Coastal Sediments. In: *Progress in Belgian Oceanographic Research*. p 13
- Plummer LN, Mackenzie FT (1974) Predicting Mineral Solubility From Rate Data: Application to the Dissolution of Magnesian Calcite. *Am J Sci* 274:61–83.
- Redfield A (1934) On the proportions of organic derivatives in seawater and their relation to the composition of plankton.pdf. In: Daniel RJ (ed) *James Johnstone Memorial Volume*. University Press of Liverpool, pp 176–192
- Shamberger KEF, Feely RA, Sabine CL, et al (2011) Calcification and organic production on a Hawaiian coral reef. *Mar Chem* 127:64–75. doi: 10.1016/j.marchem.2011.08.003
- Shum KT (1993) The Effects of Wave-Induced Pore Water Circulation on the Transport of Reactive Solutes Below a Rippled Sediment Bed. *J Geophys Res Ocean* 98:10289–10301.
- Smith S V., Kimmerer W, Laws E (1981) Kaneohe Bay sewage diversion experiment: perspectives on ecosystem responses to nutritional perturbation.
- Taguchi S (1982) Seasonal study of fecal pellets and discarded houses of appendicularia in a subtropical inlet, Kaneohe Bay, Hawai‘i. *Estuarine, Coastal, Shelf Sci* 14:545–555.
- Tribble GW (1990) *Early Diagenesis in a Coral Reef Framework*. University of Hawai‘i
- Tribble GW (1993) Organic Matter Oxidation and Aragonite Diagenesis in a Coral Reef. *SEPM J Sediment Res Vol.* 63:523–527.
- Tribble GW, Sansone FJ, Li Y, et al (1988) Material Fluxes from a Reef Framework. *Proc 6th Int Coral Reef Symp Aust* 2:577–582.
- Tribble GW, Sansone FJ, Smith S V. (1990) Stoichiometric modeling of carbon diagenesis within a coral reef framework. *Geochim Cosmochim Acta* 54:2439–2449.
- Tribollet A (2008) Dissolution of dead corals by euendolithic microorganisms across the northern Great Barrier Reef (Australia). *Microb Ecol* 55:569–80.
- Tribollet A, Langdon C, Golubic S, Atkinson M (2006) Endolithic Microflora Are Major Primary Producers in Dead Carbonate Substrates of Hawaiian Coral Reefs. *J Phycol* 42:292–303. doi: 10.1111/j.1529-8817.2006.00198.x
- Walter LM, Morse JW (1985) The dissolution kinetics of shallow marine carbonates in seawater: A laboratory study. *Geochim Cosmochim Acta* 49:1503–1515.
- Wanninkhof R (1992) Relationship between wind speed and gas exchange. *J Geophys Res* 97:7373–7382.
- Zhong S, Mucci A (1989) Calcite and aragonite precipitation from seawater solutions of various salinities: precipitation rates and overgrowth compositions. *Chem Geol* 78:283–299.